Studying excited states of the nucleon with the HADES detector at GSI

Studium von angeregten Nukleon-Zuständen mit dem HADES Detektor an der GSI
Etudes d'états excités du nucleon avec le détecteur HADES à GSI

Thesis by M. Sc. Federico Scozzi from Torino

Date of submission: 13.11.2018
Date of defence: 19.12.2018

Darmstadt 2018 – D 17

1. Supervisor: Senior scientist at CNRS Beatrice Ramstein
2. Supervisor: Prof. Dr. phil. nat. Tetyana Galatyuk
3. Referee: Senior scientist at CNRS Hélène Fonvieille
4. Referee: Priv.-Doz. Dr. Michael Buballa

TECHNISCHE
UNIVERSITÄT
DARMSTADT

UNIVERSITÉ
PARIS
SUD

Comprendre le monde,
construire l'avenir®

Studying excited states of the nucleon with the HADES detector at GSI

Studium von angeregten Nukleon-Zuständen mit dem HADES Detektor an der GSI
Etudes d'états excités du nucleon avec le détecteur HADES à GSI

Thesis by M. Sc. Federico Scozzi from Torino

1. Supervisor: Prof. Dr. phil. nat. Tetyana Galatyuk
2. Supervisor: Senior scientist at CNRS Beatrice Ramstein
3. Referee: Senior scientist at CNRS Hélène Fonvieille
4. Referee: Priv.-Doz. Dr. Michael Buballa

Date of submission: 13.11.2018
Date of defence: 19.12.2018

Darmstadt 2018 – D 17

Erklärung zur Dissertation

Hiermit versichere ich, die vorliegende by ohne Hilfe Dritter nur mit den angegebenen Quellen und Hilfsmitteln angefertigt zu haben. Alle Stellen, die aus Quellen entnommen wurden, sind als solche kenntlich gemacht. Diese Arbeit hat in gleicher oder ähnlicher Form noch keiner Prüfungsbehörde vorgelegen.

Darmstadt, den 13.11.2018

(F. Scozzi)

Kurzfassung

Das Thema dieser Dissertation ist die Analyse der Kanäle zur Erzeugung von Dielektronen (e^+e^-) in Pion induzierten Reaktionen bei einer Schwerpunktsenergie von ungefähr 1.5 GeV. Bei solchen Energien können baryonische Resonanzen in einem energetisch höher liegenden Resonanzbereich (N(1440), N(1520), N(1535),...) angeregt werden. Ziel ist es die elektromagnetischen Übergänge von Baryonen in einem bislang unerforschten kinematischen Bereich zu untersuchen, in dem Vektormesonen (ρ, ω) eine wichtige Rolle spielen. Diese Messungen dienen auch als Bezugspunkt für Untersuchungen von e^+e^- Zerfällen bei höheren Baryonendichten, wo die Spektralfunktionen von Vektormesonen modifiziert werden. Die Pion induzierten Reaktionen sind experimentell herausfordernd, bilden jedoch ein wichtiges Werkzeug zur direkten Untersuchung von Übergängen von Baryonen.

Die Messungen (der HADES Kollaboration) von hadronischen Kanälen in von Pion induzierten Reaktionen haben den bisweilen knappen Datensatz erweitert. Zusammen mit einem großen Datensatz aus Photon induzierten Reaktionen haben sie es ermöglicht eine neue Partialwellenanalyse durchzuführen, die es erlaubt neuen Informationen über die Eigenschaften der Baryonenresonanzen zu extrahieren.

Die Ergebnisse der vorliegenden Analyse sind ein bedeutender Beitrag zur Auswertung der elektromagnetischen Kanäle. Es wurde ein Experiment mit dem High Acceptance Di-Electron Spectrometer (HADES) und dem GSI Sekundärstrahl von Pionen, die auf Kohlenstoff- und Polyethylen- Targets geschossen wurden, ausgewertet.

Diese Dissertation gibt einen Überblick über die bisherigen Ergebnisse der HADES Kollaboration zur Erzeugung von Dielektronen in Nukleon-Nukleon-, Nukleon-Kern- und Kern-Kern-Reaktionen. Die wenigen bisherigen Daten aus Pion induzierten Reaktionen werden diskutiert und der Aufbau des HADES Experiments und der Pionen-Strahführung beschrieben.

Im Folgenden werden die Schritte der Datenanalyse vorgestellt. Schwerpunktsmäßig wird die Leptonenidentifikation diskutiert. Die sorgfältige Anpassung von Simulationsparametern des RICH Detektors, der einen essentiellen Beitrag zur Unterscheidung zwischen Elektronen und Pionen liefert, ermöglicht eine präzise Effizienzkorrektur der rekonstruierten Daten. Die Bestimmung und der Abzug des kombinatorischen Untergrundes, sowie die Normierung and die Subtraktion des Beitrags von Pion- Kohlenstoff Reaktionen im Falle des Polyethylen Targets werden erläutert. Letzteres ist bei der Untersuchung von Pion-Nukleon-Reaktionen von Bedeutung.

Alle Beiträge zur Effizienzkorrektur der Messung werden sorgsam berücksichtigt und die systematische Unsicherheit abgeschätzt. Die vorhandenen Werkzeuge zur Interpretation der experimentellen Ergebnisse werden vorgestellt: Modelle der Reaktionen $\pi^-p \to ne^+e^-$, aber auch die Partialwellenanalyse von $\gamma n \to \pi^-p$ zusammen mit $\pi^-p \to 2\pi N$ Kanälen.

Bei der Verteilung der invarianten Masse von e^+e^- ist ein klarer Überschuss über die Erwartung für einen Zerfall von punktartigen Baryonen zu sehen. Dies bestätigt die wichtige Rolle von ρ-Mesonen außerhalb der Massenschale in diesem kinematischen Regime. Die Analyse von Winkelverteilungen mithilfe des Formalismus der Spindichtematrix werden mit theoretischen Modellen, die auf verschiedenen Resonanzbeiträgen basieren, verglichen. Somit kann eine zusätzliche Information über die Struktur elektromagnetischer Übergänge gewonnen werden. Diese Analyse dient als Motivation für weitere Experimente zur Erforschung elektromagnetischer Übergänge nicht-seltsamer Resonanzen im dritten Massenbereich oder von Hyperonen.

Résumé

Le sujet de cette thèse est l'analyse de la production de di-électrons dans des réactions induites par des pions à une énergie dans le centre de masse proche de 1.5 GeV, dans lesquelles des résonances baryoniques dans la deuxième région de résonances (N(1440), N(1520), N(1535),..) peuvent être excitées. L'objectif est d'obtenir des informations sur les transitions électromagnétiques dans une région inexplorée cinématiquement, où l'on s'attend à ce que les mésons vecteurs jouent un rôle important. Ces mesures peuvent aussi être utilisées comme référence pour les études de production de paires e^+e^- dans la matière hadronique visant à explorer les modifications de la fonction spectrale du ρ à des densités baryoniques finies. Bien qu'expérimentalement plus difficiles, les réactions induites par des pions constituent un outil très performant pour étudier les résonances baryoniques.

La mesure des canaux hadroniques par la collaboration HADES dans les réactions pion-nucléon a enrichi considérablement la très pauvre base de données existante. Ces mesures, combinées aux données très abondantes de photoproduction ont permis de réaliser une nouvelle analyse en ondes partielles pour extraire les propriétés des résonances baryoniques. Les résultats de cette analyse sont utilisés pour l'analyse des canaux électromagnétiques. L'analyse présentée est basée sur une expérience-test réalisée avec le détecteur de grande acceptance HADES, le faisceau secondaire de pions de GSI et des cibles de polyethylene et de carbone. Le document commence par une présentation des résultats déjà obtenus par la collaboration HADES pour la production de di-électrons dans les réactions noyau-noyau, nucleon-noyau et nucleon-nucleon et des rares données existantes pour les réactions induites par des pions. Suit une description de l'expérience HADES et de la ligne de faisceau de pions Les différentes étapes de l'analyse sont ensuite présentées, en insistant sur l'identification des électrons. Une étude détaillée de l'ajustement de la réponse du détecteur RICH, qui est crucial pour la discimination entre électrons et pions est réalisée. Puis, l'extraction du signal de production de diélectrons, incluant la soustraction du bruit de fond combinatoire et la normalisation est discutée, ainsi que les problèmes de soustraction de la contribution de noyaux de carbone pour étudier les interactions pion-nucléon. Toutes les contributions à l'efficacité de la mesure sont prises en compte avec soin et les erreurs systématiques sont estimées. Les outils existants pour l'interprétation des donn'ees sont ensuite introduits. En plus des modèles existants pour la réaction $\pi^- p \rightarrow ne^+e^-$, les résultats de l'analyse en ondes partielles des canaux $\pi^- p \rightarrow 2\pi N$ peuvent être utilisés. La distribution de la masse invariante des paires e^+e^- présente un excès par rapport à la production attendue pour des baryons ponctuels, ce qui confirme le rôle important de mésons rho hors-couche dans les facteurs de forme de transition électromagnétique dans ce domaine cinématique. Les résultats de l'analyse des distributions angulaires en utilisant le formalisme de la matrice densité sont aussi comparés à un modèle théorique basé sur les contributions de plusieurs résonances. Cette comparaison montre que les distributions angulaires apportent des informations supplémentaires sur la structure des transitions baryoniques électromagnétiques. Cette analyse est utilisée pour motiver des expériences futures pour étudier les transitions électromagnétiques mettant en jeu des baryons non-étranges dans la troisième région de résonance ou des hypérons.

Abstract

The subject of this thesis is the analysis of dielectron (e+e-) production channels produced in pion induced reactions at a center of mass energy close to 1.5 GeV, where baryon resonances in the second resonance region (N(1440), N(1520), N(1535),...) can be excited. The objective is to bring information on electromagnetic baryon transitions in an unexplored kinematic region, where vector mesons (ρ, ω) are expected to play an important role. These measurements can also be used as a reference for studies of in-medium e+e- production, aiming at investigating the modifications of the ? meson spectral function at finite baryonic densities. While experimentally more challenging, pion-induced reactions constitute a more direct tool to study baryon transitions. The measurement of hadronic channels by the HADES collaboration in the pion-nucleon reactions allowed to enrich the very scarce existing data base and, using also the very rich photon-induced data, to perform a new Partial Wave Analysis to extract information on baryonic resonance properties. The results of this analysis are used as a valuable input for the analysis of the electromagnetic channels. The present analysis is based on a commissioning experiment carried out with the High Acceptance Di-Electron Spectrometer (HADES), using the GSI secondary pion beam impinging on carbon and polyethylene targets. The document begins with a presentation of the results already obtained by the HADES collaboration concerning dielectron production in nucleus-nucleus, nucleon-nucleus or nucleon-nucleon and of the scarce existing results for pion-induced reactions. It is followed by a description of the HADES experiment and of the pion beam line.

Then the different steps of the data analysis are presented, with a focus on the electron identification. For this purpose a careful study on how to tune in simulation the response of the RICH detector, fundamental for the discrimination between pions and electrons, is performed. The extraction of the signal for dielectron production, including combinatorial background subtraction and normalization is then discussed, together with the problems of subtracting the carbon contribution from the polyethylene target to study pion-nucleon interactions. All the contributions to the efficiency of the measurement are carefully taken into account and the systematic errors are estimated. The existing tools for the interpretation of the data are then presented. In addition to existing models for the $\pi^- p \to n e^+ e^-$ reaction, the results of Partial Wave analysis of the $\gamma n \to \pi^- p$ reaction as well as for $\pi^- p \to 2\pi N$ channels can be used.

The e^+e^- invariant mass distribution shows a clear enhancement with respect to a production by point-like baryons, and confirms the significant role of off-shell ρ mesons in electromagnetic form factors in this kinematic range. Results of the analysis of the angular distributions using the framework of the spin density matrix are also compared to a theoretical model based on several resonance contributions. This demonstrates the additional information provided by angular distributions to extract information on electromagnetic structure of baryon transitions. This analysis is used to motivate further experiments to study electomagnetic transitions involving non-strange baryons in the third resonance region or hyperons.

Contents

1 Introduction **9**

1.1 Studies of baryon dominated matter . . . 9

1.1.1 QCD phase diagram . . . 9

1.1.2 QCD vacuum and chiral symmetry restoration . . . 10

1.1.3 Vector meson spectral functions . . . 11

1.1.4 Role of baryonic resonances . . . 12

1.2 Baryon Dalitz decays . . . 13

1.2.1 Baryon electromagnetic transitions . . . 13

1.2.2 Results in the space-like region . . . 15

1.2.3 Results in the time-like region . . . 16

1.2.4 Existing models . . . 17

1.3 Results for e^+e^- production in HADES experiments . . . 18

1.3.1 Results from QCD matter studies . . . 18

1.3.2 Results from elementary reactions studies . . . 18

1.4 Extension of the Dalitz decay studies to π beam experiments . . . 23

1.5 Existing data for pion induced reactions . . . 24

1.5.1 Experimental information for π^- p reactions . . . 24

1.5.2 Comparison of π^-p and π^-n cross sections . . . 29

1.5.3 Experimental information for pion interactions with nuclei . . . 30

1.6 Conclusion . . . 36

2 The HADES experimental set-up **37**

2.1 Tracking system . . . 38

2.1.1 Magnet . . . 38

2.1.2 Mini Drift Chambers . . . 39

2.2 Ring Imaging CHerenkov detector . . . 39

2.3 META detector . . . 40

2.3.1 Resistive Plate Chamber . . . 41

2.3.2 Time-of-flight . . . 41

2.3.3 Pre-Shower detector . . . 41

2.4 Silicon beam tracking stations . . . 41

2.5 Start detector . . . 42

2.6 Trigger and Data Acquisition System . . . 43

3 Methods for particle reconstruction **45**

3.1 Run conditions and targets . . . 45

3.2 Beam particle reconstruction . . . 46

3.2.1 The pion beam line . . . 46

3.2.2 Beam contamination . . . 47

3.2.3 Pion beam momentum reconstruction . . . 48

3.3 Track reconstruction procedure . . . 50

3.4 Momentum reconstruction 53
3.5 Matching of a track with a time-of-flight information 53
3.6 RICH Ring reconstruction 54
3.7 Data Summary Tapes 55
3.8 Event selection and particle identification 56
  3.8.1 Global event selection criteria 56
  3.8.2 Track sorting procedure 56
  3.8.3 Cleaning of the particle candidates 57
  3.8.4 Velocity and energy loss selection criteria 57
  3.8.5 Backtracking algorithm for lepton identification 58

4 RICH performance study **61**
4.1 RICH stability 61
  4.1.1 HV stability 61
  4.1.2 RICH observables stability 61
4.2 Optimization of the RICH digitizer 63
  4.2.1 Simulation of the Cherenkov effect 63
  4.2.2 Optimization procedure 64
  4.2.3 Selection of a pure lepton sample in experimental and simulation data 65
  4.2.4 Sensitive RICH observables 65
  4.2.5 Estimation of the RICH efficiency 68
  4.2.6 Influence of the lepton purity in the efficiency calculation 69
  4.2.7 Results of the optimization procedure 70
  4.2.8 Consistency of the parameters 71
  4.2.9 Model dependence of the calibration 72
  4.2.10 Stability of the RICH efficiency as a function of the beam time . . . 74
4.3 Conclusion 76

5 Extraction of the dielectron signal **79**
5.1 Combinatorial background 79
  5.1.1 Origin of the combinatorial background 79
  5.1.2 Combinatorial background estimation 80
5.2 Photon conversion 81
  5.2.1 Single lepton cuts 82
  5.2.2 Pair cut 82
5.3 Purity of the e^+e^- signal 83
5.4 Results for inclusive analysis 83
  5.4.1 Comparison of ring finder and backtracking analysis 84
  5.4.2 ”Close neighbour” cut 84
5.5 Results for exclusive analysis 86
5.6 Carbon subtraction 88
  5.6.1 Relative carbon/polyethylene target normalization 88
  5.6.2 Cross section ratios 89
5.7 Normalization 90

6 Efficiency corrections and systematic errors **93**
6.1 Single lepton correction 93
  6.1.1 Correction using the ideal values of momentum, θ and ϕ angles . . . 94
  6.1.2 Self-consistency check 95
  6.1.3 Efficiency as a function of ”reconstructed” values of momentum, θ and ϕ angles 97
6.2 Correction of spectra on the pair level 100

6.2.1 Correction factor for the backtracking analysis 100
6.3 Estimation of systematic errors 101
6.4 Final efficiency corrected spectra 103

7 Theoretical approaches for the $\pi^- p \to n e^+ e^-$ reaction 105
7.1 Graphs contributing to the $\pi^- p \to n e^+ e^-$ reaction: 105
7.2 Early approaches 106
7.3 Dalitz decays of baryon resonances 109
7.3.1 QED formalism 109
7.3.2 Form factor models for baryon transitions 112
7.4 Transport models 117
7.5 Results from partial wave analysis of π^-p reactions 118
7.5.1 Results for $\gamma n \to \pi^- p$ 125
7.6 Density matrix formalism for angular distributions 127
7.7 Conclusion 131

8 Results and discussion 133
8.1 General procedure for data/model comparison 133
8.2 Dilepton cocktails simulated with the Pluto event generator 134
8.2.1 Contribution of pseudo-scalar mesons 134
8.2.2 Dalitz decay of baryonic resonances 135
8.2.3 Off-shell ρ contribution 137
8.2.4 Reaction on carbon 138
8.2.5 Summary of the input cross sections for Pluto simulations 141
8.2.6 Comparison of Pluto cocktail to inclusive e^+e^- production data . . 142
8.2.7 Comparison of Giessen BUU transport model predictions to inclusive e^+e^- data 149
8.2.8 Comparison of Pluto cocktail to exclusive $\pi^- p \to n e^+ e^-$spectra . . 150
8.3 Comparison to models based on off-shell vector meson production 155
8.4 Comparison to Lagrangian model 156
8.5 Spin density coefficients 156

9 Conclusion and Outlook 161
9.1 Conclusion 161
9.2 Outlook 162
9.2.1 Further pion beam experiments 162
9.2.2 Studies of Hyperon Dalitz decays with HADES 163

Chapter 1

Introduction

In this introduction chapter, we will discuss the motivations of studying the $\pi^- p \to n e^+ e^-$ reaction in the region of the N(1520) resonance. We will start with the general objectives of the HADES experiments at GSI. In particular, we will show how the exploration of the QCD phase diagram using the dilepton probe (Sec. 1.1) is connected to the study of Dalitz decays of baryonic resonances (Sec. 1.2). We will then briefly present the results of the HADES experiments concerning dielectron production (Sec. 1.3) and the objective of the extension to pion beam experiments (Sec. 1.4). The last section of this chapter (Sec. 1.5) will be devoted to a review of existing data obtained with pion beam experiments in our energy range.

1.1 Studies of baryon dominated matter

1.1.1 QCD phase diagram

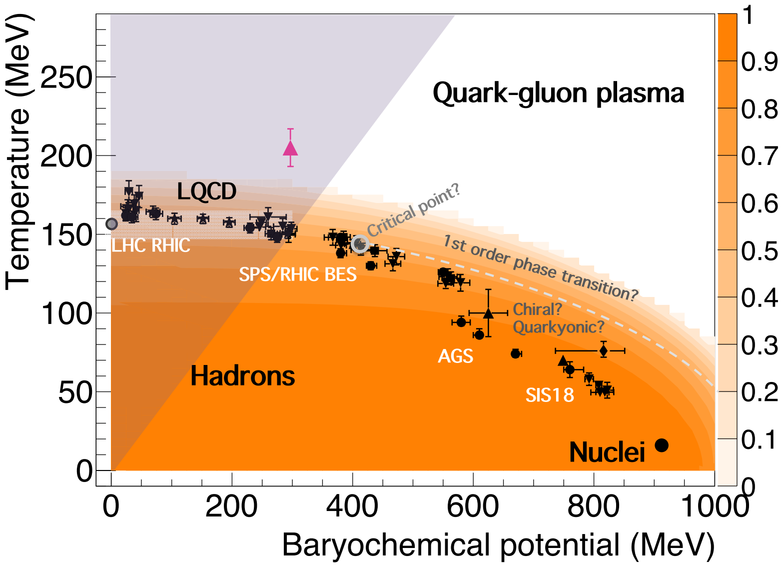

Figure 1.1: Conjectured QCD phase diagram (temperature versus baryochemical potential). The data points are deduced from measurements of particle production analyzed with statistical hadronization models [1]. The white region at vanishing μ_B depicts lattice QCD calculations. The expectation value of the chiral condensate relative to the vacuum is shown as the orange contour plot.

The exploration of the different phases of the strongly interacting matter, as illustrated in Fig. 1.1 is one of the important fields of modern physics. The matter around us consists mostly of atomic nuclei, made of bound neutrons and protons which can be studied in nuclear reactions at low energies. In the early universe, a few μs after the Big Bang, a deconfined phase of quarks and gluons (the Quark Gluon Plasma) existed, at very high temperatures (T >> 150 MeV) and zero baryochemical potential. Experiments with heavy ion collisions at ultrarelativistic energies try to reproduce these conditions in the laboratory.

Very dense stellar objects, with densities up to 10 times the normal nuclear matter density, as neutron stars, also exist in the universe. Moderately hot (T < 70 MeV) and dense matter can also be produced in the universe in the collision of compact stellar objects as recently observed thanks to the detection of gravitational waves [2]. This region of high baryon densities has been much less explored. This can be done using heavy ion collisions in the few GeV energy range which allow to produce QCD matter at similar conditions.

The open questions motivating the study of dense matter are, for example, the existence of a critical point in the QCD phase diagram, the nature of the transition between the hadronic and the partonic phase and the existence of exotic phases with mixed properties between the two phases. In addition, dilepton spectroscopy is used to find signs of a partial restoration of the chiral symmetry, as will be discussed in more details in the following section.

1.1.2 QCD vacuum and chiral symmetry restoration

Chiral symmetry is a fundamental approximate symmetry of the QCD lagrangian [3]. However, this symmetry is spontaneously broken and it is therefore absent in the QCD vacuum and excited states. This is clearly visible at the level of the low mass part of the hadronic spectrum, where there is no degeneracy between chiral partners such as the pion and the σ meson, or the $\rho(770)$ and $a_1(1260)$ mesons, or the nucleon and N(1535). The violation of the symmetry can be quantified by different order parameters. One of them is the quark condensate $< 0|\bar{q}q|0 >$.

While the Higgs mechanism generates the current quark masses, and therefore contributes to only about 2% of the mass of a proton, the chiral symmetry breaking and the trace anomaly, which is related to the fact that the gluons carry colour charge and hence interact, are responsible for the hadronic masses in a much larger extent. The underlying mechanism at the origin of this dynamical mass generation is the coupling of the constituent quarks with the QCD vacuum quark gluon condensate, resulting in an effective quark mass of about 300 MeV.

The spontaneous chiral symmetry breaking is therefore an essential feature of the hadron spectrum in vacuum. In adddition, a reduction of the quark condensate, as a function of increasing baryon density or temperature is predicted [4]. It has been checked for vanishing baryonic densities using numerical computations on the lattice at finite temperatures. These calculations predict that chiral symmetry restoration occurs at a temperature of 160-190 MeV [5, 6].

Lattice QCD calculations cannot be performed at high net-baryon densities due to the notorious sign problem [7]. As shown in Fig. 1.1 for the Polyakov-Quark-Hadron model [1], the quark condensate is predicted to be strongly reduced already at normal nuclear matter density. The data points shown in Fig. 1.1 are deduced from measurements of particle production analyzed with statistical hadronization models. Temperatures around 155 MeV at vanishing μ_B are reached at LHC- and top RHIC energies and they extend down to around 50 MeV at high μ_B for collision systems at SIS18 energies. Since these particles are produced after some expansion and cooling of the system, it is believed that already at low energies, the chiral condensate in the nuclear fireball is highly reduced.

1.1.3 Vector meson spectral functions

The challenge for experimentalists is that the quark condensate is not an observable, it is therefore needed to find a signal of its decrease is reflected in the hadron properties. In fact, while QCD sum-rules provide useful constraints for the integral of the hadron spectral functions, the connection between chiral quark condensates and hadronic observables cannot be made in a model independent way. However, early predictions of dropping hadron masses in the nuclear medium driven by changes of the quark condensates by Brown and Rho [8] and Hatsuda and Lee [9] motivated experimental studies of in-medium masses of the vector mesons (ρ, ω, ϕ).

meson	mass (MeV/c^2)	Γ (MeV/c^2)	cτ (fm)	main decay	e^+e^- branching ratio
ρ	768	152	1.3	$\pi^+\pi^-$	4.4 10^{-5}
ω	782	8.43	23.4	$\pi^+\pi^-\pi^0$	7.2 10^{-5}
ϕ	1019	4.43	44.4	K$^+$K$^-$	3.1 10^{-4}

Table 1.1: Main characteristics of vector mesons

Dilepton spectroscopy was used as a favored tool for this study. With spin (J) and parity (P), such that J^P=1$^-$, *i.e.* the same quantum numbers as a photon, vector mesons have indeed a direct decay to dilepton channel (see Table 1.1). Despite the small branching ratio, dileptons, which are not affected by the strong interaction, are indeed better suited than pions for such studies. In addition, they are unique to study the electromagnetic properties of hadrons in the vacuum and in the medium. Dilepton experiments have not confirmed the Brown and Rho conjecture of dropping vector meson masses. The present experimental results are rather consistent with the predictions of hadronic models [11, 10] which were developed in the mean time. These models have shown to be very successful in describing the dielectron spectra measured at SPS [10] and RHIC [12] in a wide range of energies in terms of in-medium modifications of the ρ spectral function.

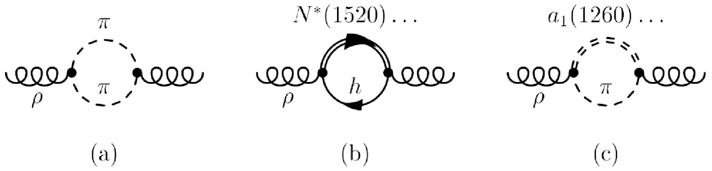

Figure 1.2: Dressing of the ρ in the nuclear medium via the 2π propagator (a) the coupling to baryonic resonances (b) and the coupling to mesonic resonances (c).

In these models, the spectral function of the meson is related to the imaginary part of the propagator which is modified in medium due the dressing of the pions and the coupling to baryons and mesons (see Fig. 1.2 and 1.3). These modifications depend on the momentum, but also on the polarization of the vector meson.

The coupling of vector mesons to the baryonic resonances is an essential ingredient of the in-medium modification of the vector mesons. It is important in particular at lower energies, where the hadronic matter is baryon rich. HADES experiments, in the range of 1 - 3.5A GeV are therefore well adapted to study the role of the coupling to baryon resonances in the in-medium modifications of ρ meson spectral function.

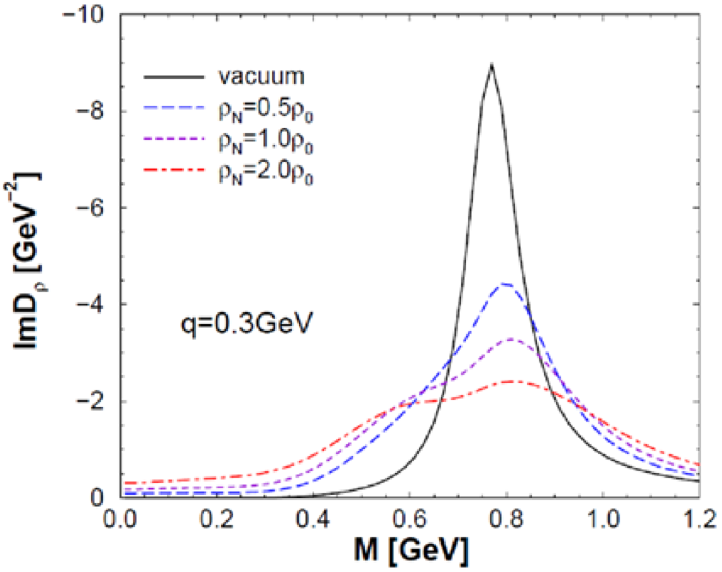

Figure 1.3: Imaginary part of the ρ meson propagator (or spectral function) plotted for a constant momentum (q = 0.3 GeV) as a function of the mass for different baryon densities [10].

1.1.4 Role of baryonic resonances

Nucleon-nucleon reaction cross sections at incident energies between 1 and 4A GeV are dominated by the excitation of nucleon resonances [14]. The $\Delta(1232)$ resonance, is the most copiously produced, and it plays a dominant role for one pion production. When the energy is large enough, higher lying resonances contribute to meson production, depending on their specific coupling to the various meson-nucleon channels. The N(1535) for example is important for the η production and the N(1520) plays an important role for the ρ production.

In reactions involving nuclei at these energies, baryonic resonances can propagate and regenerate due to their short life-time with respect to the long life-time of the dense phase in these collisions (respectively of the order of 1.5 and 12 fm/c). This is illustrated in Fig. 1.4, where the total baryonic density is plotted as a function of time and shows a peak with a value of ρ/ρ_0 close to 3 at about 12 fm/c. Via the coupling to mesons and their subsequent Dalitz (*e.g.* $\eta \rightarrow \gamma\ e^+e^-$) or direct (*e.g.* $\rho \rightarrow e^+e^-$) decays, baryonic resonances can emit e^+e^- pair in a two-step process. In addition, baryonic resonances are known to have a certain probability to undergo radiative decays ($R \rightarrow N\gamma$). It is therefore also expected that they emit directly virtual photons, in the so-called Dalitz decays ($R \rightarrow Ne^+e^-$). In the GSI energy range e^+e^- can then be produced by the following sources:

- π^0 Dalitz decay ($\pi^0 \rightarrow \gamma e^+e^-$)
- η Dalitz decay ($\eta \rightarrow \gamma e^+e^-$)
- nucleon-nucleon or π-nucleon bremsstrahlung (non resonant $NN \rightarrow NNe^+e^-$ or $\pi \rightarrow \pi Ne^+e^-$ processes)
- baryon Dalitz decays (N/$R \rightarrow$Ne$^+e^-$)
- vector meson direct decays ($\rho/\omega/\phi \rightarrow e^+e^-$), if the energy is high enough.

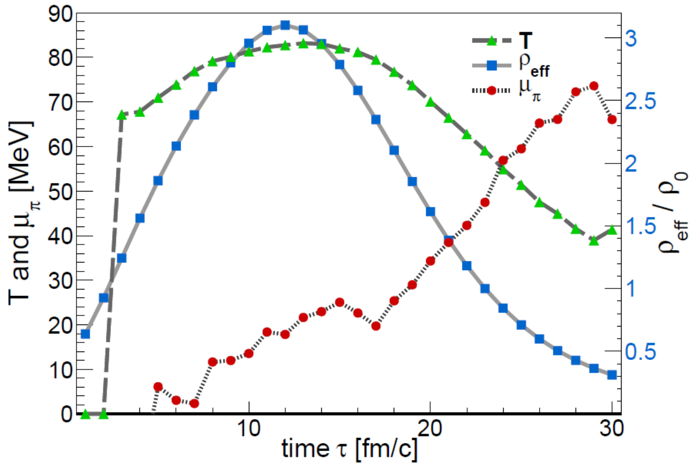

Figure 1.4: Evolution of average temperature (green), pion chemical potential (red) and density (blue) as a function of time in a Au+Au collision at an energy of 1.23A GeV in a coarse-grained approach based on the UrQMD transport model [13].

To study the in-medium vector meson properties, it is therefore needed to subtract the e^+e^- from π^0, η, ω and ϕ meson decays (the so-called freeze-out contribution). In addition, to better quantify the medium effects, the bremsstrahlung, baryon Dalitz decays contributions expected from a superposition of nucleon-nucleon collisions are also subtracted, as will be discussed in Sec. 1.3.1. Please note that the emission of e^+e^- pairs by baryonic resonances via intermediate vector mesons ($R \to N\rho/\omega$ ($\rho/\omega \to e^+e^-$)) is in fact part of the baryon Dalitz decay process. It is also clear that, since baryon-hole states are excited in the in-medium propagation of the ρ meson (graph (b) in Fig. 1.2), the baryon resonance Dalitz decay process contributes to the imaginary part of the ρ meson propagator and therefore plays a significant role in the in-medium modification of the ρ meson spectral function reconstructed from dilepton emission (Fig. 1.3).

1.2 Baryon Dalitz decays

1.2.1 Baryon electromagnetic transitions

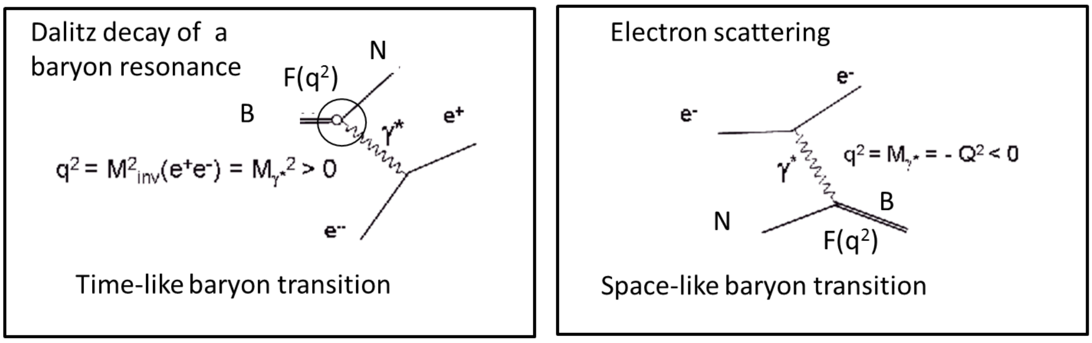

Figure 1.5: Sketch of a Dalitz decay of a baryon resonance process. Left: The four-momentum transfer q^2 is positive corresponds to time-like baryon transition. Right: Excitation of a nucleon by electron scattering. The four-momentum transfer q^2 is negative0, the so-called space-like baryon transition.

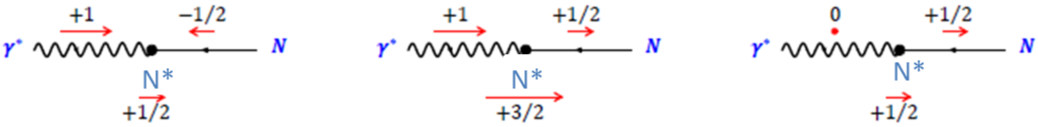

(a) $A_{1/2}$ (b) $A_{3/2}$ (c) $S_{1/2}$

Figure 1.6: The three helicity configurations are displayed in the case of a spin 3/2 resonance.

Baryon Dalitz decays are electromagnetic baryon transitions and they are therefore sensitive to the electromagnetic structure of the baryon and of the nucleon involved in the transition. These transitions are characterized by the four-momentum transfer at the electromagnetic vertex, $q = p_N - p_B$, where p_N and p_B are respectively the nucleon and excited baryon four momenta. The four-momentum squared q^2 is equal to the squared mass of the virtual photon involved in the transition:

$$M_\gamma^2 = q^2 = (W_B - W_N)^2 - (\vec{p_B} - \vec{p_N})^2 \tag{1.1}$$

where $W_B, W_N, \vec{p_B}$ and $\vec{p_N}$ are the total energies and momentum vectors of the excited baryon and nucleon, respectively. One distinguishes two different types of electromagnetic transitions, depending on the sign of q^2:

- The time-like region where q^2 is positive, *i.e.*, according to Eq. 1.1, the energy transfer is larger than the momentum transfer;
- The space-like region where q^2 is negative, *i.e.*, the momentum transfer is larger than the energy transfer.

The Dalitz decay process belongs to the first category of time-like electromagnetic transitions, since the mass of the virtual photon is a positive quantity which is equal to the squared invariant mass of the dielectron (see Fig. 1.5 ($left$)). In this process, q^2 has a maximum value equal to $q^2_{max} = (M_B - M_N)^2$, where M_B and M_N are the excited baryon and nucleon mass respectively.

Electromagnetic transitions between a nucleon and a baryon resonance B with positive q^2 can also be studied in annihilation reactions $e^+e^- \rightarrow \bar{B}N$. In this case, the minimum value of q^2 is $(M_B + M_N)^2$. But the time-like region $(M_B - M_N)^2 < q^2 < (M_B + M_N)^2$ remains experimentally unaccessible.

The space-like region can be studied using electron scattering (see Fig.1.5($right$)). In this case, the maximum value of q^2 is just limited by the energy of the incident electron. It also depends on the angle and energy of the scattered electron.

In a general way, the electromagnetic structure of baryons is taken into account in the calculation of electromagnetic vertices by using form factors F(q^2), which are analytic functions depending on the virtual photon four-momentum transfer q^2 and are used as weights in the calculation of the electromagnetic currents (see Sec. 7.3). It is expected that at very large q^2, form factors can be predicted by perturbative QCD calculations and follow quark counting rules. At lower q^2(q^2< 1 GeV^2), form factors are non-perturbative objects, which reflect the very complex interaction between quarks and gluons.

Form factors are related to the helicity amplitudes corresponding to the different projection of spins of the photon, nucleon and excited baryon along the nucleon momentum in the baryonic resonance rest frame, as illustrated in Fig. 1.6 for the case of the transition to a spin 3/2 resonance. In a general way, in the transition between the nucleon and a baryon of spin J, there are 2J+1 independent helicity amplitudes or form factors. A global information on the electromagnetic structure of baryon transitions requires the

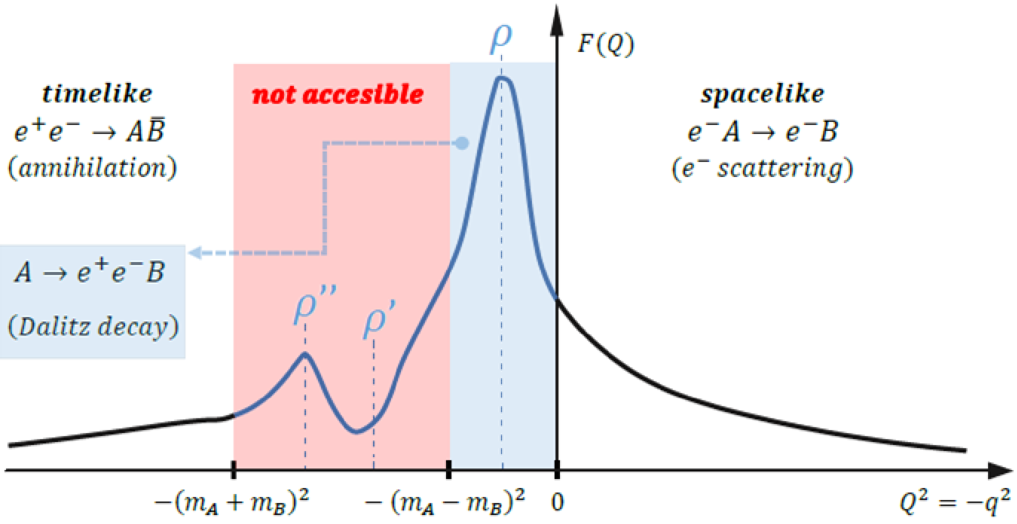

Figure 1.7: Schematic representation of a formfactor F(Q) with characteristic ρ meson poles in the time-like region.

knowledge of these form factors for any values of the four momentum transfer squared q^2, as illustrated in Fig. 1.7. If q^2 is negative (*i.e.* space-like), using appropriate kinematical transformations, the electromagnetic form factors can be related to the spatial distributions of charge and magnetization. For positive q^2 (*i.e.* time-like), the response of the baryon to the electromagnetic probe shows peaks due to the open channels (*i.e.* vector meson or multiparticle production channels).

1.2.2 Results in the space-like region

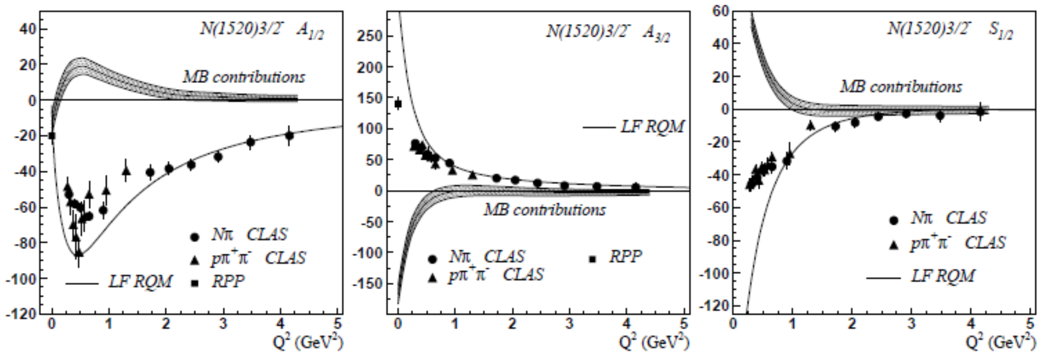

Figure 1.8: Results for form factors in the space-like region measured by the CLAS collaboration for the N(1520) resonance [15]. The hatched area shows the meson-baryon (MB) contribution obtained by difference between the data points and the Light Front Relativistic Quark Model (LF RQM) calculation, shown as a full line [15].

Up to now, electromagnetic transitions between baryons have been mostly studied in meson electroproduction experiments. In this case, a wide range of negative (space-like) four-momentum transfer squared q^2 can be probed. This technique has been intensively

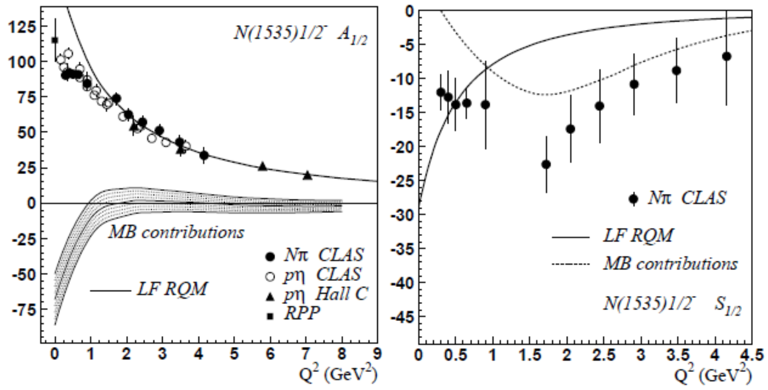

Figure 1.9: Results for form factors in the space-like region measured by the CLAS collaboration for the N(1535) resonance. the meaning of the curve is the same as in Fig. 1.8 [15].

used recently at CLAS (see [16] and references therein for a recent update) and from these experiments, information on the evolution of the meson cloud and quark core contributions to the electromagnetic structure of various baryon transitions has been inferred. This is illustrated in Figs. 1.8 and 1.9, respectively for the case of the N(1520) and N(1535) resonances, which are central for our studies. It can be observed that light-front calculations reproduce well the trend of helicity amplitudes at large q^2. The deviation at small q^2 is attributed to the meson cloud contribution. The size of the latter is different for the different amplitudes and for the N(1535) and N(1520) case, which shows the sensitivity to the different quantum numbers involved in each transition, but also probably to the different nature of the two states. With the on-going extension to larger energies with CLAS12, the aim is to reach the region where the meson cloud contribution is negligible in order to study specifically the evolution of the constituent quark mass as a function of 4-momentum transfer .

1.2.3 Results in the time-like region

The experimental situation for positive q^2 is much more scarce. Using e^+e^- annihilation into baryon-antibaryon pairs ($e^+e^- \leftrightarrow B\bar{B}'$) positive q^2 values can be achieved, with values above the two baryon production threshold (*i.e.* $q^2 > (M_B + M_{B'})^2$, where M_B and $M_{B'}$ are the B and B' baryon masses). However, the existing studies mainly focus on elastic form factors of nucleons or hyperons [17, 18, 19] and little is known about the baryon transitions. One of the far-reaching goals at large q^2 is to compare the asymptotic behaviors in both space-like and time-like region which should merge in the high q^2 region governed by pQCD.

The Dalitz decay of baryons (of the type $B \to Ne^+e^-$) probes a different part of the time-like region corresponding to the q^2 interval $[4m_e^2, (M_B - M_N)^2]$, where m_e, M_B and M_N are the electron, baryon and nucleon masses, respectively. This region is connected to the space-like region at q^2=0, where information on the electromagnetic couplings is provided by meson photoproduction experiments ($\gamma N \to B$) or radiative decays ($B \to \gamma N$). As will be discussed in Sec. 1.3.2, using proton-proton collisions, the HADES collaboration provided the first measurement of the Dalitz decay branching ratio of the $\Delta(1232)$ resonance and information on Dalitz decays of higher lying resonances. The goal of this analysis is to study the Dalitz decay of baryons in the region of the N(1520) resonance.

1.2.4 Existing models

Vector Dominance model

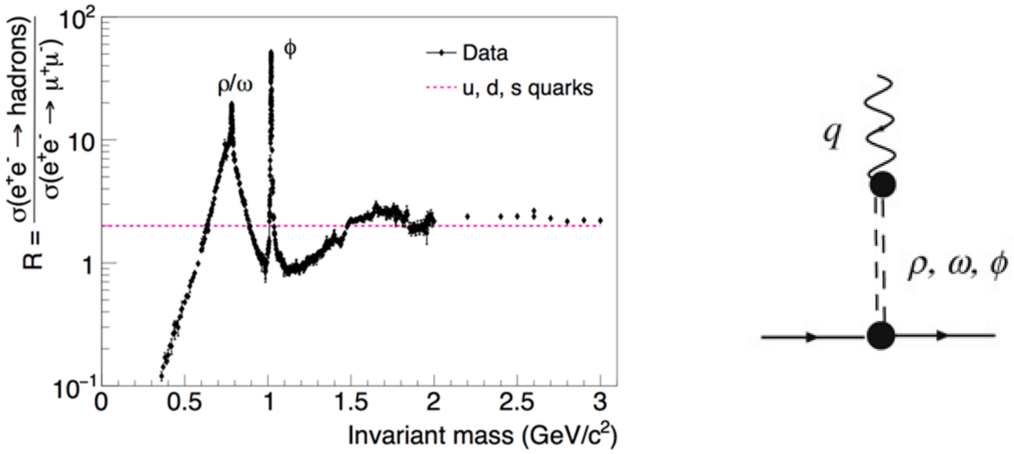

Figure 1.10: Left: Ratio of cross sections for the reactions $e^+e^- \rightarrow$ hadrons and $e^+e^- \rightarrow \mu^+\mu-$ showing the production of vector mesons at small invariant mass. A factor 2 is expected for invariant masses between 2 and 3 GeV/c^2 in a simple quark-parton model with u, d, s quarks. Right: Sketch of the Vector Dominance Model.

As clearly shown in Fig. 1.10 (left), vector mesons are the dominant feature in e^+e^- annihilation at low energies and therefore play a crucial role in any hadronic electromagnetic current.

Starting form the hadronic couplings, it seems obvious, that, due to the coupling of baryons to vector mesons which have a direct decay into e^+e^-, vector mesons are expected to strongly contribute to the Dalitz decay process and therefore to play an important role especially in the time-like electromagnetic structure of baryons.

This role is obvious in the vicinity of their poles, where vector mesons are produced closed to the mass-shell, but it is expected that the vector mesons influence the electromagnetic structure of baryons in a broad region of positive q^2 due in particular to the large width of the ρ meson and the coupling to off-shell vector mesons. Moreover, this influence is extended also to the space-like region. Indeed, due to the analyticity of form factors, values in the space-like and time-like regions are related by dispersion relations, which derive from the general properties of analytical functions in the complex plane:

$$F(q^2) = \frac{1}{\pi} \int_{t}^{\infty} dq'^2 \frac{\Im m F(q'^2)}{(q'^2 - q^2)}, \tag{1.2}$$

where t is the threshold for particle production (*e.g.* $t = 2m\,{}^{2}_{\pi}$).

The simplest model to take into account vector meson contribution to the electromagnetic structure of hadrons is the Vector Dominance Model, which assumes that the coupling of a real (or virtual) photon to the electromagnetic hadronic current is mediated by a vector meson [20], as sketched in Fig. 1.10(right). Early models of elastic and transition form factors were directly inspired by Vector Dominance. In 1973, the model of Iachello *et al.* [21], featuring a two-step (direct and vector meson) interaction with a three constituent quark core was one of the first models to predict the correct behavior of elastic nucleon form factors with only five parameters. Much later, the extension of this calculation to time-like elastic form factors was also very novel [22]. Iachello's calculation of the N-$\Delta(1232)$ transition [23] was the first constituent quark model to be extended to the time-like region, together with the HADES collaboration [24]. Along the same line, the model of G. Ramalho and T. Pena, which was originaly developed for baryon transitions in the space-like region was extended to the time-like region for the N-$\Delta(1232)$ resonance [25, 26] and more recently for the N(1520) [26]. This model describes the baryon in terms of a meson cloud and a quark core contribution.

In the mean time, a lot of models, especially constituent quark, including light front approach were developed for electromagnetic transitions in the space-like region, but without extension to the time-like region. Among the most recent and most promising ones are the approaches based on the Dyson-Schwinger equation [27]. The recent availability of lattice QCD calculations of electromagnetic form factors for baryon transitions opens a new era (see [27] and references therein). Indeed lattice calculations solve directly the QCD equations and allow for calculations valid both in the perturbative QCD and in the strong coupling regimes.

1.3 Results for e^+e^- production in HADES experiments

Following the motivations described above, the study of e^+e^- emission in the HADES experiment is therefore two-fold:

- use the e^+e^- probe for studying the QCD matter in heavy-ion collisions;
- understand the elementary sources of e^+e^- and in particular the baryon Dalitz decays which are sensitive to the time-like baryon electromagnetic structure.

1.3.1 Results from QCD matter studies

The HADES collaboration has already published several analyses of dielectron emission from ion-ion collisions, as C+C at 1A GeV [32], C+C at 2A GeV [33] and Ar+KCl at 1.76A GeV [34] and the publication of the results of the study of Au+Au at 1.23A GeV is submitted [30]. In Ar+KCl and Au+Au experiments, an excess of dilepton production with respect to the emission from nucleon-nucleon reactions is observed, after subtraction of the contribution from the long-lived sources (π^0 and η Dalitz decays), in the region of e^+e^- invariant masses below the vector meson poles. As shown in Fig. 1.11 (top), the excess increases as a function of the size of the system. This is interpreted as being due to the propagation and regeneration of virtual ρ mesons. The dilepton invariant mass spectrum for the Au+Au system at 1.23A GeV, which is of course the most interesting to pin down medium effects, is shown in Fig. 1.11 (bottom). The observed shape of the spectrum supports the assumption that the emission stems from a thermalized system where the ρ meson spectral function is modified according to [10].

The HADES collaboration also studied e^+e^- emission from the cold nuclear matter in p+Nb experiments at 3.5 GeV [31]. The advantage of HADES experiments is the possibility to measure e^+e^- pairs with momentum lower than 0.8 GeV/c, where medium effects are expected to be maximum. As show in Fig. 1.12, in these conditions, an excess yield is observed below the omega pole mass with respect to the proton-proton reactions at the same energy.

1.3.2 Results from elementary reactions studies

The studies of elementary reactions (*pp* and *np*) with the liquid hydrogen target have also been an important part of the HADES program in the last years. The study of np collisions is performed using dp reactions where the quasi-free np process is selected using the detection of forward spectator protons. At 1.25 GeV, *i.e.* below the η production

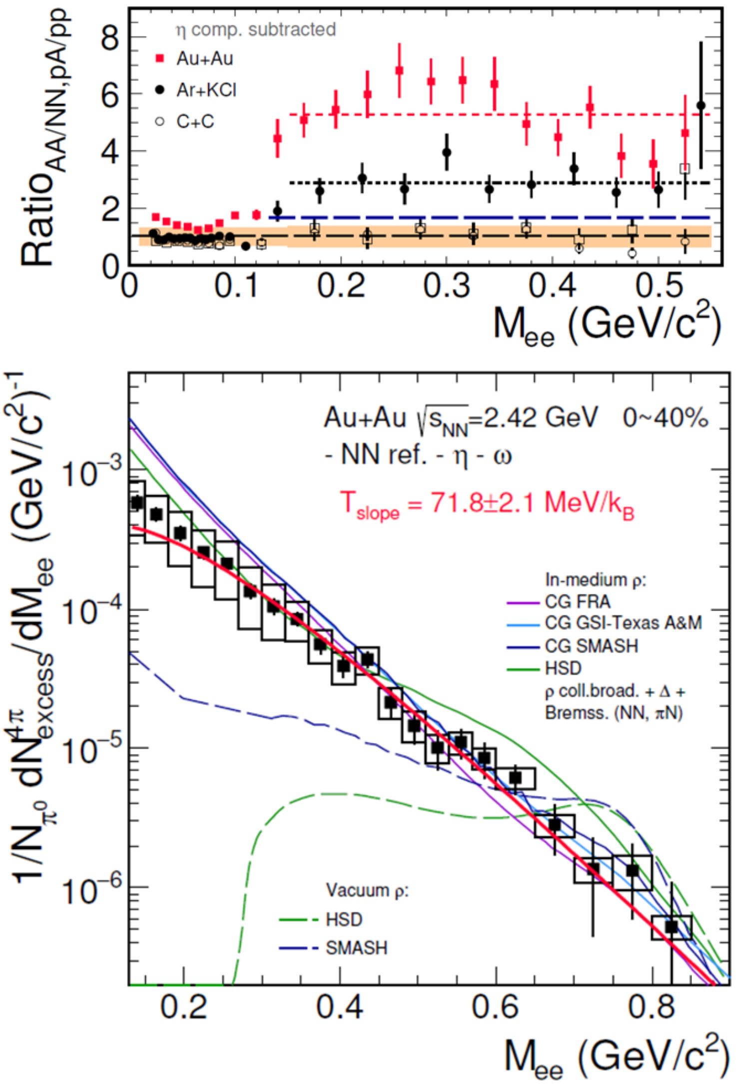

Figure 1.11: Top: Ratio of the invariant mass yield measured by HADES in A+A collisions to the corresponding N+N reference. The η contributions are subtracted from all spectra. Bottom: Black squares: Acceptance corrected dilepton excess yield extracted by subtracting η contributions as well as the NN reference normalized to the number of neutral pions. Dashed curves: ρ (”vacuum” spectral function) contribution from HSD [28] and from SMASH [29] (dark blue) transport model calculations. Solid green curve: total HSD calculation. The blue, pink and dark blue curves show the results of three versions of coarse grained calculations using the modified ρ meson spectral function. See [30] for details.

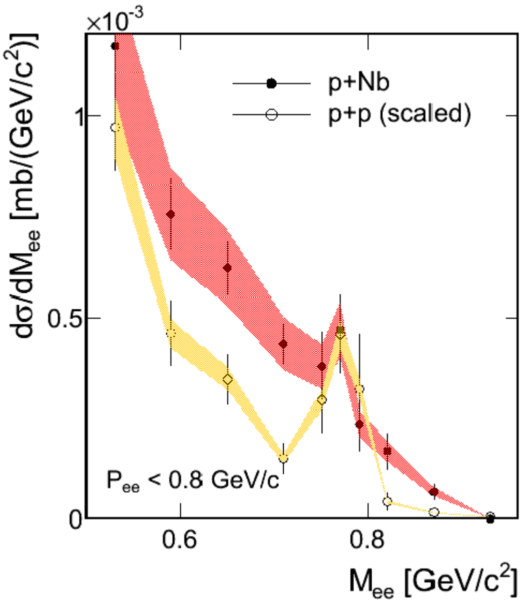

Figure 1.12: Comparison of the invariant mass distribution of e^+e^- pairs with pair momentum $p_{ee} < 0.8$ GeV/c in $p+p$ (open circles) and $p+Nb$ (full circles) collisions measured by HADES at the same kinetic beam energy of 3.5 GeV [31].

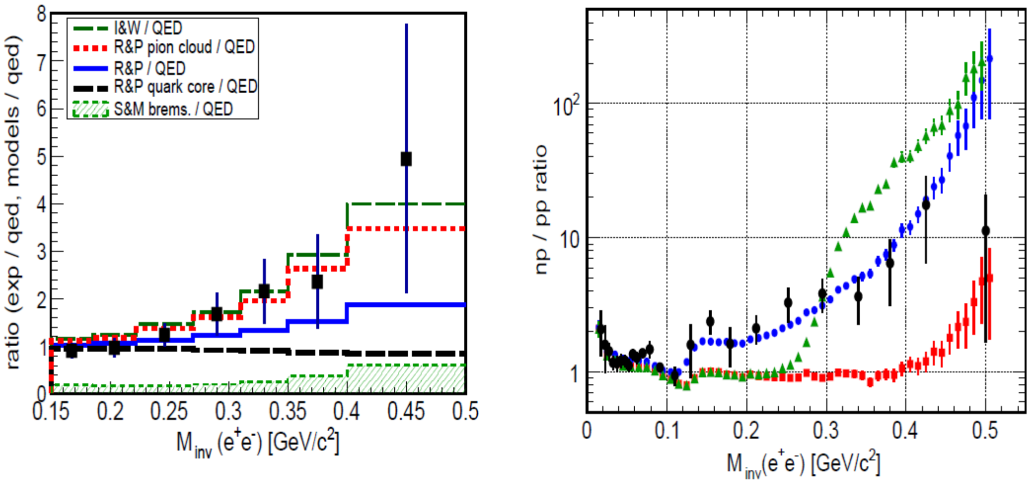

Figure 1.13: Left: analysis of the $pp \to ppe^+e^-$ reaction at 1.25 GeV. Ratio of the experimental e^+e^- invariant mass distribution to the invariant mass distribution expected for a point-like ('QED') Δ transition (black squares) compared to the same ratios for the model predictions with form factor models [35] (I&W) (dashed dark green) and [25, 26] (R&P) (total: full blue, meson cloud contribution: dashed red, quark core contribution: dashed black). Right: Ratio of the differential cross sections as a function of the e^+e^- invariant mass in np and pp collisions at 1.25 GeV. Data (full dots), Shyam and Mosel model (blue circles), Bashkanov and Clement (green triangles). Red squares display the ratio expected for the point-like Δ contributions only.

threshold, the dielectron spectrum can be mainly explained by a superposition of the π^0 Dalitz decay process ($\pi^0 \rightarrow \gamma e^+e^-$) and of the $\Delta(1232)$ Dalitz decay ($\Delta(1232) \rightarrow Ne^+e^-$). The contribution of non resonant $pp \rightarrow ppe^+e^-$ is predicted to be only of the order of 10% [36].

The detailed analysis of the exclusive $pp \rightarrow e^+e^-\ pp$ reaction allowed to extract for the first time the branching ratio of the $\Delta(1232)$ Dalitz decay branching ratio BR = 4.19 ± 0.62 (syst) ± 0.34 (stat) 10^{-5} [37]. This measurement was also recently reported in the Review of the Particle Data Group [38]. The branching ratio is mainly due to the behaviour of the form factor at small q^2. The value is compatible with a calculation with constant form factors in agreement with measurements at q^2=0. As shown in Fig. 1.13 (left), the dielectron yield shows a slight increase with respect to the predictions of a Dalitz decay simulation with a point-like electromagnetic vertex, *i.e.* constant electromagnetic form factors. The model of Pena and Ramalho [25, 26] allows for a better description of the data, especially when the quark core contribution is neglected. The model of Iachello and Wan [35] gives a good description of the data. However, this model lacks a realistic description of the pion electromagnetic form factor.

In the case of the np reaction, an excess of e^+e^- production, with respect to standard calculations of the $\Delta(1232)$ Dalitz decay and of non-resonant bremsstrahlung was observed both in the inclusive production [39] and in the exclusive $np \rightarrow npe^+e^-$ reaction [40]. This triggered new theoretical calculations. Martemyanov and Krivoruchenko [41] demonstrated that the inclusion of the $np \rightarrow de^+e^-$ process (inverse of deuteron radiative capture) improved the description of the data, without fully explaining the measured yield. An upper limit of the cross section for the $pn \rightarrow pne^+e^-$ reaction [42] was extracted and it was found in agreement with the predictions of [41]. Another important difference between the exclusive $pp \rightarrow ppe^+e^-$ and $np \rightarrow npe^+e^-$ reactions is the emission of e^+e^- pairs from charged pionic currents, which is only possible in the np case. Using VDM time-like electromagnetic form factors for the exchanged charged pion in the pn non resonant graphs, Shyam and Mosel's calculation gets close to the data (Fig. 1.13, right). Bashkanov and Clement [43] also reach a good description by considering double $\Delta(1232)$ excitation. In this model, an enhanced dielectron yield is obtained due to the pion electromagnetic form factors in the charged pion exchange between the two Δs. The detailed analysis of the $np \rightarrow npe^+e^-$ exclusive channel by the HADES collaboration [40] were consistent with the interpretation of this excess as being due to an off-shell ρ production. In addition, this interpretation was corroborated by the measurement of the lepton angular distribution (see [40] for details). However, the statistics was not high enough to disentangle between the two models.

The dielectron production has also been studied in the $p+p$ reaction at 2.2 GeV [47] and 3.5 GeV [45]. At these higher energies, the η contribution becomes significant and many baryon resonances contribute, in addition to the $\Delta(1232)$. As displayed in Fig. 1.14 for the case of the pp reaction at 3.5 GeV, a large excess with respect to the expectations from a point-like cocktail of baryonic resonance is observed (Fig. 1.14, left). As shown in Fig. 1.14 (right), this excess is mainly concentrated for low pe^+e^- invariant masses. This effect is interpreted as being due to an off-shell ρ production due to the coupling of light baryonic resonances (as N(1520),...) to the ρN channel, or in other words to VDM time-like electromagnetic form factors. VDM form factors have been implemented in calculations of the Dalitz decay of baryon resonances, using the known couplings to the Nρ channel [46]. Fig. 1.15 shows the comparison of these calculations after adding the eta and omega decays to the inclusive dielectron spectrum measured by HADES in the pp reaction at 3.5 GeV [45]. A quite good agreement is obtained which confirms the strong effect of time-like transition electromagnetic form factors of the Vector Dominance type. However, due to the overlap of the different baryons excited in the pp reaction, information

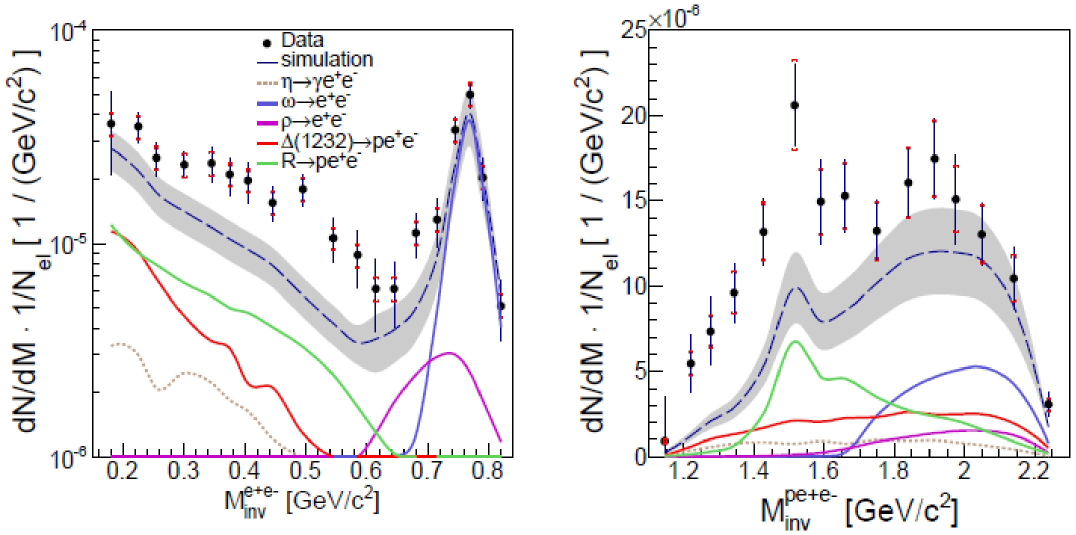

Figure 1.14: Differential distributions measured by HADES for the ppe^+e^- reaction at 3.5 GeV (full dots) as a function of the dielectron invariant mass (left) and pe$^+e^-$ invariant mass (right) compared to the simulation result assuming a point-like RNγ^* coupling ("QED-model") [44].

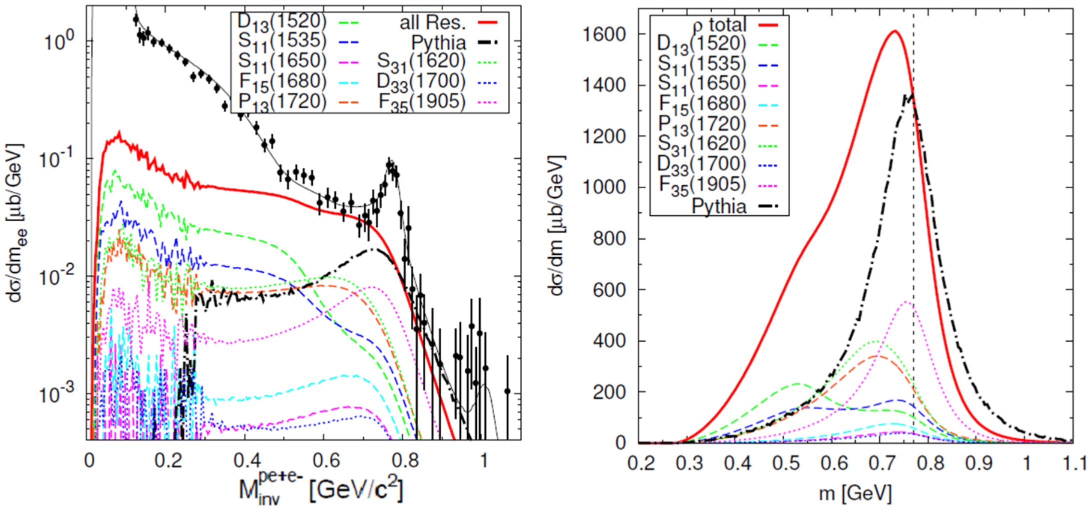

Figure 1.15: Predictions of GiBUU transport model for the $pp \rightarrow e^+e^-X$ reaction at 3.5 GeV. Left: dilepton mass spectrum compared to HADES data. The black curve displays the total calculation, including η and ω contributions (not shown) and the resonance contribution (shown as a red curve). The individual resonant contributions are also displayed as colored curves ($R \rightarrow N\rho \rightarrow Ne^+e^-$). The contribution obtained in the Pythia model with a free rho meson mass distribution is shown as a dashed-dotted curve for comparison [45]. Right: ρ mass distribution. The total is shown in red and the colored curves display the different resonant components. The dashed curve indicates the vacuum pole mass of the ρ meson and the dash-dotted black curve (Pythia) the free ρ meson mass used in the Pythia model is shown for comparison (see [46] for more details).

on individual transitions cannot be obtained.

1.4 Extension of the Dalitz decay studies to π beam experiments

The π-nucleon reaction has several advantages with respect to the pp reaction for studying Dalitz decay of baryon resonances, which make them very attractive. The most important one is that in the s-channel in a π-nucleon reaction, baryonic resonances are produced with a fixed mass equal to the center-of-mass energy $\sqrt{s}$, while in a proton-proton reaction, baryonic resonances are produced in t or u-channel processes with variable masses. The energy of the pion beam can then be fixed according to the mass of the resonance of interest. Due to the large width, a few resonances can still be excited for a given π beam energy, but much fewer than in the case of the pp reaction.

In addition, in the s-channel, the kinematics of all decay products (hadrons, real or virtual photons) is fixed by the quantum numbers of the baryon resonances. It is therefore much easier to extract the amplitudes corresponding to the different contributions in a model independent way, using, *e.g.* Partial Wave Analysis or the spin density formalism, as will be explained in Chapters 7 and 8.

From an experimental point of view, the fact that pion beams are secondary beams with limited intensity is a major disadvantage for studying dielectrons which are very rare signals. However, the $\pi^- p \to n e^+ e^-$ reaction can be easily selected, just by detecting an $e^+ e^-$ pair and using the missing mass constraint, while in the case of the $pp \to pp e^+ e^-$ reaction, the detection of an additional proton is needed.

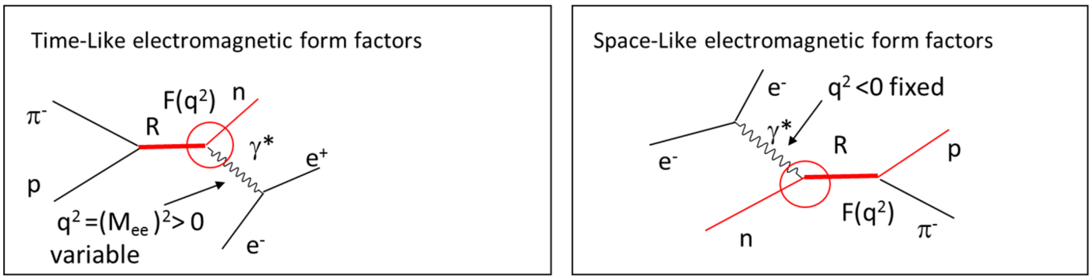

Figure 1.16: Graphs of the $\pi^- p \to n e^+ e^-$(left) and $en \to e' p \pi^-$(right) reactions giving access to the time-like and space-like baryon transition form factors respectively [48]. The circles depict the form factors F(q^2) of the RNγ^* vertices.

As displayed in Fig. 1.16, the $\pi^- p \to n e^+ e^-$ reaction is just the reverse reaction from the pion electroproduction reaction, which is one of the experiments used to extract baryon transition form factors in the space-like region. To start the experimental program with the pion beam, the region of the N(1520) resonance is chosen, due to its strong coupling to the ρ-N channel and hence its important contribution to the in medium ρ meson modification.

This PhD work is mainly focused on the analysis of the $e^+ e^-$ production channel. A long data taking period was devoted to this measurement, using a polyethylene target (C_2H_4) and a pion beam with a momentum of 0.69 GeV/c. A smaller statistics was also collected at three other measurements with pion beam momenta of 0.656, 0.748 and 0.8 GeV/c in order to provide new pion production data for Partial Wave Analysis, which, as will be shown in Sec. 7.5 are very useful for the interpretation of the dielectron channels. Measurements with a carbon target were also performed simultaneously to subtract events coming from the interaction with carbon nuclei in the polyethylene target. However, as will be explained in Sec. 5.6, the recorded statistics for the dielectron channels was limited and a precise subtraction of interactions with carbon nuclei in the polyethylene target was possible only in the case of pion production channels. This is why, when reporting about the existing data in the next section, we consider both reactions on proton and on carbon.

1.5 Existing data for pion induced reactions

Some measurements for e^+e^- production exist for low pion beam energies (below or in the Δ resonance region) [49, 50, 51, 52, 53, 54, 55, 56, 57, 58, 59, 60]. They have focused either on the π^0 Dalitz decay in the reaction $\pi^- p \to n\gamma e^+e^-$or on helicity amplitude measurements in the $\pi^- p \to ne^+e^-$ reaction. The latter results have been interpreted in the context of the Inverse Pion Electroproduction model as discussed shortly in Sec. 7.2. The e^+e^- production has also been studied at incident pion momenta of 4 GeV/c, *i.e.* above the vector meson poles [61]. However, there are no measurements of e^+e^- production with pion beams in our energy range. Nevertheless, some information exist on the production of mesons, which can be used for the interpretation of our data, as will be discussed in Chapter 8.

1.5.1 Experimental information for π^- p reactions

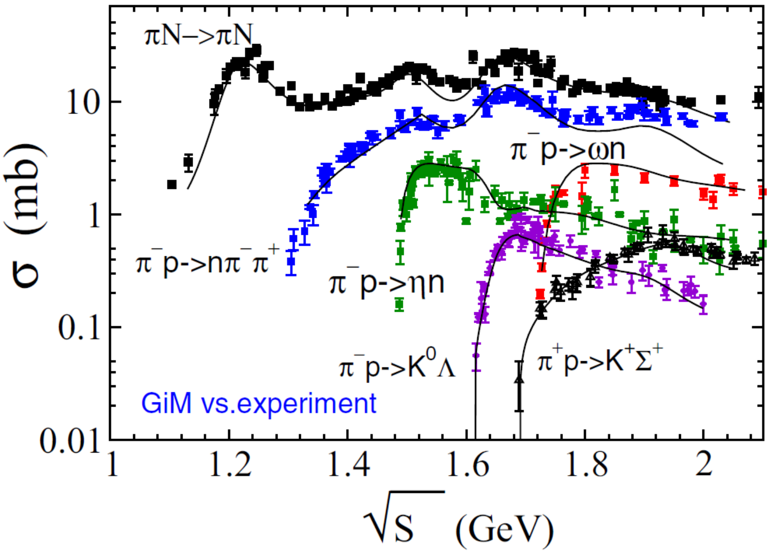

Figure 1.17: Total cross sections for pion-induced reactions calculated in Giessen Model vs experimental data [62].

As shown in Fig. 1.17, cross section measurements for the various hadronic exit channels in π^--nucleon reactions exist in a wide range of energies. It can be observed that the $\pi N \to \pi N$ (*i.e.* elastic or charge-exchange) and, above the threshold, the two-pion production channels are the dominant channels, at least for pion energies up to 2 GeV. As our experiment was performed at $\sqrt{s}$=1.49 GeV, just above the η threshold, we are interested only in the π and η production. As will be discussed in the following, the information on cross sections is rather precise, but the situation is very different concerning differential distributions. We will focus on the channels which have a decay into e^+e^-, *i.e.* the production of a baryonic resonance ($R \to ne^+e^-$), a π^0($\pi^0\to \gamma\ e^+e^-$) or an η ($\eta \to \gamma\ e^+e^-$) (see Sec. 1.1.4).

Baryon resonance production

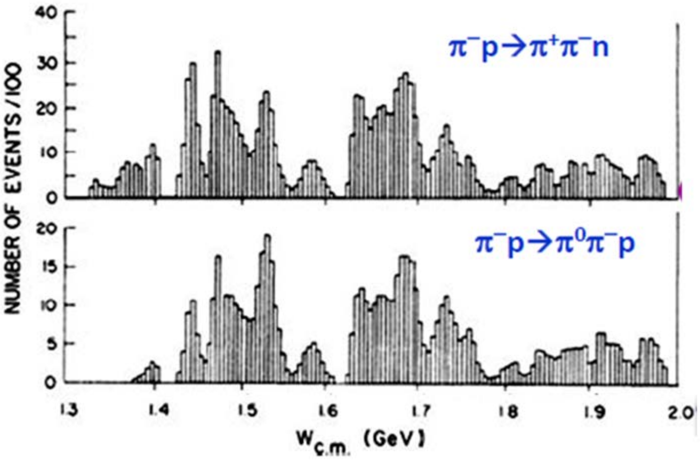

Figure 1.18: Number of events recorded for the π^-p $\rightarrow$ $\pi^+\pi^-$n and $\pi^- p \rightarrow \pi^0\pi^-$p channel in the existing data base.

Information on the baryon resonance production is obtained from Partial Wave Analysis (PWA), which consists in global fits of many different exit channels. Here, both pion and photon induced data need to be taken into account, since they provide complementary information. As a matter of fact, thanks to an enormous experimental effort in the last twenty years, the data base for photon induced reactions is very rich. The situation is very different for pion induced reactions, where few experiments were performed since the bubble chamber experiments in the 80's.

The two pion production channel is important to fix the couplings to $\Delta\pi$, ρ N and σ N of the baryonic resonances. Good statistics in many bins for these three particles final state is in principle needed to obtain a good precision on these couplings, but this is by far not the case. This is illustrated in Fig. 1.18 for the charged two pion production channel in the π^-p reaction, for which the data base did not change at all since then. The well-known Manley analysis [63] was based on only 241 thousand events recorded over the center-of-mass energy range between 1.3 and 1.93 GeV. More recently, new precise data were provided by the Crystal Ball collaboration at BNL, but they concerned only the $\pi^0\pi^0$ channel [64]. New measurements in the two charged pion channels were also performed at center-of-mass energies close to 1.3 GeV at TRIUMF [65] and at ITEP at 2 GeV [66], but there is no new data for charged pion channels between 1.3 and 2 GeV.

New PWA analyses were still performed for the 2π production channel [67, 68, 69] as well as coupled-channel analysis [70, 62]. These analyses show a large scatter, as demonstrated in [44] for the couplings to the Nρ channel, which is particularly important for our analysis. For example, for the N(1520), the Bonn-Gatchina PWA analysis [69] predicts a branching ratio of 10% towards the ρN channel, while the KSU PWA gives a value of 21 % [68]. As will be explained in Sec. 7.5, the data measured in the present experiment for the reactions $\pi^- p \rightarrow n\pi^+\pi^-$ and $\pi^- p \rightarrow p\pi^0\pi^-$ allow for a new determination of the contributions of the main resonances in the region of $\sqrt{s}$=1.5 GeV (*i.e.* N(1440), N(1520), N(1535)) and of the couplings to the $N\rho$ channel, which will be used for the interpretation of the data.

The $\pi^- p \rightarrow \pi^0 n$ channel

The largest contribution to the π^0 production comes from the exclusive charge exchange reaction $\pi^- p \rightarrow n\pi^0$. Previous measurements of total cross sections and/or angular distributions exist for these reactions and have been used in the SAID Partial Wave Analysis (PWA) [71] together with results from photon induced experiments to determine the properties of baryonic resonances. The most relevant total cross section measurements for our analysis have been provided by experiments at BNL with cross sections of 7.71 ± 0.62 mb [72] at an incident beam energy of E=565 MeV and 8.33 ± 0.56 mb [73] at E=568.3 MeV, respectively. However, according to the SAID data base information [71], these cross section measurements do not seem to have been directly used in the SAID analysis, which is then presumably based only on differential distributions measured in the charge exchange reaction.

The cross sections resulting from four different PWA solutions for the charge-exchange reaction at E=564 MeV are displayed in Table 1.2 in comparison to the experimental measurements. It can be noticed that the oldest solution (KH80) provides a cross section of 8.99 mb, in agreement with [73] and slightly larger than [72]. Besides, the most recent solutions converge to a higher value.

PWA solution at E=564 MeV				[72] (E= 565 MeV)	[73] (568.3 MeV)
KH80	KA84	CMB	WI08		
8.99	9.49	9.71	9.77	7.71± 0.62	8.33±0.56

Table 1.2: Comparison of cross sections (mb) for the $\pi^- p \rightarrow n\ \pi^0$ reaction extracted in four different PWA solutions at E=564 MeV and existing measurements.

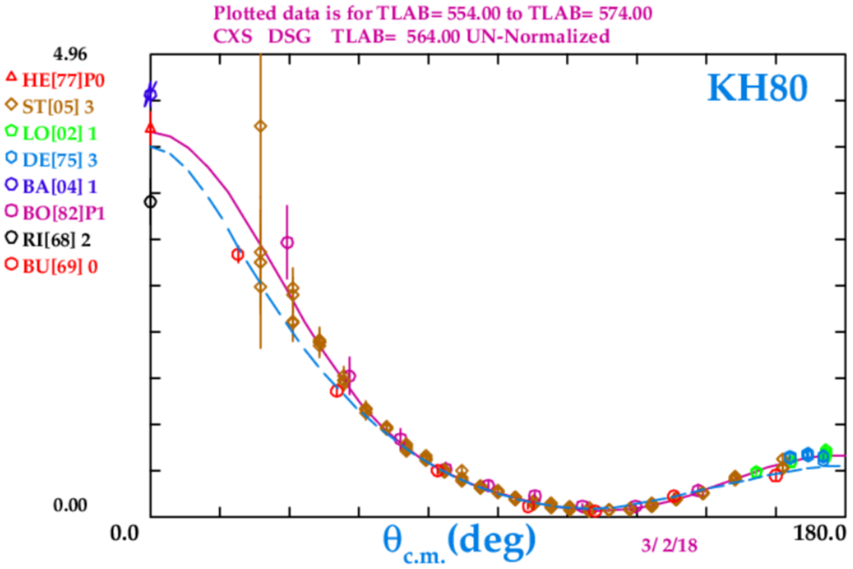

Figure 1.19: Existing data for the $\pi^- p \rightarrow \pi^0 n$ reaction for incident energies in the range [554 – 564] MeV compared to the WI08 (pink) and KH80 (blue) PWA solutions. Picture extracted from the SAID web page `http : //gwdac.phys.gwu.edu/analysis/pin`$_{\mathtt{a}}$`nalysis.html`.

As can be seen in Fig. 1.19, several experiments have provided differential cross sections as a function of the π^0 center of mass angle at incident energies close to our experiment and most of them have been taken into account in the SAID PWA. The most recent and complete among these data are measurements with the Crystal Ball (CB) at BNL [74] published in 2005 and labeled as St[05]. Despite the lack of precise measurements at angles smaller than 20°, it can be clearly observed that the pion angular distribution is strongly forward peaked. It can also be noted that the KH80 solution, which did not take into account the CB data and provides the smallest total cross sections (see Table 1.2) is still in reasonable agreement with the CB data. However, an overall better agreement is obtained using the more recent WI08 solution.

The most important result that we will keep in mind for the description of our data is that the pion angular distribution in our energy range is strongly forward peaked, with a decrease of about a factor of 2 between 0 and 40°. As we will see, the correct description of this angular distribution, combined with the acceptance of the HADES detector is an important feature of the simulations of π^0 production.

The $\pi^-p\to\ \pi^0\pi^-p$ and $\pi^-p\to\ \pi^0\pi^0n$ reactions

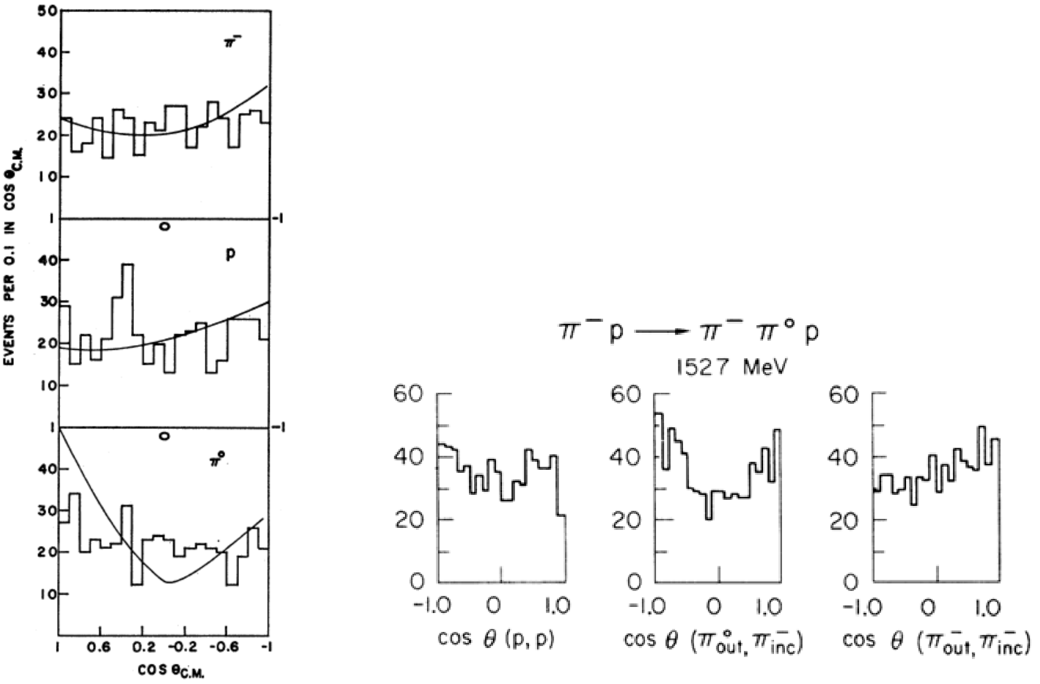

Figure 1.20: Angular distributions measured in the center-of-mass for the reaction $\pi^-p\to\pi^0\pi^-p$ at an incident energy E = 558 MeV at BNL [75] (left) and E = 573 MeV at Berkeley [76] (right).

For the $\pi^-p\to\ \pi^0\pi^-p$ reaction, only old and imprecise information exist. However the cross sections of 3.99 ± 0.5 mb and 3.98 ± 0.35 mb obtained at BNL [75] at an incident beam energy of 558 MeV and at Berkeley at 573 MeV [76], respectively are in very good agreement. Despite the small statistics of these data, it seems that the π^0s angular distributions are rather symmetric with no or small anisotropy, as can be seen in Fig. 1.20.

The $\pi^-p\ \to\ \pi^0\pi^0\ n$ reaction has been measured very precisely by the Crystal Ball collaboration. The cross section value at our energy is σ=1.880 ± 0.015 mb. Fig. 1.21 displays the measured differential distributions at different energies. A significant forward/backward enhancement in the emission of the $\pi^0\pi^0$ pair can be observed, together with a small asymmetry favoring π^0 emission in the forward direction.

The $\pi^-p\ \to\ \pi^0\pi^0\ n$ cross section is roughly half the $\pi^-p\to\ \pi^0\pi^-p$ cross section. However, due to the presence of two π^0 s in the exit channel, the two channels will have a

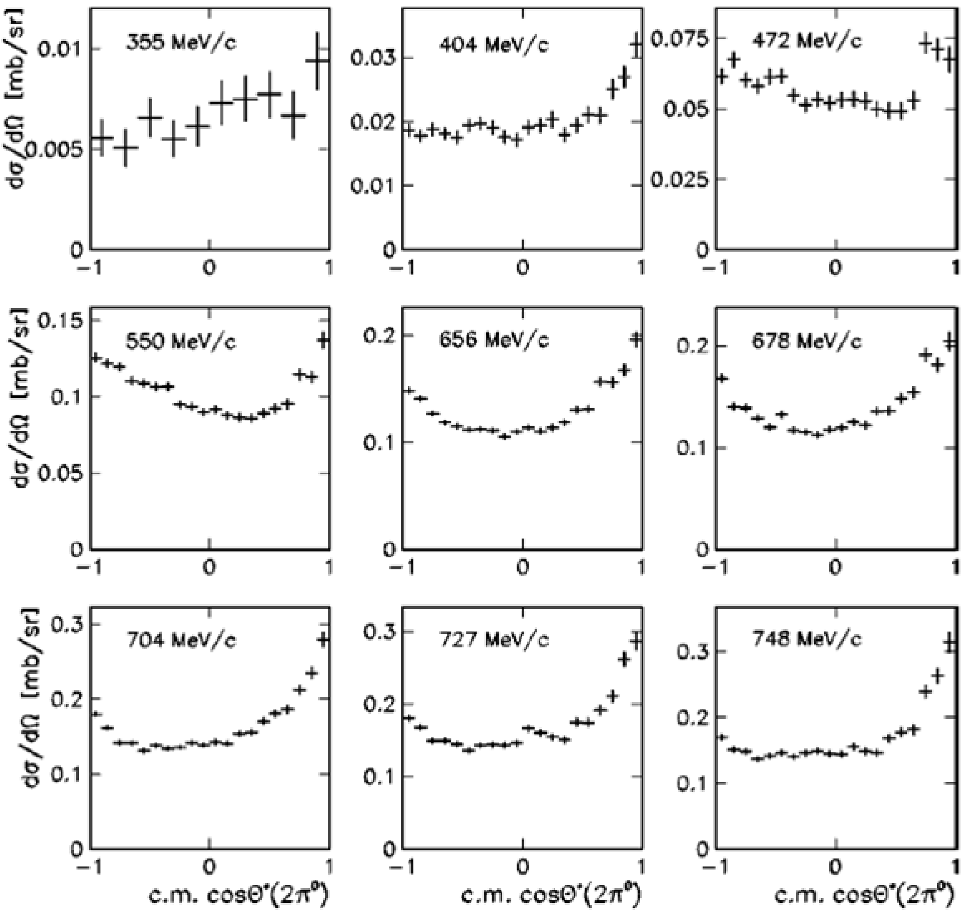

Figure 1.21: Differential cross sections as a function of the angle of the $2\pi^0$ system in the center-of-mass in the reaction $\pi^- p \rightarrow \pi^0 \pi^0\, n$ at different π^- momenta [74].

similar contribution to the π^0 Dalitz decay contribution. The angular distributions differ from phase space, but the anisotropy is much lower than for the single pion channel.

Our experiment is well above the threshold for three pion production, but few available data indicate that this contribution is lower by one order of magnitude with respect to the two pion production.

η production

The threshold for η production is $\sqrt{s}$=1.487 GeV, corresponding to E_π=0.56 GeV or p_π=0.6854 GeV/c. Fig. 1.22 displays the measurements which were available in 2002 for the total cross section in the $\pi^- p \rightarrow \eta n$ reaction in comparison with the coupled-channel analysis of the GiBUU group [79]. It can be clearly seen that the η production in our energy range is totally dominated by the N(1535) S_{11} resonance. Most of these data date back to the seventies or eighties, but of particular importance for our studies are the more recent measurements close to threshold at BNL by the E909 experiment [77, 78], which are shown as empty circles. In addition, the CB collaboration provided other measurements of the same reaction at BNL [80], which are displayed in Fig. 1.23 as a function of the η center-of-mass momentum. Although not fully compatible, these measurements give good constraints for the evolution of the η production cross sections in the vicinity of the threshold that can be used for our data analysis.

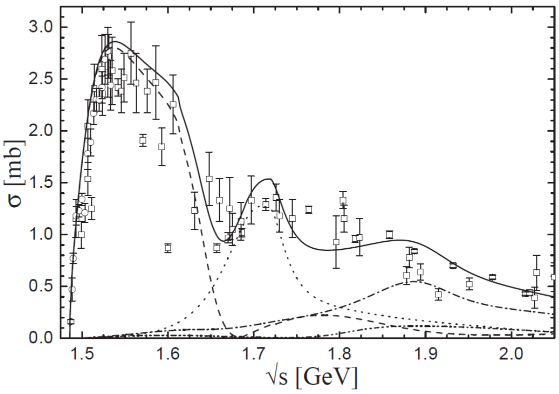

Figure 1.22: $\pi^- p\to \eta n$ total cross sections. The threshold data [77, 78] obtained by E909 at BNL are denoted by empty circles. The curves show the PWA decomposition in the coupled channel analysis of the GiBUU group: $\mathrm{J}^P = \frac{1}{2}^-(S_{11})$ (dashed line), $\mathrm{J}^P = \frac{1}{2}^+(P_{11})$ (dotted line) $\mathrm{J}^P = \frac{3}{2}^+(P_{13})$ (dash-dotted line), $\mathrm{J}^P = \frac{3}{2}^-(D_{13})$. The sum of all partial waves is given by the solid line. Figure from [79].

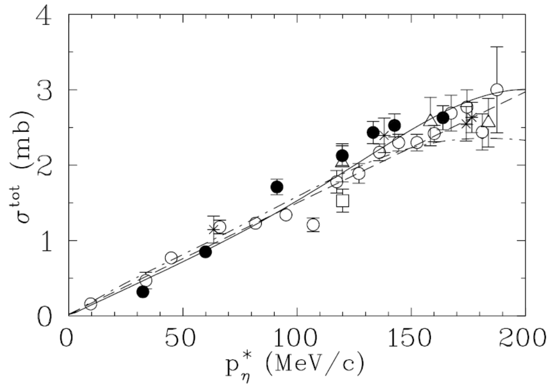

Figure 1.23: Dependence of the total cross section of the reaction $\pi^-\mathrm{p}\to \eta\ n$ as a function of the η center -of-mass momentum compared to various fits or calculations [78]. Open circles display the BNL/E909 data [77] and filled circles the BNL/CB data [80].

1.5.2 Comparison of $\pi^- p$ and $\pi^- n$ cross sections

In the reaction on ^{12}C, π^- can interact either with protons or with neutrons. Figure 1.24 displays the total cross-section for the $\pi^- p$ and $\pi^+ p$ (equivalent to $\pi^- n$) in a wide range of energies. In the region of the $\Delta(1232)$ resonance, the cross section for the $\pi^+ p$ reaction is larger than the one for the $\pi^- p$ by about one order of magnitude due to the different isospin factors for the $\pi^+ p \to \Delta^{++}$ and $\pi^- p \to \Delta^0$ reactions, respectively.

This is very different in the region of the second and third resonances, due to the high number of isopin 1/2 resonances. The $\pi^- p$ cross section is much larger than the $\pi^+ p$, since the former can couple to both I=1/2 and 3/2 channels, while the latter couples only to the I=3/2 Δ resonances. The ratio of cross sections between the two channels is about a factor of 3 at pion momenta of 700 MeV/c. So we can conclude that the interaction in a carbon nuclei will take place mostly with the bound protons.

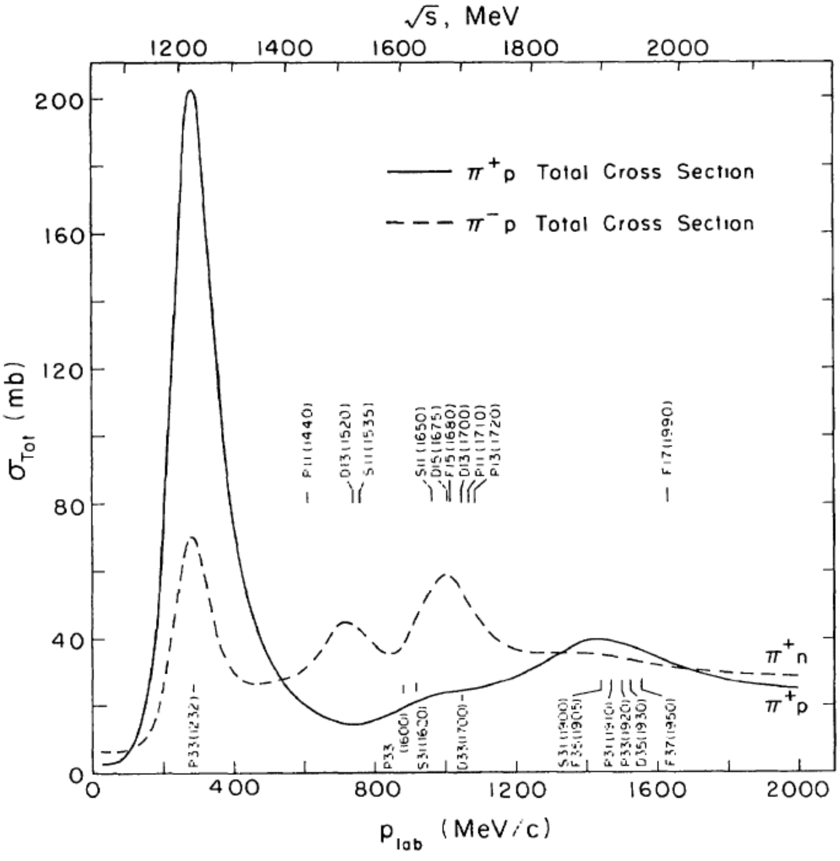

Figure 1.24: Total π^+p and π^-p cross sections plotted against the π momentum (p_{lab}) and total center-of-mass energy $\sqrt{s}$. The positions of several prominent N* and Δ resonances are indicated [81].

1.5.3 Experimental information for pion interactions with nuclei

The region of the Δ(1232) resonance (*i.e.* $p_\pi < 450$ MeV/c) has been studied in great detail in pion beam experiments in the 70's and 80's at LAMPF, TRIUMF and PSI (see *e.g.* [82, 83] for reviews in 1988). The dominant process in a π-nucleus interaction in this energy range is a quasi-free scattering, which is however modified by several medium effects (Fermi motion, Δ-hole potential, multistep processes, absorption,...). These effects are included in the Δ-hole model [84, 85] which provided a very successful description of inelastic and charge-exchange data. The key result of the studies performed in the Δ resonance region, is therefore that the Δ-isobar still appears as a distinct baryonic species in the nuclear medium and can be treated as a quasi-particle.

For higher energy pions, with wave lengths closer to the internucleon distances, this picture should hold even better. A pion at 0.7 GeV/c has indeed a De Broglie wavelength of 1.8 fm, to be compared to the value of 4 fm for a pion with a momentum of 0.3 GeV/c. On the other hand, due to the lower πN cross sections (see Fig. 1.24) above the Δ resonance and the relative decrease of the absorption contribution in the reaction cross section, the mean free path of the incident pions is much larger, allowing them to scatter more deeply inside the nucleus which is more favorable to probe medium effects. However, due to the overlap between the different baryon resonances, detailed studies of their in-medium properties are much more difficult than in the Δ resonance region.

High energy pion beams were used for nuclear structure studies [93, 94] using elastic scattering, single or double charge exchange reactions. This is not very relevant for our

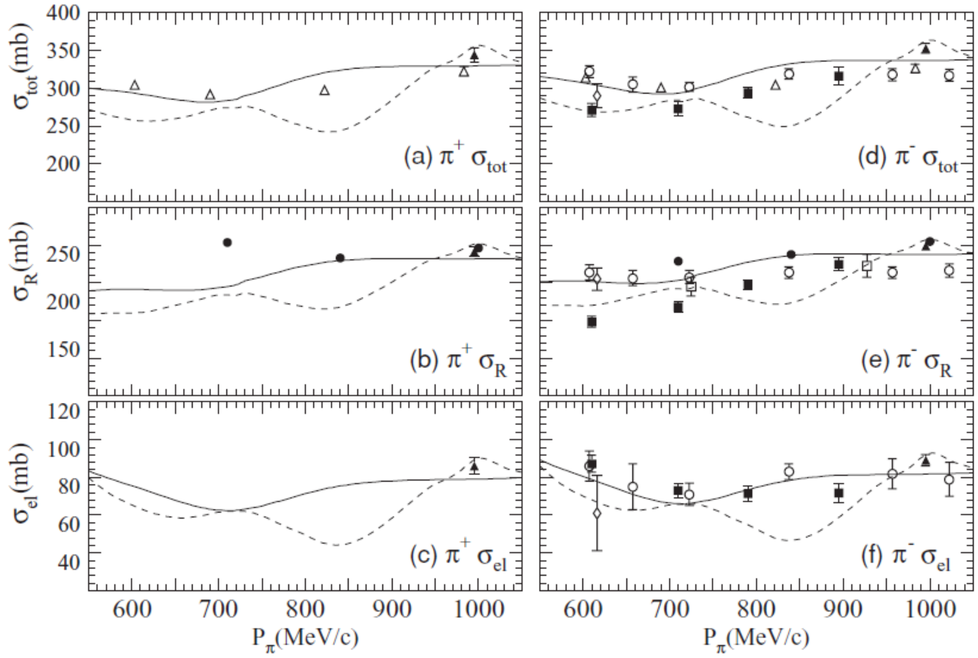

Figure 1.25: Total π^+ + C (left) π^-+ C (right) cross sections from measurements at KEK [86] (solid triangles), Clough *et al.* at NIMROD [87] (open triangle), Allardyce *et al.* at NIMROD [88] (solid circle), Takahashi *et al.* at KEK [89] (solid square), Crozon *et al.* at SATURNE [90](open circle), Cronin *et al.* at the Cosmotron [91] (open square) and Gelderloos *et al.* at LAMPF [92] (open diamond). The dashed and solid curve display results of an optical model with free amplitudes and taking into account the effect of Fermi motion, respectively.

studies, since reactions induced by π^- on carbon nuclei and leading to excited states of the ^{12}B nucleus are expected to produce extremely forward peaked π^0s and no additional particles with significant energies, so that the contribution of these processes is expected to be negligible in our analysis. We are therefore mostly interested in reactions where the π^- loses a substantial fraction of its energy and a π^0 is scattered at large angles.

Rather precise measurements of total and absorption cross sections were already provided in 1957 by Cronin *et al.* from measurements at the Cosmotron in Brookhaven for pion energies between 0.6 and 1.2 GeV and in 1965 by C. Crozon *et al.* at Saturne, between 0.5 and 1.3 GeV. As shown in Fig. 1.25, the total cross section is of the order of 225 mb at an incident pion momentum of 700 MeV/c, while the average of the π^-+ p and π^++ p (equivalent to π^-+n) is of the order of 27 mb, which indicates an effective number of participating nucleons of about 8 among the 12 nucleons of the carbon nucleus in a very simplistic way.

Using the BGO ball array at LAMPF, Jones *et al.* have derived cross sections for many exit channels in π^+ induced reactions on various nuclei [95] with incident pion energies between 250 and 500 MeV. For a carbon target, inclusive (π^+, π^0) charge exchange cross sections values increase from 46 to 91 mb when the pion energy increases from 250 to 500 MeV, while absorption cross sections decrease from 73 to 39 mb. This confirms that absorption is a much weaker effect than at pion energies corresponding to the Δ resonance, where the absorption cross section is four times larger than charge exchange. It is also worth to be noted that for this inclusive charge exchange process at 500 MeV, where only neutrons contribute, a number of participant neutrons of 4.8 was found.

Existing results for ^{12}C(π, π^0) reactions

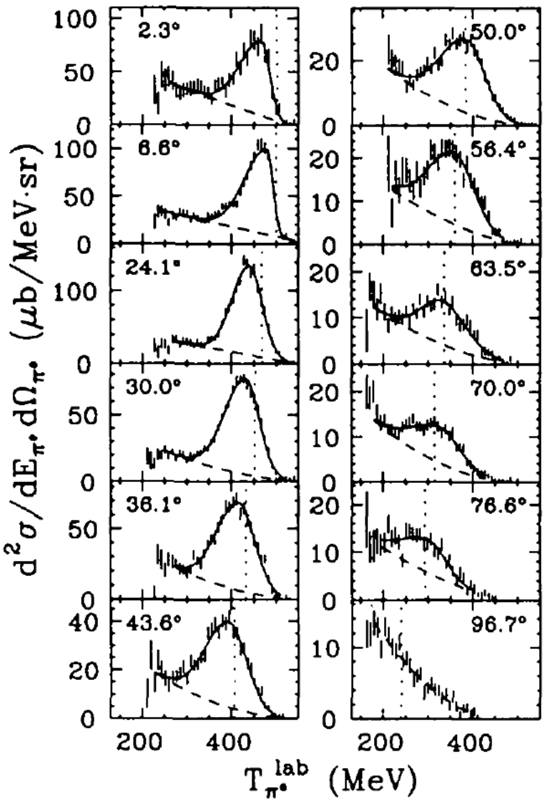

Figure 1.26: Differential cross sections for C(π^-, π^0) reactions at 500 MeV as a function of the π^0 kinetic energy for different π^0 angles. The solid curves are fits to the data with two half-gaussians + a second order polynomial for the background. The dotted lines indicate the π^0 energy for the free $\pi^- p \rightarrow \pi^0 n$ reaction [96].

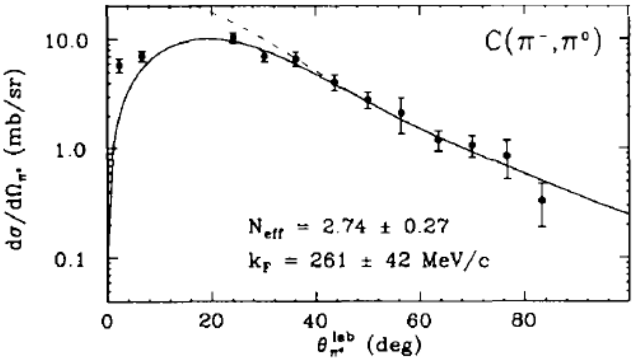

Figure 1.27: Integrated (π^-, π^0) quasi-free charge-exchange cross sections at 500 MeV as a function of laboratory scattering angle. The solid curves show fits obtained using a product of the free πN cross sections and a Fermi-gas Pauli-blocking factor (varying the overall normalization N_{eff} and the Fermi momentum k_F [96]).

A series of experiments has been performed in LAMPF to measure inclusive pion scattering (π, π') [99] and charge exchange (π^-, π^0) [97, 96, 100] on carbon and other target nuclei for incident pion energies between 400 and 500 MeV. A clear quasi-free peak

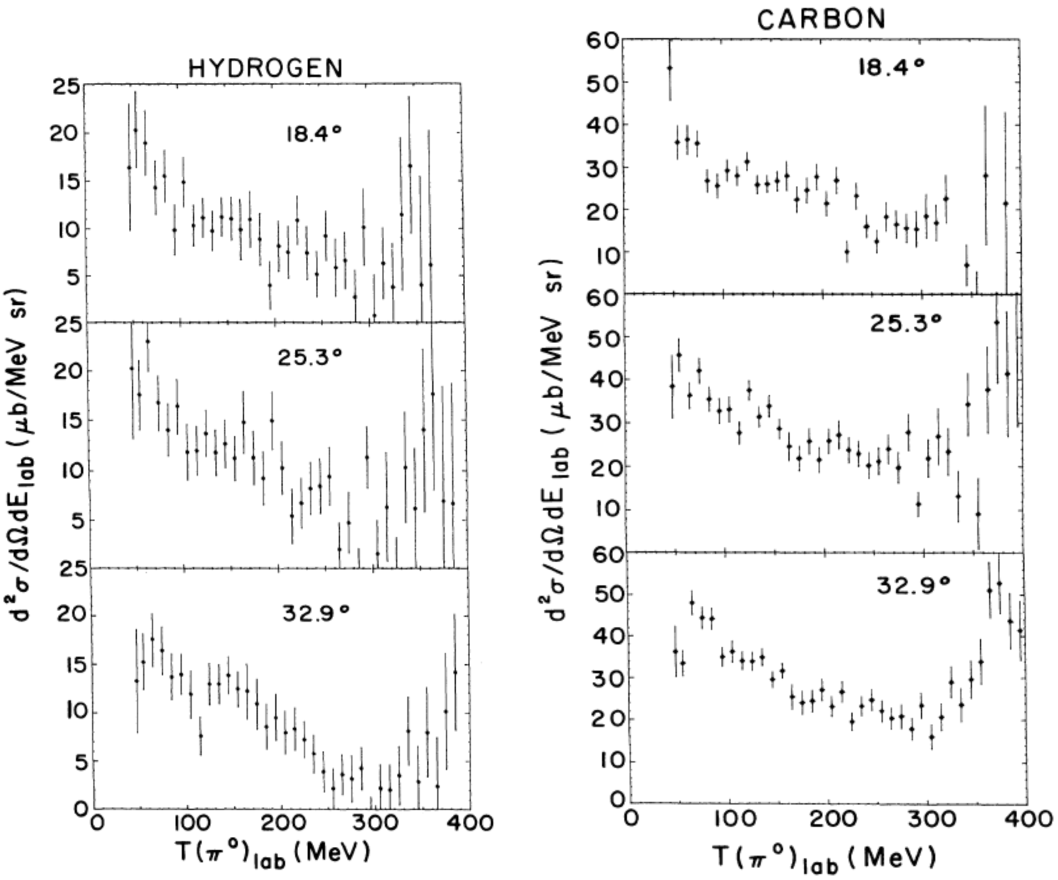

Figure 1.28: Laboratory π^0 energy spectra from reactions induced by a π^- beam at 475MeV on proton (left) and carbon (right) for three angle bins [97].

is observed in the π^0 energy distribution for a kinematics close to the $\pi N \to \pi\ N$ kinematics (Fig. 1.26). It can be seen that this quasi-free charge-exchange peak is dominant at the most forward angles, but vanishes at larger angles, leaving the scene to other processes.

It was found that, for π^0 angles larger than 36°, corresponding to momentum transfers larger than 370 MeV/c, where the Pauli blocking effect vanishes, the quasi-free yield follows an angular distribution similar to the free one (Fig. 1.27). Calculations taking into account the nuclear response have also been compared to the differential pion energy loss distributions at the different angles [101]. It was observed that for momentum transfers above 370 MeV/c, the effect of the nuclear correlations is rather limited and in a first approximation, the free calculation gives a fair reproduction of the quasi-free charge-exchange peak. In fact, due to the possible emission of at least one additional pion, the π^0 energy spectra extend towards much lower energies, as displayed in Fig. 1.28, where energy loss spectra measured in the (π^-, π^0) reaction at 475 MeV by [97] can be directly compared for proton and carbon targets. It is interesting to note that the spectra measured on the two targets do not show very striking differences. However, here the scaling factor between the hydrogen and carbon differential cross section is about 2.4, *i.e.* much lower than for the ^{12}C(π^+,π^0) reaction at 500 MeV [95].

The observation that the π^0 production on a carbon target does not differ much from the free process justifies the fact that we use a participant-spectator approach for the π^0 production to describe our data (see Chap. 8).

Fig. 1.29 shows other examples of spectra measured at LAMPF in the charge exchange ($\pi^\pm$,π^0) channel [97, 96]. They were compared to intranuclear cascade and transport

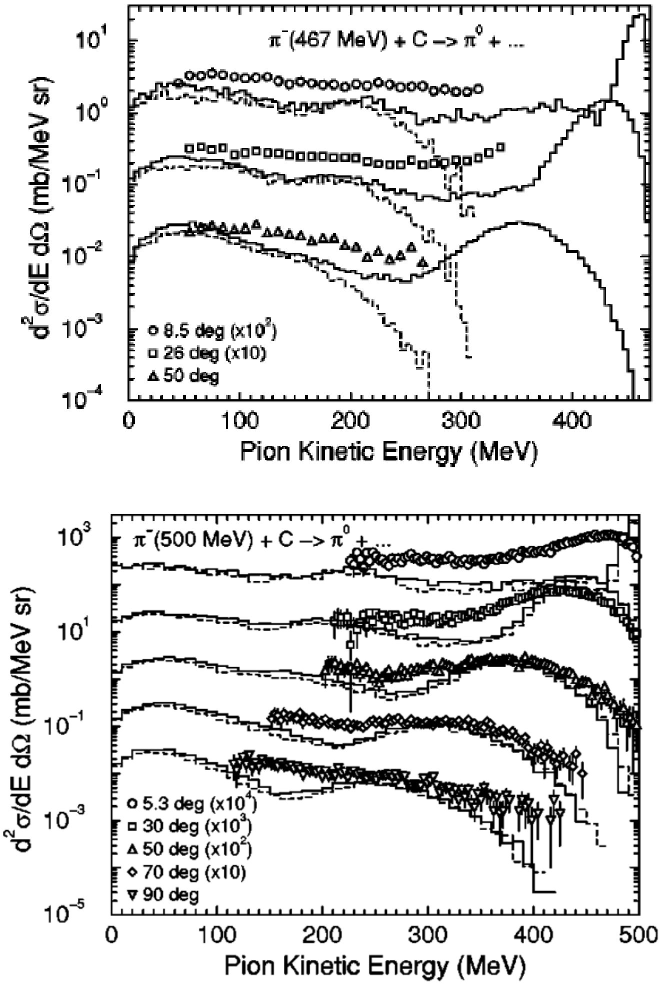

Figure 1.29: Measured π^0 spectra for 467 MeV (top) and 500 MeV (bottom) π^- beams on a carbon target are compared to calculations in the Cascade Exciton Model without medium modifications (solid line). The dashed lines in the top and bottom pictures display the contributions from the $(\pi, 2\pi)$ process and a calculation with a different data set for the elementary πN interactions respectively [98].

model calculations [102, 98] which did not include explicitly $\Delta(1232)$ and higher lying resonances. These calculations, based on π-nucleon cross sections, were not able to describe quantitatively the data. However, they confirmed that the pions measured at forward angles are mostly due to the quasi-elastic process while those produced at large angles and large energy losses are due to the $(\pi, 2\pi)$ processes. It would be valuable to see how modern transport model calculations explicitly including various baryonic resonances, as GiBUU (see Sec. 8.2.7) compare to these charge exchange data.

The two-pion production processes $^{12}C(\pi^-, \pi^-\pi^+)$ and $^{12}C(\pi^-, 2\pi^-)$ have been investiagated at PSI [103] and TRIUMF [104] up to 320 MeV, only. High precision differential spectra on many nuclei, including carbon, were later measured at the same energies for the $(\pi^+, \pi^+\pi^-)$ and $(\pi^+, \pi^+\pi^+)$ reactions at TRIUMF by the CHAOS collaboration and $(\pi^-, \pi^0\pi^0)$ by the Crystal Ball collaboration at BNL. The emphasis was put on the $\pi\pi$ dynamics and the search for a signal of chiral symmetry restoration in nuclear matter [105, 106, 107]. However, the energy of these measurements is much too low to provide useful information for our analysis. In more recent years the KEK and TRIUMF pion beams were mostly used at energies above the $\Delta(1232)$ resonance to study elastic or double charge exchange pion scattering for nuclear structure studies and even more intensively for strangeness and hypernuclei production.

In summary, rather scarce information exist for pion production on nuclei above the Δ resonance region. It is however commonly admitted that the inelastic (π, π), charge-exchange or $(\pi, 2\pi)$ process in nuclei proceeds via a quasi-free process above the Δ resonance region. While medium effects are important to describe these reactions in details, their gross features are driven by the free amplitudes.

η production

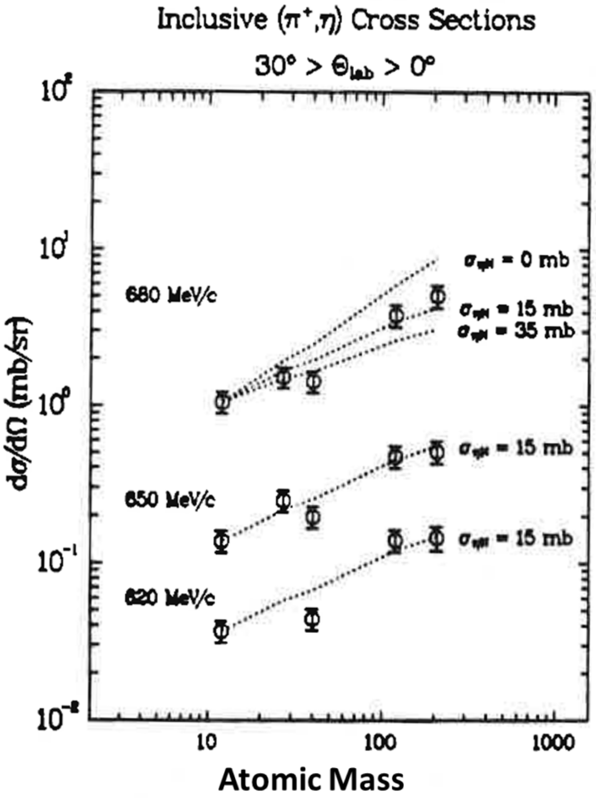

Figure 1.30: Inclusive η production cross sections measured at LAMPF on various nuclei [108]. The cross sections are integrated over the laboratory angular range between 0 and 30°.

Most of the experiments measuring η production in pion induced experiments off nuclei focused on interactions with light nuclei, *i.e.* d or ^{3}He, but still some measurements on heavier nuclei were performed at LAMPF [108] for pion momenta up to 680 MeV/c. The cross sections integrated over the laboratory angular range between 0 and 30° are displayed in Fig. 1.30 as a function of the atomic number of the target.

To probe the sensitivity to the ηN interaction, the differential cross sections were compared with a Glauber model using different ηN cross sections, showing a better agreement with a rather small ηN cross section of 15 mb. DWIA calculations have been performed for the η production on the ^{12}C nucleus [110, 109, 111]. The two calculations disagree for the absolute value of the cross sections as can be seen in the left part of Fig. 1.31, but both show the influence of the medium, via the N(1535) potential. The proton final state interaction is also shown to reduce significantly the cross section. However, these effects seem not to affect seriously the shape of the differential distributions. These observations

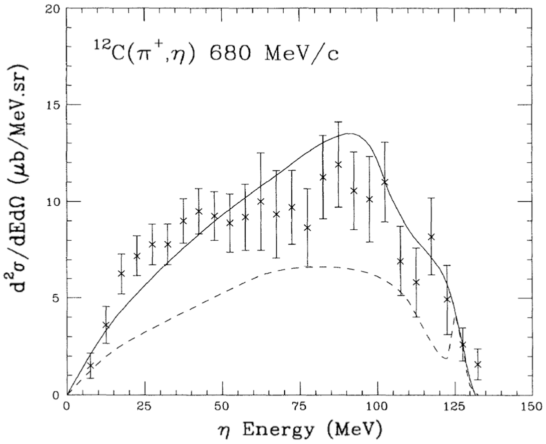

Figure 1.31: (π^+,η) inclusive cross sections on C target at a pion incident momentum of 680 MeV/c as a function of the η kinetic energy [108] compared to DWIA calculations of [109] (solid curve) and [110] (dashed curve).

have to be kept in mind in our analysis, where we use a participant-spectator model for the reaction on the carbon.

1.6 Conclusion

In this chapter, we have presented the main motivations of measuring the dielectron production with HADES at GSI and we have summarized the results obtained so far by the HADES collaboration. In particular, the study of the proton-proton reactions allowed to study for the first time Dalitz decay of baryon resonances. A detailed study of the Δ(1232) resonance Dalitz decay was possible. For higher lying resonances, a sensitivity to the off-shell ρ meson contribution was shown, however individual contributions can not be isolated, which motivates experiments with a pion beam. As shown above, very little data for pion induced reactions are available for energies above the Δ(1232) resonance region. Still, the differential distributions for π^0 production in the π^-p reaction are known with a good precision, except for the $\pi^0\pi^-p$ channel. The η production has also been measured close to production threshold. Concerning π^-C interactions, no data exist in our energy range. But, from scarce data obtained at lower energies, it seems reasonable to assume that the distributions follow the ones predicted by a quasi-free process.

In the following, we will present the analysis of the e^+e^- production in a commissioning experiment using π^- beam at momenta covering the N(1520) resonance region.

Chapter 2

The HADES experimental set-up

HADES is a fixed target experiment located at the SIS18 accelerator of the GSI Helmholtzzentrum für Schwerionenforschung in Darmstadt[1], which provides a large variety of ions (up to Uranium) with beam energies up to 1.25A GeV for heavy ions (Au) as well as pion and proton beams with incident beam energies of up to 4.5 GeV for protons. The experiment, discussed here, was the first to use the secondary pion beam in the HADES beam line, which required an optimization of the magnetic elements as will be explained in more detail in Sec. 3.2.1. A START detector has also been specially designed for this experiment.

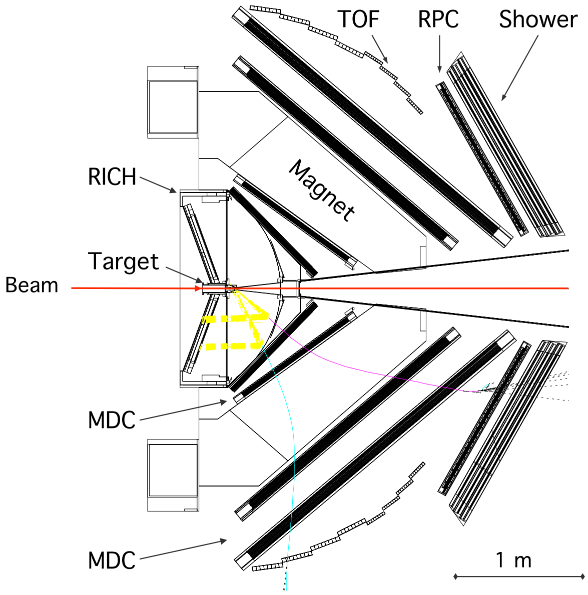

Figure 2.1: Schematic layout of the HADES detector.

As shown in Fig. 2.1, the HADES detector consists of 6 identical sectors covering the full azimuthal range and polar angles from 18° to 85° with respect to the beam direction. Each sector contains:

- a Ring Imaging CHerenkov (RICH) detector used for electron identification;
- two sets of Mini-Drift Chambers (MDC) with 4 modules per sector placed in front and behind the magnetic field to determine momenta of charged particles;

---

[1] http://www.gsi.de/

- time-of-flight (TOF/RPC) and Pre-Shower detectors which are part of the Multiplicity and Electron Trigger Array (META) improving the electron identification and providing charged particle multiplicity for the trigger;

Special care has been put in a low-Z design, in order to reduce the electron energy loss induced by the bremsstrahlung process. In addition, for some experiments, a wall of scintillators, the Forward Wall was placed 7 m downstream from the target. In [112], a detailed description of the set-up in its 2009 configuration can be found. The HADES experimental set-up has also been described in many recent papers and PhDs. Details about the new RPC detector which now replaces the former scintillator time-of-flight system at the most forward angles can be found in [113]. The beam detectors specially designed for the pion beam experiment are described in great detail in a recent article [114]. We therefore limit ourselves in this chapter to a rather schematic presentation of the experimental setup. We start with the different sub-detectors, *i.e.* tracking system in Sec. 2.1, RICH detector in Sec. 2.2, META in Sec. 2.3, we continue with the in beam-line Silicon Tracking Sections (Sec. 2.4) and the START detector (Sec. 2.5) and conclude with the trigger and data acquisition in Sec. 2.6.

2.1 Tracking system

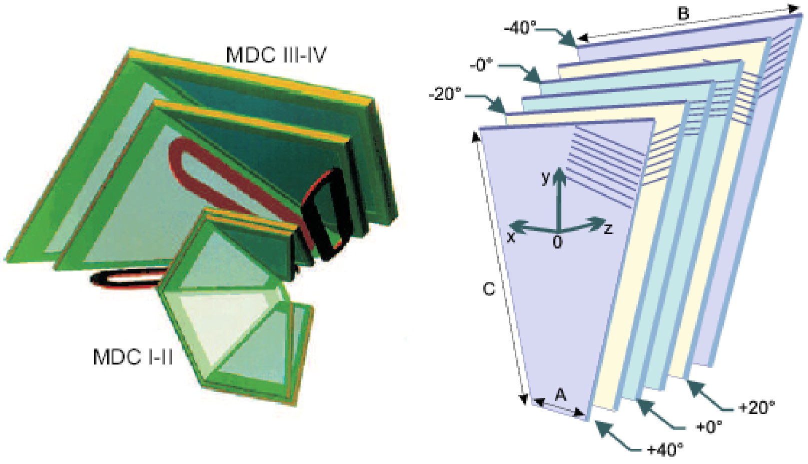

Figure 2.2: Schematic layout of the HADES tracking system [112]. Left: Arrangement of the MDC chamber with respect to the magnetic coils. Right: View of the six anode wire frames inside a HADES MDC, with the respective wire angles.

The reconstruction of the particle momentum and angles is obtained by the measurement of their deflection in the magnetic field. The HADES tracking system is designed to reconstruct the particle trajectories for polar angles between 18° and 85° and to determine the particle momentum in the range between 0.1 GeV/c and 2.0 GeV/c, with a resolution better than 2% for electrons and positrons. It consists of a toroidal magnetic field and four planes of mini drift chambers (MDC) (see left panel of Fig. 2.2) measuring the positions of the particle in front of and behind the magnet.

2.1.1 Magnet

A compact design was chosen for the magnet, in order to reduce the acceptance losses. It consists of six supraconducting narrow coils placed behind the lateral frames of the MDCs (Fig. 2.2, left). The field is very inhomogeneous, with maximum values of 3.6 T inside the coils, and 0.9 T within the acceptance region. The field integral for particles in the

HADES acceptance and hence the momentum kick decreases as a function of their polar angle. Since in overall the average momentum of particles is decreasing with the polar angle, the dependance of the relative value of the momentum resolution on the polar angle is limited.

2.1.2 Mini Drift Chambers

The four planes of trapezoidal MDCs allow for a measurement of particle positions in front of and behind the magnet. Each chamber is composed of six anode sense wire layers oriented in different stereo angles from the inner layer to the outer: 40°, −20°, 0°, 0°, +20°, 40° in order to have an optimum spatial resolution (see right panel of Fig. 2.2). Each anode wire layer is in between two cathode planes, which creates drift cells. All four chambers contain about 1100 drift cells each with a size in average varying from 5 x 5 to 14 x 10 mm^2 from plane I to plane IV to take into account the different detector occupancy. For the present data taking, the chambers of plane I and plane II were filled with Ar/CO_2 (in proportion 70%/30%) while the outer chambers were filled with Ar/C_4H_{10} (84%/16%). The change of gas mixture for planes I and II with respect to previous experiments where all chambers were operated with Ar/C_4H_{10} was motivated by the observed degradation of their performances. Isolating deposits have been observed on the wires and have been attributed to the fragmentation of isobutane molecules. The outer chambers are submitted to a lower flux of particles and were operated with the standard gas mixture.

Due to the geometry of the cells, the relation between the drift time and the distance of the particle to the anode wire is not linear and was deduced using Garfield simulation [112]. For each hit wire, the comparison of the signal amplitude with an adjustable threshold leads to two time signals in the rising and falling edge. The first one is used for drift time measurement and the difference between the two times (time-over-threshold), which is related to the energy loss of the particle in the cell is used for particle identification. The position resolution is about 60-100 μm in the y direction and 120-200 μm in (x-z) direction [115], where x and y are defined as shown in Fig. 2.2.

2.2 Ring Imaging CHerenkov detector

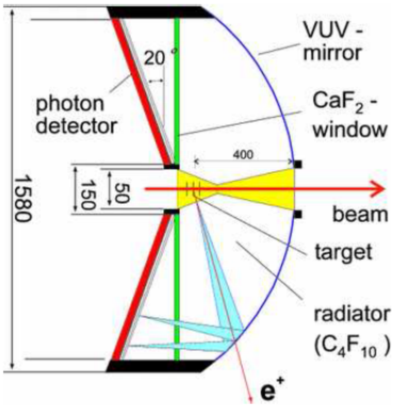

Figure 2.3: Schematic layout of the RICH, with its main elements. See [112] for details.

The most important detector for electron identification is the Ring Imaging Cherenkov detector (RICH) shown in Fig. 2.3. It is located in the innermost part of the spectrometer. For charged particles with velocity larger than the speed of light in a medium of refraction index n, the Cherenkov light is emitted in a cone with an angle θ_C with respect to the particle direction given by:

$$\begin{aligned} \cos\theta_C &= \frac{1}{n\beta}, \\ \beta &= \sqrt{1-\frac{1}{\gamma^2}}, \end{aligned} \tag{2.1}$$

where β and γ are the velocity and Lorentz factor of the particle respectively. The choice of the radiator gas, C_4F_{10}, with a refraction index of n=1.00151 and a corresponding Cherenkov threshold $\gamma = 18.2$ qualifies the RICH as a "hadron-blind" detector in the HADES energy range. Indeed, only particles with a velocity β greater than 0.9985 can produce light, which corresponds to 0.009 GeV/c for an electron, 2.5 GeV/c for a pion and 17 GeV/c for a proton. This threshold will clearly be reached only by electrons. The photons are mostly produced at vacuum ultra-violet (VUV) frequencies. They are reflected by a spherical mirror (4 carbon and 2 glass mirrors) placed downstream of the gas radiator to the photon detector. They traverse a separating $\mathrm{CaF_2}$ window which ensures a good transparency to VUV photons. The photon detector, is placed upstream to reduce the direct interaction of particles emitted from the target. The photon detector consists of CsI pads that have a width of about 6.6 mm x 6.0 mm acting as a photo-electron converter. The pads also act as a cathode and collect the signal induced by the avalanche in the Multi Wire Proportional Chambers. The pads fired by the reflected Cherenkov photons are located on a ring with a radius of about 4 pads. The number of Cherenkov photons is proportional to the path length in the radiator gas. In average, electrons produce about 110 photons along their trajectory in the radiator but less than 20 are detected. In Chapter 4, we will discuss in detail the procedure to take into account the RICH efficiency in the data analysis. To enhance the efficiency of the RICH device in future, the photon detector has recently been exchanged with a system of multi-anode photomultipliers.

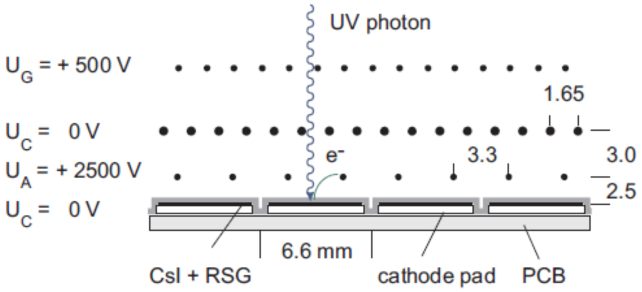

Figure 2.4: Working principle of the photon detection is displayed. Electrons are emitted by photo-electrical effect on the pads, which are coated with Resin Stabilized Graphite (RSG) and a reflective CsI layer. The signal induced by the avalanche close to the anode wire is collected on the pads. All distances are in mm. See [112] for details.

2.3 META detector

The Multiplicity Electron Trigger Array (META) system is essential for triggering and particle identification. It is located behind the outer MDCs and consists of two sets of time-of-flight detectors (RPC and TOF) and an electromagnetic shower detector.

2.3.1 Resistive Plate Chamber

The low granularity TOFINO detector which was composed of scintillators and formerly equipped the region of polar angles 18°-45° was replaced in 2008 by Resistive Plate Chambers (RPC) in the six sectors. This was particularly useful for the Au+Au system study at 1.25 GeV/nucleon in 2012. This detector indeed provides a high rate capability (up to 1kHz/cm^2) and a good position resolution (8 mm in the longitudinal direction and 22 to 42 mm, depending on the cell width), which helps for track matching in a high multiplicity environment. Each sector consists of 187 cells arranged in two layers and comprising three stacked aluminum electrodes and two glass plates in-between. The width of the cells increases with the polar angle. The detector is operated at 5600V. The signal is induced by the ionization of the gas filling the gaps between the plates and is strongly amplified due to the very large electrical field.

2.3.2 Time-of-flight

The TOF detector is providing time-of-flight measurements in the polar angle region from 44 to 85°. Following the hexagonal geometry of the whole spectrometer, the TOF detector is divided into six sectors comprising 64 scintillator rods coupled on both ends to photomultipliers (PMT). From the measured signals three pieces of information are extracted : the time-of-flight of particles with a resolution of about 150 ps, the hit position on the rod (x) with a resolution $\sigma_x \sim 25\ mm$ and the energy deposited in the rod which can be used for particle identification, in addition to the (momentum, time-of-flight) correlation.

2.3.3 Pre-Shower detector

The role of the Pre-Shower detector is to enhance the separation of electrons from hadrons in the low polar angle region where higher momenta can be reached and time-of-flight measurements are less useful. It is located behind the RPC and consists of a stack of three trapezoidal wire chambers separated by two lead converter plates with a thickness of about two radiation lengths. When traversing the lead convertors, electrons produce an electromagnetic shower due to bremsstrahlung and pair production processes and the energy collected in the wire chambers is much larger than for hadrons which mainly loose energy through ionization. The integrated charge of the particle in the three layers, is therefore used to distinguish electromagnetic showers from hadronic tracks. Recently, the Pre-Shower detector has been replaced by a lead glass calorimeter, which will improve the electron to hadron discrimination and will enable the detection of real photons.

2.4 Silicon beam tracking stations

For the pion beam experiment, two position sensitive detectors were installed in the beam line, close to the horizontal and vertical focal planes (see Sec. 3.2.1). They form the so-called CERBEROS system dedicated for track reconstruction of beam particles [114]. Each detector (Fig. 2.4) is 300 μm thick and has an active detection area of $10x10$ cm^2 to detect most of the pions which hit the HADES target. Both sides are segmented into 128 parallel strips with a width of 700 μm each. The strips on the rear and front side are oriented perpendicularly to each other. A pulse height measurement helps to remove noise and to correlate the hits on each side of the detectors. The detectors are cooled to -5° in order to minimize the electronic noise induced by the alteration of the material under high particle load and to reduce the overheating of the detector, which could arise, due to the operation in vacuum.

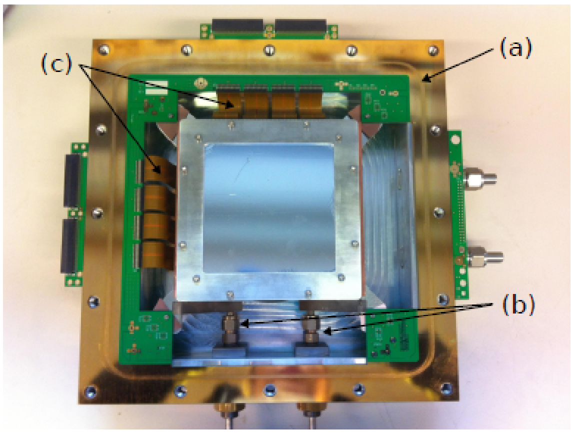

Figure 2.5: Top view of one of two CERBEROS detectors for beam particle tracking. The PCB frame (a), the refrigerant tubes (b) the signal read-out flat cables (c) are indicated by arrows.

2.5 Start detector

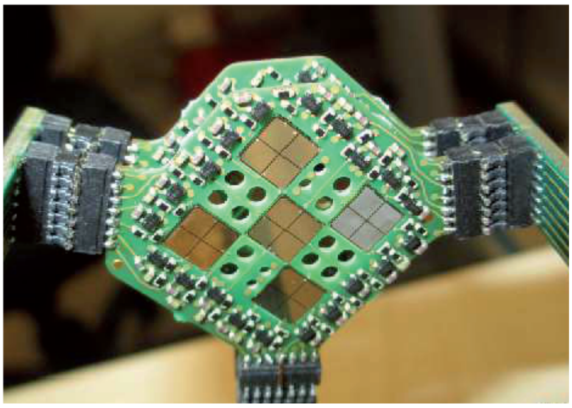

Figure 2.6: Photograph of the START detector: the nine diamond sensor plates are installed on two printed circuit boards (PCB). One PCB with five sensors is visible. the other with four sensors is located behind.

The START detector (Fig. 2.6) was specially designed for the pion beam experiment and had two functions: first, to trigger on beam particles that are likely to interact with the target, which is especially important in the case of a secondary beam with a large halo and second, to provide a reference for time-of-flight measurements. To fulfill the many-fold constraints (good timing, large efficiency to minimum ionizing particles, good timing for time-of-flight measurements, low material budget, good stability to fluxes of about 10^7/s) a mono-crystalline diamond material produced with the Chemical Vapor Deposition (CVD) process was chosen [114]. The detector consists of nine diamond sensors. Each of them has an area of $4.3x4.3$ mm^2, a thickness of 300 μm and is segmented in four quadrants to ensure a reasonable position resolution as well as a low detector capacitance. The detector has a time resolution of about 90 ps and a signal/noise ratio of 30. It was located 17 cm upstream of the target center.

2.6 Trigger and Data Acquisition System

The HADES trigger is usually organized in two levels, LVL1 and LVL2, where LVL1 is based on the charged particle multiplicity (numbers of hits in the META detector) and LVL2 requires a potential lepton candidate (one ring in the RICH detector). In the case of high rates, only an adjustable fraction of LVL1 triggers is recorded in order to enrich the data sample with lepton candidates. For the pion beam experiment, this was not necessary, due to the moderate rate of interactions and therefore only a LVL1 trigger based on a coincidence between a signal in the START detector and a multiplicity of at least two hits in the META detector was required as a condition for the data acquisition.

In order to cope with the high particle multiplicities and reaction rates in Au+Au collisions, the data acquisition system was upgraded [116] to achieve data rates of up to 400 MByte/s which correspond to a rate of up to 80 kHz in light collision systems and up to 20 kHz in Au+Au collisions. This performance is not needed in our experiment where the limitation comes from the pion beam flux and where the trigger rate was less than 2 kHz.

Chapter 3

Methods for particle reconstruction

In this chapter, we will discuss the experimental conditions specific to the pion experiment as well as the reconstruction of pion beam and leptons.

3.1 Run conditions and targets

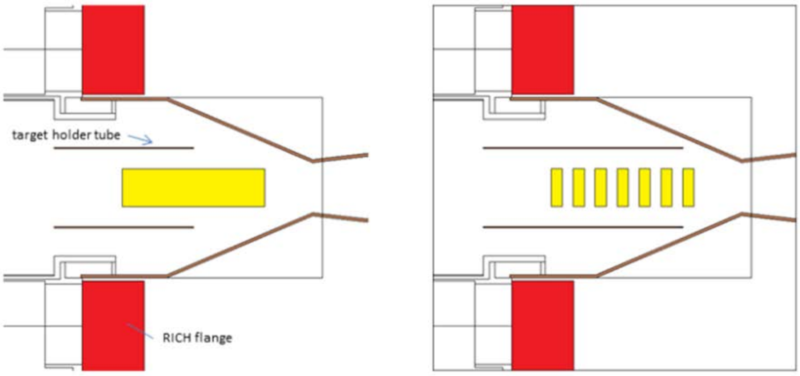

Figure 3.1: Target arrangement for the experiment in August 2014. The polyethylene target is shown in the left panel of the picture and the carbon target in the right panel.

The pion beam at GSI had been previously used by the FOPI collaboration to study strangeness production in pion induced reactions on nuclei [117]. Since the HADES collaboration aims at measuring the dielectron production, which is a very rare process, the requirements on the beam yield were much more strict. It was necessary to study the specific optics of the HADES beam line. In addition, in order to increase the resolution for exclusive channels, a pion beam tracker was developed to reconstruct the pion momentum on an event-by-event basis.

The pion beam was used by the HADES collaborations in two different campaigns in summer 2014: one in July and the second one between the end of August and the beginning of September. The first experiment was mainly performed with a pion beam momentum of 1.7 GeV/c in order to study the strangeness production on carbon and tungsten nuclei.

In August, the pion beam was used at four different momenta (0.656, 0.69, 0.745 and 0.8 GeV/c) in order to provide four energy points for a PWA analysis of hadronic channels. The measurement at 0.69 GeV/c was much longer than the others in order to accumulate statics for the study of e^+e^- production channels. Both a polyethylene and a carbon target were used in order to extract the yield corresponding to the $\pi^- p$ reaction.

The polyethylene target is a homogeneous cylinder 46 mm long and 12 mm in diameter, while the carbon target consisted of seven 7.1 mm thick segments with same diameter and occupying the same total length as the polyethylene target (Fig. 3.1). The center of these targets was placed 3.2 cm upstream from the center of the HADES detector. The target holder was a carbon-fiber tube with an outer diameter of 26 mm and a wall thickness of 0.5 mm.

The choice of a solid polyethylene target instead of a liquid hydrogen target was made in order to avoid technical problems with the operation of the liquid target below 20 K. In addition, one major drawback of the liquid hydrogen target is the thickness of the material surrounding the target which makes it not well suited for operating with a secondary beam with a large halo.

Target	p_π^- [GeV/c]	Events
Polyethylene (PE)	0.690	774.7M
Polyethylene (PE)	0.748	76.5M
Polyethylene (PE)	0.656	42.4M
Polyethylene (PE)	0.800	52.4M
Carbon (C)	0.690	115.7M
Carbon (C)	0.800	41.2M
Carbon (C)	0.748	42.2M
Carbon (C)	0.656	41.9M

Table 3.1: Collected statistics for the August 2014 pion beam run for the different targets and pion beam settings.

3.2 Beam particle reconstruction

3.2.1 The pion beam line

The secondary pion beam was obtained using a primary beam of N_2 at an energy of $2A$ GeV with an intensity of 0.8-1.0 10^{11} ions/spill hitting a target of Beryllium with a thickness of 10 cm. In these conditions the pion beam intensity in the HADES cave is maximum at 1 GeV/c and then it decreases by about a factor 2 at 0.7 GeV/c and 1.5 GeV/c [118] (see Fig. 3.2). The measured pion flux in August runs at a pion beam momentum of 0.69 GeV/c was around $2x10^5$ pions/spill.

After their production, negative pions are transported to the HADES target, placed 33 m downstream the production point, with a beam line composed of nine quadrupoles and two dipoles (see Fig. 3.3). The current in the dipoles and therefore the magnetic field can be changed, selecting the different requested momenta. Two silicon detectors were placed in the pion beam line in order to reconstruct the pion trajectories and estimate the pion momentum event-by-event. The position of the last three quadrupoles and of the silicon detectors has been optimized using TRANSPORT simulations [119] in order to maximize the acceptance and minimize the resolution on the pion momentum reconstruction.

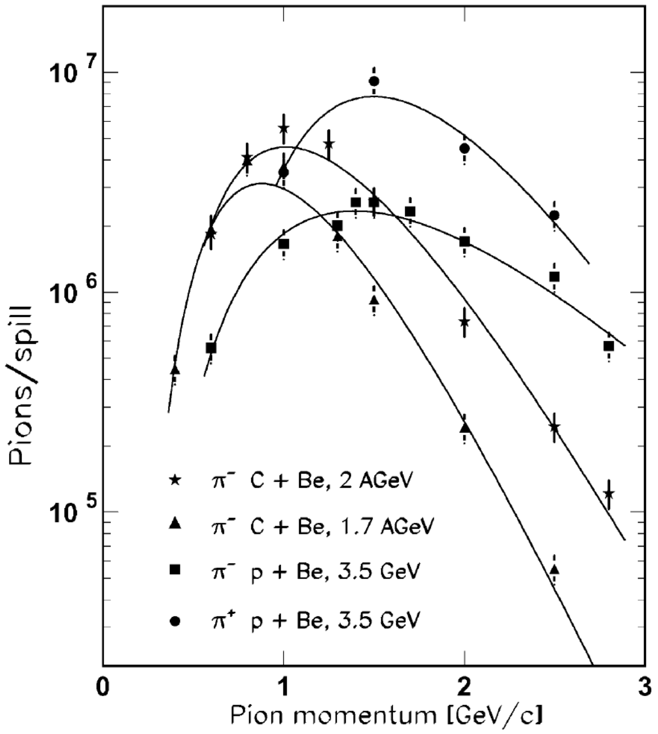

Figure 3.2: Pion intensity measured in previous experiments in the target detector for p and ^{12}C primary beams at different energies as a function of the central momentum of the beam-line. The primary beam intensities correspond to the maximum intensity to be extracted from SIS, *i.e.* 1.7x 10^{11} protons/spill and 5x 10^{11} carbon ions/spill, respectively. The solid curves represent fits to the data (see [118]).

3.2.2 Beam contamination

For the secondary negative pion beam it is important to know what is the contamination of electrons, muons and kaons, having similar rigidity as the pions which might be transported and might interact with the target or with target detector. The electrons with the correct momenta to be accepted by the chicane are created in the decay chain of the neutral pions produced in an abundant way at the production target. These pions can generate electrons directly via Dalitz decay ($\pi^0 \to \gamma e^+ e^-$) or via the conversion in the matter of the γs coming from the main decay ($\pi^0 \to \gamma\gamma$). An estimation of the ratio electron/pion was carried out simulating the reaction N+Be and the thickness of the target to find the fraction of photons that convert. It follows that the contamination, dominated by electrons from the conversion process, is very low at 1.7 GeV/c (0.84 %), while it is larger at 0.7 GeV/c (9.6 %) due to the larger overlap with the electron momentum distribution [120].

The muon contamination is due to the in-flight decay of the pions and it depends on the pion momentum and the kinematics of the decay. For the two reference momenta 0.7 GeV/c and 1.7 GeV/c, the effective decay lengths are 39.3 m and 95.4 m, respectively, so a large fraction of pions decay before reaching the target. However considering the momentum and angle distributions of these muons, only a very small fraction reaches the target area. After checking the different tracks resulting from the decay, an estimation of the ratio muons/pions can be made and it results to be low for both momenta (0.65 % and 0.75 %) [120].

The last source of contamination (negative kaons) can be produced via the process $NN \to NNK^+K^-$ having a threshold of 2.5 GeV in the incident nucleon energy. In this

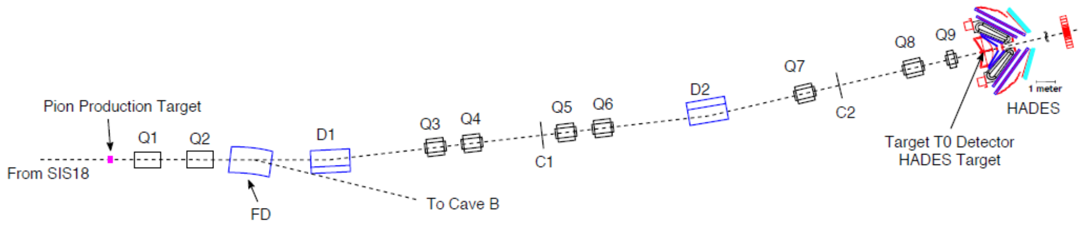

Figure 3.3: Schematic overview of the beam line between the pion production target and the HADES cave [118], displaying the dipole magnets (D), quadrupoles (Q), tracking detectors (C1,C2) and the target T0 detector. The FD dipole used to direct the beam to cave B is not powered.

case, the generated particles have, on average, small momenta and short decay length. Anyway, this process does not play a role in our energy range.

Finally, only the electron contamination is significant. These electrons will not affect the measurements in the HADES detector, since they have a much smaller interaction probablility than pions. However, they can increase the yield measured in the START detector (see Sec. 2.5), which has to be taken into account if this information is used for the normalization of the experimental data (see Sec. 5.7).

3.2.3 Pion beam momentum reconstruction

Description of the method

As previously said (see Sec. 2.4), two silicon detectors were placed into the chicane transporting the pions at the HADES target in order to estimate the momenta of the pions interacting with the target, event-by-event. To this end, the relation between the measured positions (X_1, Y_1, X_2, Y_2) in the (x-y) planes in the two detectors and the five beam particle coordinates at the production target (x_0, θ_0, y_0, ϕ_0, δ) is used. These coordinates are defined as follows:

- x_0 is the coordinate along the horizontal axis;
- θ_0 is the angle in the horizontal plane, defined as $\tan\theta = \frac{dx}{dz} = \frac{px}{pz}$;
- y_0 is the coordinate along the vertical axis;
- ϕ_0 is the angle in the vertical plane, defined as $\tan\phi = \frac{dy}{dz} = \frac{py}{pz}$;
- $\delta = \frac{p - p_{ref}}{p_{ref}}$ is the momentum offset with respect to the momentum p_{ref} of particles on the optical axis.

These quantities can be combined using the first and second order transport coefficients equations, which were determined using TRANSPORT calculations [114], [119].

This system of 4 equations with 5 unknown values can be solved setting the value of x_0 to 0. The x_0 dependent terms contribute to the resolution. To simplify the calculation, the terms which have a contribution smaller than the position resolution on the detectors were neglected. The resulting equations are the following:

$$X_i = T^i_{12}\theta_0 + T^i_{14}\phi_0 + T^i_{16}\delta + T^i_{126}\theta_0\delta + T^i_{146}\phi_0\delta + T^i_{166}\delta^2 \tag{3.1}$$

$$Y_i = T^i_{32}\theta_0 + T^i_{33}y_0 + T^i_{34}\phi_0 + T^i_{36}\delta + T^i_{336}y_0\delta + T^i_{346}\phi_0\delta + T^i_{366}\delta^2 \tag{3.2}$$

in which the index i refers to the detectors and T_{jk} or T_{jkl} are the transport coefficients. The solution of these equations is found in an iterative way.

The most important coefficients for the momentum reconstruction are the horizontal dispersion coefficient at the first plane of detectors T^1_{16}, and in a smaller extent the dispersion in the vertical plane at the second detector T^2_{36}, but significant contributions arise from other terms. The angular magnification coefficients T_{12} and T_{34} play an important role for the acceptance of the beam line. The distribution of pion momenta at the end of the pion beam line mainly results from the values of the dispersion coefficients T_{16} and T_{36} at the location of the different vacuum chambers of dipoles and quadrupoles (see [114]) but second order coefficients also play an important role. At 0.7 GeV/c, the multiple scattering in the detectors has an important effect, both by reducing the global acceptance of the beam line and by increasing the error on the pion momentum reconstruction.

According to the simulations, the fraction of pions entering the beam line, which hit the target is about 5%. The momentum resolution was estimated to be better than 0.4%.

Position measurement on the Si detectors

To reconstruct the correct momentum, a careful evaluation of the hits in the two detectors is needed since the presence of multi-hits is not negligible due to the detector noise. This can be satisfied searching for single hit tracks and suppressing the fake tracks due to multi-hits by means of strict conditions on the correlation between the y coordinates measured in the two detectors, as explained in [114].

Checks of the pion momentum reconstruction

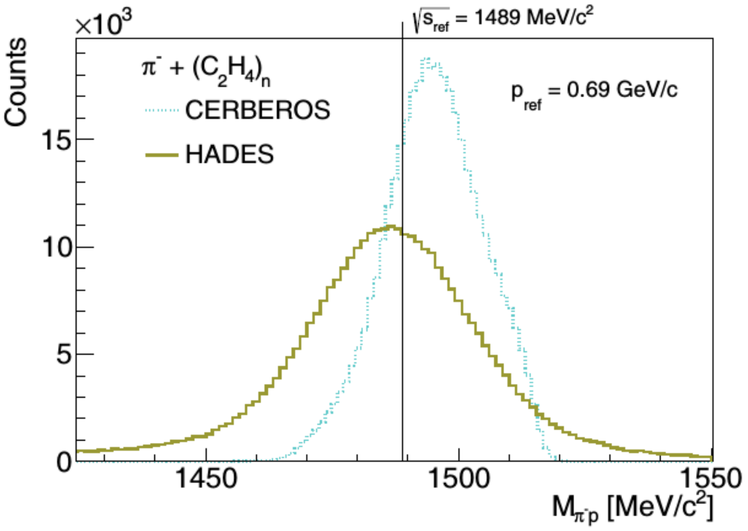

Figure 3.4: Distributions of the center of mass energy $\sqrt{s}$ calculated using the pion beam tracker (CERBEROS) and of the $\pi^- p$ invariant mass $M_{inv}(\pi^-, p)$ measured using the HADES detector for π^- p elastic scattering events for the setting at a reference momentum p_{ref}=0.69 GeV/c.

A calibration run was realized in May 2014, using a proton beam at a known momentum of 2.7 GeV/c and different settings of the beam line. The value of the most important dispersion term T_{16} was found to be only 3% lower than the theoretical value. The principle of the momentum reconstruction could therefore be validated and the expected resolution could be confirmed. The precision of the momentum reconstruction can also be checked during our experiment using the $\pi^- p$ elastic scattering. Such a process is selected using events with both a π^- and a proton detected and using angular correlations which are specific to the elastic scattering kinematics. The center-of-mass energy $\sqrt{s}$

calculated using the reconstructed incoming pion momentum should therefore be equal to the invariant mass $M_{inv}(\pi^+, p)$ of the outgoing pion and proton measured in HADES:

$$\sqrt{s} = M_{inv}(\pi^-, p) \tag{3.3}$$

In Fig. 3.4 the comparison between $\sqrt{s}$ and $M_{inv}(\pi^-, p)$ is shown. The reconstructed invariant mass is characterized by a mean value of $M_{\pi^- p} = 1487$ MeV/c^2 and a width of 33 MeV/c^2 (FWHM). The mean value of the distribution coming from the reconstructed momenta in the pion tracker is higher ($\sqrt{s} = 1496$ MeV/c^2), while the width of the distribution is significantly smaller (18 MeV/c^2 (FWHM)). The latter corresponds to a momentum distribution centered at $\delta = 0.45\%$ and with a width of 1.7% (RMS). This width is larger than the value of 1% expected using the theoretical TRANSPORT coefficients. This is probably due to systematic errors on the linear and angular magnification terms, as suggested by the results of the calibration run with the proton beam.

The systematic discrepancy of the order of 10 MeV/c^2 between the two values is observed for all the runs in August taken at pion momenta close to 0.7 GeV/c. This deviation was surprising since in the calibration procedure with the proton beam at 2.7 GeV/c, the offset for the momentum of the particle on the optical axis was found to be of the order of 0.1% [114], which would correspond to a shift of the invariant mass smaller than 1 MeV/c^2 on the invariant mass at 0.7 GeV/c. In addition, in July 2014, the polyethylene target was also used for a short time with the pion beam at a central value of 1.7 GeV/c and the center-of-mass energies measured with HADES and with the pion tracker were found to be consistent.

Calculations using GEANT 4 lead to an estimation of the energy loss, however the obtained value (about 8 MeV/c^2) explains only part of the effect. Further explanations were checked: a shift of the primary beam in the vertical and/or horizontal plane cannot explain shifts larger than 1 MeV/c^2. However, remanence effects appeared as the best explanation, as they can distort the relation between the current in the magnets and the magnetic field and could introduce such a systematic shift. This interpretation seems to be confirmed by the fact that the shift is absent in the runs at 1.7 GeV/c.

The offset observed on the reconstructed momentum using the pion tracker has finally been corrected for each file measured on the polyethylene target. Taking into account this correction, the estimated average pion momentum for our experiment is 0.685 GeV/c instead of 0.690 GeV/c.

For the measurements on the carbon targets, we adopted as uncertainty on the center-of-mass energy the value of 5 MeV/c^2 corresponding to the average correction measured in the case of the proton target.

3.3 Track reconstruction procedure

Reconstructing the tracks of the particles with high efficiency is one of the main tasks of detector system. In HADES case this goal is obtained using impacts of the particles on the MDC detectors placed in front and behind the magnetic field (see Sec. 2.1.2). The starting points are the raw signals that are measured by each layer, from which an information on the drift time in the corresponding cell can be obtained, after calibration of each individual channel. As mentioned in Sec. 2.1.2, the relation between this time information and the drift distance is known thanks to GARFIELD simulations of the electron drift in the electric field in a cell. However, this information is not sufficient to determine the position of the particle in the drift cell and, in particular, whether the particle crossed the left or the right side of the cell with respect to the anode wire (so-called left-right ambiguity). The reconstruction of the track can therefore only be obtained using an algorithm combining the information on the different layers, which have different inclinations. This algorithm has to be able to reconstruct tracks minimizing the fake combinations, which are a huge problem in high multiplicity collisions (such as Au-Au data in 2012) but are not negligible even in low multiplicity environments. Some details about the search for the track candidates are summarized below.

Reconstruction of inner clusters

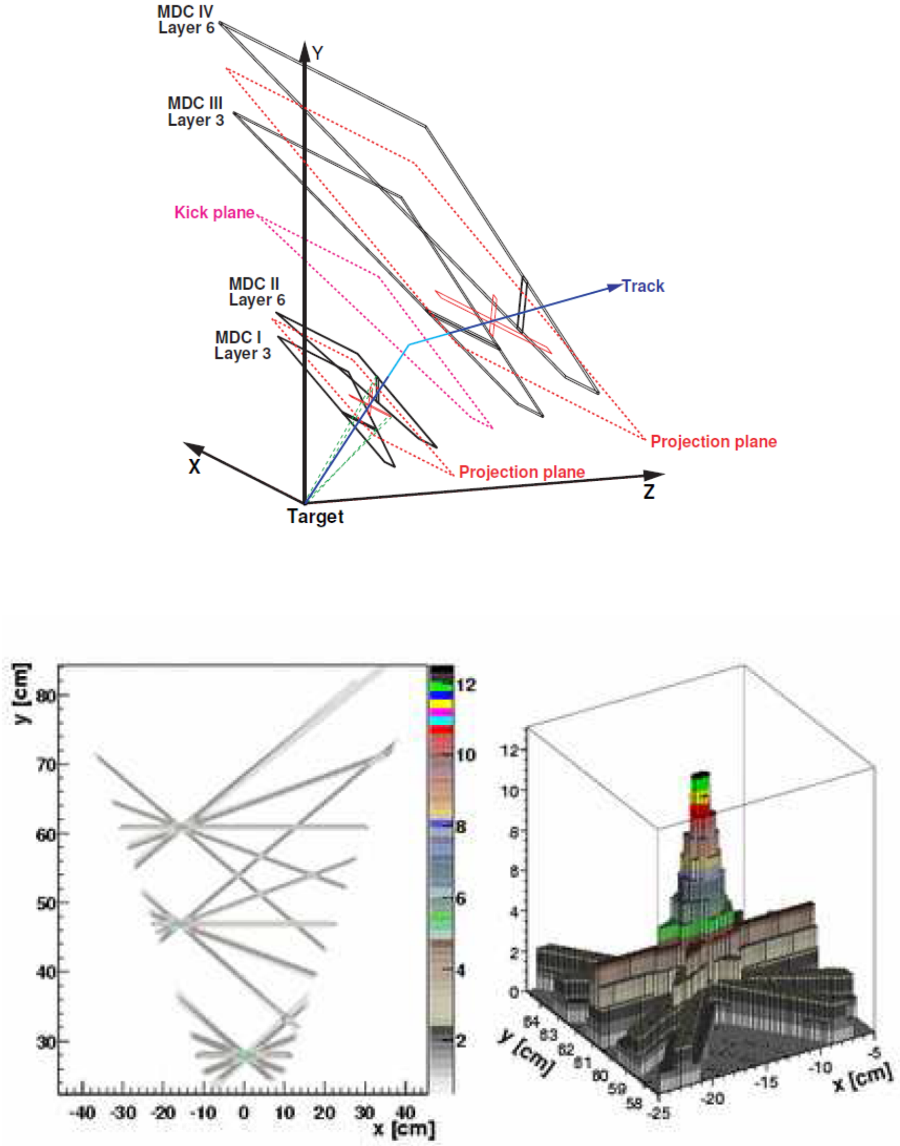

Figure 3.5: Top: Definition of the projection and kick planes and of the inner and outer segments used in the reconstruction of tracks using hits in the four MDC chambers. Bottom: 2-dim (left) and 3-dim (right) representations of the projections of the hit cells onto the projection planes in the cluster finding procedure. The x-y axis are spatial axis in the projection plane and the z-axis indicates the number of cells which contribute to a given (x-y) bin.

In the first step, only the hits reconstructed in the first two MDC chambers (inner MDCs) are used and the goal is to associate the cells corresponding to the same track in clusters. First, fifteen equidistant points are chosen in the target area and are used as anticipated event vertex. For each cell with given signal, the volume defined by the hit

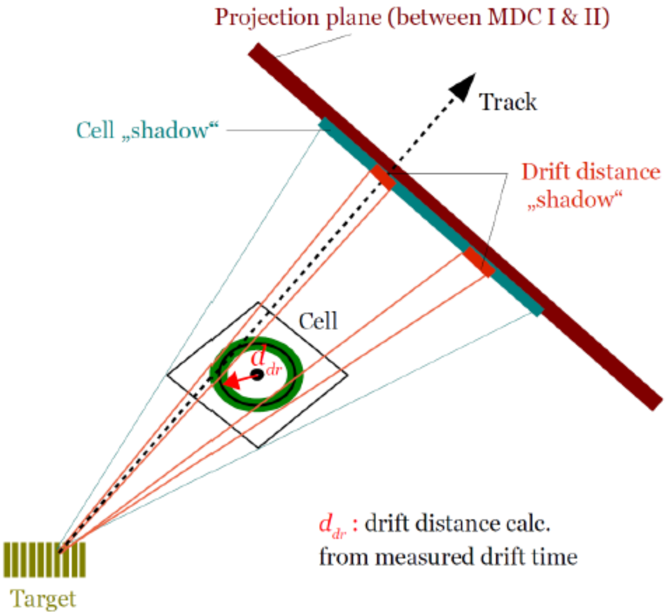

Figure 3.6: Application of the drift time to reduce the size of the projected area corresponding to a hit cell. The ”drift distance shadow” can be compared to the ”cell shadow”. The drift distance d_{dr} and the corresponding error, displayed as a green area are calculated from the measured time using GARFIELD simulations.

cell is projected with respect to one of the fifteen points onto a plane between the two chambers (Fig. 3.5 top and bottom left). On the projection plane, using an appropriate x-y binning, a search for local maxima generated by the overlap of projections of different cells is performed. A cluster is defined when more than ten cells are hit. The cluster finding procedure is repeated for all of the 15 points on the z-axis and the point corresponding to the highest number of clusters or to clusters with the highest number of cells is kept as the ”cluster vertex” and the corresponding clusters are stored (Fig. 3.5 bottom right).

Previously, this cluster finder procedure used only the cell number, as illustrated in Fig. 3.5. It has been recently improved to take into account the drift time already at the level of the cluster finder (see Fig. 3.6) increasing the number of bins in the projection with respect to the previous case, where only the cell number was taken into account.

Fake clusters are produced in this procedure. They are due either to combinations of wires differing from the real track by only few wires, due in particular to the above mentioned left-right ambiguity, or to different combinations of wires in case of noise or high multiplicities. Fake clusters are removed by exploiting the fact that they have particular signatures (the peak in the projection is lower and narrower and the wires are more often associated to several different clusters).

Reconstruction of inner segments

In the next stage, the cluster information is used to fit an inner segment with the simple assumption of straight lines without any constraint on the vertex [121]. A pre-fit procedure neglecting the drift time information is first applied to produce reasonable initial values and to avoid local maxima leading to fake tracks. The final fitting procedure takes into account the drift times. The χ^2 value for the fitted segment can be used to judge about the quality of the fit to select the best track candidates.

Reconstruction of outer clusters and outer segments

The inner segment is then propagated to the so-called kick plane, which is a surface determined using simulation (see Fig. 3.5). It allows to approximate the effect of the magnetic field with the assumption of a simple kick occurring at this surface. The hit on the kick plane is used as vertex for the cluster finding for the outer MDCs. Again a procedure to reduce the fake clusters is applied. In addition, the clusters are searched for in a limited region corresponding to the possible deflection of the inner segment. In this way, the cluster search is limited to the physical region in which the particle can be deflected. Then the outer segment is estimated in a similar way to the inner segment: a pre-fit using a straight line is performed and the result is used as starting point for the final χ^2 minimization using also the drift times.

The combinations of the inner MDC segments and the outer MDC segments constitutes a list of MDC track candidates.

3.4 Momentum reconstruction

The momentum of the charged particles can be estimated using the deflection of the trajectory of a charged particle traversing a magnetic field due to the Lorentz force $\vec{F} = q(\vec{v} \times \vec{B})$ where $\vec{v}$ is the velocity of the particle and $\vec{B}$ is the magnetic field. The difference between the incoming $\vec{p}_{in}$ and the outcoming $\vec{p}_{out}$ vectors writes:

$$\Delta\vec{p} = \vec{p}_{out} - \vec{p}_{in} = \int \vec{F} dt = -q \int \vec{B} \times d\vec{s}$$

where $\int d\vec{s}$ is the whole path inside the magnetic field. The deflection angle can be calculated as:

$$sin\frac{\Delta\Theta}{2} = \frac{|\Delta\vec{p}|}{2|\vec{p}|}$$

where $|\vec{p}| = |\vec{p}_{out}| = |\vec{p}_{in}|$.

The momentum can de derived using three different methods which have different characteristics in terms of momentum precision and computing time: the kick-plane, the spline and Runge-Kutta methods. In the kick-plane method, the bending due to the magnetic field is approximated by a simple kick occurring in the kick-plane (Fig. 3.5). The procedure is very fast, but has a low resolution. The spline method approximates the path of the track inside the magnetic field with a fifth order spline function which is interpolated between the inner and outer segments. The best method in terms of resolution is the Runge-Kutta, that solves the equations of motion inside the magnetic field area in a numerical way. Input information is given by the results of spline method (momentum, direction of the particle). Solving the equations of motion provides the expected positions of the hits for each layer which are compared to the real hits. Then a least square minimization permits to adjust the particle trajectory and to find the momentum. As output of the method the χ^2_{RK} provides an information about the quality of the track. With such a procedure, the momentum resolutions are of the order of 1-2 % for electrons, and 2-3 % for pions and protons. The discrepancy between the 2 values is due to the different impact of multiple scattering.

3.5 Matching of a track with a time-of-flight information

To provide particle identification, the particle trajectory obtained by the Runge-Kutta method needs to be combined with a time of flight measurement, which is provided by the so-called META (Multiplicity Electron Trigger Array) detectors (see Sec. 2.3), that includes TOF and RPC detectors.

The position of hits reconstructed in the META detectors are compared with the projection of the outer MDCs segments on the META plane using straight lines, which is justified by the negligible curvature of the track due to the magnetic field in outer region. The deviations between the propagated trajectory and reconstructed hits in a restricted region around the track are combined to form a quality factor:

$$MetaQa = \sqrt{(\frac{x_{tof} - x_{int} - x_{offset}}{\sigma_x})^2 + (\frac{y_{tof} - y_{int} - y_{offset}}{\sigma_y})^2} \qquad (3.4)$$

where x_{tof} and y_{tof} are the coordinates of the reconstructed hit in TOF or RPC detector, x_{int} and y_{int} are the coordinates of the point obtained from the projection of the outer MDC segment, x_{offset} and y_{offset} are values chosen in order to have the residuals centered around zero and σ_x and σ_y are the resolutions in the two directions, which are adjusted with simulations. Among all the possible combinations of the MDC track with META hits in the search region, the one with the lowest $MetaQa$ (see Eq. 3.4) is chosen (Fig. 3.7).

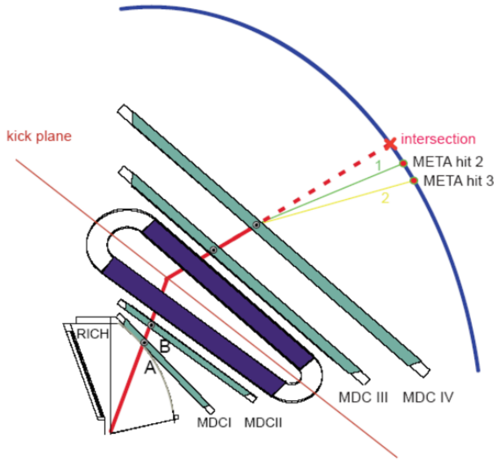

Figure 3.7: Schematic representation of the matching between the MDC segments and the META hits.

3.6 RICH Ring reconstruction

The main detector used for the separation between leptons and hadrons is the RICH detector. The approach commonly used by the HADES collaboration is based on the RICH ring finder technique, that exploits the fact that Cherenkov photons emitted by the leptons and reflected on the mirror form a ring on the photon detector plane which can be measured by reconstructing the photoelectrons (see Sec. 2.2). A so-called cleaning and labeling procedure described below is first applied before searching for a ring. The following cuts are applied to reject direct hits and electronic noise:

- ”Large Clusters”: to remove clusters with large number of fired pads, that are likely formed by direct impacts of particles on the photon detector;

- ”Single Pads”: to remove fired pads that are isolated by seven pads from an other fired pad and are likely arising from noise;

- ”Sector”: a sector is excluded from further analysis if too many pads in the corresponding sector were fired, since such a behavior suggests a dysfunction.

The labeling procedure consists in tagging the areas of the pad plane which contain groups of fired pads. Rings will be searched for only in these areas, which will reduce the computation time significantly. Two different algorithms were written to find the position of the rings. The first algorithm is the pattern matrix algorithm. It is based on the comparison between the measured hit pads configuration and 11x11 matrices describing expected pad patterns for each possible ring center in the selected region. These matrices were built using experimental data for which it was possible to correlate the rings with MDC tracks [112]. They are used as masks and allow to build a quality factor from the comparison with the experimental hit pad distribution. The ring center corresponds to the position of the matrix leading to the best quality factor. This quantity is then further used to select higher quality rings.

The second algorithm is the Hough transform, that is suited to identify certain types of objects. In this case the objects are circles, that are parametrized in terms of the coordinates of the center x and y and of the ring radius r, which is set to be equal to four pads (see Sec. 2.2). Then an iterative procedure starts and in each step three fired pads are combined and the circle passing through them is calculated. A two dimensional histogram with the x and y coordinates of all the ring centers is obtained and the cell with the maximum yield is taken as the ring coordinates. The height of the maximum can be used to judge the Hough transform quality.

The pattern matrix algorithm is very fast, however its reconstruction capability is strongly influenced by the presence of electronic noise and it doesn’t work well in case of two overlapping rings. The Hough transform has the advantage to be less sensitive to the ring radius so that it can reconstruct a ring even in case of distortions due to noise or overlapping rings. The disadvantage, on the other hand, is that large pad clusters could be recognized as rings. These are the reasons for which a combination of the two approaches is needed to reconstruct properly a ring.

When a ring is found, a measurement of the quality of the track-to-ring matching is given by the so called *RichQa* variable, which is defined as

$$RichQa = \sqrt{(\Delta\theta)^2 + (\Delta\phi \times \sin\theta)^2}, \tag{3.5}$$

$\Delta\theta$ and $\Delta\phi$ are the differences between the angles of the track candidate and of the RICH ring center. This parameter can be used to judge the quality of the matching between the MDC track and the RICH ring and identify possible random matches. The default lepton selection tags as lepton tracks for which the *RichQa* goes up to around 10.5°. This large value is due to the fact that electrons are subjected to the multiple scattering in the RICH mirror, which affects the track angle. In the previous HADES data-taking with higher multiplicity it was possible to improve the angular resolution of the track and therefore make the $RICHQa$ distribution narrower by fixing the origin of electrons in the reconstructed vertex. This kind of approach cannot be used for the pion beam data since, as already mentioned, the vertex resolution is very poor due to the very low multiplicity.

3.7 Data Summary Tapes

Finally, the reconstructed events are stored in Data Summary Tapes (DST) as a list of particle candidates consisting of a track matched to a META information and, if available, to a ring. The time-of-flight, energy loss in MDCs and in TOF and momentum of the particle candidates are also stored, as well as the information about the quality of the tracks (*e.g.* χ^2_{RK}) and matching with the rings (*RichQa*, see Eq. 3.5) and $METAQa$

(see Eq. 3.4). In addition, for each event, the information about the signals in the START detectors and pion beam reconstruction is also provided. These DST are the starting point for specific analyses, where different criteria on the particle candidates could be applied, depending on the reaction channel of interest.

3.8 Event selection and particle identification

The goal of this analysis is the reconstruction of lepton pairs. A high efficiency is desired, but at the same time it is crucial to keep a high purity of lepton sample. Indeed, the contamination of the lepton sample with other particles or fake tracks would affect the physics observables and at the same time increase the combinatorial background, since any not correctly identified lepton enters into the pairing procedure.

3.8.1 Global event selection criteria

The first step of the analysis consists in selecting useful events which originate from the target and have the START time information that is needed for particle identification. The following conditions were implemented one after the other:

- Good cluster vertex: The cluster vertex is calculated as explained in Sec. 3.3. It consists of a z-coordinate value only (z_{vertex}) which is used to reject events not coming from the target. In particular in our experiments, using the condition that the vertex position z has to be larger than -160 mm, interactions with the START detector can be suppressed.

- Good candidate vertex: This vertex is obtained by combining at least two tracks in the event. It has information on the x and the y-coordinates in addition to z. Again the condition is to have $z_{vertex} > -160$ mm.

- START Hit: an event is requested to have a START hit, which is necessary in order to have a correct measurement of the time-of-flights.

- No pile-up in START: an event should have only one hit in the START detector, in order to avoid ambiguity in the calculation of the time-of-flight. In case a second hit is found the event is rejected.

3.8.2 Track sorting procedure

In the DST files, a large number of possible track candidates are generated. This is possible because the reuse of the different MDC hits is allowed, which generates a high number of track segment combinations. At the same time, one single track can be associated with up to 3 different META hits and one single RICH ring. These META hits and RICH rings can be used again with different tracks to form a very high number of possible combinations. For two particles with an opening angle lower than 2°, the inner MDC segment (and the RICH ring for leptons) might be shared by two outer segments and META hits. However, in the majority of cases, such a situation is due to wrong combinations. In order to solve this problem an algorithm of track sorting is necessary.

All track candidates sharing the same inner MDC segment are sorted in a list according to the track quality, using the χ^2_{RK}. At the end of the analysis procedure, where different criteria on the tracks are applied, only the candidate with the smallest χ^2_{RK} is kept in the further analysis.

3.8.3 Cleaning of the particle candidates

First, to avoid fake tracks, specific criteria on the inner and outer segments in the MDC detectors obtained from segment fit (see Sec. 3.3) are applied. The quality of the full reconstructed track is also checked by applying a limit to the χ^2_{RK} from the Runge-Kutta algorithm procedure (see Sec. 3.3). In order to provide a good matching between time-of-flight and track information, a limit of 3σ is also set to the distance between the MDC segment and the META hit in the direction along the rod (Sec. 3.5) has to be lower than 3. Finally all the tracks are requested to be reconstructed in some fiducial volume. In practice, it means that the edges of the six HADES sectors are excluded from the analysis. This cut was introduced since the efficiency is not precisely described by the simulation in these areas.

The specific conditions for leptons are then applied: the track of the electron or positron candidates is required to match with one RICH ring ($RichQa < 4$). As a consequence, the number of candidates in the list is reduced. Finally, the track candidate at the top of the rearranged list is chosen as particle candidate.

3.8.4 Velocity and energy loss selection criteria

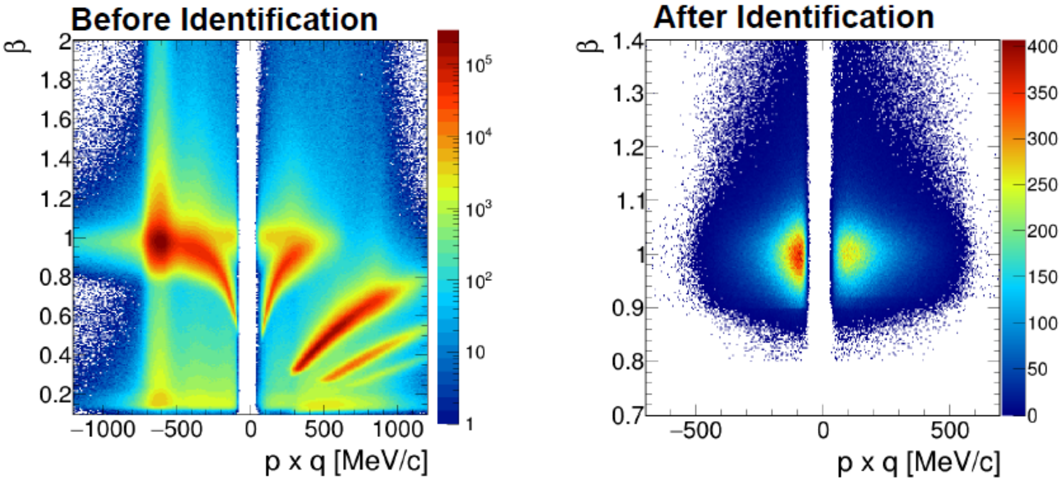

Figure 3.8: Distribution of all tracks (left) and selected lepton candidates (right) as a function of the velocity and the product of momentum and polarity.

To separate the different species, one can first use the relation between the reconstructed momentum and the velocity of the particle, usually expressed in β units. The curvature of the track provides the polarity q of the particle.

The velocity of a particle can be deduced by a time of flight measurement, *i.e.* a difference of time $\Delta t = t_1 - t_0$ between the reaction time, given by the START detector (t_0) and the time in which the particle hit one of two META detectors (TOF or RPC) (t_1). Therefore one can calculate β as:

$$\beta = \frac{v}{c} = \frac{s}{c\Delta t}$$

where s is the flight path which can be calculated from the track reconstruction. This kind of information can also be given using the mass of the particle, which can be estimated as follows:

$$\frac{m}{q} = \frac{p}{q\gamma\beta c}$$

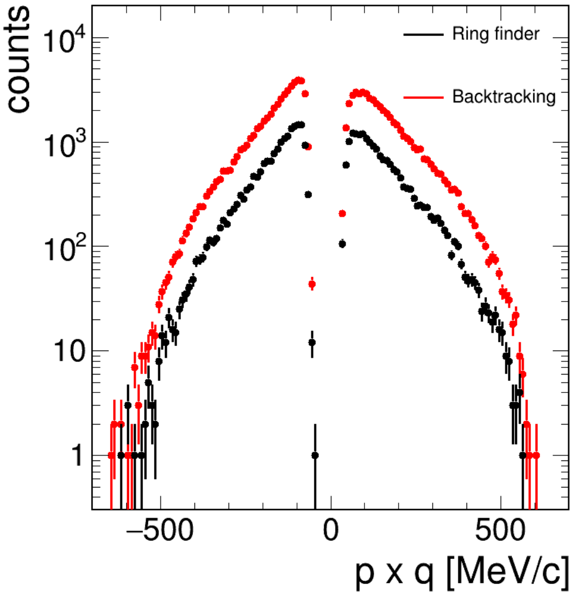

Figure 3.9: Distribution of the product of momentum and polarity for leptons reconstructed with the ring finder (black) and backtracking (red) algorithms.

in which γ is the Lorentz factor $\gamma = \frac{1}{\sqrt{1-\beta^2}}$. Since the reconstructed β may have values larger of 1, due to the detector resolution, the quantity m^2 is used instead of the simple mass to avoid to get unphysical masses. For the electron identification, the criterium $\beta > 0.8$ is used. The distribution of the selected tracks as a function of their velocity and product of polarity and momentum is displayed in Fig. 3.8 before (left) and after (right) the lepton selection criteria. This plot shows that lepton reconstruction algorithms are able to disentangle the very rare lepton signal in a hadron dominated environment.

The distribution of the product of polarity and momentum is also displayed in Fig. 3.9. For momenta lower than 250 MeV/c, the number of positive reconstructed leptons is much lower than for the negative leptons. This is due to the lack of acceptance at forward angles. The positively charged particles are indeed more sensitive to this cut, since they are bent towards the beam axis, while the negatively charged ones are bent outwards. The second physical quantity, that can be used for particle identification, is the energy loss in the MDC detector. Particles lose energy crossing the MDC chambers and a value of the energy loss is provided for each layer, but in practice only the total energy loss is used. Moreover also the TOF detector can provide an information about the energy loss, for tracks with θ larger than 45°. The capability of the energy loss to distinguish between leptons and other particles is however quite poor in the kinematical region in which most of the lepton candidates are.

3.8.5 Backtracking algorithm for lepton identification

A second approach was developed for lepton identification. It is called backtracking and was developed [115] for the HADES Au+Au data analysis in order to improve the efficiency of reconstruction of leptons, that is very challenging in a high multiplicity environment. At the same time, the other problem already mentioned for the ring finder approach is the identification of the close pairs since for small opening angles only one ring can be reconstructed. In this case, only one electron is identified, which therefore does not contribute to the e^+e^- pair signal, but might contribute to the combinatorial background.

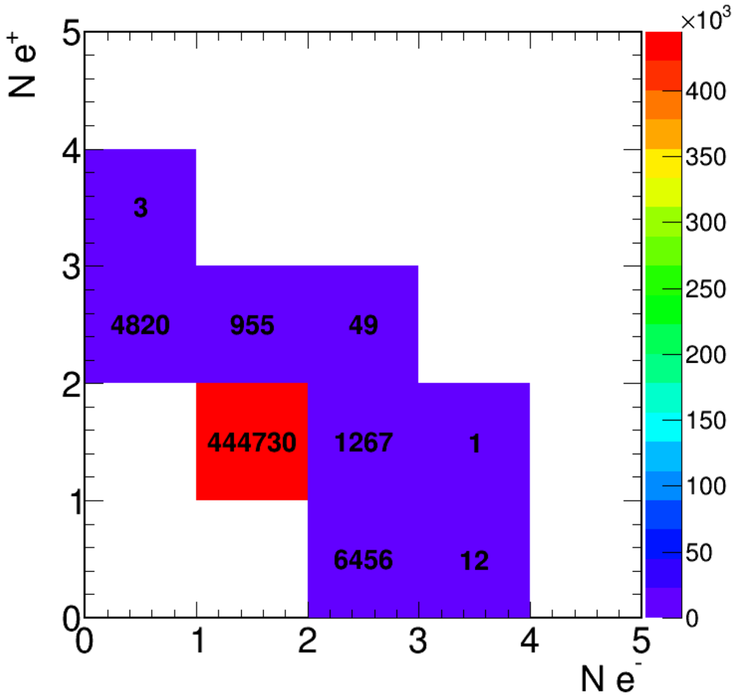

Figure 3.10: Distribution of the number of positive reconstructed leptons as a function of the number of negative reconstructed leptons in one event with the backtracking algorithm.

We give here only the main features of the method and refer to [115] for further details. The idea of the backtracking algorithm is to use in addition the information provided by the tracking, time of flight and energy loss to identify electrons. Combining information coming from the other detectors (RPC, TOF and MDCs) a preselection of possible lepton candidates is therefore first performed. Then for these selected tracks, the tracking algorithm gives the possible position of the ring center and then the RICH information is analyzed in this area in order to select electrons.

The pre-selection procedure is important to start to discriminate leptons from hadrons. A pre-selection of the tracking variable is done, requesting that the χ^2_{RK} has to be smaller than 1000. The multiple use of inner and outer MDC segments is allowed to improve the efficiency. The most important information is given by the measurement of the velocity β which is expected to be close to 1 for electrons, while for hadrons, it is smaller in the momentum range of interest. The original cuts, implemented for the Au+Au data, corresponded to $\beta > 0.95$ for the RPC system and 0.93 for the TOF system, however they were adjusted for pion beam data since the time resolution was worse than in the heavy ion case. Therefore these cuts were released and the tracks having $\beta > 0.9$ for the RPC system and 0.87 for the TOF system were selected. The energy loss is expected to be larger for hadrons in our momentum range, therefore a quite loose cut is applied on this quantity ($\Delta E < 10$ MeV cm^2/g).

After preselecting the tracks for possible lepton candidates, it is possible to calculate the intersection between the Runge-Kutta reconstructed track and the RICH mirror, from where the information is propagated to the RICH pad, finding the region of interest in the pad plane. At this point a parametrization of the ring radius and the width is needed and it is obtained by a study of the Cherenkov radiation emitted by electrons in simulation. This parametrization is given as a function of the vertex position, the polar angle and the azimuthal angle to take into account the dependance on these quantities for the ring shape. Finally a region of interest of radius R ± 3σ is considered and the number of fired pads in this region is used to extract quantities able to distinguish a good electron candidate.

Fig. 3.10 shows the distribution of the number of positively and negatively charged leptons reconstructed for each event. In most of the cases, only one unlike sign pair of leptons is reconstructed. However, the number of events with more leptons is quite significant and will contribute to the combinatorial background as will be discussed in Chapter 5.

Chapter 4

RICH performance study

As discussed in Chapter 2, the RICH detector plays the most important role for the lepton identification. To ensure the quality of the data, careful and systematic checks of its performance are therefore needed. It is also important to adjust the RICH digitizer, which is part of the simulation code, in order to have a realistic description of the lepton reconstruction in the simulations. In Sec. 4.1 the stability of the RICH response is studied as a function of time and in Sec. 4.2 the method to adjust the parameters of the RICH digitizer is described, a short conclusion is drawn in section 4.3.

4.1 RICH stability

4.1.1 HV stability

The main element that one has to control is the high voltage (HV) that was applied to the anode planes of the MWPC (see Fig. 2.4), which has a direct effect on the amplification of the signal (see Sec. 2.2). Small variations in the HV can therefore cause quite large differences in the efficiency of the detector. During the period of the data taking, all sectors were kept at the same HV (around 2440 V), except sector 3, for which three periods with roughly the same duration can be distinguished. This sector was indeed first operated at 2398 V, then the HV was decreased by 20 V and again by 20 V more in the last period. The reduction of HV in this sector was needed due to the large numbers of disjunctions due to a large current.

This situation is illustrated in Fig. 4.1, which displays the HV for the six sectors as a function of the number of files. One file corresponds approximately to 100 000 events. One can also see that there are files for which some sector was working at lower voltage and some blank spaces that correspond to files for which the HV was lower than 1500 V, which induces a huge reduction in the efficiency.

4.1.2 RICH observables stability

The change of HV is directly reflected in the performance of the detector. In Fig. 4.2 a clear correlation can be observed between the HV applied and the number of reconstructed rings, which is one indicator of the lepton reconstruction efficiency: the deviations from the constant trend correspond to the files for which the HV was not set at the nominal value, leading to a drop in the efficiency.

It can also be observed that the different sectors have a quite large difference in the number of reconstructed rings and especially that sector 3, although it had a lower voltage, is, by far, the most efficient. A hypothesis to explain this contradictory behaviour is that this sector is more efficient than the others because it had been working at lower voltage since 2001 and therefore it suffered less from the normal aging of the detector. Moreover,

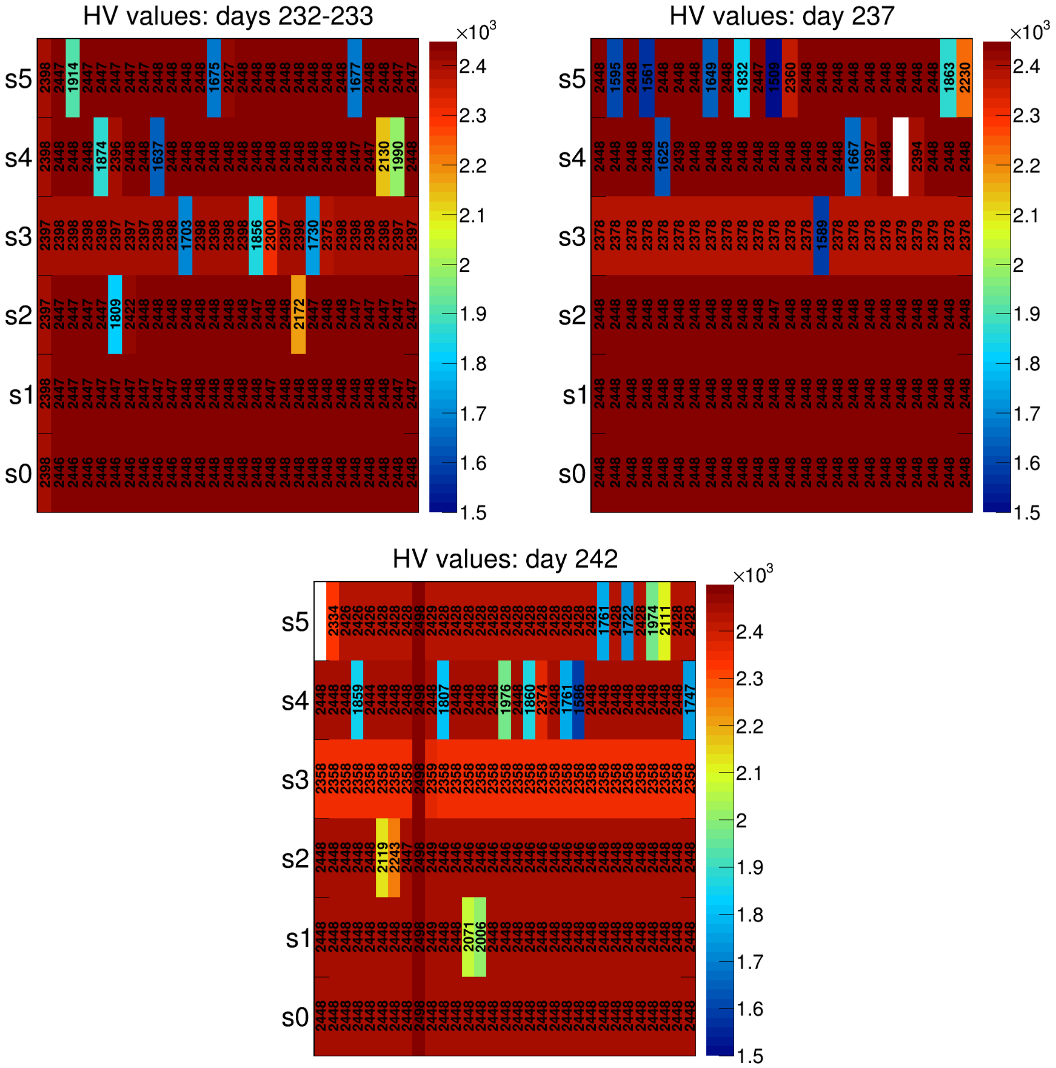

Figure 4.1: HV configurations for the six sectors of the RICH detector for selected days in the first (top), second (middle) and third (bottom) parts of the beam time. Each column corresponds to one file, i.e. approximately 100 000 events. The HV values for 5 sectors remained constant, throughout the beam time, while for sector 3, the HV was lowered twice by 20 V.

a different aging can also explain why sectors, having the same HV, present a different mean number of rings. As discussed above, the HV was rather stable, except for sector 3. These changes have a direct impact on the efficiency of this sector as one can see from the Fig. 4.2 that shows the relative distribution of lepton candidates among the different sectors. In the first part of the beam time, sector 3 has much higher efficiency than the other sectors, while in the last part of the beam time, sector 3 has a very similar efficiency with respect to sector 1. This different response due to the high voltage can also be observed in the distribution of the number of fired pads. In the Fig. 4.3 this distribution is shown for the three different periods of the data taking. One can see that the lowering of the HV by 20 V leads to a lower average number of pads by approximately two pads. This is explained by the lower avalanche amplification in the MWPC which reduces the number of pads collecting the signal (see Sec. 2.2). The fact that the different sectors have a different efficiency is not a problem if this behavior is correctly taken into account by the simulation. As described in the following section, a special effort is made to tune

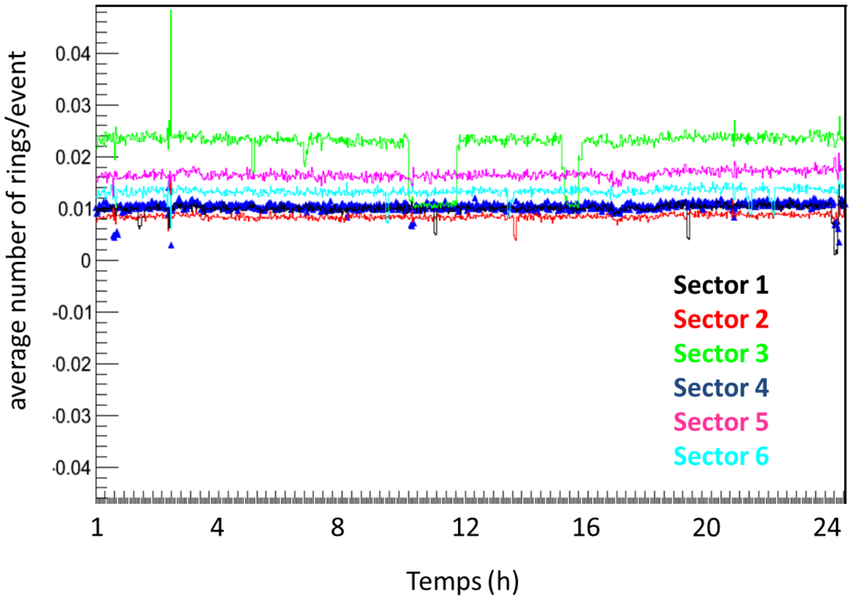

Figure 4.2: Evolution of the average number of rings per event as a function of time during approximately one day of data taking. Each point corresponds to one file (approximateley 100 k events). The 6 sectors have quite different efficiencies. Sector 3 is, by far, the one with the highest value. The holes in the distribution correspond to moments in which the HV was lower and therefore a clear drop in the number of reconstructed rings can be observed. Each point corresponds to one file, i.e. about 100 000 events.

the RICH detector efficiency sector wise with a great precision. The time dependence of the efficiency was however not taken into account. The drops of efficiency (Fig. 4.2) are indeed occurring for all sectors except sector 3 for very short periods of time, which does not impact significantly the final number of reconstructed leptons. It is considered that for sector 3, the simulation was tuned to reproduce the average response of the detector during the full period of data taking and that the errors related to this procedure are taken into account in the systematic errors (see Sec. 6.3).

4.2 Optimization of the RICH digitizer

4.2.1 Simulation of the Cherenkov effect

In the GEANT simulation code, electrons and positrons generate Cherenkov photons when traveling through the radiator material of the RICH detector. The distribution of the number of photons as a function of their energy E_γ is given by:

$$\frac{dN}{dE_\gamma} = \frac{Z^2 \alpha * \sin^2\theta_c(E_\gamma)}{\hbar c} l_{rad} \tag{4.1}$$

α=1/137 is the fine structure constant, l_{rad} the path length through the radiator and θ_c is the angle of the emission cone.

$$cos\theta_c(E_\gamma) = \frac{1}{n(E_\gamma)\beta}, \tag{4.2}$$

where β is the particle velocity, in units of c and $n(E_\gamma)$ is the refraction index of the radiator material.

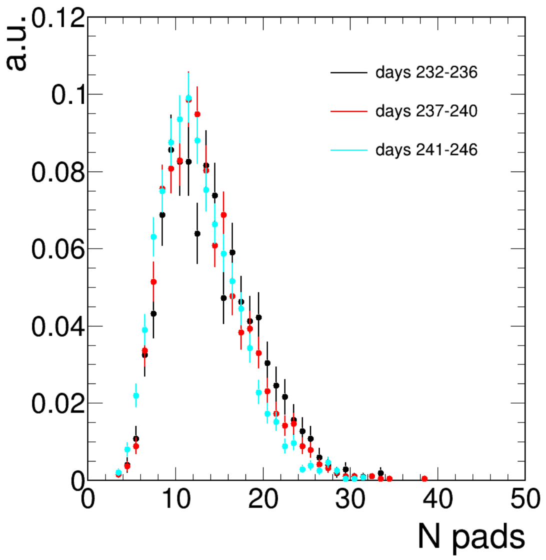

Figure 4.3: Number of fired pads distribution for three different periods in the data-taking, measured for sector 3.

Parametrization of the detector response

The role of the RICH digitizer in the simulation code is to provide for each electron a realistic estimate of the number of fired pads and their collected charge.

First, the photon detection efficiency is taken into account. The most important loss of Cherenkov photons is due to the quantum efficiency of the CsI layer of the pad plane, which determines the probability that a photo-electron is ejected. However, the global effect includes contributions from the transmissions of the C_4F_{10} radiator, of the CaF_2 window and of the CH_4 detector gas, as well as the mirror reflectivity and the single electron efficiency of the MWPC. This photon detection efficiency is given in 18 bins in wave length with values which were measured using a vacuum Ultra Violet lamp [122]. However, it was observed by comparing the distributions of numbers of pads hit in the simulation and in the experimental data that the efficiency was degrading with time. Hence, for each data taking period, a correction factor is determined for each sector, after adjustment to the data, as shown in the following.

Then, the charge associated to each single photon is sampled according to a simple exponential law :

$$P(Q) = Ae^{-kQ} \tag{4.3}$$

The slope parameter k depends on the HV and is adjusted for each sector and each experiment. The charge is then distributed among the pads that are close to the pad hit by the photon. This distribution among neighboring pads depends on the position of the impact of the photon on the central pad and follows a procedure checked on experimental data [122].

4.2.2 Optimization procedure

As discussed above, the RICH digitizer uses two sets of parameters, which can be tuned

- *fExpSlope*, which is the parameter of the exponential slope describing the single photon charge distribution. It is connected to the charge gain created by the HV. This set is composed of six parameters, one for each sector;

- *CorrSec*, which is a correction to the photo-detection efficiency. This set of parameters is composed of 6x18 parameters, since for each sector there are 18 parameters for 18 bins in wavelength. However, the correction will be assumed not to depend on the wavelength, *i.e.* only one correction factor has to be determined for each sector.

The principle of the calibration of the RICH detector is as follows:

- Identify leptons in data;
- Generate leptons in the simulation with similar kinematics as in the data;
- Tune the parameters in simulation in order to have a similar RICH response in the data and in the simulation.

4.2.3 Selection of a pure lepton sample in experimental and simulation data

Since the simulation has to be based on a model, it is important to select events corresponding to a well known source of dileptons, that one can simulate in a realistic way. To this end, the region of invariant mass M $<$ 140 MeV/c^2 is selected, since it is dominated by the π^0 Dalitz decay, which is a well known process. Simulation events are generated using the PLUTO event generator developed by the HADES collaboration [35], with a cocktail of dilepton sources as described in Sec. 8.2.

Leptons are selected in data using appropriate cuts on velocity and on momentum (see Sec. 3.8). Only tracks with a good RICH ring-MDC matching (*RichQa* > 4, see Sec. 3.6) were selected. Then only e^+e^- pairs with invariant mass smaller than 140 MeV/c^2 and an opening angle larger than 9 degrees are considered in the analysis. As will be discussed in Sec. 5.2.2, this allows to reject a lot of pairs coming from real photon conversion. In particular, the conversion pairs produced in the RICH detector have a lower number of photons than pairs emitted from the target, since they don't cross the full length of the radiator. The opening angle cut is therefore particularly important for the correct adjustment of the digitizer for signal events. These cuts are applied to the experimental data and to the simulation events.

As will be demonstrated in Sec. 3.8.5, in the π^0 region, the signal to background ratio is large (S/B>10), so that one can neglect the contribution of the background pairs. Therefore, a direct comparison of the RICH observables for measured e^+e^- pairs (including a small amount of background pairs) and for correlated e^+e^- pairs from the simulation is relevant.

4.2.4 Sensitive RICH observables

The two variables characterizing a ring which are the most directly connected to the efficiency of the detector are its number of fired pads N$_{pads}$ and its charge Q. These two variables are strongly correlated, but the number of pads is more directly related to the single photon efficiency, while the charge is mostly sensitive to the amplification gain in the MWPC. It means that the comparison of charge per ring and the number of pads per ring in the data and in the simulation can be used to tune the parameters $fSlope$ and $CorrSec$, respectively (see Sec. 4.2.2).

The distributions of number of pads are displayed as black dots in Fig. 4.4. Sector 3 has the largest most probable value (about 12) and the broadest distribution while sector 1 has the smallest probable value (about 10) and the narrowest distributions. This trend is consistent with the number of rings of each sector as discussed in sec. 4.1.2.

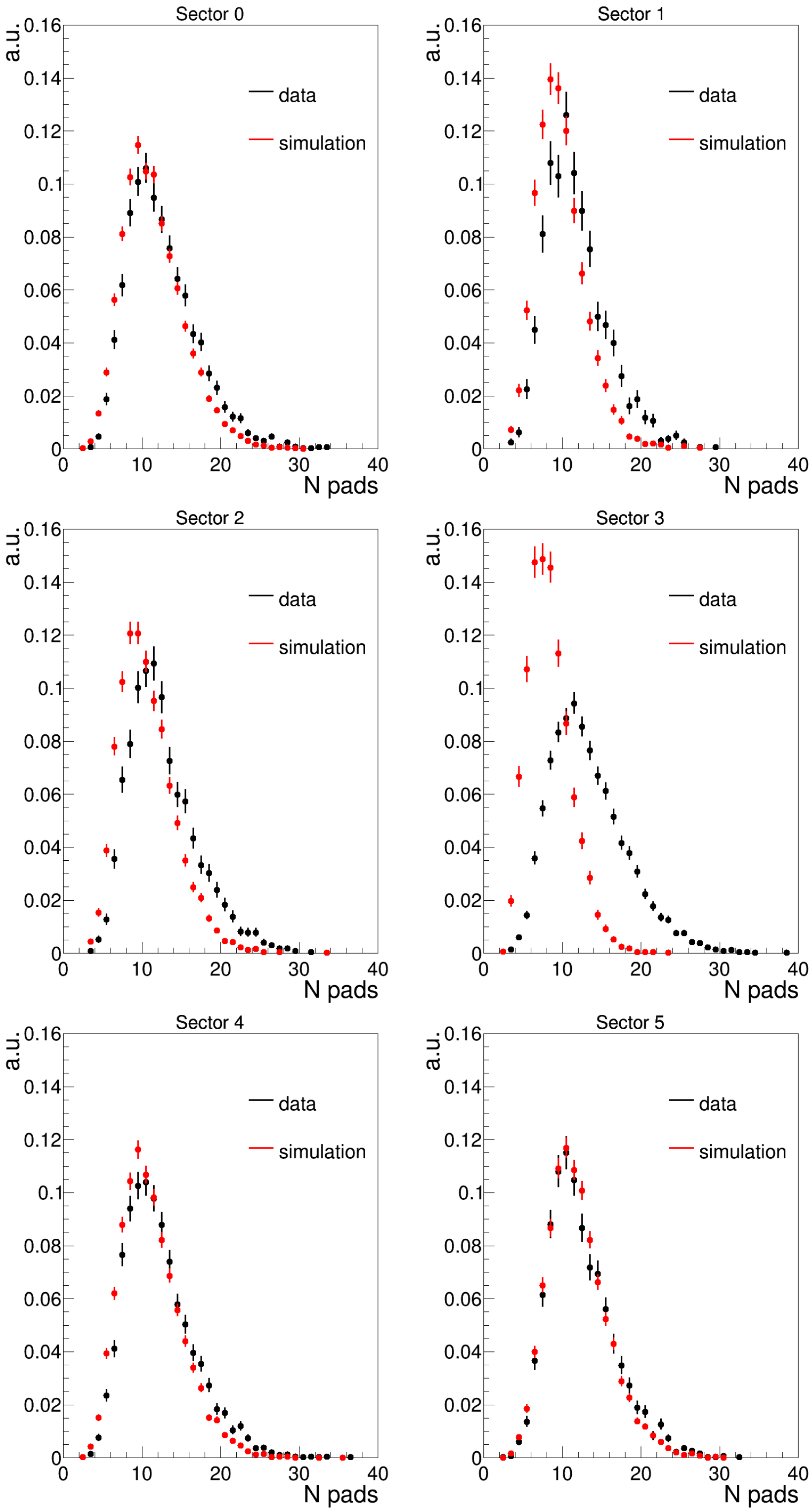

Figure 4.4: Number of fired pad distribution for the different sectors for data (black dots) and simulation using the digitizer tuned for the previous Au+Au experiment (red dots).

The distributions of average charge per ring are shown in Fig. 4.5. Here one can observe that sector 3 has the narrowest charge distribution, which is consistent with the lower HV.

Before the parameter tuning under discussion the default values used for the simulation were the ones used in the last data taking (Au+Au collisions at 1.23*A* GeV). The

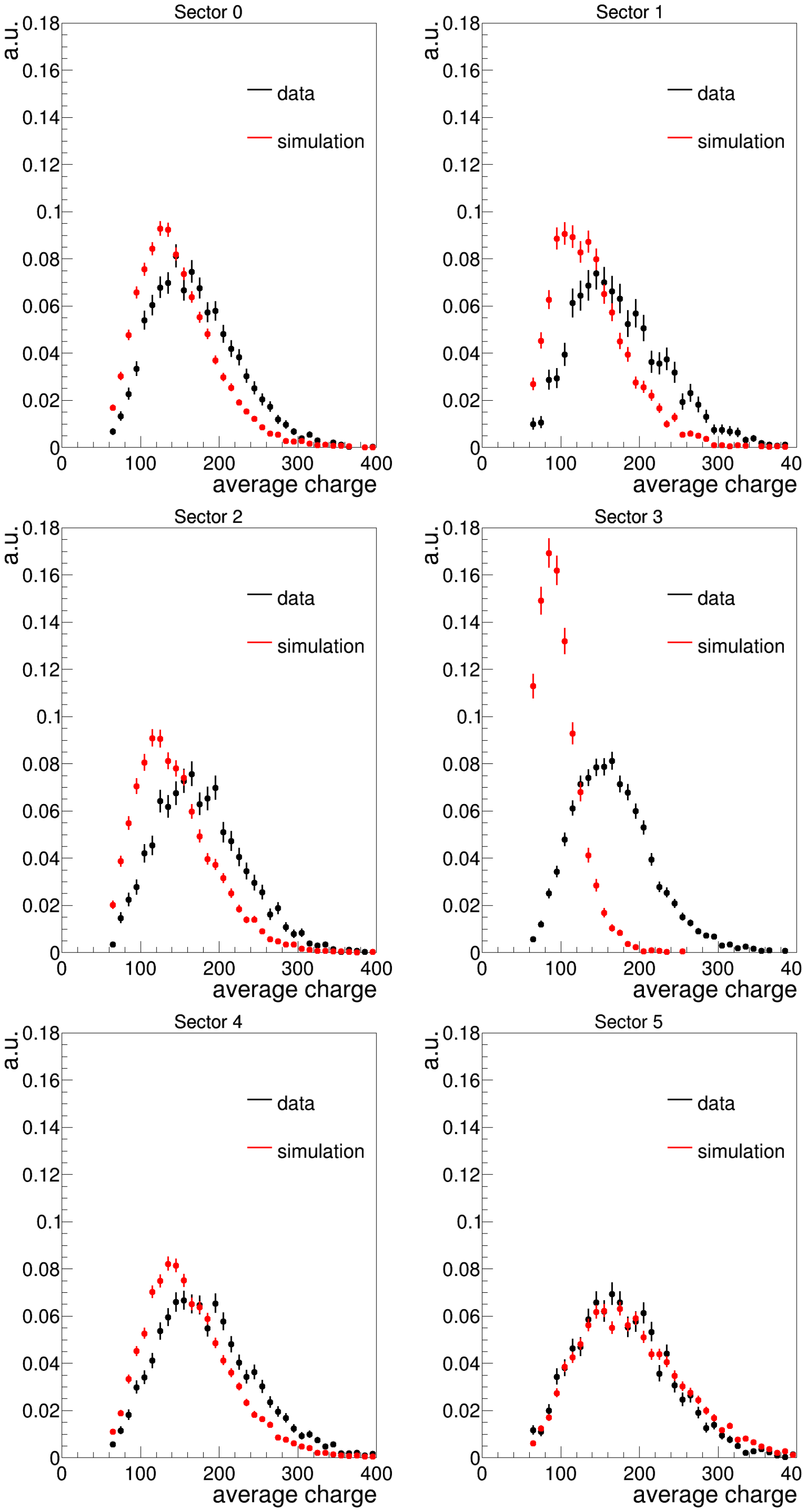

Figure 4.5: Comparison of the average charge per ring in the data (black dots) and in the simulation (red dots) for the six sectors using the digitizer tuned for the previous Au+Au experiment (red dots).

comparison between the number of pads distributions in data and in simulation can be observed in Fig. 4.4. The simulation overestimates in general the average number of pads distribution, and especially for sector 3, there is a very large difference. This is expected since the HV values in the pion beam time are higher by 48 to 128 V for sector 3, by 48 V for sector 4 and by 28 V for the other sectors with respect to the HV used in the previous experiment. The comparison of the charge distribution (Fig. 4.5) is also consistent with larger gains for the pion beam experiment. The charge distribution is well reproduced only for sector 5. For the other sectors, the simulation predicts too small values of the collected charge. For sector 3, the discrepancy is the most important. This clearly shows that a tuning of the digitizer is needed for the present experiment. Using the parameters optimized for the previous experiment would indeed lead to a significant underestimation of the efficiency of the RICH detector.

4.2.5 Estimation of the RICH efficiency

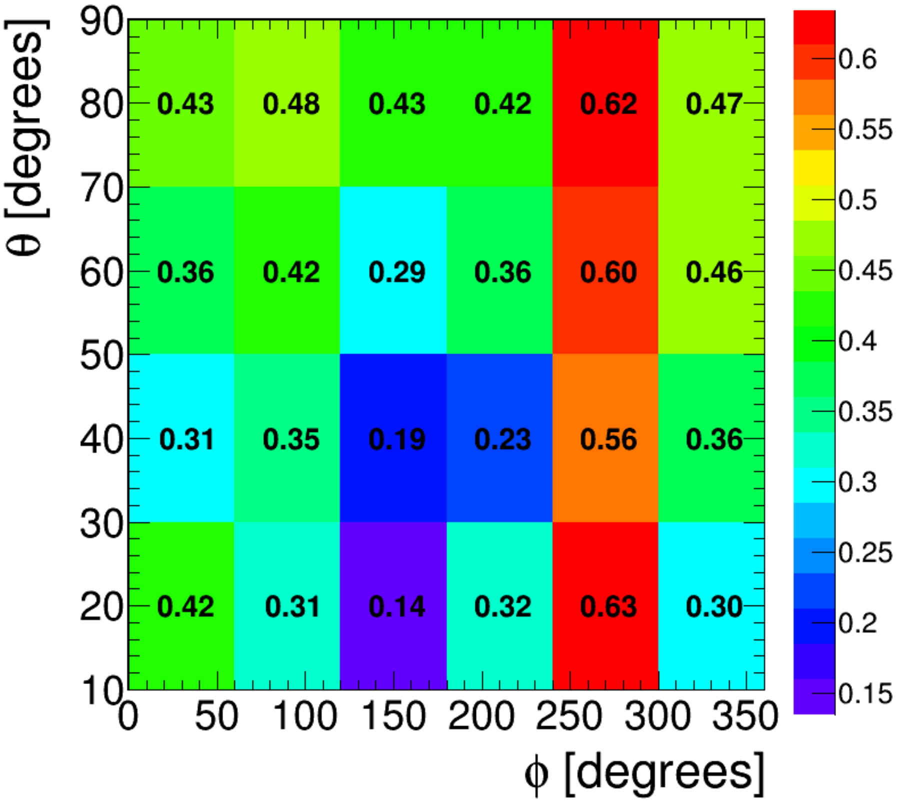

Figure 4.6: RICH efficiency in θ and ϕ bins for positrons for data events in the π^0 invariant mass region, showing the dependence as a function of the sectors. Considering the convention for azimuthal angle, the six columns correspond respectively to sectors 5, 0, 1, 2, 3 and 4.

It turned out that several sets of parameters *fSlope* and *CorrSec* can reproduce well the number of pads and charge distributions but lead to a different number of reconstructed rings. This can be explained because the charge gain and the photo detection efficiency have a correlated effect on the average charge per ring and on the number of hit pads, and both the ring finder (see Sec. 3.6) and the backtracking procedure (see Sec. 3.8.5) are sensitive to the detailed configuration of the charge deposit on each pad.

We found therefore necessary to improve the standard procedure by checking that the data and simulation match also at the lepton reconstruction level. However, since the cross sections for the π^0 production are not known with a sufficient precision, we cannot use directly the number of reconstructed rings. Instead, we developed a method to calculate the efficiency of the RICH detector.

To estimate the efficiency of the lepton reconstruction with the RICH detector, the proportion of reconstructed leptons in a reference sample of leptons identified without the use of the RICH detector is necessary. This is not a very easy task as discussed in Sec. 3.8, due to the contamination of pions. However, this can be realized under some conditions.

The pion contamination is larger for e^-, because the π^-s are much more abundant than π^+s. One can therefore try to use the RICH detector only for the identification of electrons and not for the identification of the positron. In addition, the pion contamination also depends on the momentum and, with the increasing of the momentum, becomes much higher. Therefore also an appropriate cut on the momentum as a function of the velocity is applied to try to minimize the pion contamination. Moreover all tracks having a momentum larger than 300 MeV/c are rejected, due to the pion contamination. In a second step, the RICH detector information is used also for the positron identification. The positron efficiency is then estimated as the ratio of the yields of positrons identified with the RICH detector to the ones in the reference sample.

$$\epsilon = \frac{N_{e^+RICH}(\theta, \phi)}{N_{e^+ref}(\theta, \phi)}$$

We have already observed (see Sec. 4.1.2), that the RICH efficiency depends on the sector. In addition, since the number of Cherenkov photons is proportional to the path length in the radiator, the efficiency is expected to increase with the polar angle. Therefore, the efficiency is calculated in six bins in the azimuthal angle, one for each sector and in 4 bins in the polar angle (see Fig. 4.6). This limited granularity is due to the low statistics in the data, that does not permit to have a more accurate binning. Considering the convention for azimuthal angle, the six columns correspond respectively to sectors 5, 0, 1, 2, 3 and 4. One has to keep in mind that the first and fourth θ bins have a lower statistics, therefore we focus more on the behavior of the central bins. To visualize the statistical errors on the efficiencies, they are also displayed as six individual graphs in Fig. 4.7.

Except for the first bin, which has a low statistics and might also be affected by systematics, the efficiency is found to increase with increasing polar angle. This is expected due to the increase of the path length in the radiator as a function of the polar angle. The sector 3 has the largest efficiency, with values of 0.56 and 0.60 in the two central bins and the sector 1 the lowest one with 0.19 and 0.29. These results are consistent with previous observations of the RICH observables and the method allows to quantify the part of the lepton reconstruction which is due to the RICH detector.

4.2.6 Influence of the lepton purity in the efficiency calculation

One key feature in the efficiency calculation explained in Sec. 4.2.5 is the selection of the reference sample. It is indeed necessary to find a way to determine a sample free of pions in order to calculate the RICH efficiency. Since the contamination is very sensitive to the momentum, one can think to check the stability of the results when different momentum cuts are used. As said in the previous part the maximum momentum was set to 300 MeV/c. Different cuts were then used: maximum momentum 250 MeV/c, 200 MeV/c and 150 MeV/c. If present, the pion contamination should decrease when lowering the maximum momentum allowed and therefore discrepancies in the ratio between data and simulation should be seen in the different cases. Since it is not the case, one concludes that the efficiency determination is not affected by purity problems. As an example, the ratios of efficiencies for the cases with maximum momentum equal to 300 MeV/c and 200 MeV/c are shown in Fig. 4.8.

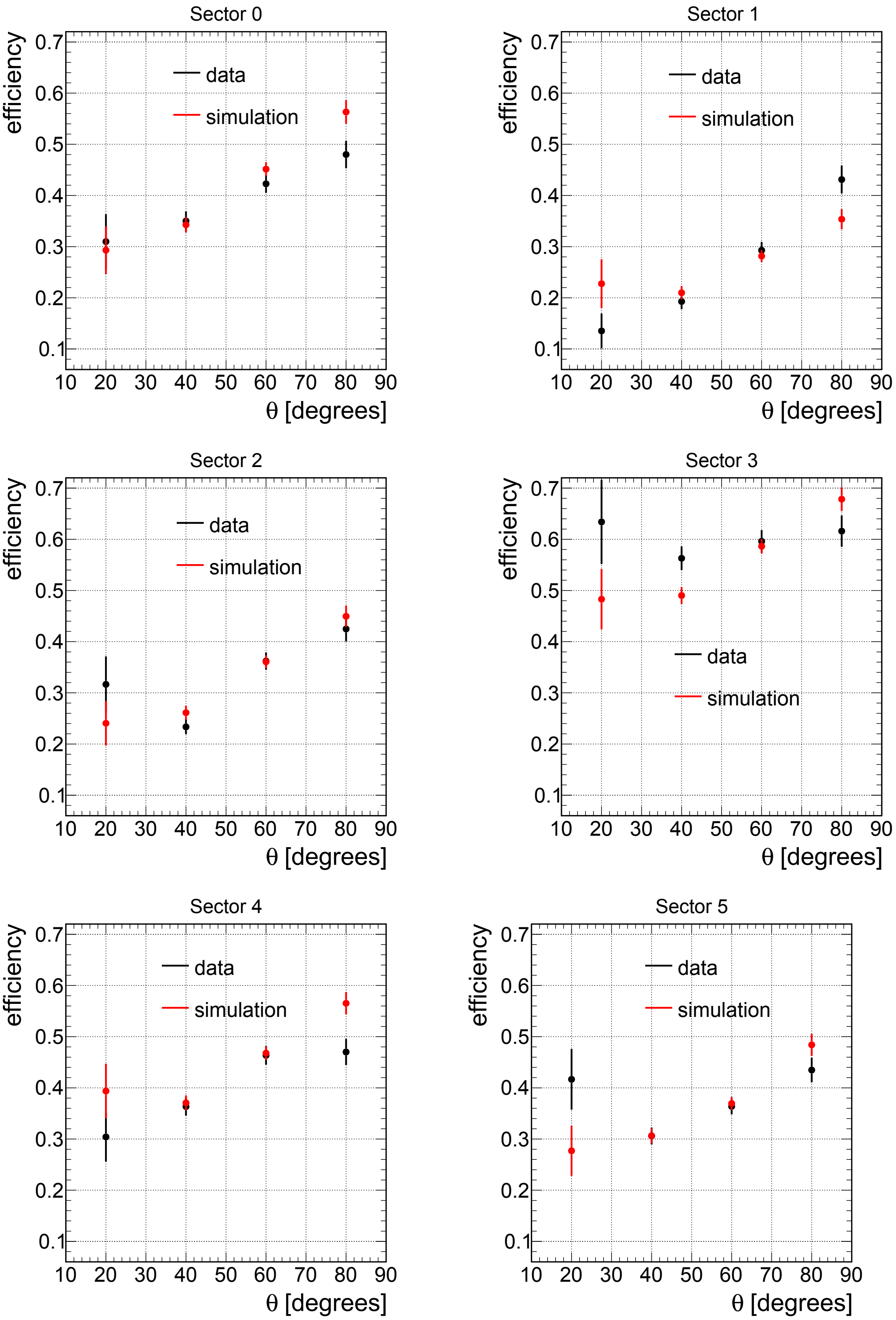

Figure 4.7: RICH efficiency for the six sectors in simulation (red points) and in data (black points) in four bins in polar angle.

4.2.7 Results of the optimization procedure

An iterative procedure starts with the aim to match as best as possible the RICH observables obtained in the simulation with the measured ones. Many attempts are made until a

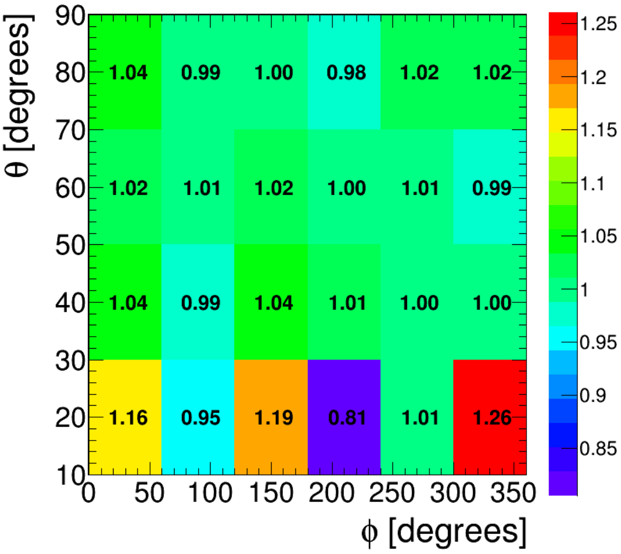

Figure 4.8: Ratio between the RICH efficiencies in data events for the case with p_{max} = 200 MeV/c and p_{max} = 300 MeV/c.

good agreement is reached. The final choice of the parameters is reached as a compromise between the values of the efficiencies, that can be easily evaluated in the ratio between data and simulation, and the comparison of the RICH observables, namely the number of pads and the average charge per ring. The final result for the comparison of the RICH observables, used in the tuning procedure, between data and simulations is displayed in Fig. 4.9 and Fig. 4.10. The left part of Fig. 4.11 and the red dots in Fig. 4.7 show the values of the efficiencies obtained with the final values. One can observe a general good agreement. The right part of Fig. 4.11 and Fig. 4.12 display the ratios between the efficiencies. Some deviation from the unity can be noticed at low theta angle, but the error bars in this region are very large, therefore the result can be considered acceptable. For angles between 30 and 70°, where most of the yield stands, the deviations do not exceed 10%, which is very satisfactory. Since the tuning was realized taking into account these variables, it sounds natural that a satisfactory agreement was reached. Other RICH observables are available and can be checked in the simulation after the tuning procedure. A good agreement is also obtained as one can see in the Fig. 4.13 for the number of clusters.

4.2.8 Consistency of the parameters

It is worth to compare the values of the parameters after the final tuning and the initial parameters adjusted for the Au+Au experiment. As shown in Fig. 4.14, the charge gain parameter *fSlope* is smaller in absolute values for most sectors, and in particular for sector 3, which reflects the different HV configurations (see Sec. 4.1.1).

The correction factor *CorrSec* to the photon detection efficiency is about 10% lower than for the previous experiment, meaning a larger correction, which is consistent with an aging effect. This is not unexpected after the high multiplicities experienced by the RICH detector in the Au+Au run. The sector 3 has on the contrary a much larger value for this parameter for the pion beam time. A possible explanation is the imprecise tuning of this parameter in the Au+Au experiment where this sector was working with a very low efficiency. The fact that sector 1 and 3 have the smallest and largest values of the photon detection efficiency parameter, respectively, is also consistent with our observations of the RICH observables and efficiencies.

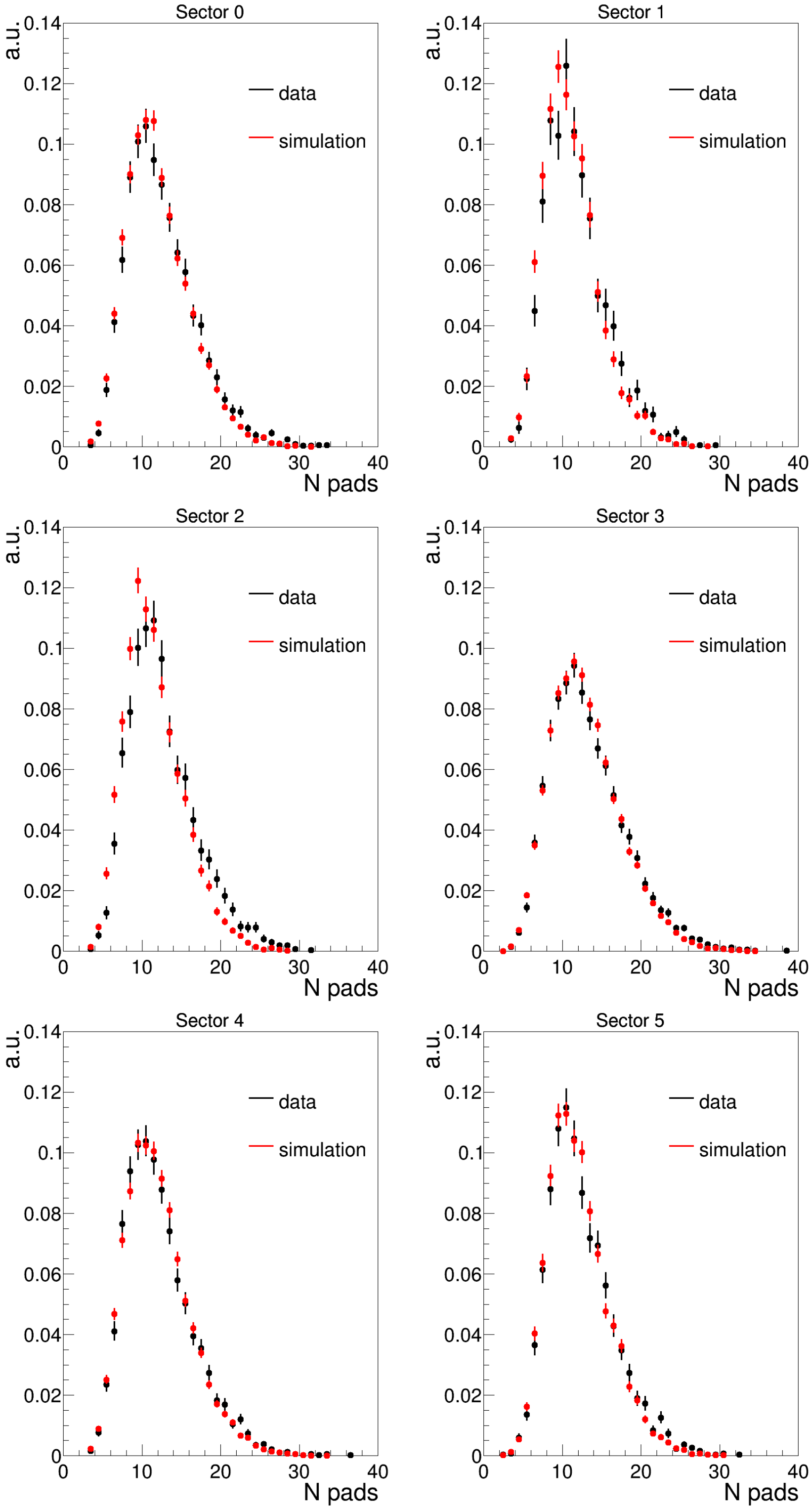

Figure 4.9: Comparison of the number of pads in data and simulation for the six sectors with the final RICH digitizer parameters.

4.2.9 Model dependence of the calibration

A key feature of the RICH detector is the dependence of its performance as a function of the θ angle of the lepton since the path length inside the radiator gas is different. The tuning of the digitizers was realized using a simple model, including channels with

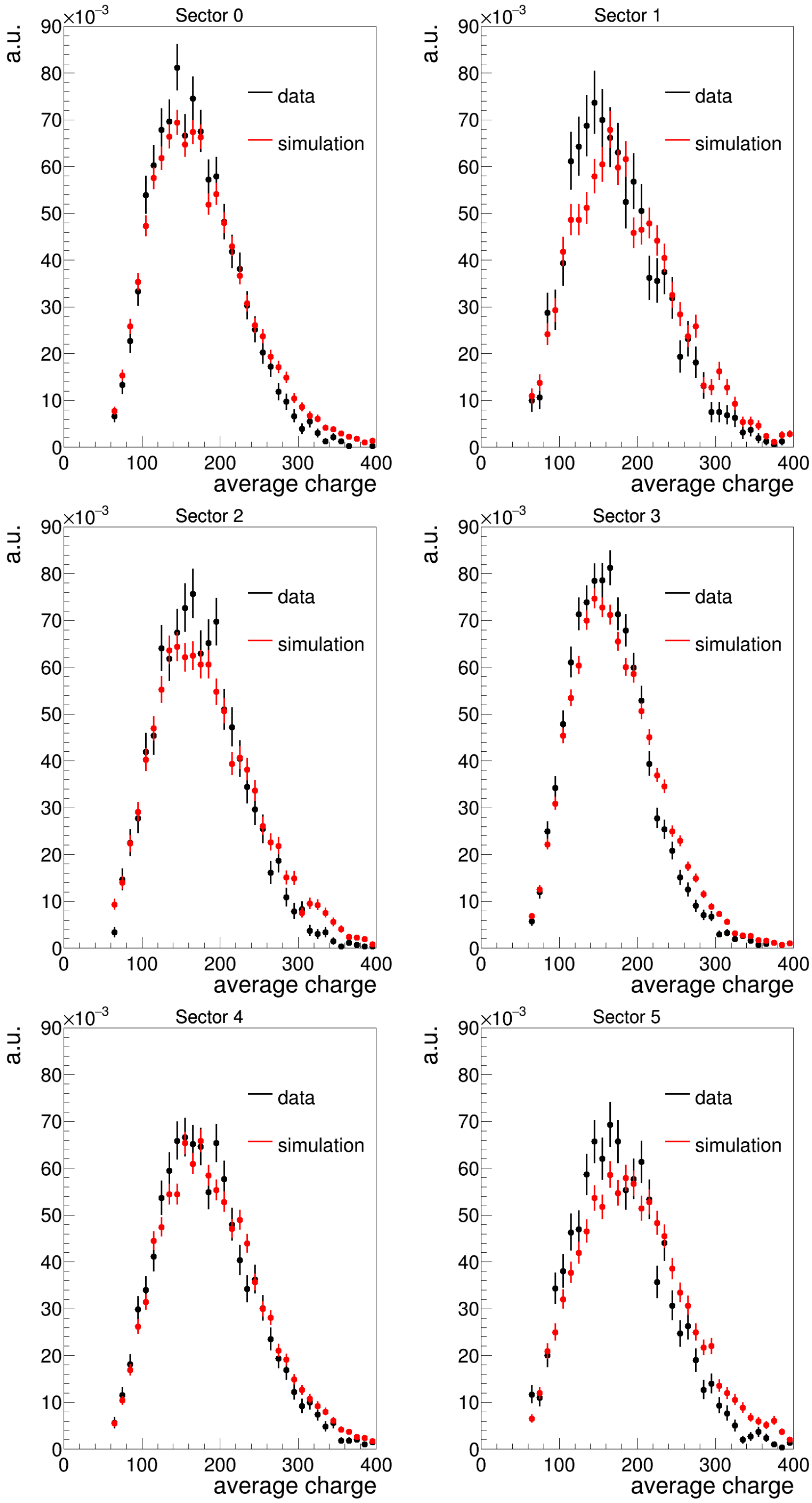

Figure 4.10: Comparison of the average charge per ring in the data and in the simulation for the six sectors with the final RICH digitizer parameters.

1 pion, 2 pions, η and N(1520), with phase space distributions for each channel. This model provides only an approximate description of the lepton angular distribution, which might affect the average value of the number of hit pads. However, the RICH efficiency is calculated in four bins of θ, which reduces significantly the dependence of the tuning on the lepton angular distribution. This is an additional interest of having introduced the

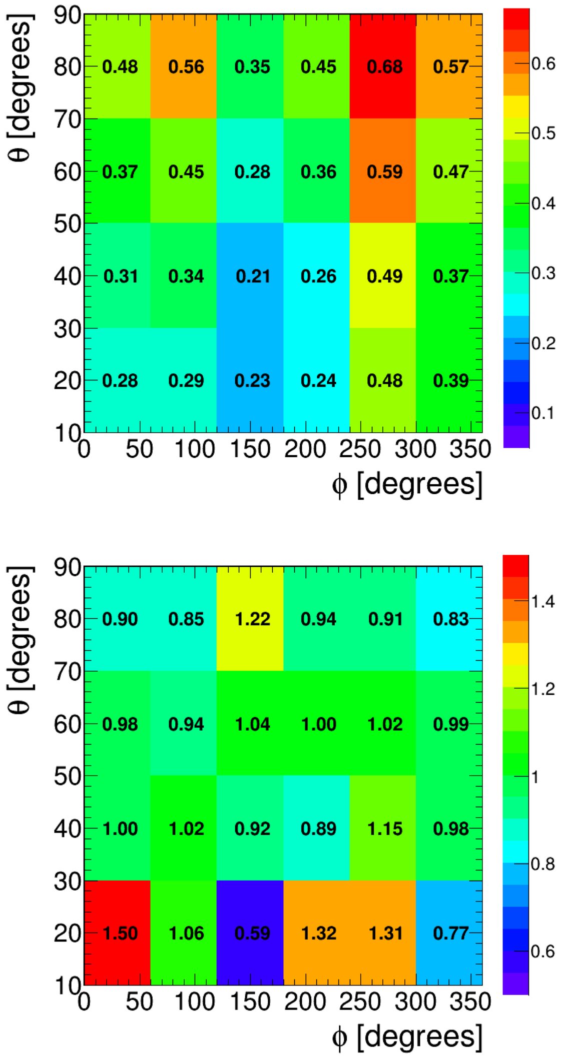

Figure 4.11: Left: same as Fig. 4.6 for simulation events. Right: Ratio between RICH efficiencies in data and in simulation.

efficiency as a new feature in the tuning procedure.

This is illustrated in Fig. 4.15 which displays the ratio between the efficiencies obtained in the simulation of π^0 produced in single and double pion production processes, respectively. Although these processes present very different kinematical features (see Sec. 8.2), no significant difference in the efficiency can be seen.

So, the tuning does not seem to be too much affected by the model dependence of the simulation. However, since the good description of the lepton angular distribution is important for the description of the RICH observables, and the statistics is not large enough to make narrow bins, a possible improvement of the procedure would be to use an iterative procedure with lepton angular distributions adjusted to reproduce the measured distributions, but this is beyond the scope of this work.

4.2.10 Stability of the RICH efficiency as a function of the beam time

As already mentioned at the beginning of this section, since the values of the HV were not constant over the full period for all sectors, the tuning of the digitizer is therefore made on quantities, averaged over time. As our analysis will use data summed over the six sectors,

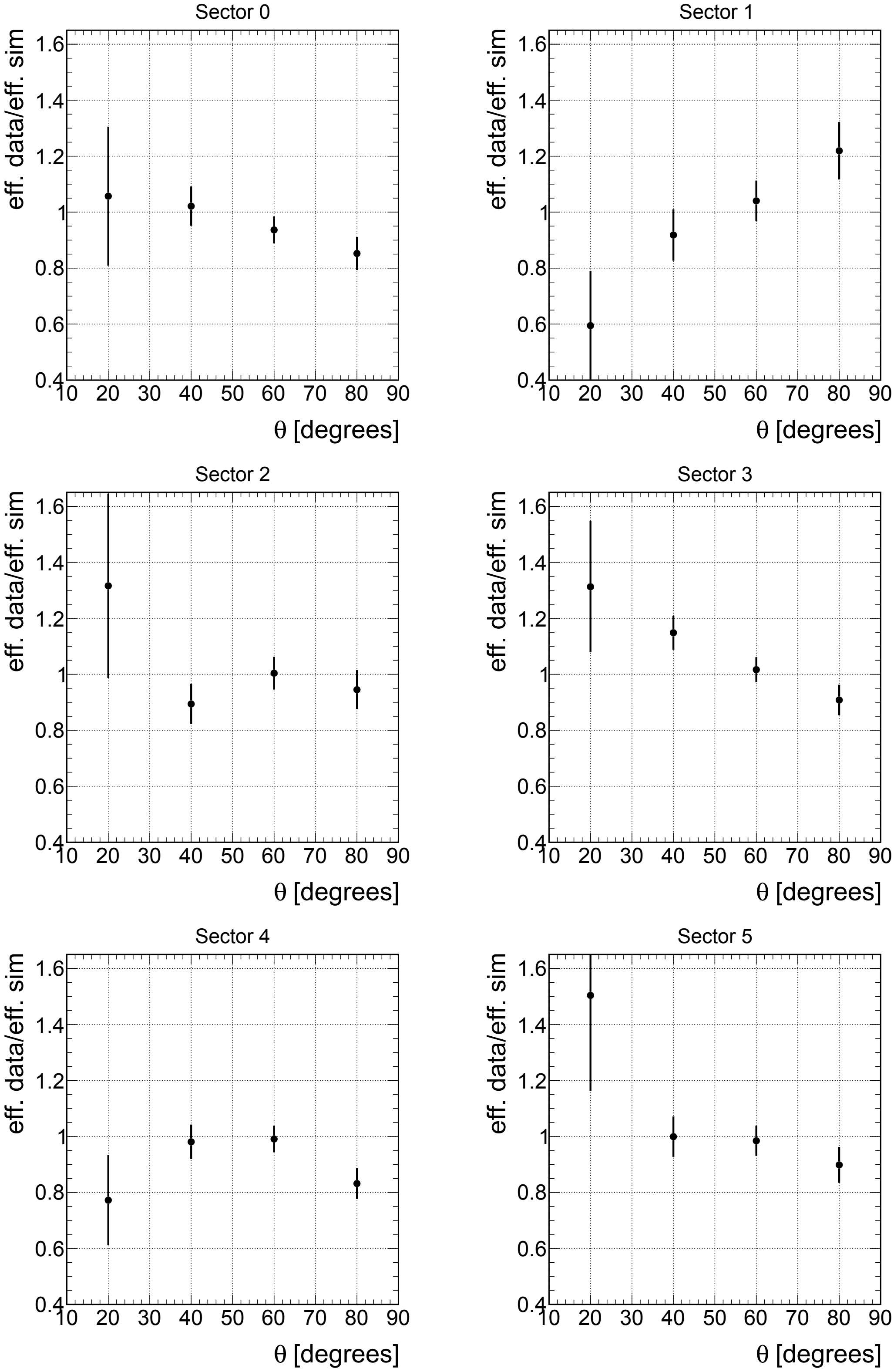

Figure 4.12: Ratio between RICH efficiencies in data and in simulation for the 6 sectors

one can check the stability of the global RICH lepton identification efficiency, as a function of the beam time day. As can be seen in the Fig. 4.16, no significant deviation is present for the different days, which means that the change in HV for sector 3 has no effect on the global efficiency. The efficiency of the RICH reconstruction for one lepton is about 40%.

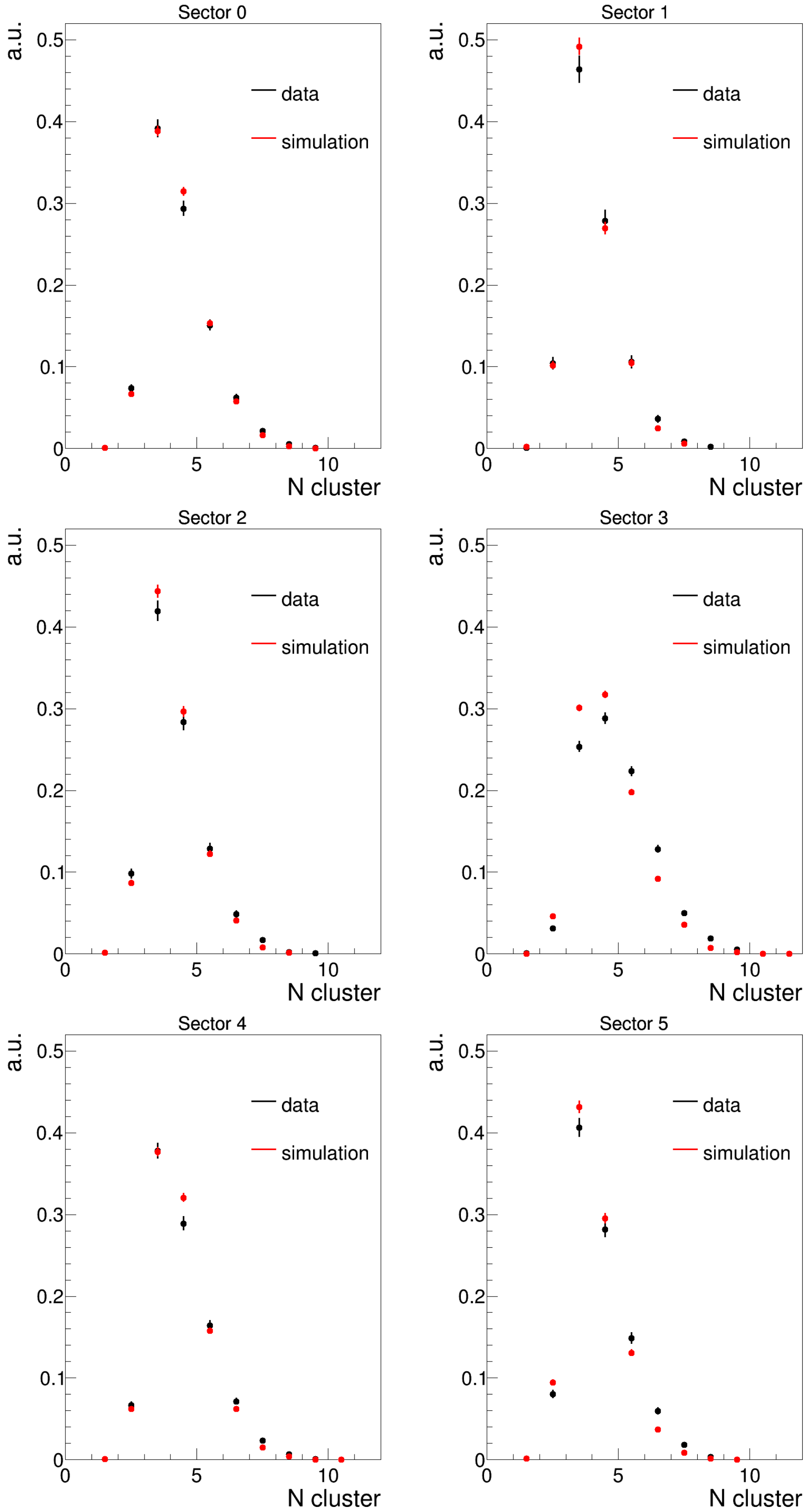

Figure 4.13: Comparison of the number of clusters between data (black dots) and simulation (red dots) for the six sectors.

4.3 Conclusion

A procedure for the tuning of the RICH digitizer using real and simulated data was developed. We implemented a calculation of the RICH efficiency for positrons, which

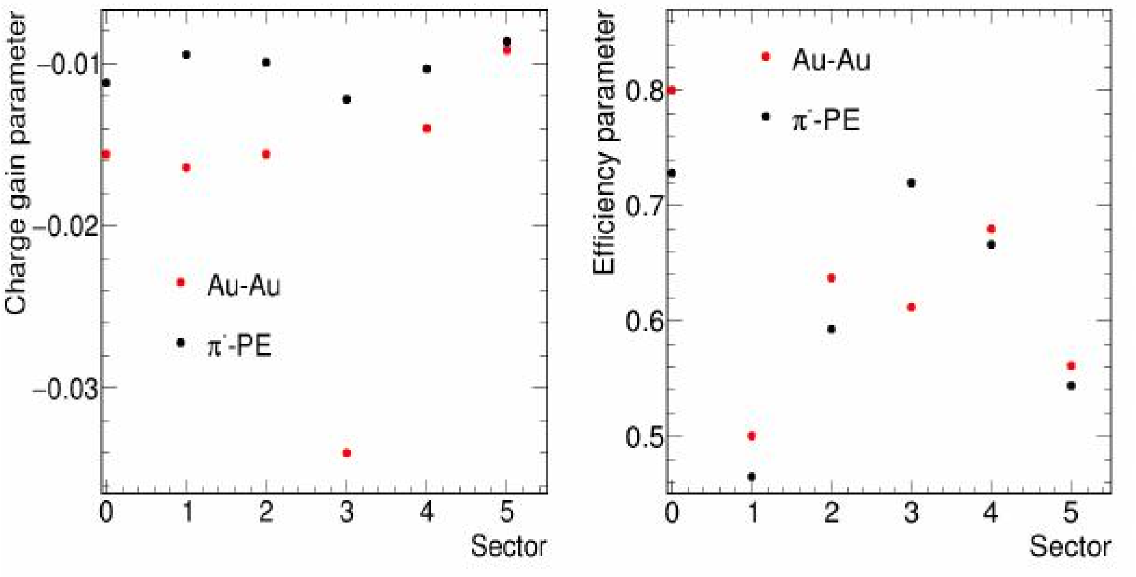

Figure 4.14: Final values for the parameters *fSlope* (left) and *CorrSec* (right) for the pion beam experiment compared to the parameters adjusted for the Au+Au experiment are shown as a function of the sector number.

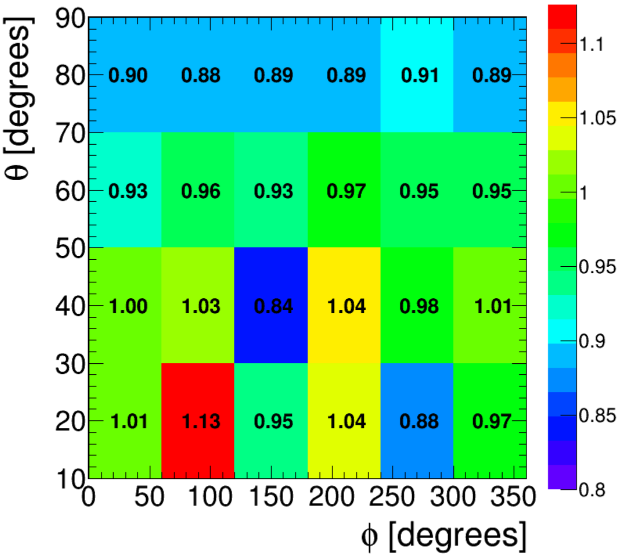

Figure 4.15: Ratio between the RICH efficiency in the simulation for 1 π^0 production and 2 π^0 production.

can be compared in the simulation and in the real data. This procedure allows to take into account the sector and polar angle dependence of the efficiency. The stability of the global RICH identification efficiency during the beam time was demonstrated. The procedure is not completely model independent and to optimize the procedure and reduce systematic errors, the lepton polar angle distribution in the simulation should be adjusted to reproduce the data.

Finally, one can conclude that a consistent optimization of the digitizers was achieved and it is possible to use it for the generation of simulated events based on models.

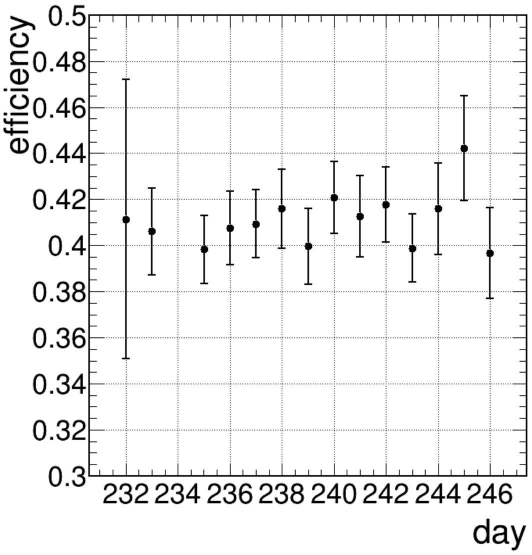

Figure 4.16: Evolution of the RICH efficiency in real data as a function of the data taking day number. The error bars show statistical errors.

Chapter 5

Extraction of the dielectron signal

In Chapter 3, the single lepton identification was presented, but the real objective of our analysis is to select combinations of e^+ and e^- (dielectrons) that originate from the same electromagnetic vertex (same virtual photon). By studying kinematical properties as invariant mass and p_t spectra of these pairs, information about the source can be obtained.

We can distinguish three sorts of background which can contaminate the signal:

- The combinatorial background due to combinations of e^+ and e^- originating from different virtual or real (after conversion) photons;
- The conversion pairs due to conversion of real photons in the target or in the detector material;
- The combination between leptons and misidentified hadrons as electrons or positrons.

5.1 Combinatorial background

5.1.1 Origin of the combinatorial background

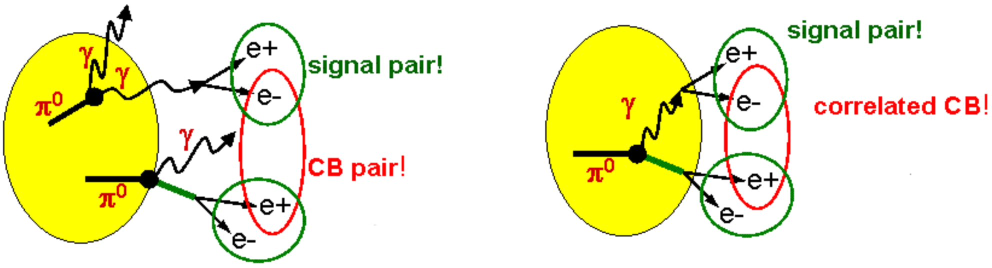

Figure 5.1: Illustration of uncorrelated (left) and correlated (right) combinatorial background.

Unfortunately there is no available information to distinguish the lepton pairs coming from the same virtual photon. Therefore it is needed to create all possible unlike sign pairs event-by-event and estimate the combinatorial background due to the combination of leptons coming from different virtual photons.

The combinatorial background arises from two different situations, as illustrated in Fig. 5.1:

- The uncorrelated background (left part of Fig.5.1) is due to the combination of electrons and positrons coming from the decay of different particles. This kind of background is characterized by the absence of particular kinematical correlation between the leptons. These dielectron pairs can be either produced directly from a virtual photon at the electromagnetic vertex or via the conversion of real photons.
- The correlated background (right part of Fig.5.1) is due to the decay of one single particle into 2γ or into $\gamma\ e^+e^-$ (like $\pi^0/\eta \to \gamma\gamma$ or $\pi^0/\eta \to \gamma e^+e^-$) and the subsequent conversion of one or two γ. Therefore, pairs of leptons can be produced from the decay of the same particle, but from two different real or virtual photons. In this case, the leptons are correlated in the phase space.

The main source of photons and lepton pairs in our experiment are neutral pions, that decay into 2γ with a probability of 98.8% or via Dalitz decay in γe^+e^- , with a probability of 1.2 %. Since the probability of photon conversion is of the order of a few %, mainly due to the material budget in the target region or in the RICH radiator, one can clearly realize that photon conversion is a major background, which will contaminate the signal pairs and contribute to the combinatorial background.

Due to the low multiplicity of particles in our reaction, we expect most of the combinatorial background to be of the correlated type and to arise from the combination of two real or virtual photons from the π^0 decay. The production of $2\pi^0$ production is about 13% of the inclusive π^0 production cross section and hence can still contribute to the uncorrelated background. As can be deduced from Table 8.2, where the cross sections for the different dilepton sources are listed, the production of η is much lower. The baryon Dalitz decay, either directly from baryons produced in the s-channel or via $\Delta(1232)\pi$ contribution to the e^+e^- production, is almost two orders of magnitude smaller than the π^0 decay. Baryons can also emit real photons via radiative decays, with branching ratios roughly two orders of magnitude larger than for virtual photons, but this will also be a much smaller contribution than the one from π^0 decays.

Finally, we expect our combinatorial background to consist of two main contributions:

- An uncorrelated background coming from the combinations of leptons produced from two different π^0s, either after Dalitz decay or after 2γ decay followed by conversion;
- A correlated background coming from the decay of one single π^0 decaying into 2γ or γe^+e^-. In the first case, each lepton comes from the conversion of a different photon. In the second case, one lepton comes from the conversion of the real photon and the other one is produced directly from the virtual photon.

5.1.2 Combinatorial background estimation

The combinatorial background can be estimated based on the contribution of lepton pairs of the same sign. In the full phase-space, *i.e.* not considering the acceptance and the efficiency of the detectors, no difference is indeed expected between electrons and positrons, as they are always emitted in pairs. What is less straightforward to understand is which combination of like-sign pair spectra is the most appropriate for the background estimate. This topic was debated in [123] and [124] and the authors converged to the ”geometrical mean formula”:

$$BG_{-+} = 2\sqrt{FG_{++}FG_{--}} \tag{5.1}$$

where BG_{-+} is the combinatorial background to be subtracted from the opposite sign pair yield and FG_{++} and FG_{--} are the yields of the same sign pairs. The factor 2 arises from the fact that, for two correlated e^+e^- pairs, there are one e^+e^+, one e^-e^- and two uncorrelated e^+e^- pairs. To derive Eq. 5.1, it is implied that the reconstruction efficiency of like sign and unlike sign pairs is identical: $\epsilon_{+-} = \epsilon_{--} = \epsilon_{++}$. However this is not exact in general. Indeed, some discrepancy between the acceptance and efficiency for particles with positive and negative charge can arise when a magnetic field is used in the detection system. Therefore a generalization of the formula is in principle required leading to:

$$BG_{-+} = \frac{2\epsilon_{+-}}{\sqrt{\epsilon_{++}\epsilon_{--}}}\sqrt{FG_{++}FG_{--}} \tag{5.2}$$

The new factor

$$k = \frac{\epsilon_{+-}}{\sqrt{\epsilon_{++}\epsilon_{--}}}$$

in Eq. 5.2 can be estimated using simulation. To control the bias due to the possible model dependence of the effect, this factor can also be checked using the event mixing approach, that will be briefly discussed afterwards.

For the case of the analysis of the Au-Au system at 1.23A GeV by the HADES collaboration [115], for which the S/B ratio was rather low, a careful study of this k factor was carried, the minimum value of this k factor (around 0.75 for central collisions) was reached at very low values of invariant masses where the S/B ratio was largest. The systematic effect related to the k factor was therefore limited for the HADES experimental set-up. As will be shown in Sec. 5.4, the combinatorial background is rather small in our experiment and assuming $k = 1$ is accurate enough for our analysis.

Due to the low level of combinatorial background and the low statistics, as we will see, for some bins, one of the numbers FG_{++} and FG_{--} is equal to zero. In this case, the arithmetical mean

$$BG_{-+} = FG_{++} + FG_{--}$$

is used.

The second commonly used method to estimate the combinatorial background is the event mixing technique, where it is estimated by mixing particles from different events. This procedure offers the advantage of large statistics due to multiple usage of electrons from a given event. In this approach the correlation between the particles, if any, is destroyed. This makes this method impossible to be used when most of the background is correlated as it is the case in my analysis. For this reason, only the method using the geometric or arithmetic mean of like sign pairs was chosen to estimate the combinatorial background.

5.2 Photon conversion

It is clear from the discussion in Sec. 5.1.1 that the photon conversion gives a large contribution both to the correlated lepton pairs and to the combinatorial background, so it is important to find analysis cuts to suppress this contribution as much as possible. In the conversion process, e^+e^- pairs are produced in general with a small opening angle. When both leptons from these so-called ”close pairs” are detected, these pairs can be suppressed using a threshold on the opening angle, as will be explained below. However, it is important to also avoid that the reconstructed tracks from these close pairs contribute to the combinatorial background. The background rejection strategy therefore includes two steps: the first step consists in removing single tracks where the partner was closeby, even if was not fully reconstructed (single lepton cuts), the second step consists in rejecting reconstructed close pairs (pair cuts).

5.2.1 Single lepton cuts

Due to the small opening angle of the conversion pairs and the limited detector resolution, electrons and positrons are often not resolved as separate tracks in the RICH detector or in the inner MDC detectors. The ring finder procedure is indeed not able to resolve rings which are closer than 4°. The backtracking procedure is more efficient in this respect (see Sec.3.8.5), but still a lot of tracks share the same RICH pads. Unresolved close tracks that are identified as one lepton track should be ideally rejected from the analysis before further combinatorics.

Close tracks can also lead to partially reconstructed tracks. Conversion leptons produced between the target and the RICH mirror will indeed be reconstructed only if they have a momentum large enough to reach the outer chambers, after being bent by the magnetic field. This minimum momentum is of the order of 50 MeV/c. If the particle momentum is lower, two segments can be reconstructed before the magnetic field, but only one outer segment and one META hit can be found for this pair. Only one of the inner segments before the magnetic field is then matched to the outer segment and to the META hit and the other remains as "unfitted". To reject such partially recognized lepton pairs, we search in the neighborhood of the track for the closest segment (either belonging to a track or not) before the magnetic field. If it is in the angular range specified by the user (see Sec. 5.4), the fully reconstructed electron track is identified as being part of a "close pair" and it is therefore rejected and hence will not contribute to the combinatorial background. If the segment found is part of a track, then this track is also suppressed. This procedure was implemented for the Au+Au experiment and was found to be very efficient for reducing the combinatorial background.

5.2.2 Pair cut

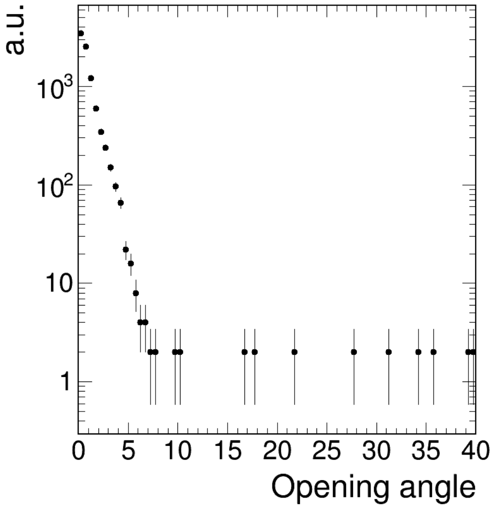

Figure 5.2: Opening angle (degrees) for e^+e^- pair in a simulation of photon conversion for photons produced by the decay of π^0 in the reaction $\pi^- p \to n\pi^0$ at an incident momentum of 0.69 GeV/c.

The previous cuts are applied on the single track level to remove from the lepton candidate list tracks which are likely to be due to the conversion process. However, the analysis also includes an "opening angle cut" (in principle more strict than the close pair cut) which suppresses the reconstructed conversion pairs, which survived the previous cuts.

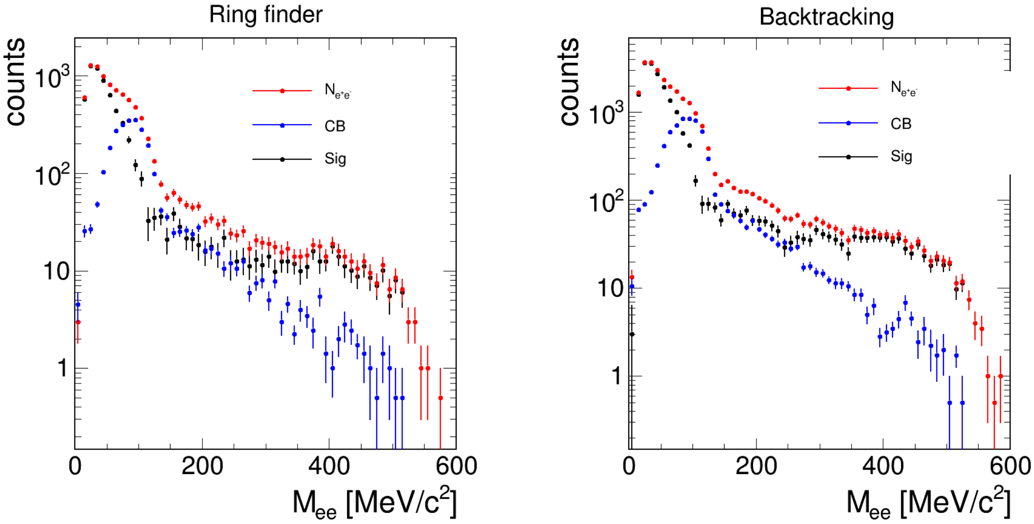

Figure 5.3: Invariant mass of e^+e^- pairs with an opening angle larger than 9° are shown for the standard ring finder procedure (left) and the backtracking method (right). The total yield is shown as red dots, the combinatorial background as blue dots and the signal pairs as black dots.

An important difference is that this "standard" cut is not recursive, which means that it rejects only the pairs with an opening angle smaller than the threshold, but the tracks can still be combined with other tracks if the opening angle of the new pair is larger than the threshold. In Fig.5.2 the opening angle distribution for lepton pairs coming from the conversion of photons from the decay of π^0 produced in the simulation of the $\pi^- p \rightarrow n\pi^0$ reaction at an incident momentum of 0.69 GeV/c is displayed. It can be observed that the fraction of conversion pairs with opening angle larger than 9 degrees is very small, therefore this value is chosen as threshold value. Considering the relative branching ratios for $\pi^0 \rightarrow 2\gamma$ (98.8 %) and $\pi^0 \rightarrow \gamma\ e^+e^-$(1.2 %), the low multiplicity of π^0 and the conversion probability of a few %, the overall production of conversion pairs is expected to be less than two orders of magnitude larger than correlated lepton pairs. A negligible conversion pair background is therefore expected in the e^+e^- sample after this cut. This cut affects only the signal yield in the region of small invariant masses (M<140 MeV/c^2).

5.3 Purity of the e^+e^- signal

After having subtracted combinatorial background and having suppressed conversion pairs, a remaining background can be due to the combination of leptons and hadrons or fake tracks, since the purity is not 100 %, hadrons and fake tracks can be reconstructed due to the wrong combinations of detector hits. The case of two fake tracks can be neglected. To get some knowledge about the origin of the background in my analysis some simulation were made using a cocktail of Dalitz decay of π^0s and ηs. The fraction of pairs created by the combination of a fake track and a lepton is very small. Pairs formed with a hadron are also very unlikely and this confirms that the method used for lepton identification gives as result a good purity.

5.4 Results for inclusive analysis

We discuss the results obtained in the inclusive analysis, where only the detection of one e^+e^- pair is requested, without any request about the other detected particles. First, we compare the results from the standard ring finder (see sec. 3.6 and from the backtracking analysis (see Sec. 3.8.5), which are shown in the following part, underlining the difference in the efficiency. Then, we discuss the effect of the close neighbor cut in the case of the backtracking analysis.

5.4.1 Comparison of ring finder and backtracking analysis

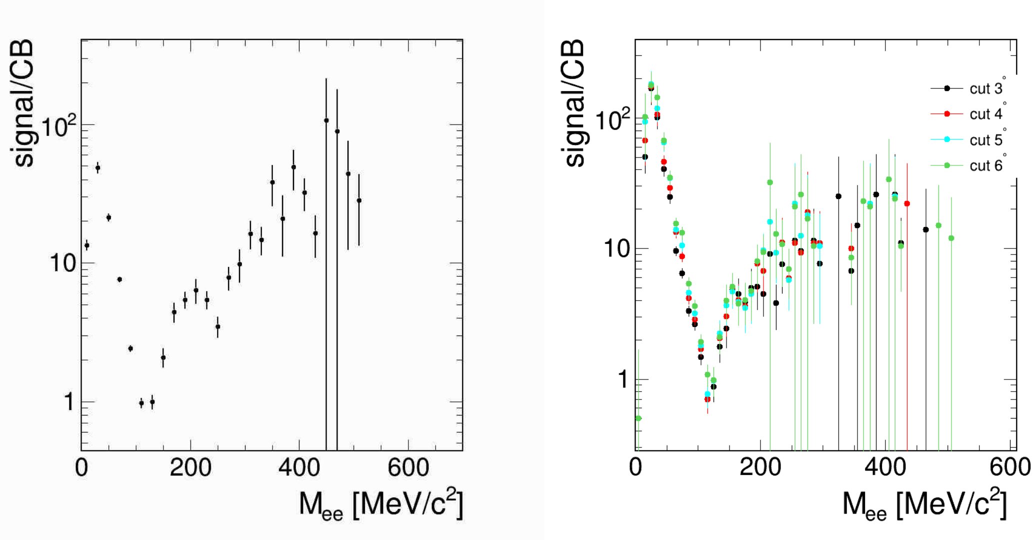

Figure 5.4: Signal over background ratio as a function of the invariant mass for e^+e^- pairs with an opening angle larger than 9° in the backtracking analysis. Left: without close neighbor cut. Right: with different thresholds for the close neighbor cut.

The e^+e^- invariant mass spectra obtained for the standard Ring finder analysis and for the backtracking method are shown respectively in the left and right parts of Fig. 5.3, together with the combinatorial background (CB) as defined in Sec. 5.1.2. The signal for correlated e^+e^- pair deduced after subtraction of the CB is also shown. It can be observed that the CB is maximum for invariant masses close to 110-120 MeV/c^2. This is due to the dominant correlated background contribution from the decay of one π^0(see Sec.5.1.1). The long tail is due to the uncorrelated background from the combination of leptons from virtual photons or real photon conversion from two different π^0.

The advantage of the backtracking method is clearly demonstrated by the comparison of the two pictures. The yield of e^+e^- pairs is increased by roughly a factor 3 and the CB is strongly reduced. The backtracking analysis will therefore be favored in the following for the extraction of the results, as it allows to reduce statistical errors as well as systematic errors due to the CB subtraction.

The signal over background ratio (S/B) is shown in Fig. 5.4 left for the backtracking method. The S/B has a sharp minimum (close to 0.2 around 115 MeV/c^2), but, it is larger than 1 for invariant masses lower than 70 MeV/c^2 or larger than 140 MeV/c^2.

5.4.2 "Close neighbour" cut

In the case of the Au+Au analysis, the S/B was lower by roughly one order of magnitude and the reduction of close pairs by means of the "close neighbor" rejection was shown to be very crucial to reduce the combinatorial background, as studied in great detail in [115]. A careful study of the optimum cut on this angle (for the definition see 5.2.1) by checking

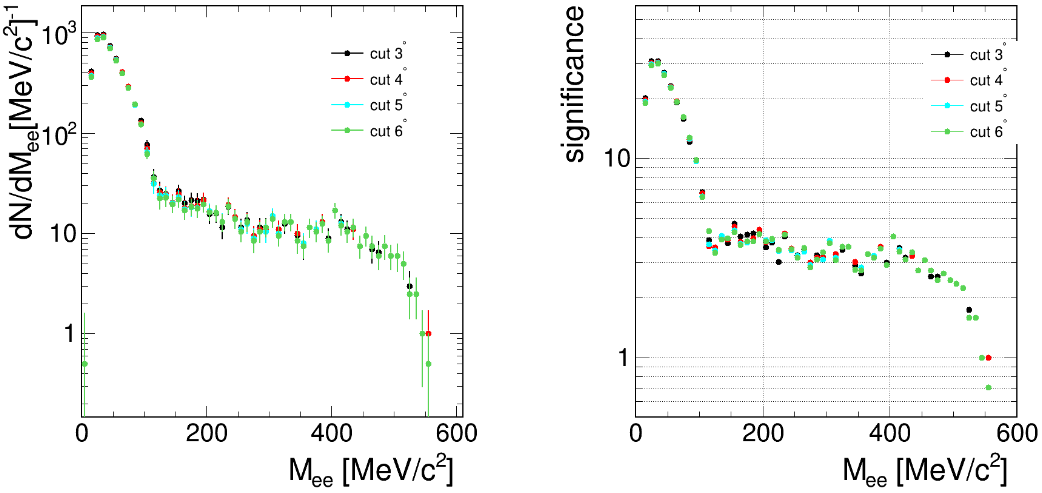

Figure 5.5: Invariant mass (left) and significance (right) are shown as a function of the invariant mass of the e^+e^- pair for different cuts on the angle to the closest segment.

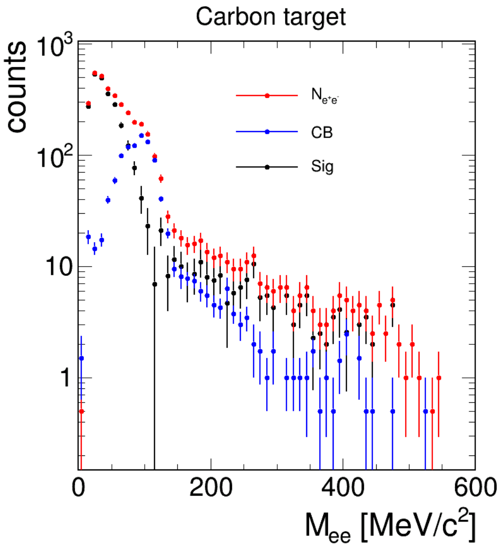

Figure 5.6: Same as Fig. 5.3 Right, but for the carbon target.

the significance of the measured yield was carried out:

$$Sign = \frac{S}{\sqrt{S+2B}}$$

The S/B distributions are shown for different values of the close neighbor cut in the right panel of Fig. 5.4. The invariant mass and significance are also displayed in the left and right panels of Fig. 5.5, respectively. We can see that the total yield is much reduced if the cut is applied (about a factor 3). Besides, when the cut is applied, there is no large difference for the different cut values. The S/B is only slightly improved when the cut increases between 3 and 7° and the significance is almost independent of this cut. This result is very different from the Au+Au experiment, where effects of the order of 20% on the significance could be observed when the cut was varied from 3 to 6°. We still set the value of the cut at 6° since it corresponds to the largest S/B. It is indeed better to maximize the S/B ratio, in order to reduce the effect of the systematic errors on the CB estimate, due, in particular to the different acceptance for the different types of lepton combinations (see Sec.5.1.2, even if the effect is expected to be small).

The spectrum measured on the carbon target (Fig.5.6) has a similar shape as the one measured on the polyethylene target with the characteristic π^0 peak at small invariant masses. It can be however observed that the statistics is much lower than the one recorded on the polyethylene target, which will induce large statistical errors for the subtraction of carbon yields from polyethylene measurements.

5.5 Results for exclusive analysis

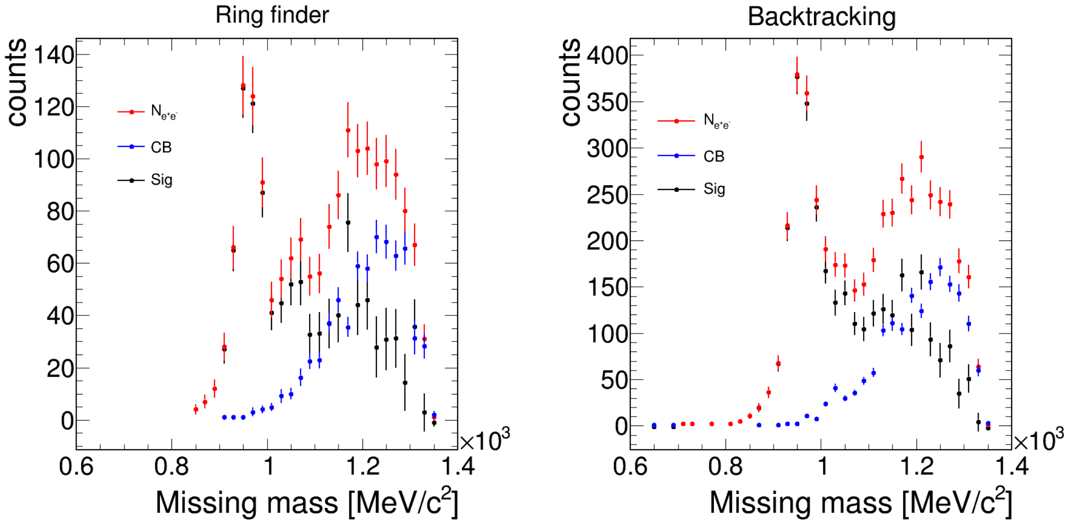

Figure 5.7: Missing mass for the reaction $\pi^- p \rightarrow e^+e^-$X for the ring finder analysis (left) and the backtracking (right) in the $M_{ee} > 140MeV/c^2$. The total yield is shown as red dots, the combinatorial background as blue dots and the signal pairs as black dots.

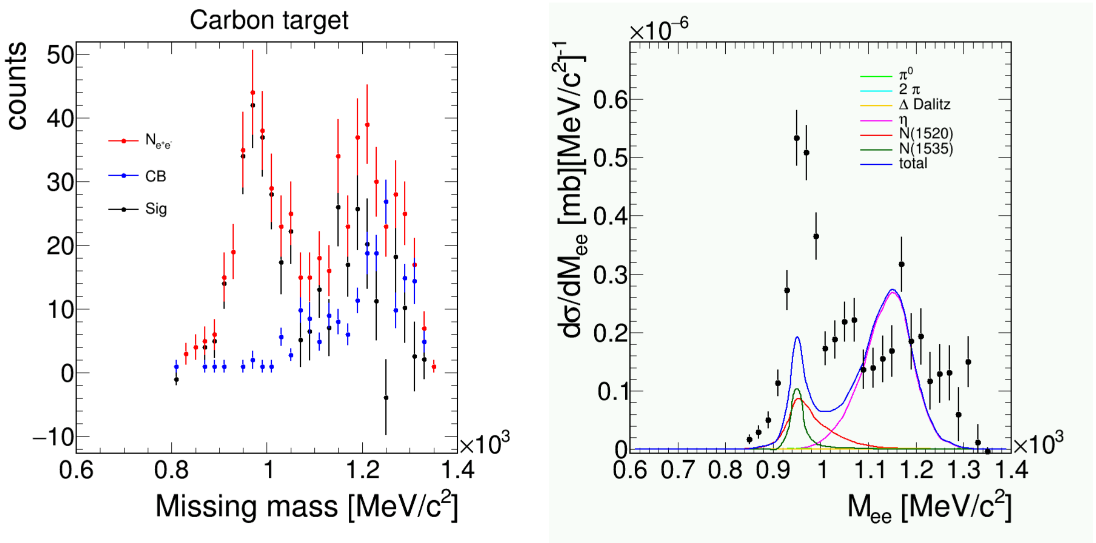

Figure 5.8: Left: Same as Fig. 5.7 for the carbon target and the backtracking method. Right: Missing mass measured on the polyethylene target compared to the simulation.

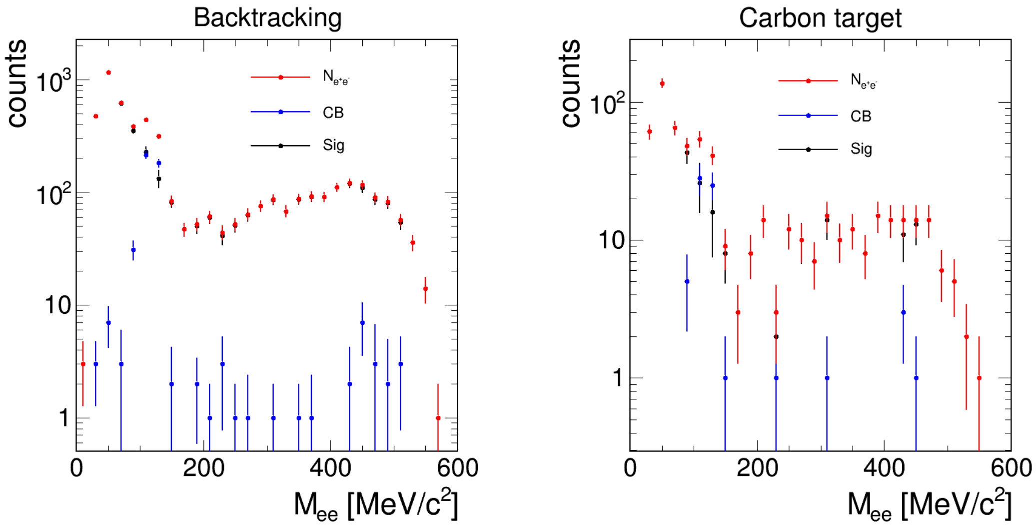

Figure 5.9: Invariant mass spectra for e^+e^- pairs after selection on the missing mass for the $\pi^-p \rightarrow ne^+e^-$X reaction (900 MeV/$c^2$ <MM< 1030 MeV/c^2). Left: polyethylene target. Right: carbon target.

In addition to the inclusive invariant mass spectra shown in the previous section, we are also interested in the exclusive analysis of the channel $\pi^-p \rightarrow e^+e^-n$. Since the neutron cannot be measured, the analysis consists in selecting events having a missing mass close the neutron mass. It is obvious from the inclusive analysis that the dominant source of dielectrons at small invariant mass is the π^0 Dalitz decay ($\pi^0\rightarrow \gamma e^+e^-$). In this case, a neutron and a photon are not detected. The missing mass is therefore expected to be larger than the neutron mass. However, the energy of the photon is most of the time rather small and the resolution is not sufficient to distinguish the final states $n\gamma e^+e^-$ and ne^+e^-. Therefore, this analysis is performed for invariant masses M$_{ee}$ of the e^+e^- pair larger than the π^0 mass, where the π^0 Dalitz decay does not contribute to the e^+e^- yield.

In the Fig. 5.7, one can see the spectrum measured for the polyethylene target shown for values of invariant masses larger than 140 MeV/c^2 for the ring finder in the left part and for the backtracking in the right part. A clear peak can be observed in a region compatible with the neutron mass which is clearly due to the $\pi^-p \rightarrow ne^+e^-$ reaction in case of interaction with a proton or to the quasi-free $\pi^-{}'p' \rightarrow e^+e^-\ n$ reaction in case of interaction with a proton in the carbon target. Again, the number of reconstructed tracks is higher by a factor close to 3 in the case of the backtracking, with about 1500 events selected for invariant masses larger than 140 MeV/c^2 and missing masses in the range 900 MeV/c^2 <MM< 1030 MeV/c^2. . The CB is higher in the case of the backtracking, however the combinatorial background is very low in the region where the missing mass is close to the neutron mass and it increases for larger missing masses. This is expected since the source of combinatorial background for invariant masses above the π^0 mass is the uncorrelated background from $2\pi^0$ decays where at least two photons and two leptons are missing and the background coming from the Dalitz decay of η in which 1 photon is missing. Under the neutron peak, the combinatorial background is only a few %. Therefore, the errors related to the subtraction of this background are negligible with respect to the statistical errors.

We can see that the position of the neutron peak does not perfectly correspond to the nominal value of the neutron mass but it is shifted towards higher values of missing mass. Part of the effect might be due to the fact that, while the energy loss by ionization is applied to the particles in HADES, the energy of electrons is also affected by the bremsstrahlung process, which is important for our thick polyethylene or carbon targets. Second, interactions with bound protons can lead to a shifted missing mass. This is confirmed by Fig. 5.8 (left) which shows that the missing mass distribution measured on the carbon target is indeed shifted towards larger values. The comparison to simulations including the bremsstrahlung effect and interactions with both protons and carbon nuclei using the hypothesis of a quasi-free interaction with carbon nuclei described in the participant-spectator approximation is shown in Fig. 5.8 (right). The ingredients of the simulation will be discussed in more detail in Sec. 8.2.8, but it can be observed that the position of the neutron peak is correctly described.

Most of the width of the neutron mass peak is due to the Fermi momentum of protons in the carbon nucleus, but the pion beam momentum distribution also plays a significant role. One can use the pion beam tracker in order to calculate the missing mass for each event using the reconstructed pion momentum. The width is reduced in a significant way. However, the efficiency of the pion tracker is only about 70% , therefore we rather chose to calculate the missing mass with the average pion momentum, since the resolution is still good enough to isolate the neutron peak. After selecting the events via the missing mass cut we can look at the invariant mass distribution for these pairs. The results are shown in the left and right parts of Fig.5.9 for the polyethylene and carbon targets respectively. This confirms that the combinatorial background is very small and the additional close pair candidate cut is not needed. The statistics is low, especially for the carbon target, which will hinder the precision of the carbon subtraction, as will be shown in the following.

5.6 Carbon subtraction

5.6.1 Relative carbon/polyethylene target normalization

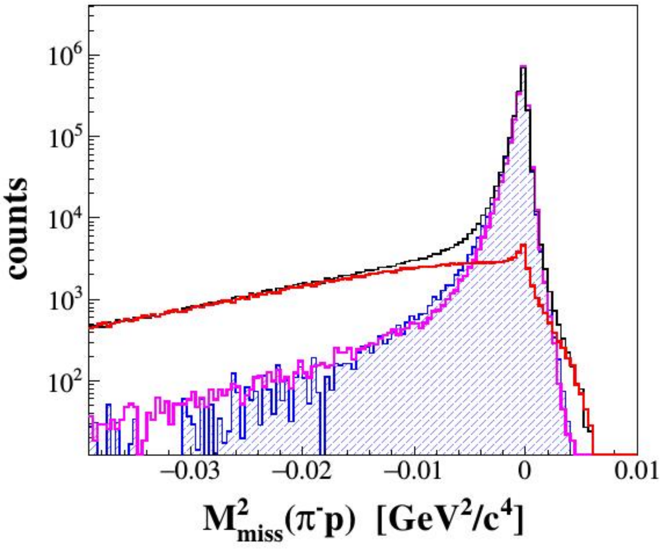

Figure 5.10: Missing mass for $\pi^- p$ events after selection of elastic scattering by angular correlation. The black and red dots correspond to data obtained respectively for the CH2 and C targets and the blue points are obtained after the subtraction. The yield obtained for the carbon target is normalized with respect to the CH2 target in order to match the left tail of the missing mass distribution.

In order to study the production of e^+e^- in the π^-p reaction from the measurement on the polyethylene target, the contribution from interactions with carbon nuclei needs to be subtracted. This can be done using the measurements performed on the carbon target. The relative normalization of carbon and polyethylene measurements has been studied in great detail by the Cracow team. The procedure which has been used is based on the comparison of missing mass spectra calculated for the reaction π^-p→ π^-p X both on the CH2 and carbon targets. As shown in the Fig.5.10 the missing mass spectra measured on the polyethylene target differ from the one measured on the carbon target by the presence of a very narrow peak close to zero, corresponding to the π^-p elastic scattering. The tail at large negative missing mass squared is due to the contribution of quasi-free elastic scattering on a bound proton, which is shifted towards negative values because of the binding energy and which is very broad due to the Fermi momentum distribution. Since the tail at large negative missing masses squared in the polyethylene data can only be due to interactions with the carbon nuclei, the yield on the carbon target is then simply normalized so that it matches the tail of the polyethylene data. The resulting data points, corresponding to a measurement on a proton target are shown as blue points in Fig. 5.10. One check of the consistency of the normalization procedure is given by the fact, that, after subtraction of the carbon contribution and after selection of the elastic scattering using angular selection cuts (see [114]), the missing mass distributions are very

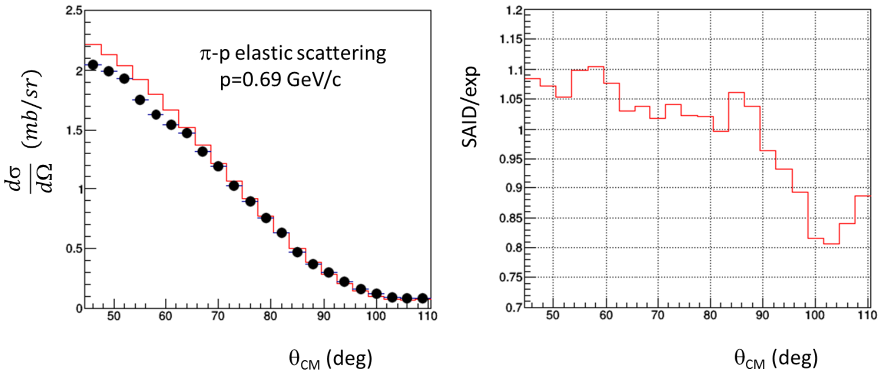

Figure 5.11: Left: Angular distribution for $\pi^- p$ elastic scattering at an incident pion momentum of 0.69 GeV/c. Data points from the HADES experiment after normalization are shown as black dots and the SAID result is shown as a red curve. Right: ratio between SAID predictions and experimental HADES yields after normalization.

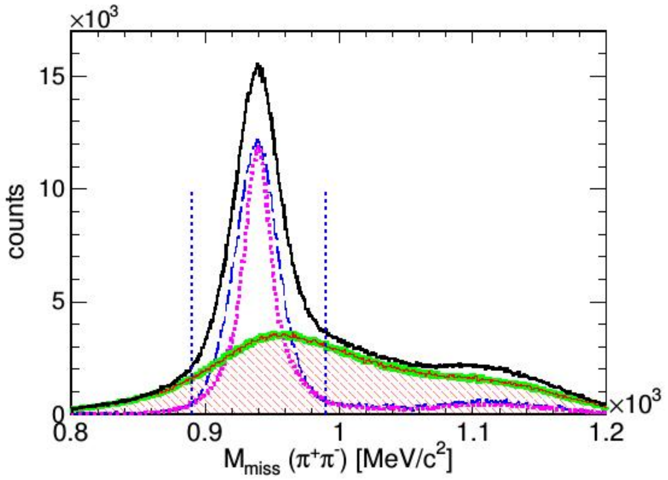

Figure 5.12: Missing mass for the $\pi^- p$→ $\pi^+\pi^-$X reaction.

well reproduced by a simulation of the π^-p elastic scattering including all experimental effects . The shape of the angular distribution for these π^-p elastic events, as shown in Fig. 5.11, is demonstrated to be in good agreement with the SAID data base. In addition, using the same relative normalization factors, the missing mass for $\pi^-\pi^+$events measured on the polyethylene targets can also be consistently described by a contribution from interactions with protons, with two peaks corresponding to a missing neutron and to missing neutron and one pion respectively (Fig. 5.12). So, the relative normalization of carbon and polyethylene measurements using the elastic scattering is quite precise and will be used in our analysis to study the ratio of carbon to proton cross sections and, when possible, to subtract the carbon contribution.

5.6.2 Cross section ratios

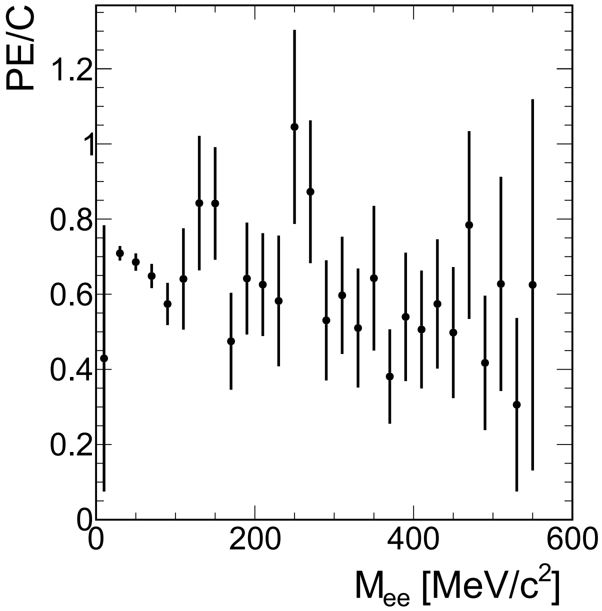

Figure 5.13: Ratio of yields measured as a function of the e^+e^- invariant mass for carbon and polyethylene targets after relative carbon/polyethylene normalization.

The ratio of yields measured in e^+e^- invariant mass bins of 10 MeV width for carbon and polyethylene targets is displayed in Fig.5.13. With the normalization that we used, this ratio reads:

$$R = \frac{\sigma_C}{\sigma_{CH2}} = \frac{\frac{1}{2}\sigma_C}{\frac{1}{2}\sigma_C + \sigma_H} \tag{5.3}$$

$$\tag{5.4}$$

Therefore,

$$\frac{\sigma_C}{\sigma_H} = \frac{2R}{1-R} \tag{5.5}$$

The mean ratio is close to 2/3, which corresponds to a cross section ratio σ_C/σ_H of a factor 4. Despite the small statistics, a tendency to a smaller ratio can however be observed at larger invariant masses. Table 5.1 shows the ratios R and σ_C/σ_H extracted in three invariant mass bins:

	0-140 MeV/c^2	140- 300 MeV/c^2	300-600 MeV/c^2
R $= \sigma_C/\sigma_{CH2}$	0.70 ± 0.01	0.71 ± 0.05	0.53 ± 0.05
R$^{'}$ $= \sigma_C/\sigma_H$	4.67 ± 0.22	5.11 ± 1.22	2.30 ± 0.46

Table 5.1: Ratios of measured cross sections in the carbon and polyethylene targets for three e^+e^- invariant mass bins and corresponding ratios of cross sections on carbon and proton nuclei.

The ratios of cross sections between carbon and hydrogen can be interpreted as an effective number of participating protons in the carbon nucleus, which depend on the reinteractions and absorption processes in each channel. Indeed, as discussed in Sec. 1.5.2, neutrons do not contribute significantly to the e^+e^- production. For the η production, phase space effects due to Fermi momentum are also important, as will be discussed in Sec. 8.2.4 since the energy is close to threshold.

5.7 Normalization

For the normalization of the yields measured in our experiment, we use the π^-p elastic scattering events, which, can be measured in the HADES experiment over a rather large range of angles in the π^-p center-of-mass. The measured yield is shown in Fig. 5.11 in comparison with the one obtained in a simulation based on differential cross sections taken from the SAID analysis, which is a Partial Wave Analysis of existing data [71]. The simulation includes all experimental effects. As mentioned above, the shape of the angular distribution is rather well reproduced, although the experimental distribution is slightly broader. The normalization factor is calculated as the averaged ratio of data to the SAID predictions in the angular range of the HADES experiment and the data are presented after including this factor. The precision of the SAID analysis is given as 2%, so the main uncertainty to the normalization comes from the dependance of the ratio as a function of the angle. The normalization factor is obtained by a reference to a simulation including all experimental effects, so it also compensates possible errors in the reconstruction of elastic yields which were not taken into account in the simulation (e.g. inaccurate global tracking inefficiency, or pion/proton identification). The systematic error related to the normalization is therefore dependent on the channel and will be estimated for the e^+e^- production channel in Sec. 6.3.

Remarks on absolute normalization

In principle, an absolute normalization of our experiment could have been calculated using the counts in the START detector located in the beam and the known thickness of our target. However, a contamination from electrons produced in the pion production target of about 10% is expected (see Sec. 3.2.2). Those electrons gives a signal in the START detector but have a very small interaction probability in the target. In addition, the START detector covers a larger area than the target. According to simulations based on a theoretical description of the beam line, and taking into account multiple scattering in the different detectors of the beam line, only 66% of the beam particles hitting the START detector also hit the target [120]. The experimental measurement of the fraction of START events interacting with the target was consistent, in average within 15% with this number. However this fraction was found to fluctuate with time, which might be due to fluctuations of the secondary beam profile. In these conditions, it is difficult to rely on a normalization based on measurements in the START detector. So, in the following, we use normalization factors derived from the comparison to the SAID data base.

Chapter 6

Efficiency corrections and systematic errors

The spectra presented in the previous chapter are affected by the detector acceptance and the inefficiencies, but also by the lepton reconstruction and identification inefficiency. All the detectors, whatever the mechanism for particle detection is used (gas ionization, electron-hole pair in semiconductor, excitation in a scintillator material, etc.) are based on stochastic processes which have a probability to occur lower than 1. Moreover, also tracking and clustering algorithms do not have a 100% efficiency. The latter affects in a dramatic way the event reconstruction in heavy-ion collisions where the density of tracks is very high. In addition, the measurements and reconstruction methods are affected by uncertainties. This directly influences the distribution of physical observables, but also impacts the efficiency of analysis cuts, which are needed to select a specific reaction channel. The yield of particles populating the tails of the distributions which are excluded by analysis cuts indeed strongly depends on the detector resolution effects. In order to compare the experimental results with theoretical predictions a method needs to be established to correct for these effects.

The aim of the current analysis is to present the results for e^+e^- pair production. Two kinds of approaches can be considered: correcting the single tracks and then combining them to pairs or correcting spectra directly on the pair level. The two approaches will be discussed. In the first case the idea is that a particle can be described with three variables: momentum, polar angle (θ) and azimuthal angle (ϕ), then a correction factor is calculated in each bin of a three dimensional histogram and finally it is used for each particle of a pair as a weight. In the following section a description of the single lepton efficiency is given.

6.1 Single lepton correction

The single lepton efficiency is estimated via Monte Carlo simulations. Using the Pluto event generator a sample of so-called ”white leptons”, having uniform distributions in momentum (in the range between 0 and 700 MeV/c), in $cos\theta$ and in ϕ are generated. The estimation was realized using a simulation with 10 millions of events for electrons and positrons. For each sample, six leptons are generated per event, one for each of the six HADES sectors. This feature is implemented in order to minimize the number of events needed for the calculation of the efficiency and at the same time to avoid the overlap of tracks that can affect the efficiency. All these tracks are then passed through the detector using the GEANT3 package to describe their interactions with the different detector materials and the possible production of secondary particles. Finally the output from GEANT3 is analyzed using the HYDRA framework with the same algorithms used for the experimental data. A key feature at this step is that the digitizers have to reproduce very well the detector response in order to estimate the efficiency in a reliable way. In previous HADES data analysis where the multiplicity of particles was higher (up to 300 for Au+Au), the white lepton tracks were also embedded into real data in order to take into account the effect of track multiplicity on particle reconstruction. In our analysis this was not necessary, since the average multiplicity is so low, that effects of the presence of other particles can be completely neglected.

Once the DSTs of the white leptons are produced, these files are analyzed using the same procedure and the same selection cuts as applied for the experimental data in terms of track quality and of lepton identification. The simulated particles are stored at different levels of the analysis in three dimensional histograms as a function of momentum, θ and ϕ.

- At the first level, so-called "4π", all generated particles are considered with their original kinematical properties.
- The second level, so-called "accepted" or "acc", corresponds to particles in the HADES geometrical acceptance, which is defined as particles crossing at least four MDC layers per chamber and one hit in the RPC detector or in the TOF detector.
- The third level, so-called "reconstructed" or "reco" is the final step of the analysis where particles are reconstructed and identified. Only simulations in this last step can be compared to the experimental data.

Combining the "acc" and "4π" information an acceptance factor can be defined as:

$$\epsilon_{acc}(p,\theta,\phi) = \frac{N_{acc}(p,\theta,\phi)}{N_{4\pi}(p,\theta,\phi)}.$$

This factor can be used to filter the events generated by theoretical models, but not to correct the data. The acceptance factors for the two leptons of one pair are indeed highly correlated, so the acceptance corrections for a pair cannot be deduced from white leptons acceptance factors. A big problem is that there bins with 0 acceptance, that cannot be corrected. Conversely, the loss of electrons and positrons between the "accepted" and "reconstructed" steps is uncorrelated. Moreover efficiency is seldom 0 within acceptance. Therefore, the efficiency factor calculated with "white leptons" as:

$$\epsilon_{eff}(p,\theta,\phi) = \frac{N_{reco}(p,\theta,\phi)}{N_{acc}(p,\theta,\phi)} \tag{6.1}$$

and can be used as a correction to be applied to each event in the bin (p,θ,ϕ). Since in the simulation, both the "reconstructed" values of the momentum and angles and the initial ("ideal") values are available, one can use one or the other to calculate the efficiency.

In previous dilepton analysis in the HADES experiment, the ideal values were chosen. In our analysis, both approaches will be followed.

6.1.1 Correction using the ideal values of momentum, θ and ϕ angles

To calculate the efficiency as a function of the ideal values, the histogram for the reconstructed particles is filled with the ideal values of the momentum and the angles and the efficiency can be calculated as the ratio between the $N_{reco}(p,\theta,\phi)$ distribution for the reconstructed particles to $N_{acc}(p,\theta,\phi)$ distribution for the particles crossing the HADES acceptance:

$$\epsilon_{eff}(p,\theta,\phi) = \frac{N_{reco}(p_{ideal},\theta_{ideal},\phi_{ideal})}{N_{acc}(p_{ideal},\theta_{ideal},\phi_{ideal})}. \tag{6.2}$$

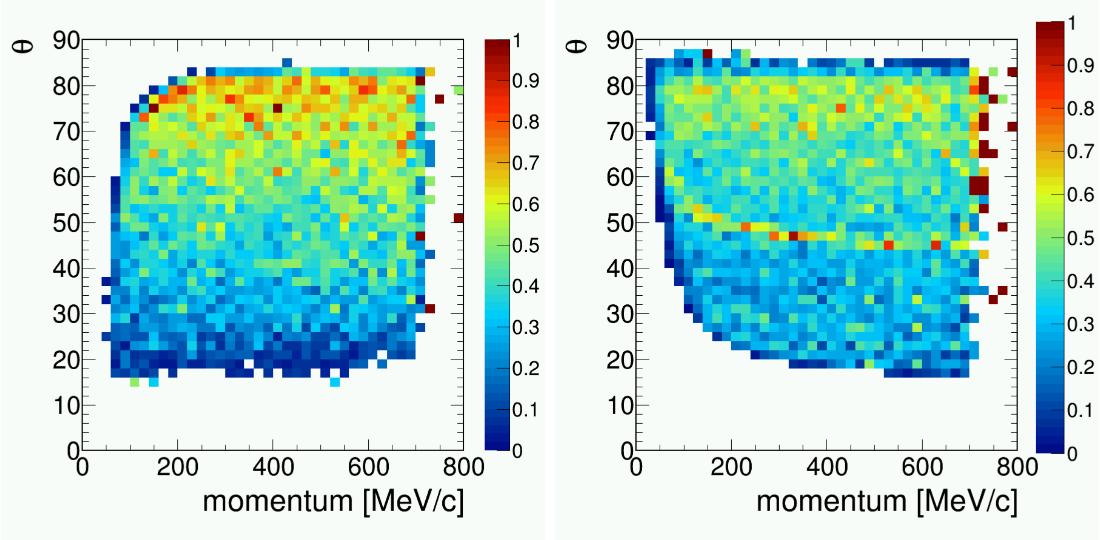

Figure 6.1: Efficiency values as a function of polar angle and momentum for electrons (left) and positrons (right).

To avoid fluctuations due to the limited statistics at the edges of the acceptance, the efficiency matrices are smoothed applying the Savitzky-Golay noise filter. The projections in the (θ, p) plane of the efficiency matrices produced with the mentioned procedure are shown in Fig. 6.1 (left) for the electrons and in Fig. 6.1 (right) for the positrons. As a general trend, the efficiency increases with polar angle, due to the higher number of Cherenkov photons produced in the RICH detector and to the higher efficiency of the TOF detector with respect to the RPC. The acceptance is significantly larger at momenta below 300 MeV/c for electrons than for positrons, since electrons are bent in the magnetic field towards the detector, while positrons are bent towards the beam axis, where there is no coverage. The efficiency below 30° is only of the order of 20-30%. Above 60°, it reaches 70-80%.

6.1.2 Self-consistency check

To check the validity of the efficiency corrections based on these matrices, the first fundamental ”self-consistency” check consists in verifying for the ”white leptons” that the corrected yields are consistent with the yields in acceptance. This can be checked by calculating the ratios N_{corr}/N_{acc} between the corrected yields and yields in geometrical detector acceptance in the same bin and by checking that it is consistent with the unity value. The results are shown as a function of momentum, polar angle and azimuthal angle, respectively in Fig. 6.2, Fig. 6.3 and Fig. 6.4 for the electrons and positrons. One can see that all the ratios are very close to 1. This just proves that no error was introduced by using different codes. The small deviations from 1, which are visible in the plot of the momenta valid for momenta $<$ 100 MeV/c and at the edges of the sectors as a function of the azimuthal angle are due to the fact that there are areas for which the geometrical acceptance of the tracks is different from 0, but no tracks at all are reconstructed there due to the lack of efficiency. This demonstrates that when comparing the data to simulations, it is important to restrict to regions where the efficiency is above a certain threshold. We use a 5% threshold.

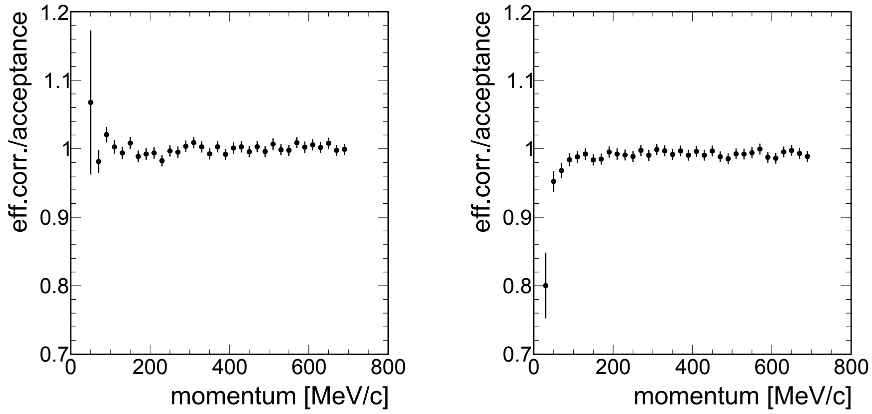

Figure 6.2: Ratio between efficiency corrected yields and yields in acceptance as a function of the ideal momentum for electrons (left) and positrons (right) generated with flat distributions.

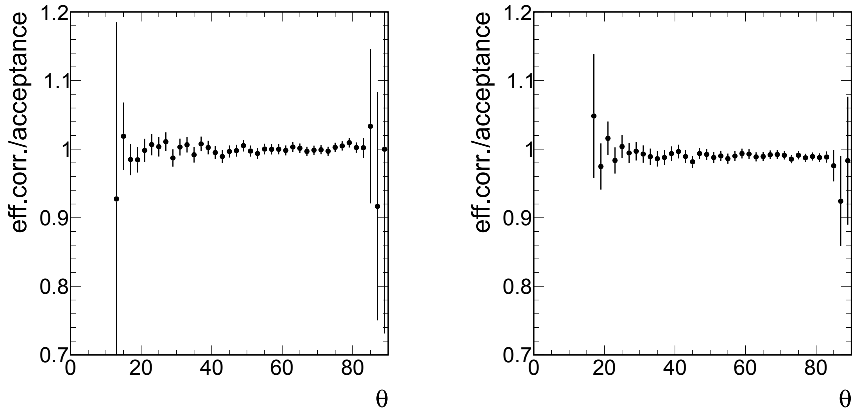

Figure 6.3: Same as 6.2, as a function of the polar angle.

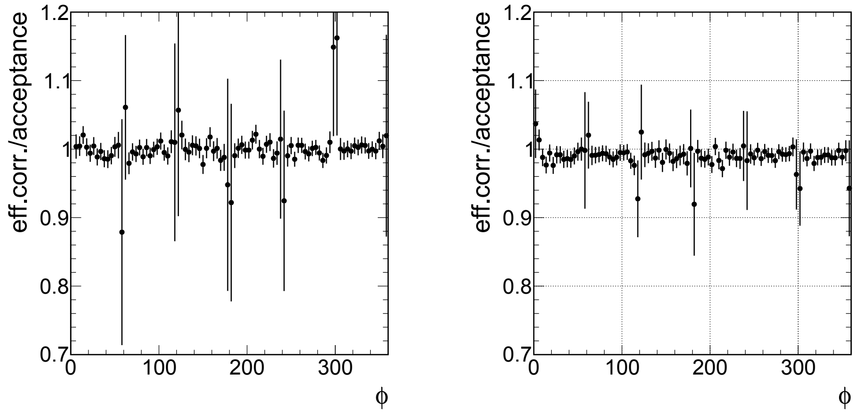

Figure 6.4: Same as 6.2, as a function of the azimuthal angle.

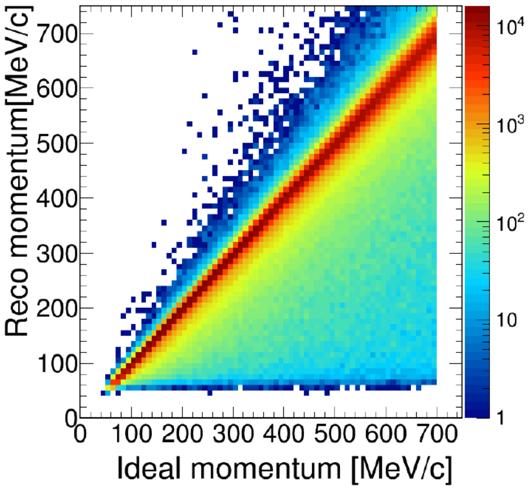

Figure 6.5: Distribution of reconstructed momentum as a function of the ideal momentum for leptons generated with a flat distribution

6.1.3 Efficiency as a function of ”reconstructed” values of momentum, θ and ϕ angles

In the analysis of real data, only the reconstructed variables are available. Therefore, the correction is applied to a number of events in a bin of reconstructed variables, which is valid if resolution effects are small enough. In our case, due to the bremsstrahlung effect ($X/X_0 \sim 9.5$ %), the reconstructed momentum is strongly distorted from the ideal momentum, as can be seen in Fig. 6.5. This means that the distribution of yields in acceptance cannot be retrieved using Eq. 6.2. The efficiency should then be estimated as a function of the reconstructed values of the momentum and angles. For this, the second step of the simulation, where the numbers of particles in acceptance is calculated, needs to be modified to take into account an estimate of the reconstructed momentum instead of the ideal momentum. A ”smearing” procedure is therefore implemented, using for each (p_{ideal},θ_{ideal}) region, the distributions of reconstructed values. The ideal momentum and angle are then replaced by ”smeared” values which are sampled in the corresponding distributions of reconstructed values. In this way, the yield of ”accepted” particles in a bin of ”smeared”’ variable can be estimated and compared to the yield of reconstructed particles in a bin of ”reconstructed” values of a given variable. This new efficiency is hence defined as :

$$\epsilon_{eff}(p,\theta,\phi) = \frac{N_{reco}(p_{reco},\theta_{reco},\phi_{reco})}{N_{acc}(p_{smeared},\theta_{smeared},\phi_{smeared})} \tag{6.3}$$

The new consistency checks are displayed in Fig. 6.6 and Fig. 6.7 as a function of momentum and polar angle.

It can be concluded that the efficiency is also consistently calculated in the case of the reconstructed momentum. The global efficiency for the e^+e^- pair is of the order of 10%. The spectra obtained after correction of electron and proton efficiencies can be compared to the theoretical predictions. However, in addition to acceptance effects, the smearing procedure needs also to be implemented on the simulated events.

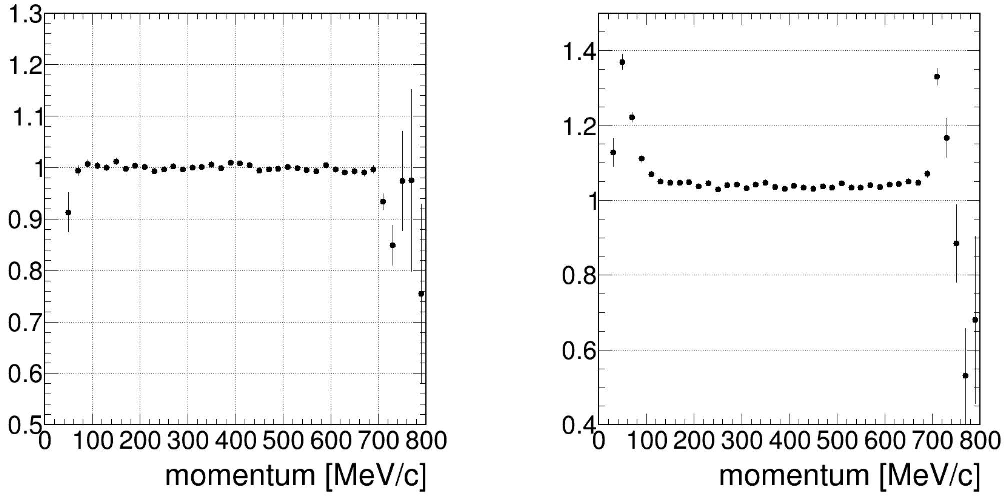

Figure 6.6: Ratio between efficiency corrected yields and yields in acceptance as a function of the reconstructed momentum for electrons (left) and positrons (right) generated with flat distributions.

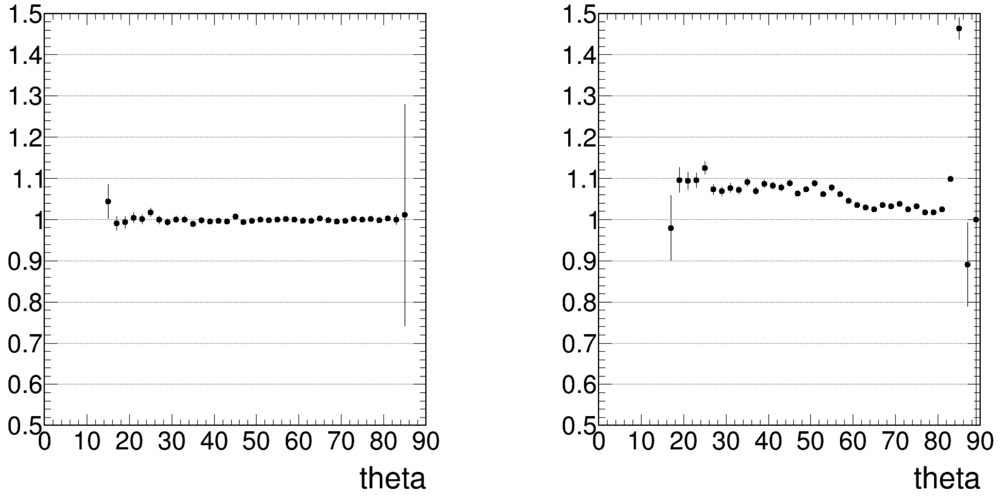

Figure 6.7: Same as Fig. 6.6 as a function of the reconstructed polar angle.

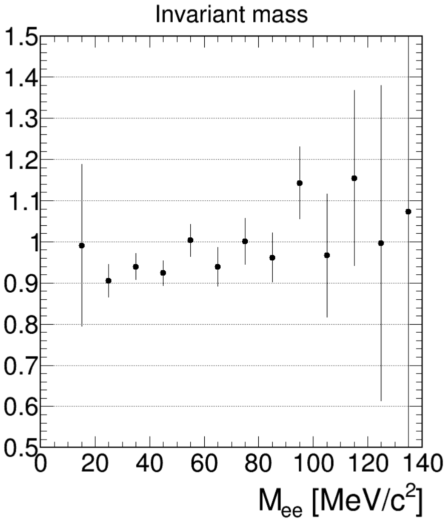

Figure 6.8: Ratio between efficiency corrected yields and yields in acceptance as a function of the invariant mass for di-electrons produced in the π^0 Dalitz decay.

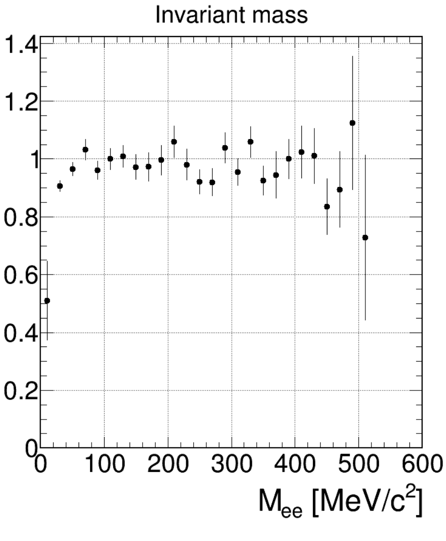

Figure 6.9: Same as Fig. 6.8 for the η Dalitz decay.

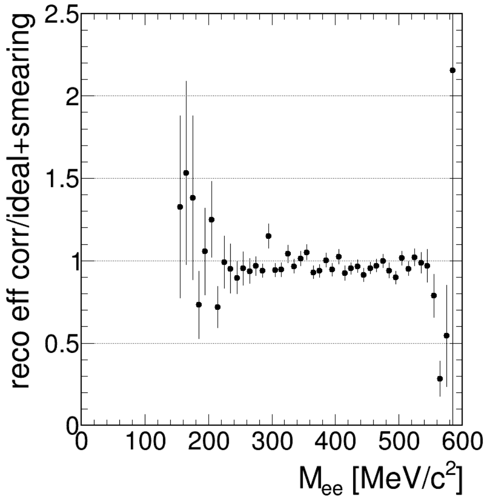

Figure 6.10: Same as Fig. 6.8 for the ρ decay.

6.2 Correction of spectra on the pair level

The next crucial step is to check the consistency of the efficiency correction for a realistic simulation, where simulated dielectrons generated from a given source are combined in pairs after reconstruction. For this, three different sources of dielectron have been chosen: π^0 Dalitz decay, η Dalitz decay and ρ decay. For each of these cases, 10 millions of events were produced using the Pluto generator, then analyzed using GEANT3 and the HYDRA framework in the same way as discussed before. For each event, a weight w is calculated as:

$$w = \frac{1}{\epsilon(p_{e-}, \theta_{e-}, \phi_{e-})\epsilon(p_{e+}, \theta_{e+}, \phi_{e+})} \tag{6.4}$$

and the distribution of weighted reconstructed events is then compared to the distributions of events in acceptance. Again, the best way to quantify possible discrepancies is to build the ratio between the number of efficiency corrected events and the number of accepted events N_{acc} in the same bin. The corresponding results are shown in Fig. 6.8, Fig. 6.9 and Fig. 6.10 for the π^0, η and ρ respectively. All ratios are close to 1, except for the edges of the distributions, where resolution effects are probably not perfectly taken into account by the smearing procedure.

6.2.1 Correction factor for the backtracking analysis

The efficiency corrections rely on the fact that the simulations describe in a realistic way the detector response and the performance of the reconstruction algorithms. This was checked for each individual detector and algorithm by previous studies. Systematic errors quoted in the next section take into account the accuracy of the simulations.

For the backtracking procedure, it was however observed during the analysis of the Au+Au experiment that the efficiency deduced from the simulation was overestimated [115]. This is probably connected to the sensitivity of this algorithm to the electronic noise which is not simulated accurately. The new efficiency tool that we developed (Sec. 4.2.5) can be used to check the backtracking efficiency, in the same way as it was used for the ring finder. As can be observed in Fig. 6.11 which shows the ratio between the efficiency (as defined in Sec. 4.2.5) for experimental data and for the simulation events, the efficiency for the reconstruction of leptons with the backtracking algorithm is overestimated by about

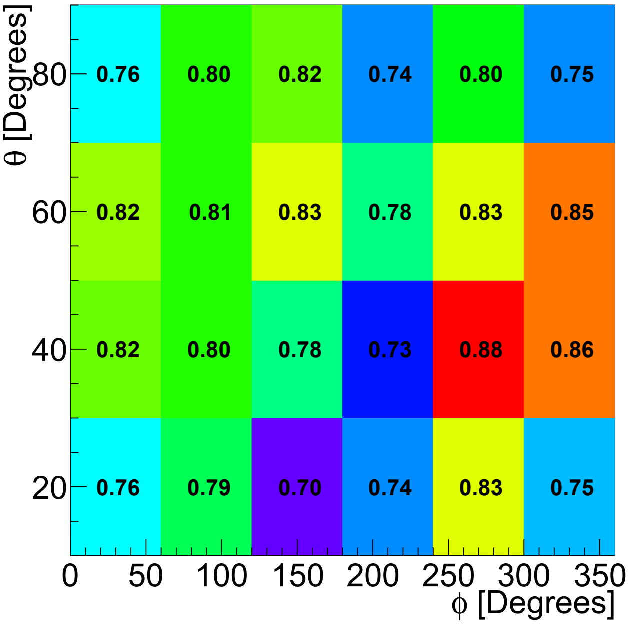

Figure 6.11: Ratio between the efficiency of the backtracking procedure and the efficiency of the simulation

20% (Hence about 40% for a pair). A correction factor was deduced for each bin in θ and ϕ and applied to each lepton of the pair. It could also be checked that this correction factor was very stable during the experiment.

6.3 Estimation of systematic errors

The last step of the analysis consists of estimating the systematic errors affecting the measurements. Here, we should distinguish correlated errors which affect the number of lepton pairs in all bins in the same way and uncorrelated errors which can be considered as independent from one bin to another. Four groups of errors are taken considered:

- Event selection cuts:

  These are cuts used to identify the e^+e^- signal, as explained in detail in Sec. 3.8. Among them, the PID cuts that are applied to reject hadrons are the most important. It is crucial to check to which extent the results are stable when varying the cuts within a small range, where the purity of the signal should not be affected. Several tests have been made: change of the β_{cut} (see Sec. 3.8.4), change of the *RichQa* cut for the ring finder algorithm, change of the minimum number of maxima for the backtracking algorithm. The relative difference between the experimental results and the simulation has been considered to evaluate systematic errors, leading to values of the order of 15% for the correlated systematic error and of 10% for the uncorrelated error.

- Efficiency correction :

  - Ring Finder efficiency: We have explained in Chapter 4 the importance of the digitization of the RICH information to get realistic simulations. This digitizer was tuned very carefully using the experimental distributions of key observables of the RICH response. In addition, the efficiency of the Ring Finder predicted by the simulation could be checked to be realistic using a reference sample of leptons identified without the RICH detector (Sec. 4.2.5). The dependance of the efficiency on the lepton angle could also be checked, though with a limited precision, due to the lack of statistics. Based on this study, we estimate a global systematic error of less than 10% for the efficiency of the Ring Finder and a 5% uncorrelated error in each bin.

  - Backtracking efficiency: As discussed in Sec. 6.2.1, the simulation overestimates the efficiency of the backtracking algorithm by roughly 20% and a correction factor was applied. Due to this correction factor, the uncertainty of the backtracking procedure is higher than for the Ring Finder. We assign a value of 15% for the correlated uncertainty and 10% for the uncorrelated one.
  - Tracking: The reconstruction of lepton pairs is also affected by the tracking efficiency. In the present work, no specific study of this effect could be performed. However, the systematic errors (both correlated and uncorrelated ones) on the tracking efficiency are usually estimated to be of the order of 10%. Due to the good stability of the MDC chambers during the pion beam experiment and the low multiplicity of particles, this number can be taken as a conservative estimate.

- Subtraction of the combinatorial background:

  The systematic error related to the subtraction of the combinatorial background is of course taken into account. Due to the overall low B/S, the associated error is smaller than the statistical error on the signal, except in the region of invariant masses close to 100 MeV/c^2. However, there is also a systematic error related to the approximation of the combinatorial background using the geometrical mean formula (Eq. 5.1). The systematic error on the combinatorial background can be checked using simulations. Indeed, in this case, the origin of all reconstructed leptons is clearly known and the reconstructed pairs belonging to the combinatorial background can be clearly identified. Their yield can therefore be easily compared to the yield calculated with the geometrical mean formula (Eq. 5.1). A systematic error of 5% on the estimate of the combinatorial background can be estimated from this study, which leads to an error of 5% × B/S on the signal yield.

- normalization:

  As discussed in Sec. 5.7, the normalization of the data is obtained with a precision of 10% using the number of events measured in the same experiment for the elastic scattering, for which the cross section is known from previous experiments. This uncertainty obviously affects all bins in the same way. Since the normalization is based on the number of reconstructed tracks, it can be considered that it compensates a possible tracking inefficiency. However, the tracking efficiency is expected to be different for leptons, than for hadrons, so we keep as a conservative number the systematic efficiency for tracking, as mentioned above.

Systematic errors	correlated	uncorrelated
Event selection	15%	10%
Tracking efficiency	10%	10%
Ring finder/backtracking efficiency	10/15%	10%/10%
Combinatorial background	-	5%× S/B
Normalization	10%	
total	20-23%	14-15 %

Table 6.1: List of correlated and uncorrelated systematic errors affecting the e^+e^- yields in each bin.

The different sources of errors and their values are summarized in Table 6.1.

6.4 Final efficiency corrected spectra

At the end of the procedure, final efficiency corrected spectra, as e^+e^- invariant mass or transverse momentum distributions, or angular distributions are produced. These spectra will be presented and discussed in comparison with theoretical predictions in Chapter 8.

Chapter 7

Theoretical approaches for the $\pi^- p \to n e^+ e^-$ reaction

In this chapter, we will describe the existing theoretical approaches for the reaction $\pi^- p \to n e^+ e^-$. In addition, we describe the results of the PWA analysis of 2π production channels, which allow to extract the $\Delta\pi$ and off-shell ρ contributions which are important sources of e^+e^- pair production.

7.1 Graphs contributing to the $\pi^- p \to n e^+ e^-$ reaction:

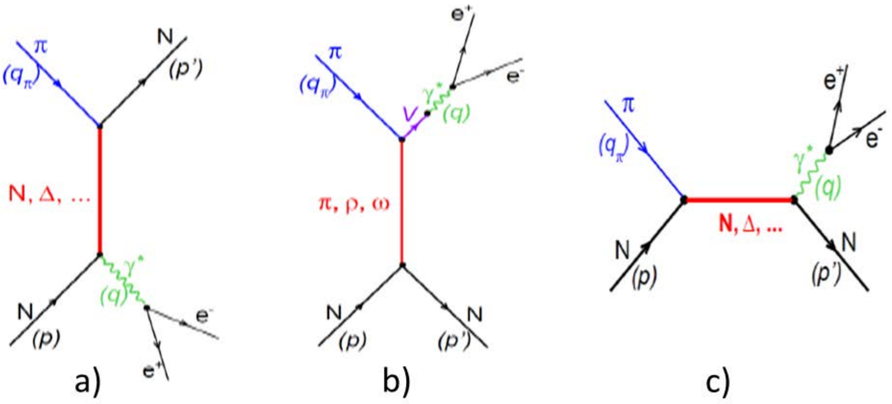

Figure 7.1: Graphs for the exclusive production of e^+e^- pairs in the π^-p reaction. a): u channel b) t channel c) s channel

As shown in Fig. 7.1, three graphs can contribute to the reaction $\pi^-\mathrm{p} \to n\ e^+e^-$. In the u (graph a) and t channel (graph b), the e^+e^- pair is emitted before the meson-baryon vertex. It is radiated from the nucleon in the u channel graph and from the pion in the t channel one. In the s channel (graph c), an intermediate baryon is produced, which then decays by emission of a nucleon and an e^+e^- pair. The three graphs imply different time-like electromagnetic form factors.

7.2 Early approaches

The interest of the $\pi^- p \to ne^+e^-$ reaction has been mentioned long time ago. In 1962, this reaction is discussed in [125], as a way to access the charged π meson electromagnetic form-factor in the time-like region, which plays a role at the $\pi\pi\gamma^*$ vertex in the t channel (graph b in Fig. 7.1).

In 1965, M.P. Rekalo [126] was interested by the u channel graph (graph a in Fig. 7.1), which is sensitive to the time-like electromagnetic nucleon form-factor at the NN$\gamma^\star$ vertex. The kinematical region of these form-factors corresponds to the so-called unphysical region, *i.e.* below the $\bar{p}p$ threshold. This region is not accessible with $\bar{p}p \to e^+e^-$ or $e^+e^- \to \bar{p}p$ reactions. However, these early approaches put emphasis on given aspects of these reactions, and did not allow for a full description, as in particular, they neglected the s channel graphs.

Later, the interpretation of measurements in the $\pi^- p \to ne^+e^-$ reaction which were performed before the HADES experiments, but at lower pion beam energies (see Sec. 1.5), was performed in the framework of the inverse pion electroproduction formalism [127], which provides a consistent description of $ep \to eN\pi$, $\gamma p \to N\pi$ and $\pi N \to Ne^+e^-$ reactions. Their extrapolation at higher energies is challenging, due to the unknown value of baryon transition form factors. However, a new calculation of the $\pi^- p \to ne^+e^-$ reaction at energies relevant for our studies has been proposed [128] and a paper is in preparation.

Models based on vector meson production

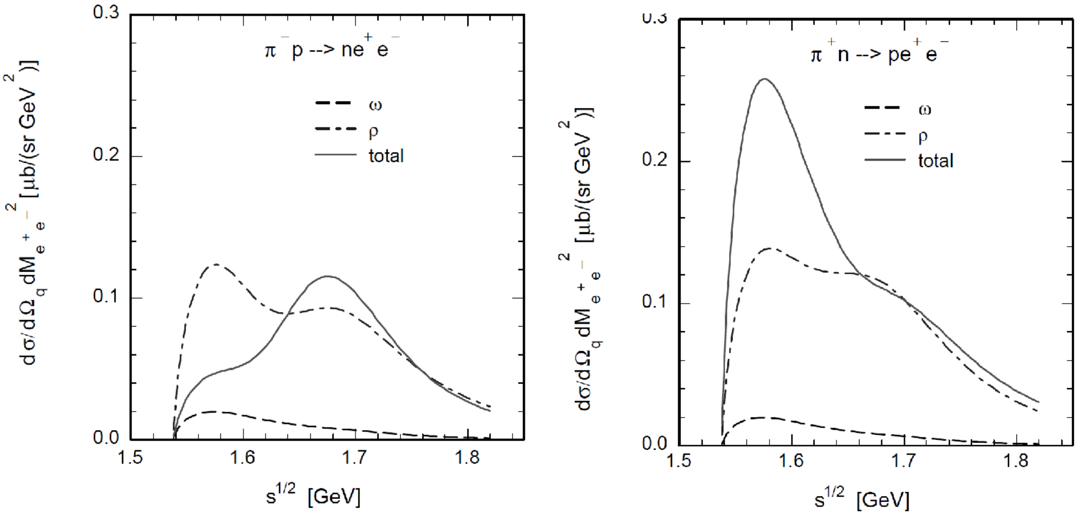

Figure 7.2: Differential cross-sections for the $\pi^- p \to ne^+e^-$ reaction (left) and π^+n→pe$^+e^-$ (right) reactions at a fixed e^+e^- invariant mass M$_{ee}$=0.6 GeV/c^2 [129].

More recent studies put emphasis on the e^+e^- production via vector meson decay and gave the motivation to the HADES collaboration for studying the $\pi^- p \to ne^+e^-$reaction. Since the electromagnetic current is the sum of isoscalar and isovector components, the amplitude of the reaction $\pi^- p \to ne^+e^-$ and $\pi^+ n \to pe^+e^-$ can be expressed as

$$T(\pi^- p \to ne^+e^-) = T^{\text{isoscalar}} + T^{\text{isovector}} \tag{7.1}$$

$$T(\pi^+ n \to pe^+e^-) = T^{\text{isoscalar}} - T^{\text{isovector}} \tag{7.2}$$

The change of sign derives from the isospin rotation leading from one reaction to the other. In the vector dominance model, the isoscalar and isovector amplitudes can be associated to the ω and ρ, respectively.

In [129], the s and u channel graphs are calculated for the different known resonances up to $\Delta(1700)$, using coupling constants to the ρN and ωN channels from either a quark-model or the measured decay widths. Predictions for both invariant masses (Fig. 7.2) and angular distributions (as will be discussed in Sec. 7.6) have been provided. This work demonstrates a very strong interference between the ρ (isovector) and ω (isoscalar) channels which is destructive in the π^-p reactions (see Fig. 7.2) and therefore positive in the $\pi^+n \to p\ e^+e^-$channel. This results from the different values and phases of the $g_{\omega NN^\star}$ and $g_{\rho NN^\star}$ couplings for the same resonances. The total angular distributions therefore depends on the very complex pattern of all these contributions, which obviously depend on the values of the coupling of the various baryonic resonances to the ρ and ω mesons. This was quantitatively demonstrated in this paper by comparing the results for couplings derived from quark model and for couplings derived from the partial decay width measurements available at that time.

A large sensitivity to the coupling constants within this Vector Dominance Model was also shown for the spin density coefficients ρ_{00} (see Sec.7.6). It was already emphasized in this work that the measurement of the angular distributions in future HADES experiments would give a powerful test of the model and of the resonance couplings. Two years later,

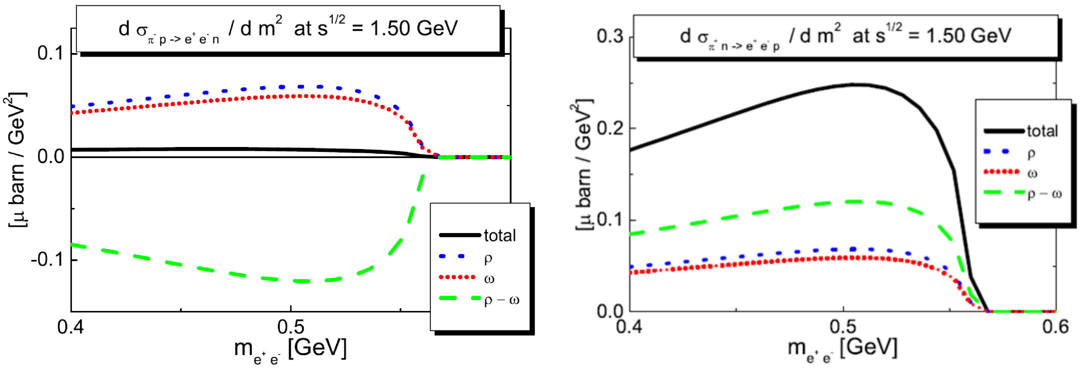

Figure 7.3: Differential cross-section for the $\pi^-p \to e^+e^-n$ reaction (left) and $\pi^+n \to e^+e^-p$ (right) at $\sqrt{s}$=1.5GeV as a function of the e^+e^- pair invariant mass. The ρ^0 and the ω contributions are shown by short-dashed and dotted lines respectively. The long-dashed line shows the $\rho^0-\omega$ interference. The solid line is the sum of the three contributions [130].

[130] published a unified description of meson-nucleon and photon-nucleon interaction, based on a coupled channel approach including γN, πN and VN, where V is a vector meson and with parameters fixed on a large set of data. In this approach, the resonances are dynamically generated and the model is well constrained by experimental data. This model is however limited to the region close to the vector meson threshold, as it takes into account only s-wave amplitudes. Fig. 7.3 demonstrates the crucial role played by the interferences in the ρ and ω channels in the e^+e^- production in these calculations, too. The interference effects are destructive in the case of $\pi^-p \to ne^+e^-$ and constructive in the case of π^+n$\to$pe^+e^-. The difference between the two calculations can be mostly explained by the different vector-meson couplings of the resonances. In [129], the $S_{11}(1535)$ is dominant at low energies for both ω and ρ production and the $S_{11}(1650)$ at larger energies. The cross-sections are smaller than in [129], especially for the ρ due to much smaller coupling constants and the interference pattern is different. As seen in Fig. 7.3, the cross-section in the $\pi^-p \to ne^+e^-$ is very small at $\sqrt{s} = 1.5$ GeV, *i.e.* about 220 MeV below the ω threshold. The effect of the destructive ρ-ω interference is very strong in [130] and this prediction was used as a motivation for experiments with HADES using the pion beam on a nucleon target.

We will show in Chapter 8 how these calculations can be checked by our experimental data. The measurements in the hadronic channels allow in addition for a more precise determination of all the baryon couplings and could allow for an update of these calculations.

Lagrangian models

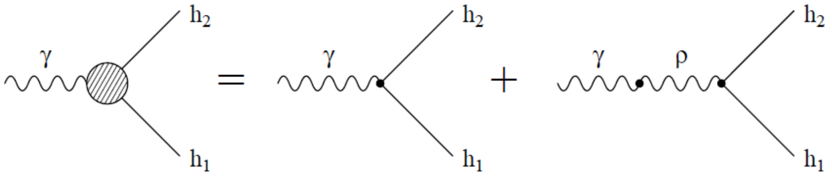

Figure 7.4: Vector Dominance Vertex used in [131], consisting of the sum of the direct photon term and the ρ meson contribution.

In the recent years, another Lagrangian model was developed by M. Zetenyi and G. Wolf [131]. It includes s, u and t channel contributions based on effective Lagrangians for the corresponding graphs. In this approach, the electromagnetic interaction consists of two parts: a direct coupling and a Vector Dominance coupling, as illustrated in Fig. 7.4. The direct photon coupling is calculated using the respective $\gamma h_1 h_2$ vertex functions with couplings fixed to reproduce the pion photoproduction cross sections (see [131]).

The VDM part of the $h_1 h_2 \gamma$ vertex function reads:

$$V_{h_1 h_2 \gamma, VDM} = F_{\rho\gamma, VDM} V_{h_1 h_2 \rho}, \tag{7.3}$$

$$\text{where } F_{\rho\gamma, VDM} = \frac{-e}{g_\rho} \frac{k^2}{k^2 - m_\rho^2 + i\sqrt{k^2}\Gamma_\rho(k^2)} \tag{7.4}$$

is the VDM form factor. The particular form of the VDM form factor (Eq. 7.4) derives from the choice of the $\rho\gamma$ Lagrangian:

$$\mathcal{L}_{\rho\gamma} = \frac{-e}{2g_\rho} F^{\mu\nu} \rho^0_{\mu\nu}, \tag{7.5}$$

where F$^{\mu\nu}$ $= \partial^\mu A^\nu - \partial^\nu A^\mu$ is the electromagnetic field tensor and $\rho^0_{\mu\nu} = \lceil^0_\mu \rho_\nu - \lceil_\nu \rho_\mu$ the ρ meson field tensor. The value of the parameter g$_\rho$ is fixed to 4.96 to reproduce the $\rho \to e^+e^-$ decay branching ratio. At k^2=0, the expression in Eq.7.4 vanishes, so only the direct photon contribution plays a role. The latter is expressed using the respective $\gamma h_1 h_2$ vertex functions with couplings which can be fitted to the photoproduction data. This difference is important, since the form in Eq. 7.35 has a finite value at k^2=0. This problem is at the origin of the overestimation of the radiative decay branching ratios in the Vector Dominance Models. The use of the Lagrangian of Eq. 7.5 and of the two component interaction (Fig. 7.4) allows to take into account consistently both the $\rho h_1 h_2$ and the $\gamma h_1 h_2$ couplings.

The invariant mass distribution resulting from this model is shown in Fig. 7.5 for different center-of-mass energies. At 1.3 GeV, the Δ(1232) contribution dominates. The enhancement due to the coupling of baryons to the ρN channel starts to be visible at $\sqrt{s}$=1.5 GeV and it constitutes also an interesting prediction for our measurement. The different resonant and non resonant components are shown in Fig. 7.6 for a center-of-mass energy of 1.5 GeV. N(1520) is the largest contribution at this energy. Here, the dominant resonant contributions are due to the N(1520) and N(1680), but the non-resonant Born

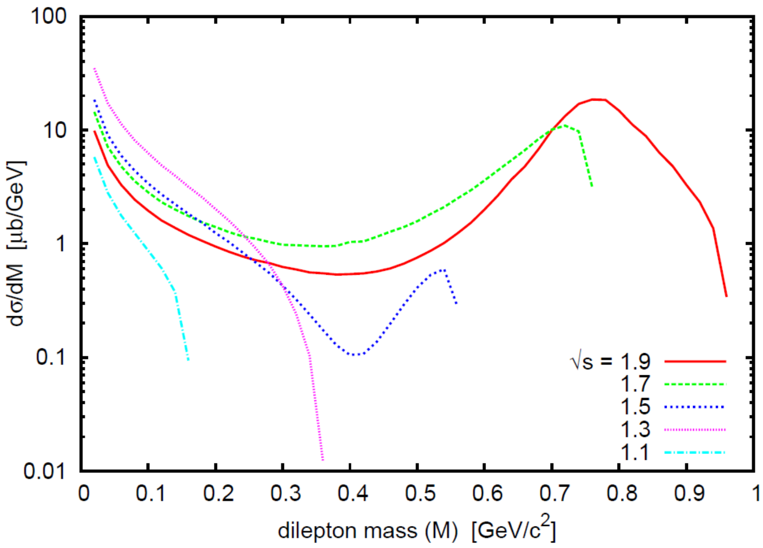

Figure 7.5: Dilepton invariant mass spectra from the reaction $\pi^- p \rightarrow n e^+ e^-$ for various center of mass energies [131].

terms are also very important. They interfere destructively with the N(1520) and N(1680) contributions. The Δ resonance has only a very small contribution. One conclusion of this work is that the transport models, which consider an incoherent sum of resonant amplitudes cannot constitute a good approach for the description of the $\pi^- p \rightarrow n e^+ e^-$reaction .

7.3 Dalitz decays of baryon resonances

7.3.1 QED formalism

The starting point for the calculation of the differential decay width of a baryon B into the N$e^+ e^-$ channel is the relation :

$$\frac{d^5\Gamma}{dq^2 d\Omega_q d\Omega_e} = \frac{1}{2m_\star}\frac{1}{4} \sum_{m^s_N, m^s_B, m^s_{e^+}, m^s_{e^-}} |\mathcal{M}|^2 \Phi(B \rightarrow N e^+ e^-), \tag{7.6}$$

where m$_\star$ is the resonance mass, $\Phi(B \rightarrow N e^+ e^-)$ is the phase space for the Dalitz decay process, and $\mathcal{M}$ is the transition amplitude for the different spin projections $m^s_N, m^s_\star, m^s_{e+}, m^s_{e-}$ of the proton, baryonic resonance, electron and positron respectively. This transition amplitude is expressed as a product of the leptonic (J$^{L\mu}$) and hadronic (J$^H_\mu$) currents:

$$\mathcal{M} = J^H_\mu(m^s_N, \vec{p}_N, m^s_\Delta, \vec{p}_\Delta) J^{L\mu}(m^s_{e^-}, \vec{p}_{e^-}, m^s_{e^+}, \vec{p}_{e^+}) \frac{1}{q^2} \tag{7.7}$$

The electromagnetic hadronic current J^H_μ consists of two or three independent amplitudes for spin 1/2 or spin 3/2 baryons respectively and each amplitude is weighted by a form factor which takes into account the electromagnetic structure of the baryonic transition. The electromagnetic current can be expressed in different ways. For example, one can use the decomposition in magnetic dipole, electric quadrupole and Coulomb quadrupole currents: J^M_μ, J^E_μ, J^C_μ and the corresponding form-factors G$_M(q^2)$, G$_E(q^2)$, G$_C(q^2)$.:

$$J^H_\mu = G_M(q^2) J^M_\mu + G_E(q^2) J^E_\mu + G_C(q^2) J^C_\mu \tag{7.8}$$

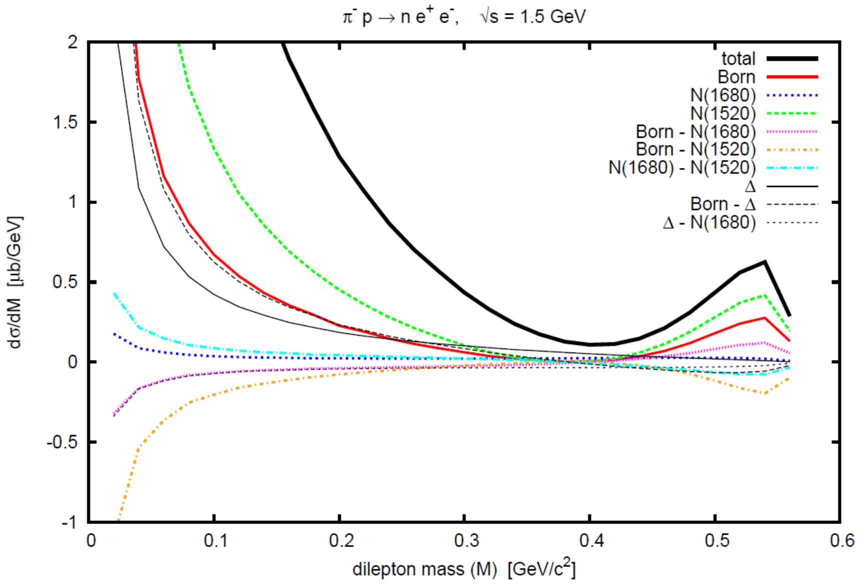

Figure 7.6: Result of the calculation for $\sqrt{s}$=1.5 GeV showing the different contributions [131].

The advantage of this set of currents is that the Dalitz decay width can be expressed as a function of the squares of the moduli of the form factors at a given e^+e^- mass M$_{ee}$ as [132]

$$\Gamma^{N^*\to N\gamma^*}_{m_{N^*}}(q^2) = \frac{\alpha}{8m_\star}\sigma_\pm^{3/2}\sigma_\mp^{1/2} \times \left|G_T(q^2)\right|^2, \tag{7.9}$$

$$\text{where } q^2 = M_{ee}^2, \tag{7.10}$$

$$m_\pm = m_\star \pm m_N, \tag{7.11}$$

$$\sigma_\pm = m_\pm^2 - M_{ee}^2, \tag{7.12}$$

$$\text{and } \left|G_T(q^2)\right|^2 = 2\left|G_{E/M}(q^2)\right|^2 + \frac{q^2}{m_\star^2}\left|G_C(q^2)\right|^2 \tag{7.13}$$

is the effective form factor for spin 1/2 resonances.
The upper sign in all the equations refers to normal parity resonances J^P=1/2$^-$, 3/2$^+$, 5/2$^-$,.. and the lower sign to abnormal parity resonances J^P=1/2$^+$, 3/2$^-$, 5/2$^+$,..

For resonances with spin J > 1/2, the equations are:

$$\Gamma^{N^*\to N\gamma^*}(q^2) = \frac{9\alpha}{8}\frac{(l!)^2}{2^l(2l+1)!}\frac{m_\pm^2\sigma_\mp^{l+1/2}\sigma_\pm^{l-1/2}}{m_\star^{2l+1}m_N^2} \times \left|G_T(q^2)\right|^2, \tag{7.14}$$

$$\text{with } \left|G_T(q^2)\right|^2 = \frac{l+1}{2l}\left|G_{M/E}(q^2)\right|^2 + \tfrac{1}{2}(l+1)(l+2)\left|G_{E/M}(q^2)\right|^2 + \tfrac{q^2}{2m_\star^2}\left|G_C(q^2)\right|^2 \tag{7.15}$$

and we take the same definition of G$_T(q^2)$ as in [26].

The radiative decays are given by the limits of $\Gamma^{N*\to N\gamma^*}(q^2)$ when $q^2\to 0$:

$$\Gamma^{N^*\to N\gamma} = \frac{\alpha}{4m_\star}m_\pm^{3/2}m_\mp^{1/2}\left|G_T(0)\right|^2 \tag{7.16}$$

for J = 1/2 and

$$\Gamma^{N^*\to N\gamma} = \frac{9\alpha}{8}\frac{(l!)^2}{2^l(2l+1)!}\frac{m_\mp^{l+1/2}m_\pm^{l+3/2}}{m_\star^{2l+1}m_N^2} \times \left|G_T(0)\right|^2 \tag{7.17}$$

for resonances with spin J > 3/2.

Then the Dalitz decay width for spin 1/2 resonances can be rewritten as

$$\Gamma^{N^* \to N\gamma^*}(q^2) \;=\; \frac{\sigma_{\pm}^{3/2}\sigma_{\mp}^{1/2}}{m_{\pm}^{3/2}m_{\mp}^{1/2}}\frac{\left|G_T(q^2)\right|^2}{\left|G_T(0)\right|^2} \times \Gamma^{N^* \to N\gamma} \tag{7.18}$$

and for resonances with spin J > 1/2:

$$\Gamma^{N^* \to N\gamma^*}(q^2) = \frac{\sigma_{\mp}^{l+1/2}\sigma_{\pm}^{l-1/2}}{m_{\mp}^{l+1/2}m_{\pm}^{l-1/2}}\frac{\left|G_T(q^2)\right|^2}{\left|G_T(0)\right|^2} \times \Gamma^{N^* \to N\gamma} \tag{7.19}$$

We are particularly interested in the decay width for the N(1535) (J^P=1/2$^-$)

$$\Gamma^{N(1535) \to N\gamma^*}(q^2) \;=\; \frac{\sigma_{+}^{3/2}\sigma_{-}^{1/2}}{m_{+}^{3/2}m_{-}^{1/2}}\frac{\left|G_T(q^2)\right|^2}{\left|G_T(0)\right|^2} \times \Gamma^{N^* \to N\gamma} \tag{7.20}$$

and for the N(1520) (J^P=3/2$^-$)

$$\Gamma^{N(1520) \to N\gamma^*}(q^2) = \frac{\sigma_{+}^{3/2}\sigma_{-}^{1/2}}{m_{+}^{3/2}m_{-}^{1/2}}\frac{\left|G_T(q^2)\right|^2}{\left|G_T(0)\right|^2} \times \Gamma^{N^* \to N\gamma} \tag{7.21}$$

The e^+e^- differential cross-section as a function of the e^+e^- invariant mass can then be calculated as

$$\frac{d\Gamma^{N^\star \to Ne^+e^-}}{dM_{ee}} = \frac{2\alpha}{3\pi M_{ee}}\Gamma_{M_{N^\star}}^{N^\star \to N\gamma^*}(M_{ee}), \tag{7.22}$$

Examples of differential e^+e^- invariant mass distributions for a resonance with mass m^*=1.5 GeV and various spins and parities are shown in Fig. 7.7. The behavior at large invariant masses depends on the angular momentum $\updownarrow$ of the virtual photon. In particular, transitions involving $\updownarrow = 0$ have a smoother beahaviour close to the kinematical limit, where the momentum of the virtual photon vanishes.

Since the differential Dalitz decay width decreases very fast as a function of e^+e^- invariant mass, the total Dalitz decay width

$$\Gamma^{N^\star \to Ne^+e^-} = \int \frac{d\Gamma^{N^\star \to Ne^+e^-}}{dM_{ee}} \tag{7.23}$$

is dominated by the behavior of the differential cross section at small virtual photon masses, where

$$\Gamma^{N^\star \to N\gamma^*} \sim \Gamma^{N^\star \to N\gamma} \tag{7.24}$$

Therefore, the Dalitz decay width can be approximated as:

$$\frac{d\Gamma^{N^\star \to Ne^+e^-}}{dM_{ee}} = \frac{2\alpha}{3\pi M_{ee}}\Gamma^{N^\star \to N\gamma}, \tag{7.25}$$

Hence,

$$\Gamma^{N^\star \to Ne^+e^-} \sim \frac{2\alpha}{3\pi}\Gamma^{N^\star \to N\gamma}\log(\frac{m_-}{2m_e}) \tag{7.26}$$

$$\text{where } m_e = 0.511\ MeV/c^2 \text{ is the electron mass} \tag{7.27}$$

$$\text{i.e. for } m^* \sim 1.52\ GeV,$$

$$\Gamma^{N^\star \to Ne^+e^-} \sim 1.35\ \alpha\ \Gamma^{N^\star \to N\gamma} \tag{7.28}$$

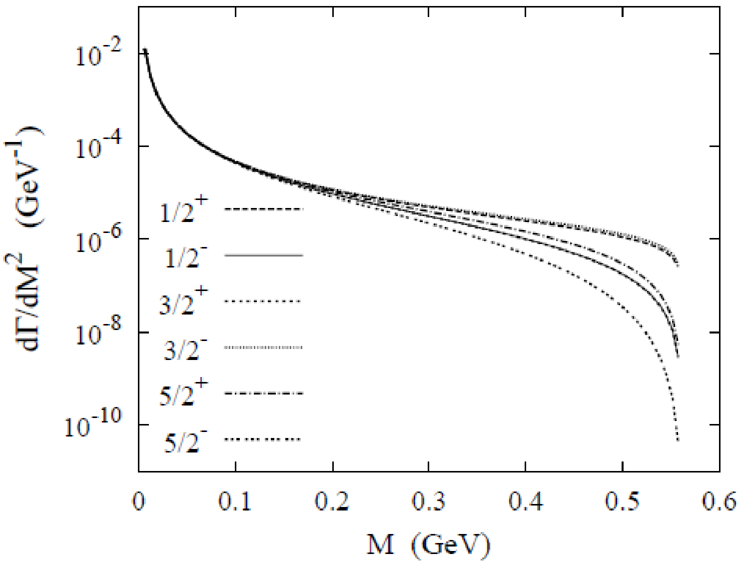

Figure 7.7: Differential invariant mass distribution for an hypothetical resonance with mass 1.5 GeV and radiative decay width 6 MeV and various spin and parities [131].

		$N(1520)^0$	$N(1535)^0$
PDG	BR(N* $\to n\gamma$)	0.3-0.53 %	0.01-0.25 %
Bonn-Gatchina	BR(N* $\to n\gamma$)	0.23 %	0.35 %
	total width (MeV)	114	116
	partial width (MeV)	0.26	0.4
	BR(N* $\to ne^+e^-$)	2.3 10^{-5}	3.5 10^{-5}
	$\mathrm{G}_T(0)$	10^3 MeV	0.33

Table 7.1: The second row gives the PDG branching ratios for the N(1520) and N(1535) radiative decays. The next rows concern the Bonn-Gatchina PWA and display the radiative branching ratio, total width, radiative partial width, Dalitz decay branching ratios and effective form factor.

These relations allow to calculate easily the Dalitz decay branching ratio, knowing the radiative decay width. The latter are however given in the PDG with a large uncertainty (see Table 7.1). To calculate the dilepton yield (see chapter 8), we will use the values of branching ratios derived in the Bonn-Gatchina PWA analysis. These values and corresponding Dalitz decay widths are given in Table 7.1, together with the effective form factors for N(1520) and N(1535) $|G_T(0)|$ that can be calculated using eq. 7.17 and 7.17. Note that for N(1535) $|G_T(0)|$ is dimensionless while for N(1520), it has the dimension of an energy.

7.3.2 Form factor models for baryon transitions

Eqs. 7.10 and 7.15 derive from a QED calculation, but the form factors need to be given by models describing the internal structure of the baryons. As already mentioned in the introduction (see Sec. 1.2.1), a lot of models exist for electromagnetic transitions in the space like region transition. However, very few of them were analytically continued in the time-like region.

"Photon-point" form factors

Since the form factors are known at q^2=0 (photon-point) from photon-induced reactions, the simplest way to take into account form factors in the time-like region is to assume that they are constant and that they keep the same values as for q^2=0. Neglecting the q^2 dependence of the form factor amounts to considering point-like baryons. This approximation is expected to be valid for small positive q^2 where the Dalitz decay differential width is not sensitive to the q^2 dependence of the form factor. Such calculation of the Dalitz decay differential distribution is known as "QED calculation", as it takes into account only the γN coupling constant and omits the effect due to the internal structure of the baryons driven by QCD. It can serve as a reference to quantify the effect of q^2 dependent form factors.

As the Dalitz decay width depends only on the effective form factor $G_T(q^2)$ defined in Eqs. 7.13 and 7.15, the approximation above comes down to assuming

$$\left|G_T(q^2)\right|^2 \sim |G_T(0)|^2 \tag{7.29}$$

In this case, Eqs 7.18 and 7.19 can be simplified as:

$$\Gamma^{N^*\to N\gamma^*}(q^2) \quad = \quad \frac{\sigma_{\pm}^{3/2}\sigma_{\mp}^{1/2}}{m_{\pm}^{3/2}m_{\mp}^{1/2}} \times \Gamma^{N^*\to N\gamma} \tag{7.30}$$

and for resonances with spin J > 1/2:

$$\Gamma^{N^*\to N\gamma^*}(q^2) = \frac{\sigma_{\mp}^{l+1/2}\sigma_{\pm}^{l-1/2}}{m_{\mp}^{l+1/2}m_{\pm}^{l-1/2}} \times \Gamma^{N^*\to N\gamma} \tag{7.31}$$

In particular, one can notice that one obtains the same trend for the N(1535) (J^P=1/2$^-$) resonance and for the N(1520) (J^P=3/2$^-$ resonance):

$$\Gamma^{N^*\to N\gamma^*}(q^2) \quad = \quad \frac{\sigma_{+}^{3/2}\sigma_{-}^{1/2}}{m_{+}^{3/2}m_{-}^{1/2}} \times \Gamma^{N^*\to N\gamma} \tag{7.32}$$

$$\Gamma^{N^*\to N\gamma^*}(q^2) = \frac{\sigma_{+}^{3/2}\sigma_{-}^{1/2}}{m_{+}^{3/2}m_{-}^{1/2}} \times \Gamma^{N^*\to N\gamma} \tag{7.33}$$

Vector Dominance model

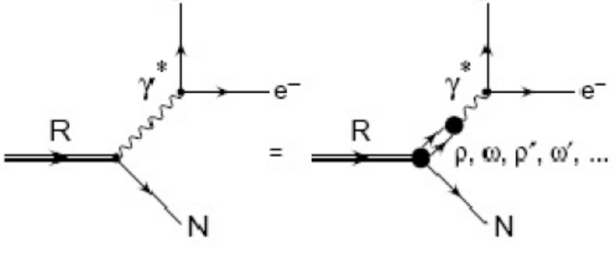

Figure 7.8: Sketch for the Vector Dominance Model for time-like electromagnetic form factors in the Dalitz decay of a baryonic resonance.

As mentioned in Sec. 1.2.4, the most commonly used approximation to take into account form factors in the time-like region is the Vector Dominance Model. This model stipulates that the baryon electromagnetic current is mediated by vector mesons (ρ, ω, ϕ,...), carrying the same quantum numbers as the photon, i.e. $J^P=1^-$ (cf Fig. 7.8).

The VDM Lagrangian is frequently taken as :

$$\mathcal{L}_{\rho\gamma} = \frac{-em_\rho^2}{g_\rho}\rho_\mu^0 A^\mu \tag{7.34}$$

In this case, the expression of the VDM form factor (Eq. 7.4) is

$$F_{\rho\gamma,VDM} = \frac{-e}{g_\rho}\frac{m_\rho^2}{k^2 - m_\rho^2 + i\sqrt{k^2}\Gamma_\rho(k^2)} \tag{7.35}$$

and the resulting expression for the ρ decay width is

$$\Gamma_{\rho\to e^+e^-}(M_{ee}) = \frac{c_\rho}{M^3}\sqrt{1-4\frac{m_e^2}{M_{ee}^2}}\left(1+2\frac{m_e^2}{M_{ee}^2}\right), \tag{7.36}$$

where c_ρ is related to the $\rho \to e^+e^-$ branching ratio at pole mass. It has to be noted that the factor $1/M^3$ strongly enhances the small invariant masses.

Constituent quark models

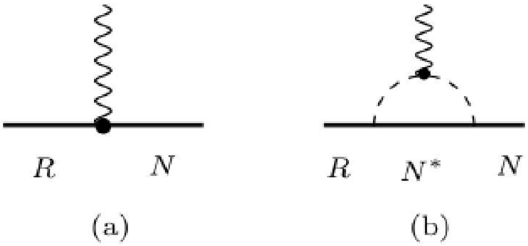

Figure 7.9: Electromagnetic interaction with the quark core (a) and with the meson cloud (b) in the electromagnetic transition between a baryonic resonance R and a nucleon N.

As mentioned in Sec. 1.2.4, both time-like form factor models of Iachello [23] and Ramalho and Pena [25] were used for the analysis of the $\Delta(1232)$ Dalitz decay [37]. Iachello's model was not extended to higher lying resonances, but Ramalho and Pena recently provided a model for the N-N(1520) transition which is highly interesting for the present study focusing to the second resonance region.

In Ramalho and Pena's model [133], baryons are described by a quark core and a pion cloud with corresponding form factors:

$$G_M(q^2,W) = G_M^B(q^2,W) + G_M^\pi(q^2,W) \tag{7.37}$$
$$G_E(q^2,W) = G_E^B(q^2,W) + G_E^\pi(q^2,W) \tag{7.38}$$
$$G_C(q^2,W) = G_C^B(q^2,W) + G_C^\pi(q^2,W) \tag{7.39}$$

where the subscripts B and π indicate the valence quark and meson cloud (treated as pion cloud) contribution respectively.

The interaction with the valence quark-core is treated in the framework of the covariant spectator theory, *i.e.* the quark core is considered as a quark-diquark system where the di-quark is a spectator in the electromagnetic interaction. In this approach, the electromagnetic current is calculated in a relativistic impulse approximation

$$J^\mu = 3\sum_\Gamma \int_k \psi_R(\bar{P}_R,k) j_q^\mu \Psi_N(P_N,k) \tag{7.40}$$

Γ is the quark-diquark polarization and P_N, P_R and k are the nucleon, resonance and diquark momenta respectively. The quark electromagnetic current depends on the quark

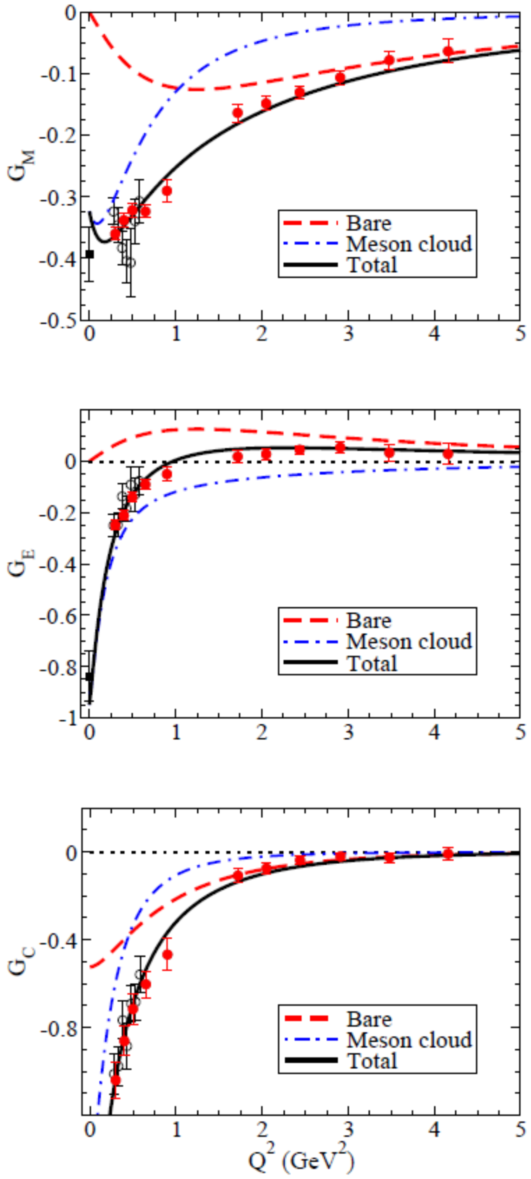

Figure 7.10: Valence quark and meson cloud contributions to the space like from factors for the N-N(1520) transition for Ramalho and Pena's model are compared to existing data [133].

form factors which have the form

$$f_{1\pm}(q^2) = \lambda_q + (1-\lambda_q)\frac{m^2_{v^2_\pm}}{v^2_\pm - q^2} - c_\pm \frac{M_H^2 q^2}{(M_H^2 - q^2)^2}, \tag{7.41}$$

$$f_{2\pm}(q^2) = \kappa_\pm \left[d_\pm \frac{m^2_{v^2_\pm}}{v^2_\pm - q^2} + (1-d_\pm)\frac{M_H^2 q^2}{(M_H^2 - q^2)^2} \right], \tag{7.42}$$

The + and - sign correspond respectively to isoscalar and isovector transitions and m_+ and m_- to the light vector meson (ω and ρ respectively) masses. M_H is the mass of an effective heavy vector meson taken as $2M_N$, which simulates the effect of short range physics. c$_\pm$ and d$_\pm$ are admixture coefficients, λ_q is a high-energy parameter and $\kappa_\pm$ is the quark anomalous magnetic moment. The parameters were all adjusted to the nucleon elastic form factors in the space like region.

For the extension to the time-like region, the vector meson width is introduced, which produces an imaginary part:

$$\frac{m_v^2}{m_v^2 - q^2} \to \frac{m_v^2}{m_v^2 - q^2 - i m_v \Gamma_v(q^2)}, \tag{7.43}$$

where $\Gamma_v(q^2)$ denotes the vector meson decay width.

The quark core electromagnetic current can be deduced following Eq.7.40 using a parametrization of the nucleon and baryon wave functions, which is fitted to the $\gamma^\star$N $\to$ N*(1520) space-like data for $Q^2 = -q^2 > 1.5$ GeV^2, where the meson cloud contribution is supposed to be negligible.

The meson cloud form factors are parametrized as:

$$\begin{aligned}
G_M(q^2) &= (1 - a_M q^2)\lambda_\pi^M \left(\frac{\Lambda_M^2}{\Lambda_4^2 - q^2}\right)^3 F_\pi(q^2)\tau_3 && (7.44)\\
G_E(q^2) &= \lambda_\pi^{(4)} \left(\frac{\Lambda_4^2}{\Lambda_M^2 - q^2}\right)^3 F_\pi(q^2)\tau_3 - G_M(q^2) && (7.45)\\
G_C(q^2) &= \lambda_\pi^C \left(\frac{\Lambda_C^2}{\Lambda_C^2 - q^2}\right)^3 F_\pi(q^2)\tau_3 && (7.46)\\
& && (7.47)
\end{aligned}$$

$F_\pi(q^2)$ is a parametrization of the pion electromagnetic form factor. The parameters a$_M$, $\lambda_\pi^{(4)}$, λ_π^C, λ_π^M, $\Lambda_\pi^{(4)}$, Λ_π^C, Λ_π^C are adjusted so that the model reproduces the space like $\gamma^\star$ N $\to$ N(1520) data. Fig. 7.10 shows the results of the model compared to the space-like data for the magnetic, electric and Coulomb form factors. It can be observed that the meson cloud contribution is dominating at low q^2. It decreases more rapidly than the bare quark contribution, which is the leading contribution above 2 GeV^2. The model gives a good description of the existing data. In particular, it reproduces the values of the form factors at q^2=0 (photon-point).

Form factors in the time-like region have been calculated using these ingredients. As shown in Fig. 7.11, the meson cloud contribution strongly dominates in the time-like region. The bare quark contribution is only visible close to the ω meson pole in G_E and G_M and the interference with the meson cloud contribution induces a sharp structure in the total form factor. Since, in the model, only the bare quark contribution depends on the mass of the resonance, the overall form factor is almost independent on the resonance mass, as can also be observed in the Fig. 7.12, which displays the effective form factor $|G_T|$ (see Eq. 7.15). The broad structures slightly below 1 GeV^2 are due to cut-off parameters $\Lambda_\pi^{(4)}, \Lambda_\pi^C, \Lambda_\pi^C$ in Eq. 7.47. The structure at 0.3 GeV^2 is due to the combined effect of the cut-off and of the pion electromagnetic form factor. It has to be noted that this structure is very prominent for $|G_C|$ form factor, but it is much weaker for $|G_E|$ and almost invisible in $|G_M|$. The structure is then washed out in the effective form factor behavior, where $|G_M|^2$ is weighted by a factor of 3 relative to $|G_E|^2$ and $|G_C|^2$ is suppressed by the factor $q^2/2W^2$.

The differential cross section as a function of the e^+e^- invariant mass for the Dalitz decay of the N(1520) is shown in Fig. 7.13. We have noticed that the form factors do not depend on the resonance mass in the model. However, a very strong effect is seen in the invariant mass distribution, when the resonance mass gets higher, due to the increase of the maximum value of the invariant mass. The effect is however already very large at the

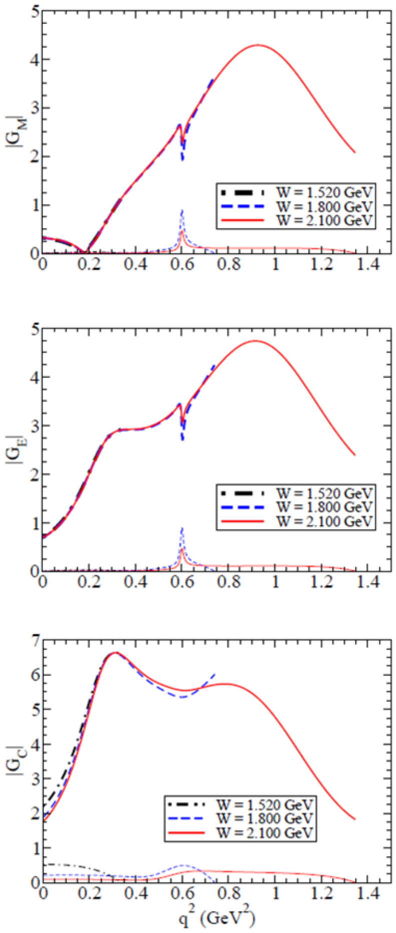

Figure 7.11: Modulus of the form factors in the time like region for different masses of the N(1520) resonance. The full and thin lines represent the full calculation and the contributions from the core, respectively [133].

pole mass (m^*=1.52 GeV/c^2). The effect of the form factor can be clearly quantified by comparing the results of the model to a calculation of the differential cross sections with a constant form factor corresponding to the values at the photon point (Sec. 7.3.2).

7.4 Transport models

Transport models are useful tools in particular to describe heavy-ion collisions. Their advantage is to cover the full space-time evolution of a collision. They allow to calculate the trajectories and the production of new particles using inputs on cross sections and differential distributions. The particles are treated as wave packets to take into account the quantum effects, but no interference between the amplitudes of the different processes is taken into account. These models need inputs from elementary reactions (πN or NN) which are sometimes very poorly known. It is therefore important to test models on new data in elementary reactions when available.

Predictions for the $\pi^- p \to n e^+ e^-$ reaction were not published, but as discussed in Sec. 8.2.7, we compared our data with the GiBUU transport model predictions. GiBUU uses the Boltzmann-Uehling-Uhlenbeck equations. It provides a unified framework for various types of reactions (pA, πA, γA, eA, A, AA, where A is a nucleus). GiBUU was successfully used for the description of HADES data in proton-induced and heavy-ion

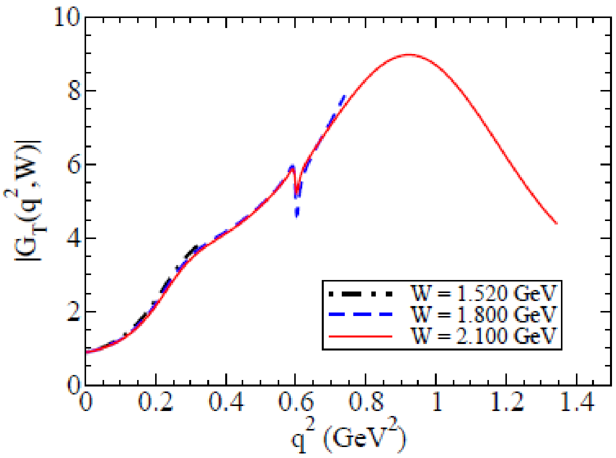

Figure 7.12: Effective form factor for the time-like N-N(1520) transition.

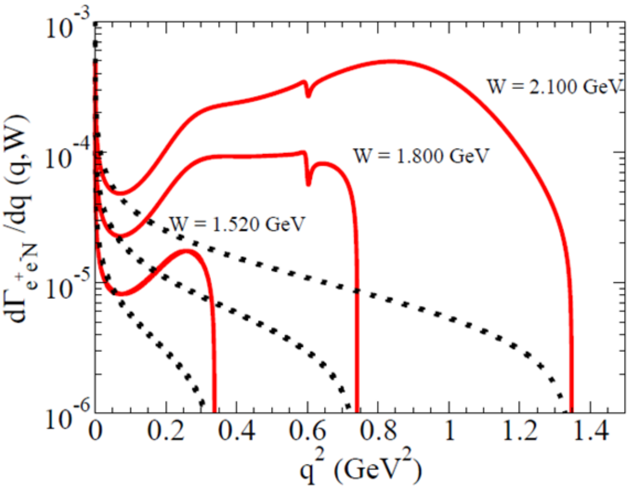

Figure 7.13: Differential dilepton invariant mass distribution for the Dalitz decay of a $3/2^-$ isopin 1/2 resonance for three different masses. The red curves show the result of the model and the black dashed curve the calculation assuming a constant form factor.

reactions [46] and can be publicly downloaded [134].

7.5 Results from partial wave analysis of π^-p reactions

New partial wave analysis of double pion production channels

The present analysis is focused on the e^+e^- production in pion induced experiments at a pion momentum of 0.69 GeV/c. During the same data taking period, shorter measurements have been performed at three other pion momenta (0.656, 0.748 and 0.8 GeV/c) with the HADES detector in order to measure pion production.

The obtained two-pion ($\pi^+\pi^-n$ and $\pi^0\pi^-p$) data samples have been included in the multichannel Partial Wave Analysis (PWA) of Bonn-Gatchina together with other world data on single and double pion production in photon, pion and electron induced reactions. The PWA analysis has been performed by Andrey Sarantsev using the method described in detail in [135]. The total amplitude is written as the sum of resonant and non-resonant

reaction	Observable	$\sqrt{s}$ (GeV)	Experiment
γ p $\rightarrow \pi^0\pi^0$p	DCS, Tot	1.2-1.9	MAMI
γ p $\rightarrow \pi^0\pi^0$p	E	1.2-1.9	MAMI
γ p $\rightarrow \pi^0\pi^0$p	DCS, Tot	1.4-2.38	CB-ELSA
γ p $\rightarrow \pi^0\pi^0$p	P, H	1.45-1.65	CB-ELSA
γ p $\rightarrow \pi^0\pi^0$p	T, P$_x$, P$_y$	1.45-2.28	CB-ELSA
γ p $\rightarrow \pi^0\pi^0$p	P$_x$, P$_x^c$,P$_x^s$ (4D)	1.45-1.8	CB-ELSA
γ p $\rightarrow \pi^0\pi^0$p	P$_y$, P$_y^c$,P$_y^s$ (4D)	1.45-1.8	CB-ELSA
γ p $\rightarrow \pi^+\pi^-$p	DCS	1.7-2.3	CLAS
γ p $\rightarrow \pi^+\pi^-$p	I^c, I^s	1.74-2.08	CLAS
π^-p $\rightarrow \pi^0\pi^0$n	DCS	1.29-1.55	Crystall Ball
π^-p $\rightarrow \pi^-\pi^+$n	DCS	1.45-1.55	HADES
π^-p $\rightarrow \pi^0\pi^-$p	DCS	1.45-1.55	HADES

Table 7.2: Information about the data sets used in the Partial Wave Analysis. "DCS" stands for differential cross section, "Tot" for total cross sections , the other observables are various polarization observables [69].

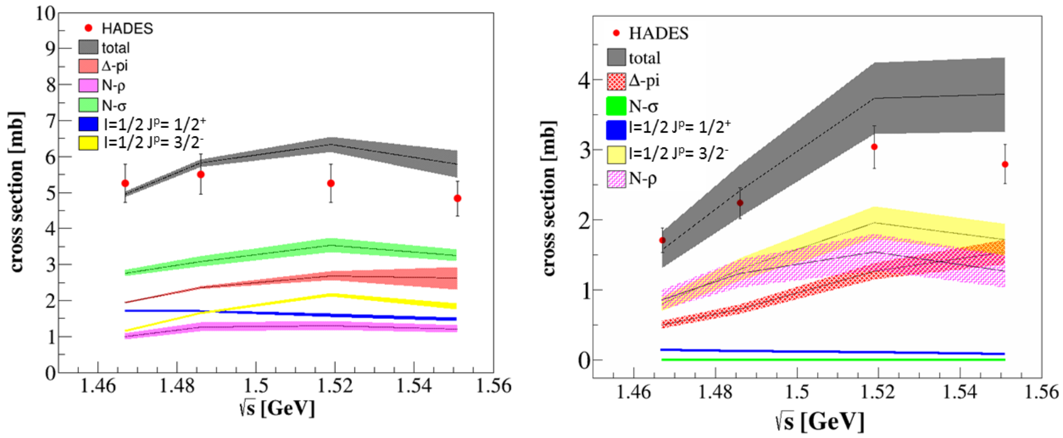

Figure 7.14: Total cross sections measured by HADES for the $\pi^+\pi^-$ n (left) and $\pi^-\pi^0$p (right) channels are shown in comparison with the results of the PWA (grey:total, red:$\Delta\pi$, green: Nσ, pink: Nρ, yellow: I =1/2 J^P=3/2$^-$, blue: I =1/2 J^P=1/2$^+$).

amplitudes for the different partial waves in the entrance and exit channels. The angular distributions of the decay products are fixed by the spin and parity of each partial wave in the exit channel.

The weight of each amplitude is extracted from the data on a event-by-event basis using a maximum-likelihood method. The likelihood function takes into account the distortion of the measured events by experimental effects. This is realized using the distribution of events generated according to the phase space distribution and passed through the simulation including detector response and signal reconstruction.

The data used for the PWA are listed in the Table 7.2. In the region around $\sqrt{s}$=1.5 GeV, precise data were provided for the $\pi^0\pi^0$ production channel in photoproduction by MAMI [136] and ELSA and in pion induced production by Crystal Ball [80]. The situation is very different for the $\pi^-p \rightarrow \pi^-\pi^+n$ and $\pi^-p \rightarrow \pi^0\pi^-p$ channels. As discussed in Sec. 1.5.1, these channels were very poorly measured before our HADES experiment. Still some cross section measurements with precision of about 10% were existing as well as some scarce differential distributions included in the Manley analysis [67]. The new HADES data are therefore very important to determine the 2πN branching ratios, because the different isospin channels bring complementary constraints to the PWA.

This is illustrated in Fig. 7.14 where the results of the PWA are shown in comparison with HADES data for the $\pi^+\pi^-\ n$ (left) and $\pi^-\pi^0 p$ (right) channels and in Fig. 7.15 which shows the comparison to the total cross sections measured by Crystal Ball for the π^-p$\rightarrow \pi^0\pi^0 n$ (left) and CB-ELSA for the $\gamma p\ \rightarrow\ \pi^0\pi^0 p$ channel. Due to isospin constraints, the ρ contribution is absent in the $\pi^0\pi^0$ channels and the N-σ contribution does not contribute in the $\pi^-\pi^0$ channel.

The presence of the N(1440) resonance can be clearly seen in the J^P=1/2$^+$ wave (yellow band in Figs 7.14 Left and Right and green curve in Fig. 7.15 Left). However, the amplitude has a flat behavior at larger energies due to the non-resonant contributions. This trend is particularly visible in the N-σ channel, while the $\Delta\pi$ contribution to the 1/2$^+$ wave shows a broad maximum at the mass of the N(1440) resonance. The N(1520) resonance shows up very clearly in the 3/2$^-$ contribution (yellow band in Figs 7.14 Left and Right and green curve in Fig. 7.15 Left). The Nρ and Nσ total components (pink and green bands in Figs 7.14 Left and Right) also display a resonant behavior in the vicinity of the N(1520). However, at the peak of the resonance, the contribution of the 3/2$^-$ wave is less than 50% of the total cross section. The rest is due to the 1/2$^+$, which has a strong contribution in the $\pi^0\pi^0$ and $\pi^-\pi^+$ channels, but also to 1/2$^-$ (not shown) as well as to interferences with isospin 3/2 waves.

The $\Delta\pi$ contribution does not present a structure at the N(1520) mass. It seems therefore that it is the most affected by non-resonant contributions and interferences.

The $\gamma p \rightarrow \pi^0\pi^0 p$ reaction is dominated by the $\Delta\ \pi$ contribution. At higher energies, one can see the contribution from cascade decays of higher lying states into N(1440)π, N(1520)π, N(1680)π.

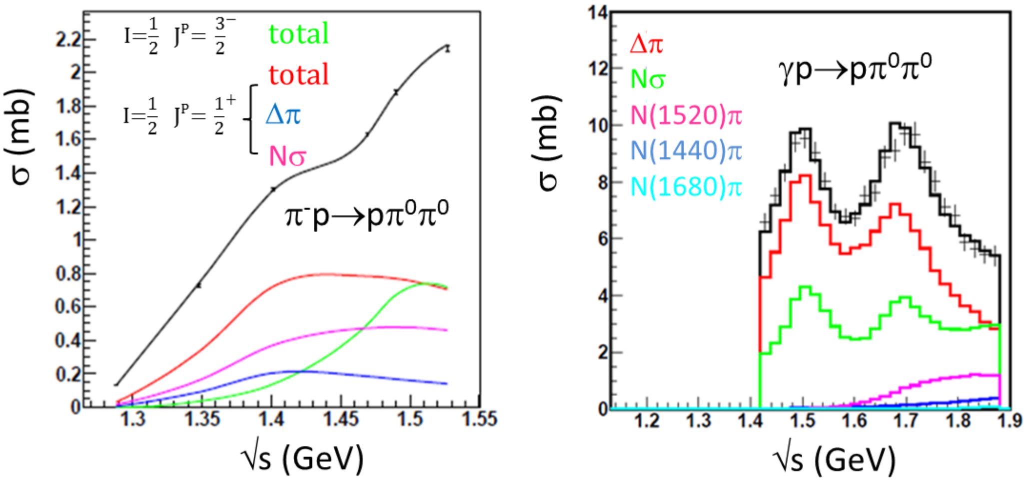

Figure 7.15: Total cross sections measured by Crystal Ball for the $\pi^- p\ \rightarrow \pi^0\pi^0 n$ (left) [64] and by MAMI for the $\gamma p \rightarrow\ p\pi^0\pi^0$ channel [137] are shown in comparison with the results of the PWA (Color code for the left plot: black: total, green: I =1/2 J^P=3/2$^-$, red: I =1/2 J^P=1/2$^+$ (total), blue: I =1/2 J^P=1/2$^+$ ($\Delta\pi$), pink= I =1/2 J^P=1/2$^+$ Nσ. Right plot: black: total, green: Nσ, red:$\Delta\pi$, blue: N(1440) π, pink: N(1520)π, cyan: N(1680) π.

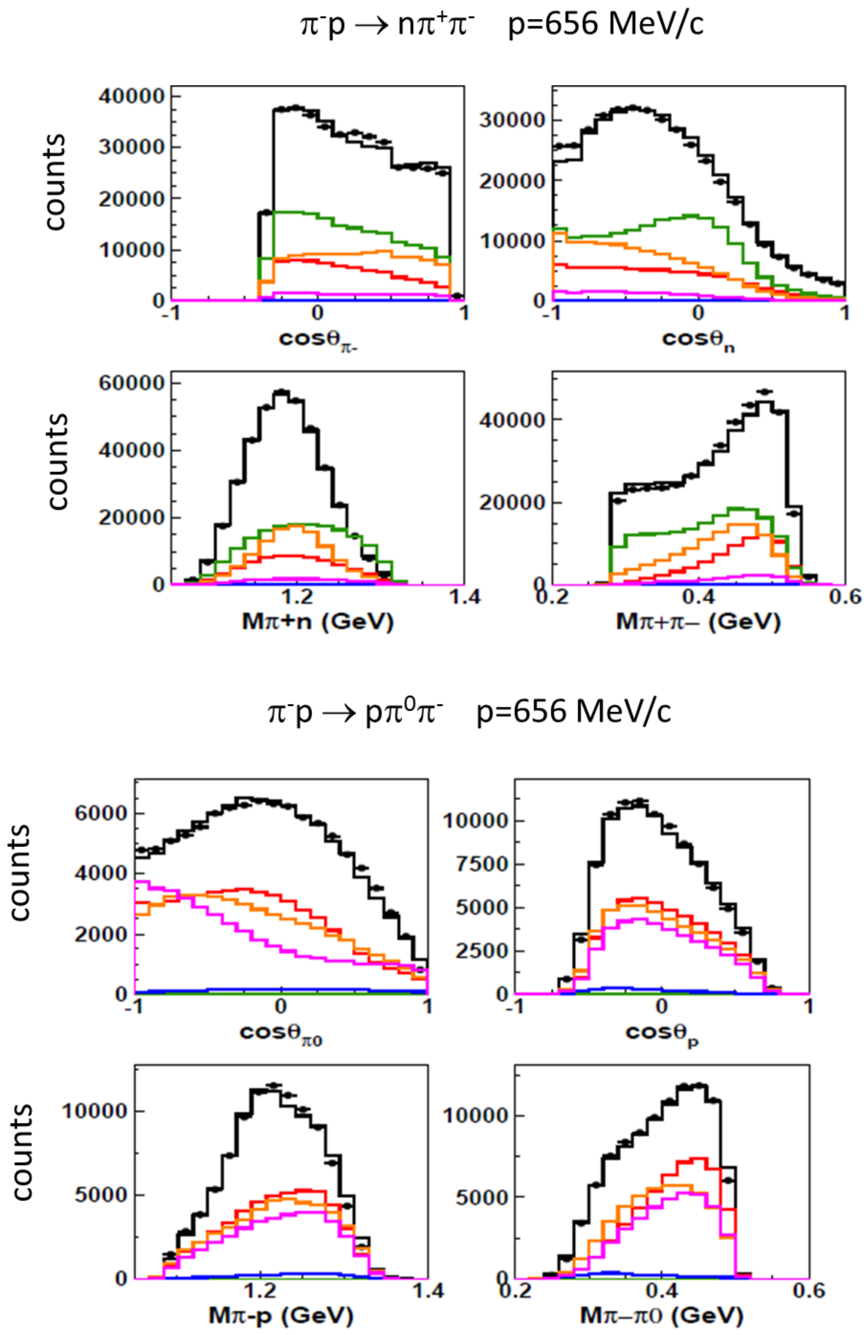

Figure 7.16: Examples of distributions measured by HADES at an incident pion momentum of 656 MeV/c in the reaction π^-p→n $\pi^+\pi^-$ (top) and π^-p→p $\pi^-\pi^0$ (bottom) in comparison with the PWA results. Black: total, red:$\Delta\pi$, green: Nσ, pink: Nρ, yellow: I =1/2 J^P=3/2$^-$, blue: I =1/2 J^P=1/2$^+$.

Determination of branching ratios

The new PWA analysis allows for a new determination of the branching ratios to the different 2πN channels of the various baryons from the N(1440) up to Δ(1905) [138]. This is particularly important, since, as already said, these values have been removed from the Review of the Particle Properties, due to the ambiguity of previous analysis based on too scarce data. The HADES data for $\sqrt{s}$ close to 1.5 GeV and are therefore crucial to

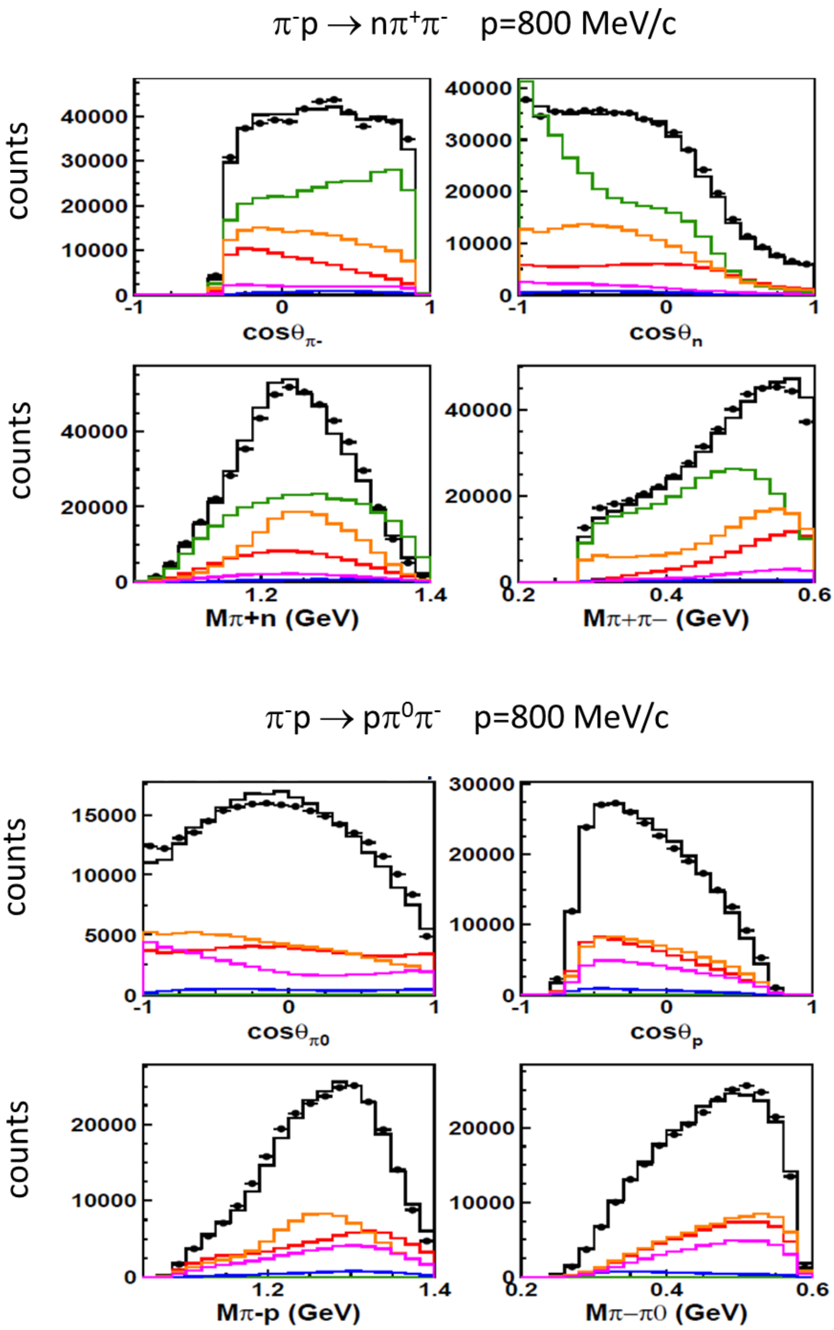

Figure 7.17: Same as Fig. 7.16 for a pion momemtum of 800 MeV/c.

determine the branching ratios of resonances in the N(1440), N(1535) and N(1520) and N(1650). As an example, the branching ratios to the ρN channel which are important for calculations of the in-medium spectral function of the ρ meson are displayed in Table 7.3. These new results might therefore impact the calculations of the emissivity of strongly interacting matter.

$\Delta\pi$ and ρ production in π^-p reaction

Figs. 7.16 and 7.17 show the description of the HADES data in the channels $\pi^- p \to \pi^- \pi^+ n$ and $\pi^- p \to \pi^+ \pi^0 p$, respectively for pion momenta of 656 MeV/c and 800 MeV/c [139].

resonance	N(1440) $1/2^-$	N(1520) $3/2^-$	N(1535) $1/2^+$	N(1650)$1/2^-$
ρ coupling	<1%	11±1.5 %	3 ±1%	8±2%

Table 7.3: Branching ratios for the decays to ρN channels from the PWA.

One can clearly see that the individual components differ in the various distributions and have a different evolution with energy. This illustrates how the distinct contributions can be extracted from the data measured at the diverse energies. One can also observe that, due to the interferences between the ΔN, σN and ρN contributions in the same partial waves, the total deviates from the incoherent sum of the individual contributions.

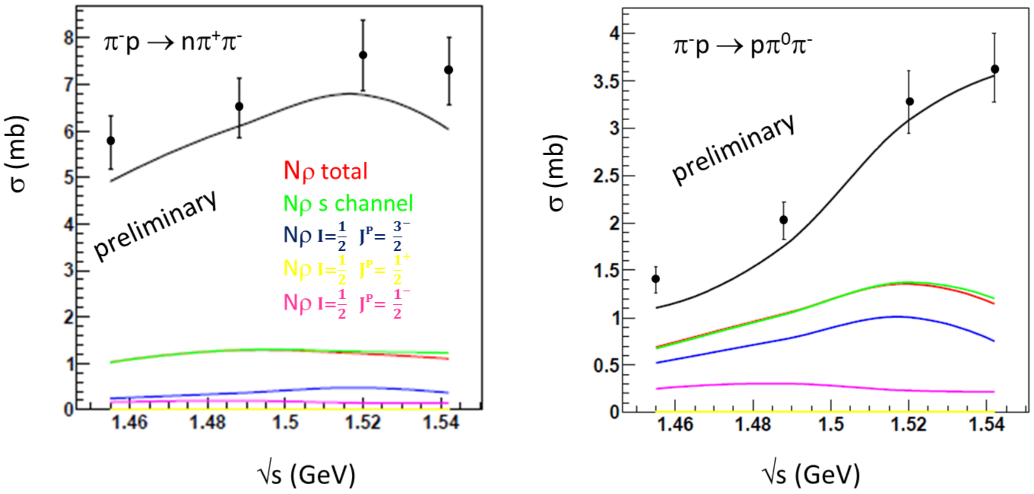

Figure 7.18: The different ρN contributions are shown in comparison with total cross sections for $\pi^-p \to n\pi^+\pi^-$ (left) and $\pi^-p \to p\pi^0\pi^-$ (right). Red: total, green: s channel, blue I =1/2 J^P=3/2 $^-$, yellow I =1/2 J^P=1/2$^+$, pink I =1/2 J^P=1/2$^-$.

In the π^-p reaction, the 2π channels contain contributions of $\Delta^+\pi^-$, $\Delta^0\pi^0$ and $\Delta^-\pi^+$:

$$\pi^-p \to \Delta^-\pi^+ \to n\pi^+\pi^- \quad I=\tfrac{1}{2}:\tfrac{2}{3}\times\tfrac{1}{2}\times 1=\tfrac{1}{3} \quad I=\frac{3}{2}:\frac{1}{3}\times\frac{2}{5}\times 1=\frac{2}{15} \tag{7.48}$$

$$\pi^-p \to \Delta^+\pi^- \to n\pi^+\pi^- \quad I=\tfrac{1}{2}:\tfrac{2}{3}\times\tfrac{1}{6}\times\tfrac{1}{3}=\tfrac{1}{27} \quad I=\frac{3}{2}:\frac{1}{3}\times\frac{8}{45}\times\frac{1}{3}=\frac{1}{54} \tag{7.49}$$

$$\pi^-p \to \Delta^+\pi^- \to p\pi^0\pi^- \quad I=\tfrac{1}{2}:\tfrac{2}{3}\times\tfrac{1}{6}\times\tfrac{2}{3}=\tfrac{2}{27} \quad I=\frac{3}{2}:\frac{1}{3}\times\frac{8}{45}\times\frac{2}{3}=\frac{1}{27} \tag{7.50}$$

$$\pi^-p \to \Delta^0\pi^0 \to p\pi^-\pi^- \quad I=\tfrac{1}{2}:\tfrac{2}{3}\times\tfrac{1}{3}\times\tfrac{1}{3}=\tfrac{2}{27} \quad I=\frac{3}{2}:\frac{1}{3}\times\frac{1}{15}\times\frac{1}{3}=\frac{1}{135} \tag{7.51}$$

$$\pi^-p \to \Delta^0\pi^0 \to p\pi^0\pi^0 \quad I=\tfrac{1}{2}:\tfrac{2}{3}\times\tfrac{1}{3}\times\tfrac{2}{3}=\tfrac{4}{27} \quad I=\frac{3}{2}:\frac{1}{3}\times\frac{1}{15}\times\frac{2}{3}=\frac{2}{135} \tag{7.52}$$

The isospin factors are indicated in the first column for I =1/2 states and in the second column for I =3/2 states in the π^-p system, respectively. They are written as a product of the isospin factors for the π^-p coupling to a I =1/2 or 3/2 state in the entrance channel, the coupling of this state to $\Delta\pi$ and finally the decay of the Δ into πN. One can see from these isospin factors that the $\pi^0\pi^0p$ channel has a very small sensitivity to the I =3/2 states, and only the $\Delta^0\pi^0$ contributes in this exit channel. The $\pi^+\pi^-p$ has the largest sensitivity to I =3/2 states. It is populated by both $\Delta^-\pi^+$ and $\Delta^+\pi^-$ but the weight for the latter is much reduced. One can use these isospin factors to write the following relations between the amplitudes A$_N$ and A$_\Delta$ for the production of I =1/2 and I =3/2 states on the one side and the amplitudes A($\Delta^+\pi^-$), A($\Delta^-\pi^+$), A($\Delta 0\ \pi^0$) for the different $\Delta\pi$ states:

$$A(\Delta^+\pi^-) = \frac{-1}{3}A_N + \sqrt{\frac{8}{45}}A_D \tag{7.53}$$

$$A(\Delta^-\pi^+) = \frac{-1}{\sqrt{3}}A_N - \sqrt{\frac{2}{15}}A_D \tag{7.54}$$

$$A(\Delta^0\pi^0) = \frac{\sqrt{2}}{3}A_N - \sqrt{\frac{1}{45}}A_D \tag{7.55}$$

If one takes into account only the dominant I =1/2 states, one can derive the following relation, using the isospin factors for the coupling of I =1/2 to $\Delta\pi$ (second term in the first bracket)

$$\sigma(\pi^-p \to \Delta^-\pi^+) = 3 \times \sigma(\pi^-p \to \Delta^+\pi^-) = \frac{3}{2} \times \sigma(\pi^-p \to \Delta^0\pi^0) \tag{7.56}$$

The PWA of the two pion channels allows to extract the different contributions unambiguously. For the energy point relevant for our analysis, the cross sections for the different $\Delta\pi$ charge states are displayed in Table 7.4. One can observe that the $\Delta^-\pi^+$ is the largest contribution. However, the isospin relations differ from Eq. 7.56, due to the contribution of I =3/2 states. Only the $\Delta^+\pi^-$and $\Delta^0\pi^0$ contributions are to be considered for the dilepton production via the Δ Dalitz decay process, as discussed in Sec. 8.2.2. We can also notice that their ratio is different from 1/2, which would be the expected ratio in the case of pure I =1/2 intermediate states.

$\sqrt{s}$ (GeV)	$\Delta^+\pi^-$	$\Delta^0\pi^0$	$\Delta^-\pi^+$
1.487	0.779	1.041	2.009

Table 7.4: Squared amplitudes (mb) for the $\Delta\pi$ channel in the π^-p reaction in the different isospin states.

One can in fact also calculate the contributions of the I =1/2 and 3/2 states.

By squaring each member of the equations Eq. 7.55, one can deduce the contributions $|A_N|^2$ and $|A_\Delta|^2$ of I =1/2 and I =3/2 states to the cross section:

$$|A_N|^2 = 4\left|A(\Delta^0\pi^0)\right|^2 - \left|A(\Delta^+\pi^-)\right|^2 + \frac{2}{3}\left|A(\Delta^-\pi^+)\right|^2 \tag{7.57}$$

$$|A_\Delta|^2 = -5\left|A(\Delta^0\pi^0)\right|^2 + 5\left|A(\Delta^+\pi^-)\right|^2 + \frac{5}{3}\left|A(\Delta^-\pi^+)\right|^2 \tag{7.58}$$

$$\Re(A_N A_D j) = -\frac{1}{6}\sqrt{(}5/2) * (6\left|A(\Delta^0\pi^0)\right|^2 - 5\left|A(\Delta^-\pi^+)\right|^2 + \frac{5}{3}\left|A(\Delta^+\pi^-)\right|^2) \tag{7.59}$$

Using the numbers for $\left|A(\Delta^0\pi^0)\right|^2$, $|A(\Delta^+\pi^-)|^2$ and $|A(\Delta^-\pi^+)|^2$ listed in Table7.4, one can deduce the values:

$$|A_N|^2 = 4.7\ mb \ \text{ and } \ |A_\Delta|^2 = 2.0\ mb \tag{7.60}$$

with a phase between A_N and A_Δ of 68°.

This confirms that the I =1/2 states dominate in the π^-p reaction, but the contribution of I =3/2 is not negligible.

The extraction of the ρ contribution is also of high importance for our analysis, since it can be directly connected to a dilepton contribution, using the VDM formalism. The most recent version of the PWA analysis provides a contribution of 1.3 ± 0.2 mb at an incident pion momentum of 0.7 GeV/c for this contribution. The contributions of the different waves to the ρN channel in the $\pi^- p \to \pi^0\pi^-$n and π^-p $\to \pi^0\pi^-$p are displayed in Fig. 7.18 in comparison with HADES data. As expected from the ρN couplings of the different resonances (Tab. 7.3), the ρ contribution is much larger in the $3/2^-$ wave, corresponding to the N(1520) resonance and has only a small contribution in the $1/2^-$ and $1/2^+$ corresponding to the N(1535) and N(1440) respectively. Another interesting result is the fact that the ρ contribution comes mainly from the s channel [138].

7.5.1 Results for $\gamma n \to \pi^- p$

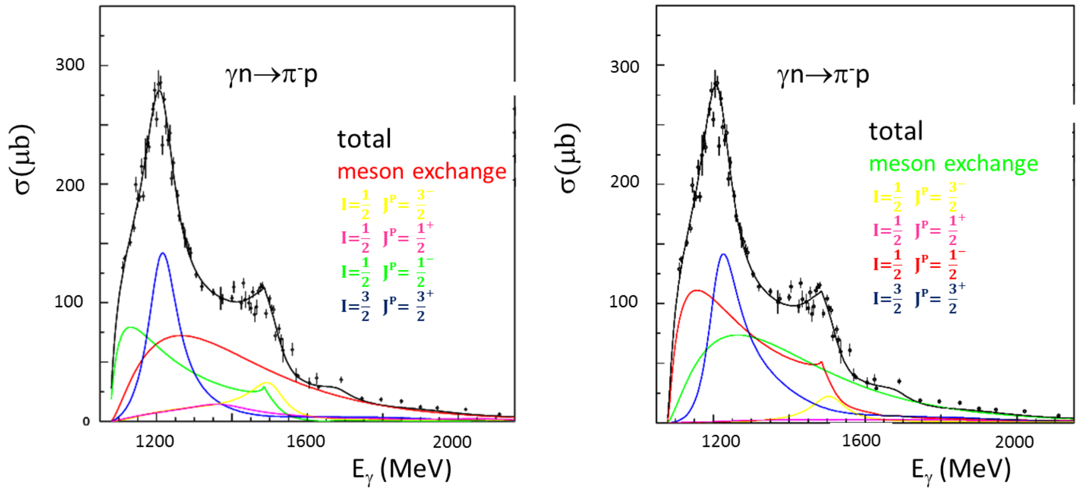

Figure 7.19: Left: cross sections from $\gamma n \to \pi^-$p compared to the Bonn-Gatchina PWA solution (black curve) [138]. The main components are displayed as colored curves. Right: same as left, but only the s channel contribution of each partial wave is shown.

As mentioned in Sec. 1.4, the reaction

$$\pi^- p \to \gamma^*(e^+e^-)n \tag{7.61}$$

is the inverse reaction with respect to

$$\gamma^* n \to \pi^- p. \tag{7.62}$$

Data exist for the latter reaction, when the virtual photon is produced in electron scattering. However, the two reactions differ by the virtuality (q^2) of the virtual photon and hence by the different values of the form factors. Still, the connection can be made with the photoproduction reaction $\gamma n \to \pi^- p$, which gives important information on the partial waves contributing to the reaction (Eq. 7.61) in the limit of small q^2. The most precise data in our energy range have been produced by the Crystal Ball collaboration at BNL [140] using the $\pi^- p \to \gamma n$ reaction. It should however be mentioned that results for the reaction $\gamma n \to \pi^- p$ were also extracted by the CLAS collaboration at Jlab, from measurements with a deuterium target in a broad energy range [141]. These results are about 30% lower than the ones of the Crystal Ball collaboration. The left part of Fig. 7.19 shows the partial wave analysis of the Bonn-Gatchina group compared to the existing data for the $\gamma n \to \pi^- p$ reaction. In the right panel, only the s channel contribution for each wave is shown.

In the region of $\sqrt{s}$=1.5 GeV, the dominant contributions are the t channel meson exchange, the $3/2^-$ and the $1/2^+$, where we expect respectively the N(1520) and N(1440) contributions. It can be observed that the $1/2^+$ where we expect the N(1440) resonance has a small total contribution and negligible s channel contribution. As discussed in Sec. 7.5, this resonance has a strong contribution to the $\pi^-p \rightarrow \pi\pi n$ channels. However, this resonance has a weak electromagnetic coupling and does not contribute much in the γn case. There is still a contribution of the order of 10% of $3/2^+$ due to the tail of the Δ(1232).

The $3/2^-$ wave displays a clear resonant behavior at the N(1520) pole mass. By looking at the right panel of Fig. 7.19, it can be checked that it is dominantly due to the s channel. This is very different for the $1/2^-$ where the presence of the N(1535) does not show up as a peak in the cross section, even in the s channel. In the case of $1/2^-$, the s channel contribution is mainly due to non-resonant multi-particle intermediate states. It is estimated that only 35% of the s channel $1/2^-$ contribution is due to the N(1535) resonance. The discontinuity at $\sqrt{s}$=1.485 GeV, is due to the opening of the ηN channel which contributes to the $1/2^-$ partial wave, as expected due to the strong coupling to the N(1535). The $1/2^-$ contribution therefore results from the superposition of various effects. Around $\sqrt{s}$=1.5 GeV, the contributions of S11 and D13 to the total cross section are similar. However, in the s channel, the S11 contribution is twice as large as the D13. This is due to the destructive interferences between s and u channels which are very important for the $1/2^-$ wave.

The cross sections of the reactions $\pi^-p \rightarrow n\gamma$ and $\gamma n \rightarrow \pi^-p$ are related by the detailed balance equations:

$$\sigma(\pi^-p \rightarrow n\gamma) = 2\frac{k_\gamma^2}{k_\pi^2}\sigma(\gamma n \rightarrow \pi^-p) \tag{7.63}$$

where k_γ and k_π are the CM momenta of the γ and π respectively. The factor 2 arises from the different number of spin states in the entrance and exit channels. Indeed,

$$N_{\gamma n}^{states} = 4 \tag{7.64}$$

$$\text{and } N_{\pi^-p}^{states} = 2 \tag{7.65}$$

At $\sqrt{s}$=1.49 GeV, the photon and pion momentum in the CM are:

$$k_\gamma = 0.449\ GeV/c \tag{7.66}$$

$$\text{and } k_{\pi^-} = 0.456\ GeV/c \tag{7.67}$$

so

$$\sigma(\pi^-p \rightarrow n\gamma) = 2.14\ \frac{k_\gamma^2}{k_\pi^2}\ \sigma(\gamma n \rightarrow \pi^-p) \tag{7.68}$$

Using the cross sections extracted in the Bonn-Gatchina PWA for the $\gamma n \rightarrow \pi^-$p reaction and Eq. 7.68, the cross sections corresponding to the total and resonant s channel contributions for the I =1/2 $1/2^-$, I =1/2 $3/2^-$ and I =3/2 $3/2^+$ for the $\pi^-p \rightarrow \gamma n$ reactions at $\sqrt{s}$=1.49 GeV can then be calculated. The results are listed in Table 7.5. The production cross sections of the resonances can further be estimated as:

$$\sigma(\pi^-p \rightarrow N^*) = \frac{1.}{BR(N^* \rightarrow N\gamma)}\sigma(\pi^-p \rightarrow N^*(N^* \rightarrow N\gamma)) \tag{7.69}$$

(7.70)

The radiative decay branching ratios and production cross sections deduced from the Bonn-Gatchina PWA are indicated in Table 7.6

cross sections (μb) for π^-p$\rightarrow \gamma n$						
	I =1/2 J^P=1/2$^-$		I =1/2 J^P=3/2$^-$		I =3/2 J^P=3/2$^+$	
total	total	N(1535)	total	N(1520)	total	Δ(1232)
220	60	34	60	47	13	18

Table 7.5: Total cross sections for the π^- p $\rightarrow \gamma n$ and contributions deduced from the PWA for the total and resonant I =1/2 J^P=1/2$^-$, I =1/2 J^P=3/2$^-$ I =3/2 J^P=3/2$^+$ partial waves at $\sqrt{s}$=1.49 GeV.

	BR (N*/$\Delta \rightarrow N\gamma$)	$\sigma(\pi^-$p $\rightarrow N^*/\Delta)$ (mb)
N(1535)	0.35%	9.7
N(1520)	0.23%	20.4
Δ(1232)	0.6%	3

Table 7.6: Radiative decay branching ratio and production cross sections for N(1535), N(1520) and Δ(1232) resonances in π^-p reaction, as deduced from the Bonn-Gatchina PWA.

7.6 Density matrix formalism for angular distributions

From the various theoretical works discussed above, it is clear that the e^+e^- invariant mass distributions contain information about the different baryon transitions and about their electromagnetic structure. As first it was pointed out in [129], additional information can however be gained by studying the γ^* and individual lepton angular distributions (Fig. 7.20).

While for a given baryonic transition in the s channel, the center-of-mass polar angle of the virtual photon θ_{γ^*} distribution is a characteristic of the quantum numbers of the excited baryon, the distribution of the electron angle in the virtual photon reference frame (so-called helicity) also contains information on the electromagnetic structure of the transition. This induces a polarization of the virtual photon which will affect the electron angular distribution.

However, although the target nucleon is not polarized, the virtual photon can already be polarized due to the π-N interaction. Since the pion has spin zero, and the orbital angular momentum affects only the spin components perpendicular to the beam direction z, the spin projection of the nucleon J_z^p is not changed in the transition, *i.e.*:

$$J_z^{'} = J_z,$$

where J_z and $J_z^{'}$ are the spin components along the beam axis of the nucleon and resonance respectively. For a spin 1/2 resonance, it means that the transition does not polarize the

Figure 7.20: Definition of the angles in the center-of-mass (CM) and helicity frames

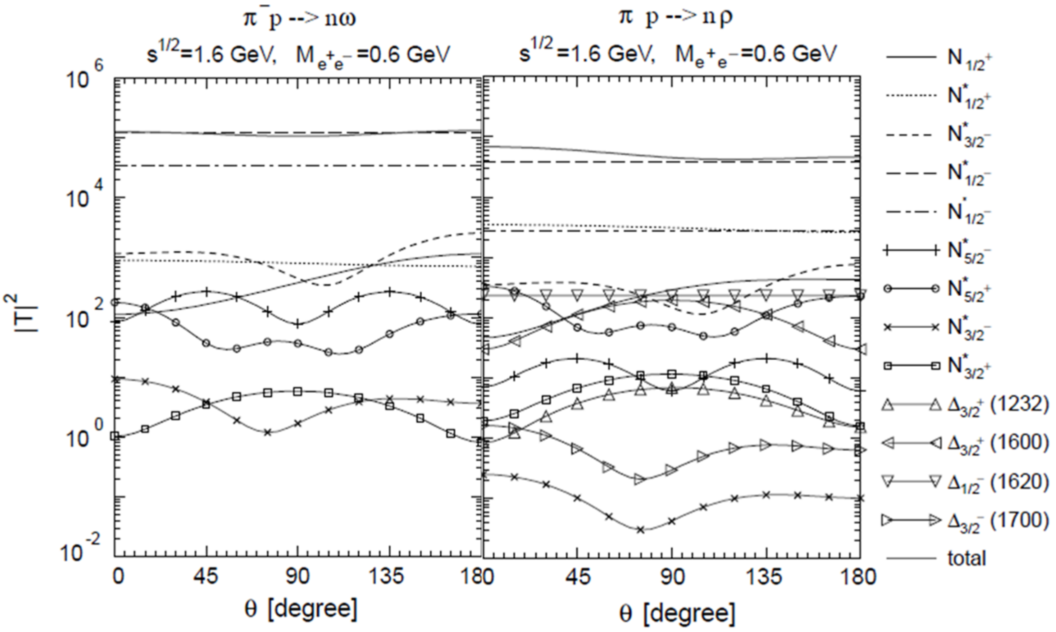

Figure 7.21: Angular distributions of the individual nucleon resonances to the amplitudes for ω (left) and ρ (right) contributions to the $\pi^- p \to ne^+e^-$ reactions at $\sqrt{s}$=1.6 GeV for M$_{ee}$=0.6 GeV.

resonance. Therefore the photon angular distribution is expected to be isotropic and the electron angular distribution will not depend on the photon angle. For resonances with spin $\geq 3/2$, however, the πN interaction induces polarization, due to the fact that only states with $J_z' = \pm 1/2$ can be populated. Therefore, the photon angular distribution presents in this case a more complex shape and the electron angular distribution will also depend on the virtual photon angle.

The dependence of the virtual photon angular distribution on the resonance quantum numbers can be seen in Fig. 7.21. The calculations have been performed in the approach of [129], but results are very general. One can notice small asymetries of the angular distributions for the baryon transitions due to the u channel contribution. The spin 1/2 resonances have almost isotropic distribution, while for the other resonances, one or several minima are observed. The forward/backward asymmetry is very clear for the nucleon (N 1/2+) contribution which is mainly due to the t channel (Fig. 7.1). For a given resonance, the shapes are identical for the isovector (ρ) and isoscalar (ω) channels, but the global angular distribution strongly depends on the ρN and ωN couplings of the different resonances.

The recent work of [142] is of high interest for our analysis, as it was performed at the same energy than our experiment. It is however exploratory since it only includes N(1440) and N(1520) u and s channel contributions, with transition form factors deduced from the VDM model [131] described above. This model also predicts a dominance of the s channel resonant contributions, with respect to the u channel. Therefore, the $\cos\gamma^\star$ distributions (Fig. 7.22) for the N(1440) and N(1520) are almost symmetric with respect to 0. However, a significant enhancement in the backward or forward direction, can arise depending on the sign of the interferences. It shows that the measurement of the virtual photon angular distributions can be useful to fix the unknown phases of these amplitudes.

To understand the information contained in the electron angular distribution, it is interesting to use the spin density matrix formalism. It allows for a convenient parametrization of the amplitudes at a given value of M_{ee} and emission angle of the virtual photon

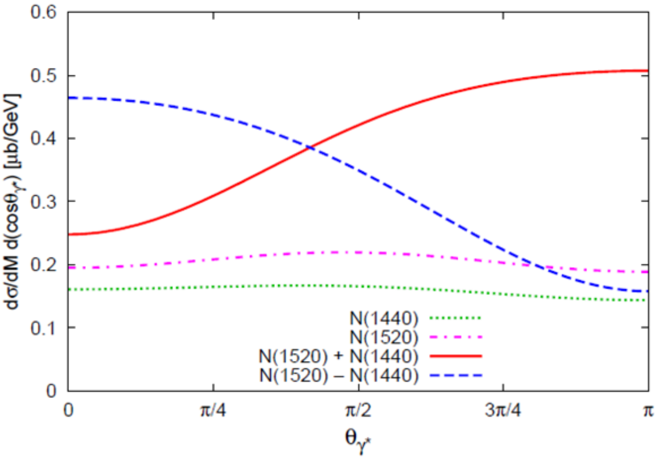

Figure 7.22: Predictions of the model of [142] for the $\pi^- p \to n e^+ e^-$ reaction at $\sqrt{s} = 1.49$ GeV: the double differential cross section is shown as a function of the virtual photon angle for an e^+e^- invariant mass of 0.5 GeV. The calculations using only one of the two dominant resonances, N(1440) and N(1520) are shown as dotted green and dash-dotted pink lines respectively. The dashed blue and full red lines show the result of the calculations with both contributions, assuming respectively a positive or a negative sign between the amplitudes of the two resonances.

θ_{γ^*} [142, 138] in the form

$$|A(\cos(\theta_e), \phi_e)|^2 \propto \quad 4k^2[1 - \rho_{11} + \cos^2\theta_e(3\rho_{11} - 1) + \sqrt{2}\sin(2\theta_e)\cos\phi_e Re\rho_{10} \\ + \sin^2\theta_e Re\rho_{1-1}\cos(2\phi_e)]. \tag{7.71}$$

Here, k^2, θ_e and ϕ_e denote the momentum, polar angle and azimuthal angles of the lepton in the virtual photon reference frame, respectively. Note that with respect to the more general formula of [142], two simplifications were introduced to reduce the number of parameters [138]. First, the azimuthal angle is measured with respect to the reaction plane and, second, the normalization of the coefficients is chosen such that $\rho_{00} + 2\rho_{11}$=1.

After integration of the amplitude (Eq. 7.71) over the azimuthal angle ϕ_e, one gets:

$$\frac{d\sigma}{dMd\cos(\theta^*_\gamma)d\cos(\theta_e)} \propto \Sigma_\perp(1 + \cos^2\theta_e) + \Sigma_\parallel(1 - \cos^2\theta_e), \tag{7.72}$$

where $\Sigma_\perp = \rho_{11}$ and $\Sigma_\parallel = 1 - 2\rho_{11}$ are the contributions of the transverse and longitudinal polarizations of the intermediate photon to the differential cross sections. For the real photon, there is no longitudinal contribution, hence ρ_{11}=1/2. Eq. (7.72) can also be written as:

$$\frac{d\sigma}{dMd\cos(\theta^*_\gamma)d\cos(\theta_e)} \propto 1 + \lambda\cos^2\theta_e, \tag{7.73}$$

where

$$\lambda = \frac{3\rho_{11} - 1}{1 - \rho_{11}}. \tag{7.74}$$

The anisotropy coefficient is λ=1 for real photons.

In [129], predictions for the ρ_{00} parameter at $\sqrt{s}$ larger than 1.6 GeV have been provided, showing a strong dependence to the coupling parameters of the baryon resonances to the ρ and ω mesons which affect the respective resonant contributions.

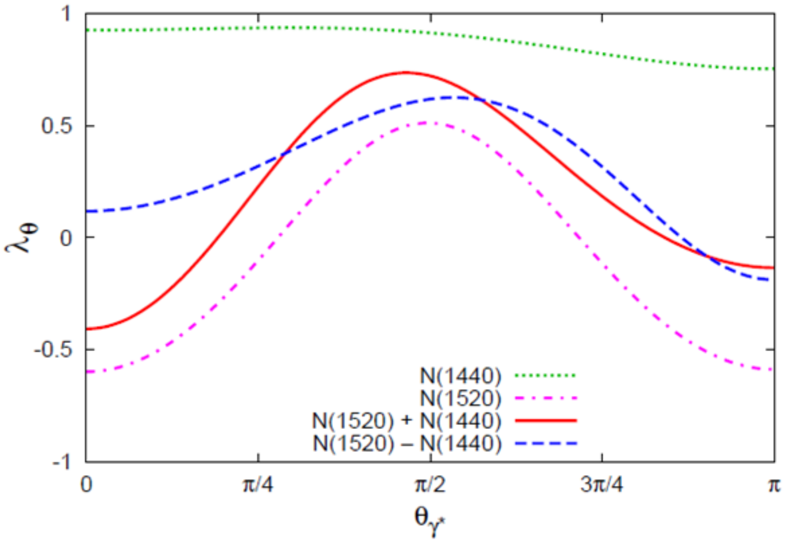

Figure 7.23: Same as Fig. 7.22 for the anisotropy coefficient of the γ^* angular distribution.

In the model [142], the anisotropies of the electron angular distributions have also been scrutinized (Fig. 7.23). As expected, for the spin 1/2 N(1440), the anisotropy has a very small dependence on the θ_{γ^*} angle, which is only due to the u channel contribution, while this dependence is much larger for the spin 3/2 N(1520) resonance, with a maximum of the anisotropy parameter for a virtual photon angle close to $\theta_{\gamma^*}=\pi/2$. In the case of the N(1440) resonance, the anisotropy parameter is close to 1, which means that there is a strong dominance of transverse photons. In the case of the N(1520), the anisotropy parameter is smaller, with a dominant longitudinal trend at 0° and 180° and a more transverse trend at 90°. The global trend follows roughly the N(1520) behavior. The dependence of the anisotropy coefficient as a function of the invariant mass is also interesting (see fig. 7.24). As expected, at low invariant masses, virtual photons behave like real photons, *i.e.* with only a transverse polarization, while the longitudinal polarization component

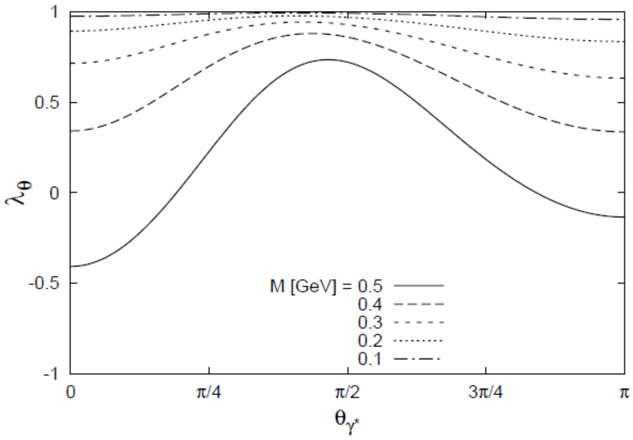

Figure 7.24: The anisotropy coefficient λ_θ as a function of the virtual photon polar angle for various dilepton masses [142] in the reaction $\pi^- p \to n e^+ e^-$ at $\sqrt{s}$=1.49 GeV . The contributions of s and u channel diagrams of the N(1440) and N(1520) and their interference term (with a positive relative sign) are included.

increase at large invariant masses.

7.7 Conclusion

Several predictions exist for the differential cross sections as a function of e^+e^- invariant mass in the reaction $\pi^- p \to n e^+ e^-$. These approaches show the sensitivity of these distributions to the underlying baryon electromagnetic transitions. We will show in the next chapter the comparison of these predictions to our data. The density matrix formalism offers a model-independent way to analyze the angular distributions at given e^+e^- invariant mass and virtual photon angle. We will also show in the next chapter how the coefficients of this matrix can be extracted from the data and compared to Speranza *et al.* [142].

Chapter 8

Results and discussion

This chapter is devoted to the interpretation of e^+e^- data measured by HADES in π^- induced reactions. Our results will be compared to model calculations, on the one hand on a simple event generator using ingredients from available data and, on the other hand on several theoretical approaches described in Chapter 7. We start by describing in Sec. 8.1 the general procedure for data/model comparison. Then in Sec. 8.2, we explain how a cocktail of dilepton sources can be constructed based on various experimental information and we discuss the comparison of simulated e^+e^- invariant mass distributions with the data in the case of both inclusive and exclusive e^+e^- production. Sec. 8.3 and Sec. 8.4 are devoted to the comparison of e^+e^- invariant mass spectra to the predictions of [130] and [143] respectively. In Sec. 8.5 we discuss the analysis of the angular distributions and the extraction of the spin density matrix coefficients.

8.1 General procedure for data/model comparison

A direct comparison of reconstructed data to model predictions is not possible, since the experimental distributions are distorted by the HADES acceptance and efficiency. As discussed in Chapter 6, efficiency effects can be corrected for in a model independent way, while it is difficult to achieve this for the acceptance corrections. We have also seen that, due, in particular to the strong bremsstrahlung effect, the reconstructed momentum is highly distorted with respect to the ideal one (Sec. 6.1.3). It is therefore needed to take the acceptance, but also the momentum and angle distortion effects into account when comparing model to data.

The first step of the procedure consists in generating a large number of events, either directly sampled according to the theoretical distributions, or generated according to phase space. In the latter case, a weight proportional to the differential cross section is attributed to each event and will be applied to generate the distributions.

For each channel, the incident pion momentum distribution is taken into account to calculate the kinematics of the emitted particles and an average cross section is used to normalize the differential distributions. These events are then passed through the simulation and analysis tool, so that both events inside the HADES acceptance and reconstructed events can be identified. After normalization, the distributions of reconstructed events can be compared to raw data. Another possibility which avoids full reconstruction of simulated events is to compare efficiency corrected data to the distributions of simulated events in acceptance. In this case, the smearing of the kinematical variables needs to be applied to the simulated events (see Sec. 6.1.3).

8.2 Dilepton cocktails simulated with the Pluto event generator

Dilepton cocktails consist of an incoherent sum of dilepton sources parametrized with simple ansatz. They are commonly used in transport models where different parametrizations for total and differential cross sections are used. Using the Pluto event generator developed by the HADES collaboration [35], we built our own dilepton cocktail to describe the data. This cocktail includes:

- the π^0 Dalitz decay ($\pi^0 \rightarrow \gamma e^+e^-$);
- the η Dalitz decay ($\eta \rightarrow \gamma e^+e^-$);
- the baryon Dalitz decays (N/$\Delta \rightarrow$Ne^+e^-) ;
- the off-shell ρ contribution ($\rho \rightarrow e^+e^-$).

In the Vector Dominance Model (see Sec. 7.3.2), the off-shell ρ contribution can be considered as a way to take into account baryon time-like electromagnetic form factors. Since the time-like electromagnetic form factor model of [133] is also available (see Sec. 7.3.2), for the N-N(1520) transition, we also performed simulations using this form factor model, instead of the off-shell ρ contributions.

8.2.1 Contribution of pseudo-scalar mesons

Treatment of the Dalitz decays

The branching ratios for the π^0 Dalitz decay ($\pi^0 \rightarrow \gamma\ e^+e^-$) and η Dalitz decay ($\eta \rightarrow \gamma e^+e^-$) are respectively 1.2% and 6.9 10^{-3}. For the differential decay width, the Pluto event generator uses expressions derived from QED with transition form factors to take into account the internal hadronic structure [144]:

$$\frac{d\Gamma(M_{ee})}{\Gamma^{A\rightarrow 2\gamma} dM_{ee}} = \frac{4\alpha}{3\pi M_{ee}} \sqrt{1 - \frac{4m_e^2}{M_{ee}^2}} \left(1 + \frac{2m_e^2}{M_{ee}^2}\right) \left(1 - \frac{m_e^2}{M_A^2}\right)^3 \left|F_A(M_{ee}^2)\right|^2, \tag{8.1}$$

where M$_A$ is the mass of the scalar meson, $\alpha = 1/137$ is the fine structure constant, $\Gamma^{A\rightarrow 2\gamma}$ is the partial width for the decay into 2γ and $F_A(M_{ee}^2)$ is the form factor for the transition A$\rightarrow \gamma e^+e^-$ taken as

$$F_{\pi^0}(M_{ee}^2) = 1 + bM_{ee}^2 \tag{8.2}$$

$$b = 5.5 \pm 1.6 GeV^{-2} \tag{8.3}$$

for the π^0 and

$$F_\eta(M_{ee}^2) = \sqrt{1 - \frac{M_{ee}^2}{\Lambda^2}} \tag{8.4}$$

$$\Lambda = 0.72 \pm 0.09 GeV \tag{8.5}$$

for the η meson [144]. The angular distributions for the Dalitz decay of pseudoscalar mesons is

$$\frac{d\sigma}{d\Omega_e{}^{\gamma^*}} = 1 + \cos^2\theta_e^{\gamma^*} \tag{8.6}$$

, where $\theta_e^{\gamma^*}$ is the angle of the electron in the reference frame of the γ^* with respect to the direction of the γ^* in the rest frame of the decaying meson (Fig. 7.20).

π^0 and η production cross sections

For the π^0 production cross section, we distinguish the different production channels:

- $\pi^- p \to n\pi^0$ or charge-exchange reaction: To take into account the discrepancy between the experimental measurement of [72, 73] and the SAID value, we use a cross section value of 9.0 ± 0.8 mb (see Sec. 1.5.1);
- $\pi^- p \to n\ \pi^0\pi^0$: According to the measurement of the Crystal Ball experiment (see Sec. 1.5.1), the cross section is 1.88 mb ± 0.04 (stat)± 0.010 mb (syst) at our energy. The effective cross section is twice larger, since each π^0 can decay;
- $\pi^- p \to p\ \pi^0\pi^-$: We use 4.0 mb ±0.5 mb in agreement with existing data, which have a precision of about 10% (see Sec. 1.5.1).

Pluto generates π^0 according to phase space in the three reactions. However, another event generator was developed by I. A. Sarantsev and I. Ciepal where the π^0 production is based on PWA results. This is particularly important for the charge exchange process where the π^0 emission is strongly forward peaked (see Fig. 1.19). In this event generator, the angular distribution for the $\pi^- p \to n\pi^0$ is taken from the SAID PWA WI[08] and from the Bonn-Gatchina PWA for the 2π production. We will use both generators for the comparison to our data.

Only part of our pion beam momentum distribution is above the η production threshold. Based on existing data, we estimate a cross section for the η production of $\sigma(\eta)$= 0.63 mb, as will be explained in detail in Sec. 8.2.4. In this case, the Pluto event generator is used with isotropic angular distribution.

8.2.2 Dalitz decay of baryonic resonances

We consider both the direct Dalitz decays of resonances produced in the s-channel, of the type ($\pi^- p \to N^* \to ne^+e^-$) and cascade decays of the type ($\pi^- p \to N^* \to \Delta\pi \to ne^+e^-$).

Direct Dalitz decay of N* resonances

We would like to estimate the baryonic contribution coming from the Dalitz decay of baryonic resonances. We know from the PWA analysis of $\pi^- p \to \gamma n$ reaction, that the dominant resonant contributions are due to the N(1520) and N(1535) (Sec. 7.5.1) with respective cross sections of 47 and 34 μb (Table 7.5). We can therefore deduce that these resonances will also play the major role in the $\pi^- p \to e^+e^- n$ reaction and we can calculate the dilepton yield corresponding to the Dalitz decay of these resonances using the branching ratios and production cross sections (listed in Table 7.6).

However, these resonant contributions constitute only a rather small part of the total $\pi^- p \to \gamma n$ cross section of 220 μb. The rest is due to non-resonant s channel, u channel and t channel contributions which interfere with the resonant contributions. The calculation of the differential e^+e^- distribution can therefore be derived only in a full model taking into account all these contributions in a consistent way as *e.g.* realized in [131].

Nevertheless, we propose the following approach to describe our data: using Eq. 7.28 which relates the total Dalitz decay and radiative decay widths, one can deduce the following relations between the cross sections:

$$\sigma(\pi^- p \to ne^+e^-) \sim 1.35\ \alpha\ \sigma(\pi^- p \to n\gamma). \tag{8.7}$$

This holds for the Dalitz decay of the resonances produced in the s channel with a given mass. It can however be noticed that the dependence on the mass of the baryon is very smooth. The approximation in Eq. 8.7 can therefore still give a useful order of magnitude for the e^+e^- yield, based on the π^-p→nγ cross sections. Thus, we used this relation to estimate the total $\pi^-p \to ne^+e^-$ cross section from the total $\pi^-p \to n\gamma$ cross section and find a value of 2 μb. This can be considered as an effective contribution, where the different resonant or non-resonant contributions are taken into account globally. However, we also need a prescription to generate the e^+e^- invariant mass distribution, which depends on the spin and parity of the transitions following Eq. 7.10 and 7.15 and this is known only for the resonant contribution. Considering that the e^+e^- invariant mass spectra are expected to be very different for the two dominant resonant N(1520) ($3/2^-$) and N(1535) ($1/2\ ^-$), we chose to use four options to generate these distributions.

"Effective N(1520)" option

In the first one, or "N(1520) effective" option, we assume that the cross section is fully due to a $3/2^-$ electromagnetic transition. Since the e^+e^- mass distribution for the transition to the N(1520) $3/2^-$ decreases less rapidly at large invariant mass (see Fig. 7.7) than for the $1/2^-$, the 'N(1520) option' leads to an overestimation of the dielectron yield at larger invariant masses. This will therefore give an upper limit of point-like baryon transition at q^2 close to the kinematical limit. In this case, the production cross-section of this effective N(1520) contribution is

$$\sigma(N(1520)_{eff}) = \frac{\sigma(\pi^-p \to n\gamma)}{BR(N(1520) \to n\gamma)} = \frac{0.220}{0.0023} = 96\ mb \tag{8.8}$$

and a branching ratio for $N(1520)^0 \to Ne^+e^-$ of 2.3×10^{-5} is used (see Table 7.1).

"Effective N(1535)" option

The second one or 'N(1535) option' presents the opposite case, where all the cross section is assigned to the N(1535) $1/2^-$ Dalitz decay. In this way, we probably underestimate the dielectron yield at larger invariant masses. This will therefore give a lower limit of point-like baryon transition at q^2 close to the kinematical limit.

$$\sigma(N(1535)_{eff}) = \frac{\sigma(\pi^-p \to n\gamma)}{BR(N(1535) \to n\gamma)} = \frac{0.22}{0.0035} = 63\ mb \tag{8.9}$$

and a branching ratio for $N(1535)^0 \to ne^+e^-$ of 3.5 10^{-5} is used (see Table 7.1).

"Mixed" option

In the third option or "mixed" option, we divide the total cross section into two fractions, that we attribute to N(1520) and N(1535) following the relative yields found as resonant s channel contributions (see Table 7.5), which is 58% for N(1520) and 42% for N(1535). The inputs are in this case:

$$\sigma(N(1520)_{mixed}) = 0.58 \times \frac{\sigma(\pi^-p \to n\gamma)}{BR(N(1520) \to n\gamma)} = 51\ mb \tag{8.10}$$

$$\sigma(N(1535)_{mixed}) = 0.42 \times \frac{\sigma(\pi^-p \to n\gamma)}{BR(N(1535) \to n\gamma)} = 26\ mb \tag{8.11}$$

with branching ratios as given above. In this way, we have an intermediate behavior.

It can be checked that in the three last options, the total cross section for $\pi^-p \to ne^+e^-$ is equal to 2 μb. As all these contributions are deduced from the $\gamma n \to \pi^-p$ cross section, which is known with a precision of about 10%, we take this number as the uncertainty on the baryonic contributions in our simple model. These errors are 100% correlated on the N(1520) and N(1535) contributions in the 'mixed option'.

"PWA option"

In the fourth option, we use the cross sections for the N(1520) and N(1535) as deduced from the PWA (see Table 7.6), *i.e.* respectively 20.4 and 9.7 mb. For these contributions with known spin and parity, the calculation of the Dalitz decay can be considered as more reliable, however, it can describe only one part (about 40%) of the total cross section. We also adopt a 10% error in this case.

$\Delta(1232)$ π contributions

In the PWA analysis of the $\pi^+\pi^0 p$ and $\pi^+\pi^-$ n channels, it is found that the $\Delta\pi$ intermediate states have a sizable contribution. The latter are partly due to t channel mechanisms and partly to the cascade decay of baryonic resonances, in particular (N(1520) or N(1440) $\rightarrow\Delta$(1232) π). In this way, the N(1440), which has a negligible contribution to the e^+e^-n exclusive channel due to its weak electromagnetic coupling, can still contribute to the e^+e^- production via the coupling to the Δ(1232) resonance and its subsequent Dalitz decay. To generate the dileptons corresponding to this $\Delta\pi$ contribution followed by the Δ Dalitz decay, we use the cross sections for the $\Delta^0\pi^0$ and $\Delta^+\pi^-$ intermediate states, which amount respectively to 1.04 ± 0.1 mb and 0.78 ± 0.08 mb. The error bars take into account the uncertainty of the PWA (grey band in Fig. 7.14). We use an isotropic production of the Δ and π . The Δ Dalitz decay is treated using form factors taken at the photon point (*i.e.* G_M=3, G_E=0, G_C=0) (see Sec. 1.3.2).

8.2.3 Off-shell ρ contribution

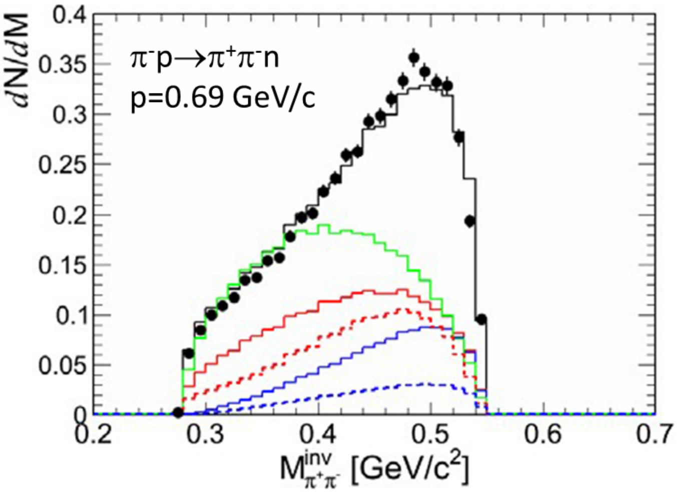

Figure 8.1: $\pi^+\pi^-$ invariant mass distribution (black circles) measured with HADES in the π^-p reaction at p=0.69 GeV/c compared to the PWA solution (black curve). The colored curves display various components of the PWA: total ρn (full blue curve), ρn via N(1520) (dashed blue), total σn (green curve) , σn via N(1520), total $\Delta\pi$ (full red) and total N(1520) (dashed red).

For the off-shell ρ contribution, we take the $\pi^-p \rightarrow ne^+e^-$ cross section of 1.65±0.2 mb extracted in the PWA of two pion production channels (see Sec. 7.5). To generate events, we use two options for the ρ mass distributions. In the first one, we use the distribution extracted in the PWA of the $\pi\pi$ channel (see Fig. 8.1). The yield in each invariant mass bin is converted into a dielectron yield in the corresponding e^+e^- invariant mass bin by using the relation:

$$\frac{d\sigma}{dM_{e^+e^-}} \propto \frac{1}{M_{ee}^3} * \frac{d\sigma}{dM_{\pi^+\pi^-}} \tag{8.12}$$

which is derived from the differential decay width expression of the VDM model (see Eq. 7.36). This mass distribution takes into account distortions due to the production mechanism, in particular phase space effects due to light intermediate baryon resonances.

The second option consists in using in Eq. 8.12 the ρ mass distribution from the Pluto generator, *i.e.* a simple Breit-Wigner distribution. We summarize in Table 8.1 all the cross section inputs used to generate e^+e^- pairs.

8.2.4 Reaction on carbon

Dominance of pion-proton with respect to pion-neutron interactions

As discussed in Sec. 1.5.2, considering the smaller cross sections for π^-n reactions with respect to π^-p, we can expect the interactions of pions with carbon nuclei to involve mainly protons. This difference is mainly due to the possibility to excite both isospin 1/2 and 3/2 in the case of the π^-p reaction, while only isospin 3/2 states can be formed in π^-n reactions. In addition, since these 3/2 states will have a charge -1, they cannot have a Dalitz decay. So the contribution of s channel baryon resonance Dalitz decay is strictly 0 in the π^-n reaction. The production of an e^+e^- pair is still possible in a π^-n bremsstrahlung emission ($\pi^-n \rightarrow \pi^-ne^+e^-$), but the cross section is predicted to be low. In the carbon target, absorption of the pion in a two-step process leading to the emission of an e^+e^- pair is not fully excluded, but very unlikely and can be neglected in first order. This explains why we will consider the reaction on the carbon target as a superposition of interactions with protons.

Participant-spectator description

The reaction on carbon is taken into account using a participant-spectator picture. As discussed in Sec. 1.5.3, the scarce experimental information for pion induced reactions on nuclei in the second resonance region indicates a significant contribution of quasi-free $\pi^-p \rightarrow n\pi^0$ process. In the absence of a detailed analysis of the other exclusive channels ($\pi^-p \rightarrow \pi^0\pi^0n$, $\pi^0\eta$,...) which could be used as an input for our simulations, we generalize the quasi-free hypothesis to all channels and use the participant-spectator picture. It means that the reaction takes place with a proton moving in the carbon nucleus reference frame with the Fermi momentum $\vec{p_F}$. The rest of the carbon nucleus is treated as a ^{11}B on its mass-shell, keeping its initial momentum -$\vec{p_F}$. It follows that the participant proton is off-shell with a total energy in the laboratory W_{part} and a mass M_{part} that are related by:

$$M_{12C} = W_{part} + \sqrt{M_{11B}^2 + (\vec{p_F})^2} \tag{8.13}$$

$$W_{part}^2 = M_{part}^2 + (\vec{p_F})^2 \tag{8.14}$$

where M_{12C} and M_{11B} are the ^{12}C and ^{11}B masses respectively.

In the Pluto event generator, for each event, the three components of the Fermi momentum of the participant proton are sampled [35], as well as the pion momentum using the experimental distribution (see Sec. 3.4). Reaction products are generated in the rest frame of the pion and participant nucleon and are then boosted to the lab frame. In this way, the modulus and the direction of the moving pions and nucleons are taken into account. One can calculate from Eq. 8.14 the center-of-mass (CM) energy in the reaction between the pion and the participant nucleon:

$$\sqrt{s_{\pi part}} = \sqrt{(W_\pi + W_{part})^2 - (\vec{p_\pi} + \vec{p_F})^2}, \tag{8.15}$$

where M_π and $\vec{p_\pi}$ are the pion mass and laboratory momentum respectively. In the case

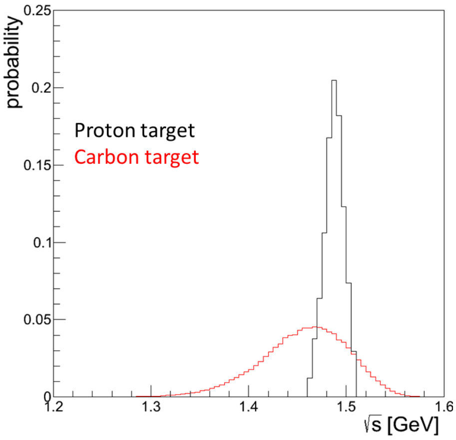

Figure 8.2: Probability density as a function of $\sqrt{s}$ for the reaction on a free proton (black) and on a bound proton (red) treated using the participant-spectator model (see text). The incident pion beam distribution has been taken into account in both cases according to the measurement.

of a free proton, the CM energy is simply:

$$\sqrt{s_{\pi p}} = \sqrt{(W_\pi + M_p)^2 - (\vec{p_\pi})^2}, \tag{8.16}$$

where the incident pion momentum distribution already induces a scatter in $\sqrt{s_{\pi p}}$.

Effective $\pi^- p \to \eta n$ production cross sections

For the generation of channels which are well above threshold (one or two pion production, baryon resonance Dalitz decays), using the cross section corresponding to the average pion momentum is an adequate assumption. This means that the effective nucleon cross section for the reaction on proton is taken as the free $\pi^- p$ cross section.

This is not the case for the η production, as part of our center-of-mass distribution is below the η production threshold ($\sqrt{s_{th}}$=1.487 GeV) and the cross section increases very rapidly above the threshold. For this case, one needs to take into account the dependence of the cross section as a function of the center of mass energy. For this, we used as cross section inputs the results of the Giessen coupled channel calculation which reproduces well the $\pi^-\mathrm{p} \to \eta n$ cross section data (see Fig. 1.22 in Sec. 1.5.1) and selected discrete values, as shown in the left part of Fig. 8.3.

For each bin in $\sqrt{s}$, one can then calculate the contribution to the cross section as the product of the cross section by the probability $\mathcal{P}(\sqrt{s})\Delta(\sqrt{s})$ of this bin:

$$\Delta\sigma(\sqrt{s}) = \sigma(\sqrt{s})\mathcal{P}(\sqrt{s})\Delta(\sqrt{s}) \tag{8.17}$$

The total cross section is then calculated as the sum over the $\sqrt{s}$ bins

$$\sigma = \sum_{\Delta(bins)} \Delta\sigma(\sqrt{s}), \tag{8.18}$$

To calculate the probabilities of $\sqrt{s_{\pi p}}$ and $\sqrt{s_{\pi part}}$ in the case of a proton and a carbon target respectively, we generated events from the $\pi^- \mathrm{p} \to \mathrm{n}\pi^0$ with a pion momentum distribution corresponding to the measurement (see Sec. 3.2.3). At our energy, this reaction is far above threshold and the phase space volume depends only very smoothly on the center-of-mass energy of the reaction. After normalization, the yield in bins of $\sqrt{s}$ can therefore be interpreted as a probability for the $\sqrt{s}$ value to be in the given bin of width $\Delta(\sqrt{s})$.

The cross sections $\Delta\sigma(\sqrt{s}$ are shown for bins of 5 MeV in $\sqrt{s}$ in Fig. 8.2 for a bin width of 5 MeV for both the proton and carbon targets. For the reaction on the free proton, the distribution is only due to the different incident pion momenta. In the case of the carbon target, the width is dominated by the Fermi momentum effect. A significant downward shift of the distribution can also be observed. It is due to the nucleon binding energy which is taken into account via the off-shell mass of the nucleon in the participant-spectator model according to Eq. 8.14. After folding these probabilities with the η production cross section according to Eq. 8.18, one gets

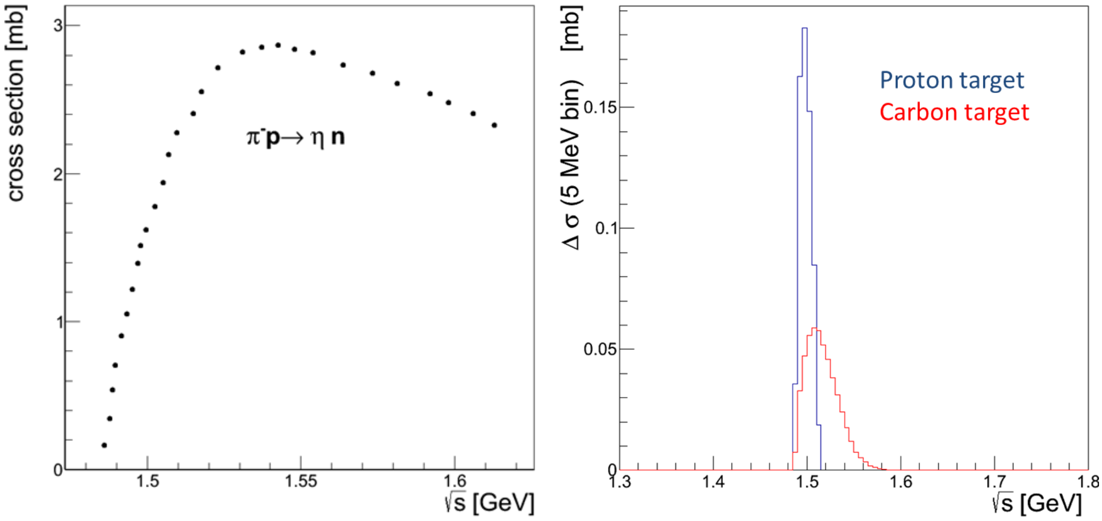

Figure 8.3: Left: Cross sections as a function of $\sqrt{s}$ for the $\pi^- p \to n\eta$ reaction derived from the Giessen BUU coupled channel (see Sec. 8.2.7). Right: Distribution of cross sections in bins of 5 MeV for the reaction on a free proton (black curve) and on a bound proton (blue curve) treated using the participant-spectator model (see text). The incident pion beam distribution has been taken into account in both cases according to the measurement (see Sec. 3.2.3).

$$\sigma_{\pi^- p} = 0.63 \pm 0.2 \text{ mb for the proton target and} \tag{8.19}$$

$$\sigma_{\pi^- part} = 0.50 \pm 0.05\text{mb for the carbon target} \tag{8.20}$$

The error on the cross sections takes into account both the uncertainty on the central center-of-mass energy and on the knowledge of the cross sections. For the proton target the first effect dominates. Considering in Eq.8.17 a maximum uncertainty on the central value of the center-of-mass energy distribution of 5%, we can deduce from Fig. 8.2 that the probabilities in the central bins above the threshold and hence the cross sections in these bins can change by up to 30% if the central value is shifted by 5 MeV. We take this error as the global error on the cross section. For the carbon target, this effect is much smaller and the error is then dominated by the uncertainty on the cross sections, which we estimate to be 10%.

Number of participant protons

It has been shown (see Sec. 5.6) by comparing the yields measured with the polyethylene and carbon targets that the ratio of cross sections on proton and carbon in the π^0 region (*i.e.* $M_{ee} < 140$ MeV/c^2) is:

$$\frac{\sigma(\pi^- + C \to \pi^0 X)}{\sigma(\pi^- + p \to \pi^0 X)} = 4.67 \pm 0.22, \tag{8.21}$$

so we use a number of participant protons of N_{part}=4.7 for the π^0 production in the carbon target.

For e^+e^- invariant masses 140 MeV/c^2 $< M_{ee} <$ 300 MeV/c^2, where the N(1520) and the η production are the dominant contributions, the ratio has a slightly larger value: 5.11 ± 1.22. We therefore use N(1520) and η production cross sections which are higher than on the proton target by a factor 5.1.

For the N(1520) case, this value can be interpreted in terms of 5.1 participant protons, but for the η production, since the effective pion-proton cross section is slightly lower than in the free case (see Eq. 8.20), the number of participants is 6.4.

8.2.5 Summary of the input cross sections for Pluto simulations

	σ(mb)		
channel	proton	carbon	CH$_2$ (x0.5)
π^0n	9.0 ± 0.8	43.2 ± 4.1 ± 2.0	30.8 ± 3.0
$\pi^0\pi^0$n	1.9 ± 0.1	8.9 ± 0.5 ± 0.4	6.4 ± 0.4
$\pi^-\pi^0$p	4.0 ± 0.5	18.8 ± 2.4 ± 0.9	13.4 ± 1.8
η n	0.63 ± 0.2	3.0 ± 0.1 ± 0.7	2.23 ± 0.43
Δ^+ π^-	0.78 ± 0.08	4.0 ± 0.4 ± 0.9	2.8 ± 0.5
Δ^0 π^0	1. ± 0.1	5.1 ± 0.5 ± 1.2	3.6 ± 0.7
nρ	1.3 ± 0.20	6.6 ± 1.0 ± 2.0	4.6 ± 1.1
N(1520) ('effective')	96 ± 10	490 ± 51 ± 115	341 ± 68
N(1535) ('effective')	63 ± 6	321 ± 31 ± 76	223 ± 44
N(1520) ('mixed')	51 ± 5	260 ± 26 ± 61	181 ± 35
N(1535) ('mixed')	26 ± 3	133 ± 15 ± 31	92 ± 19
N(1520) (PWA)	20.4 ± 2	104 ± 10 ± 25	72.4 ± 14
N(1535) (PWA)	9.7 ± 1	49 ± 5 ± 12	34 ± 7

Table 8.1: Production cross sections for the different dilepton channels for proton, carbon and CH2 targets. The purely baryonic contribution is treated using invariant mass distributions corresponding to the Dalitz decay of N(1520) and N(1535) with four options for the relative cross sections.

The cross sections used for the simulations of the reactions on proton, carbon and CH$_2$ targets are listed in Table 8.2 together with the branching ratios to the various dilepton channels. We also give in Table 8.2 the contributions of each component to the inclusive e^+e^- production cross section. It has, however, to be kept in mind that these contributions have different invariant mass distributions, in particular the π^0 Dalitz decay contributes only for invariant masses lower than the π^0 mass. The ρ contribution produces only e^+e^- pairs with masses larger than twice the π^0 mass. The other contributions (η, Δ and other baryon Dalitz decays) mainly contribute at low invariant masses, but extend up to the kinematical limit (which is almost identical to the η mass).

decay channel		branching ratio	σ(X e^+e^-) (μ b)
$\pi^0 \rightarrow \gamma e^+e^-$		1.2%	684.0 ± 66.6
$\eta \rightarrow \gamma e^+e^-$		6.9 10^{-3}	15.4 ± 0.8
$\Delta\pi$: $\Delta^{+,0} \rightarrow$ N e^+e^-		4.2 10^{-5}	0.27 ± 0.05
$\rho \rightarrow e^+e^-$		4.7 10^{-5}	0.22 ± 0.05
baryonic	N(1520)$^0 \rightarrow$ n e^+e^-	2.3 10^{-5}	7.8 ± 1.3
	N(1535)$^0 \rightarrow$ n e^+e^-	3.5 10^{-5}	

Table 8.2: Contributions of the different channels to the inclusive e^+e^- production cross section for the CH2 target normalized as $\sigma_H + 1/2\sigma_C$. The baryonic contribution is given for the mixed case.

The errors $(\Delta\sigma)_H$ on the cross sections for the proton target are just based on the knowledge of these cross sections and, for the η contribution (see Sec. 3.2.3), on the uncertainty on the mean pion momentum. For the interaction with carbon nuclei, the cross section is calculated (except for the η) by a renormalization of the proton cross section. Thus, there are two contributions to the error. The first one $(\Delta\sigma)_{C,elem}$ is deduced from the errors on the proton cross sections

$$(\Delta\sigma)_{C,elem} = R^{'} \times (\Delta\sigma)_H \tag{8.22}$$

and the second

$$(\Delta\sigma)_{C,R} = \Delta R \times \sigma_H \tag{8.23}$$

takes into account the uncertainty in the factor R (see Table 5.1). As mentioned in Sec. 8.2.4, for the η contribution, the error on the effective elementary cross section in Eq. 8.22 is smaller than for the proton due to the smearing of the Fermi momentum. The error on the CH$_2$ cross section $\sigma_{CH2} = \sigma_H + \frac{1}{2}\sigma_C$ listed in the fourth column is calculated as:

$$(\Delta\sigma)^2_{CH2} = (\Delta\sigma_H + \frac{1}{2}\Delta\sigma_{C,elem})^2 + \frac{1}{4}(\Delta\sigma_{C,R})^2. \tag{8.24}$$

The first term takes into account the correlation, in our model, between the errors due to the elementary cross section for the proton and carbon targets and the second term is the contribution due to the error on the nuclear factor R.

8.2.6 Comparison of Pluto cocktail to inclusive e^+e^- production data

In this section, we compare the results of the Pluto cocktail to two sorts of experimental spectra. Both types of spectra are presented after normalization (see Sec. 5.7).

- Raw spectra present experimental yields selected after all analysis cuts. They are presented with statistical error bars only and are compared to distributions of events produced in the simulation including all steps of the analysis;
- Efficiency corrected spectra show distributions obtained for the same experimental events than raw spectra, but after weighting by the inverse product of the electron and positron efficiencies (Sec. 6.1.3). Statistical errors and uncorrelated systematic errors (see Sec. 6.3) have been added quadratically. They are shown on the pictures and represent an error which affects all points in an uncorrelated way. In addition, the correlated systematic error is also displayed using another graphical style. These experimental spectra are compared to the distribution of events of the simulations in the HADES acceptance and after smearing of the kinematical variables (see Sec. 6.1.3).

π^0 Dalitz decay region

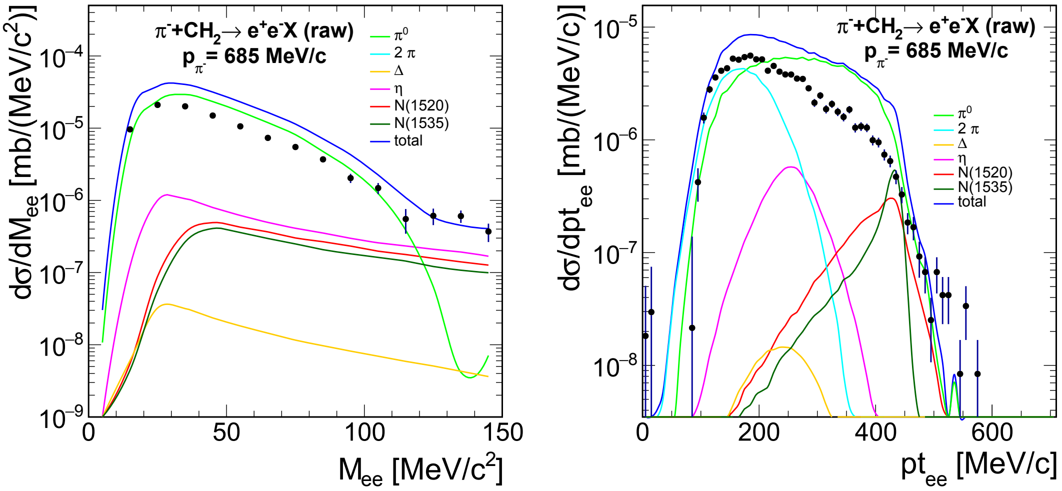

Figure 8.4: Comparison of the experimental e^+e^- raw spectra with predictions of the Pluto dielectron cocktail in the π^0 region (M_{ee} < 140 MeV/c^2). The distributions from the simulation correspond to fully reconstructed events, using the π^0 contributions from single and double pion production channels generated in phase space from the Pluto event generator. The off-shell ρ contribution is not included. The baryonic contribution is taken in the 'mixed option'. Left: Invariant mass distributions. Right: Transverse momentum distributions.

We start with the discussion of the comparison of data to the dielectron cocktail in the π^0 region. We therefore present in Fig. 8.4 a comparison of raw spectra measured on the polyethylene target with PLUTO simulations. The simulation uses the π^0 contributions from single and double pion production channels generated in phase space from the Pluto event generator. The off-shell ρ contribution is not included. The baryonic contribution is taken in the 'mixed option' and all the other ingredients are taken as described in Sec. 8.2.4. The η, N(1520) and N(1535) represent a small fraction of the yield below 100 MeV/c^2 but start to dominate at higher invariant mass values (Fig. 8.4 , left), where the experimental yield is well reproduced. Their contribution is also concentrated at high transverse momenta of the e^+e^- pair, especially for the baryonic contribution (Fig. 8.4, right).

It can be observed that the simulation overestimates the experimental yield by a factor of about 2. In addition, the shape of the pt_{ee} distribution is not well described by the simulation. This disagreement seems to be mostly related to the simulation of the one pion production (*i.e* $\pi^-p \rightarrow ne^+e^-$reaction). The different shapes of the pt_{ee} distributions for the 1π and 2π production are due to the different phase space for the π^0 production in both processes. The e^+e^- invariant mass spectrum is also different for both contributions, but this is only due to the different effect of acceptance.

As shown in Fig. 8.5, a much better agreement is obtained when the π^0 contribution is generated using the event generator based on PWA. The shape of the pt_{ee} distribution is now described very well. It has to be stressed that the single and double pion contributions have the same cross sections than in the simulation with the Pluto event generator. The different yield after reconstruction is then just due to the different shapes of the differential distributions. In particular, for the single π^0 production, the reconstructed yield is much lower for the generator based on PWA due to the forward peaked angular distributions. The different angular distributions are also reflected in the different pt_{ee} shapes (Fig. 8.5,

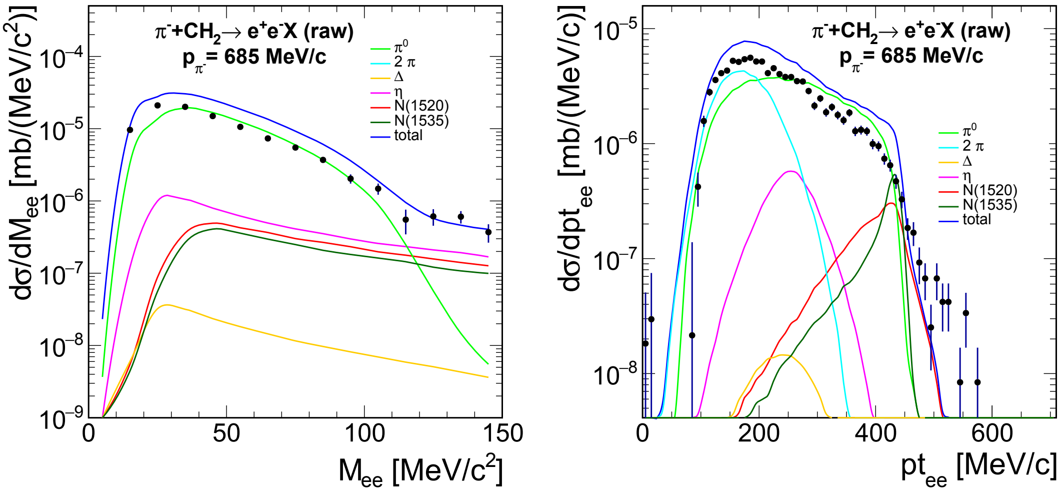

Figure 8.5: Same as Fig. 8.4, but with π^0 production according to the generator based on PWA inputs.

right). The yield at large pt_{ee}, corresponding to larger polar angles is suppressed with respect to the Pluto event generator. The difference is smaller for the 2π contribution, where the PWA angular distributions are broader, hence closer to phase space. The good description of the shapes of the experimental distributions by the generator based on the PWA can be taken as a consistency check, since this generator is based on realistic inputs. However, the experimental yield is still lower by about 30% than the simulation. Considering the uncertainty on the previous experiments, the precision of the total π^0 production cross section is of the order of 10%. Since our correlated systematic uncertainty is about 20%, our measurement is still compatible with existing information on the π^0 production. However, since the yield measured by HADES for the $\pi^0\pi^-p$ channel in the same experiment is also too low with respect to the world systematic by about 30%, it could indicate a global normalization issue. On the other hand, the yield for the $\pi^+\pi^-n$ channel is in agreement with world data, so the trend observed for π^0 production channels can not just be due to the normalization. Concerning the dilepton channel, the reconstructed yield in the simulation is sensitive to the RICH digitizer, which was tuned with a lot of care. The efficiency of the backtracking procedure which is too optimistic in the simulation (see Sec. 6.2.1) was adjusted to the data, so we do not expect a significant bias related to electron reconstruction efficiency.

Fig. 8.6 (left) and Fig. 8.6 (right) present efficiency corrected spectra. The average efficiency correction is of the order of a factor 10. The same qualitative agreement is obtained as for the raw spectra. The discrepancy between the data and the simulation is however slightly larger for efficiency corrected data, which correspond to a wider phase space than reconstructed data.

Contribution of baryonic resonances to e^+e^- spectra

Fig. 8.7 displays the comparison of the e^+e^- invariant mass distribution in the whole invariant mass domain covered by our experiment for the total raw data measured on the polyethylene target (left) and for the interactions with protons only obtained after carbon subtraction (right) as explained in Sec. 5.6. The simulation uses the π^0 contribution from the event generator based on the PWA and all other ingredients as for Fig. 8.6.

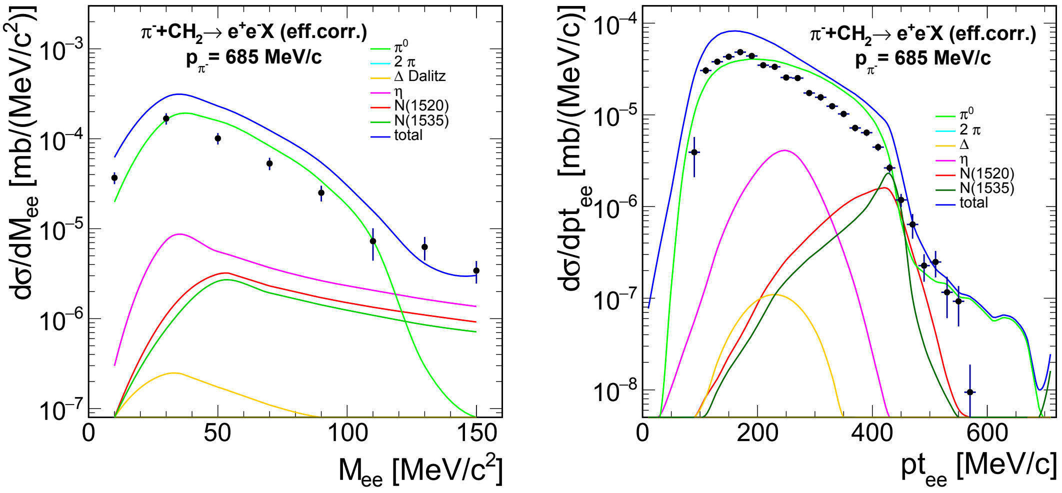

Figure 8.6: Same as Fig. 8.5 but for efficiency corrected e^+e^- spectra. The distributions from the simulation correspond to events in acceptance after smearing of their kinematical variables.

A similar discrepancy between data and simulation in the π^0 region can be observed for the total yield measured on the polyethylene target and after subtraction of carbon nuclei contribution. This is not surprising, since the carbon contribution in the simulation is scaled to match the measured ratio of cross sections between carbon and polyethylene target. It can be noticed that the statistics for invariant masses larger than the π^0 mass is too small for extracting detailed information. In the following, we will therefore discuss the results obtained on the CH$_2$ target without subtraction of the carbon nuclei contributions.

Fig. 8.8 and Fig. 8.9 display the comparison of efficiency corrected spectra with the simulation using the four different options chosen for the Pluto simulation. The e^+e^- yield in the region between 100 and 300 MeV/c^2, which is sensitive to the η and baryon Dalitz decay contributions is rather well reproduced by any of the simulations using a cross section for the $\pi^-p \rightarrow ne^+e^-$ reaction deduced from the measured $\pi^-p \rightarrow n\gamma$ cross section, *i.e.* N(1520) effective, N(1535) effective or "mixed" options (see Sec. 8.2.2). This is a very interesting result, which shows that our data are consistent with the η and baryon contributions implemented in the simulations. As expected, when only the resonant parts of the $\pi^-p \rightarrow n\gamma$ cross section are taken into account (*i.e.* 'PWA' option), the e^+e^- yield is underestimated. The η contribution decreases very rapidly for invariant masses above 300 MeV/c^2. The e^+e^- invariant mass distribution for the N(1535) is shifted with respect to the η by only about 40 MeV towards higher invariant masses, but the shape of the N(1520) distribution is much flatter. As already mentioned, this is due to the different spin and parity of the N(1520) and N(1535) resonances and the yield for invariant masses above 300 MeV/c^2 therefore depends strongly on the option for the baryonic contribution.

It is however very clear that the data present a large excess for invariant masses larger than 350 MeV/c^2 with respect to the expected yield from Dalitz decay of baryons, when they are treated point-like. This shows without any doubt the effect of the time-like electromagnetic form factors for these baryon transitions. If the discrepancy of about 40% between the simulated and experimental yields in the π^0 region is due to a global systematic error, the whole spectrum would have to be renormalized by a factor 1.4, but it would not change this conclusion.

Finally, the transverse momentum is displayed in Fig. 8.10 for the region of invariant masses between 140 and 300 MeV/c^2, where the η and baryonic contributions dominate. It

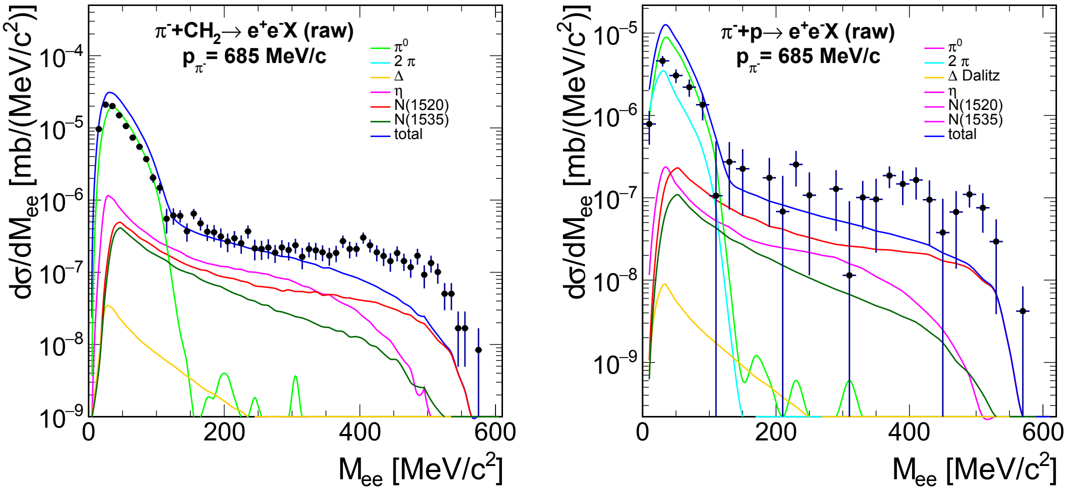

Figure 8.7: Comparison of the raw inclusive e^+e^- experimental invariant mass distributions with the Pluto cocktail in the "mixed" option. The off-shell ρ contribution is not included. Left: polyethylene target. Right: Contribution of π^-p interactions obtained after subtraction of e^+e^- from interactions with the carbon target.

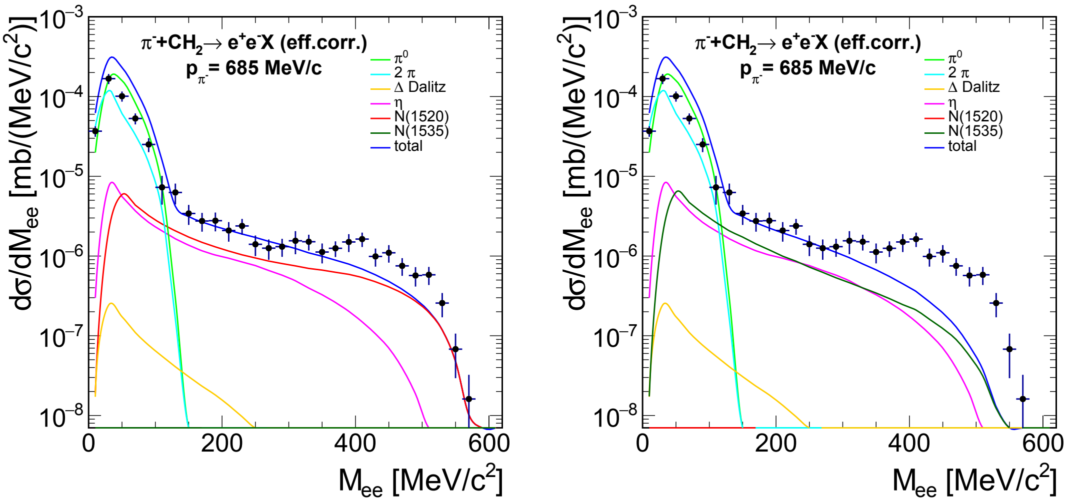

Figure 8.8: Comparison of the efficiency corrected inclusive e^+e^- experimental invariant mass distributions with the Pluto cocktail for the "N(1520)" (left) and "N(1535)" (right) effective options. The off-shell ρ contribution is not included.

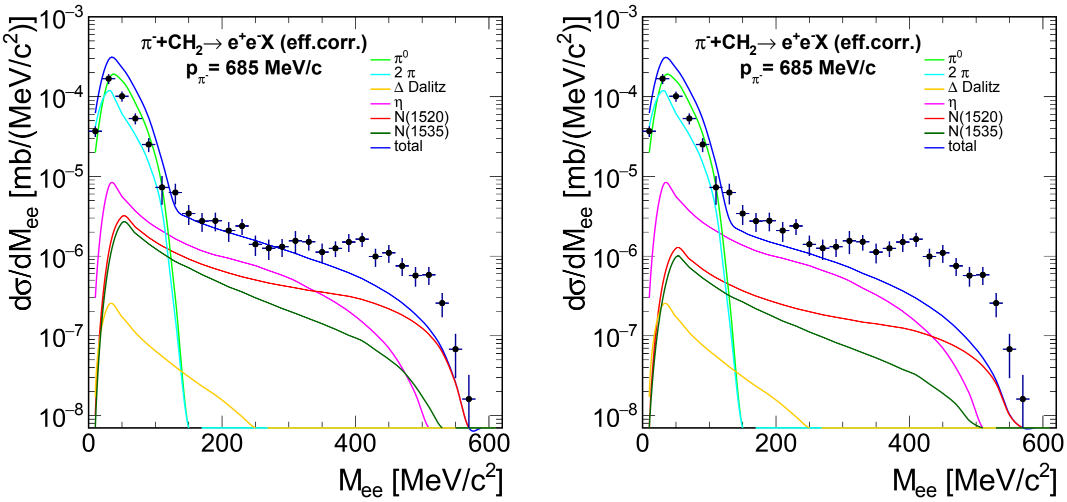

Figure 8.9: Same as Fig. 8.8 for the "mixed" (left) and "PWA" (right) options. The off-shell ρ contribution is not included.

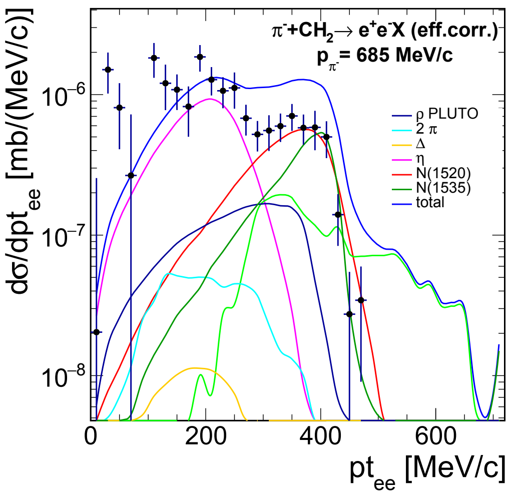

Figure 8.10: The efficiency corrected transverse momentum distributions for inclusive production of e^+e^- with invariant mass between 140 and 300 MeV/c^2 is shown in comparison with the Pluto cocktail in the 'mixed option'. The off-shell ρ contribution is not included.

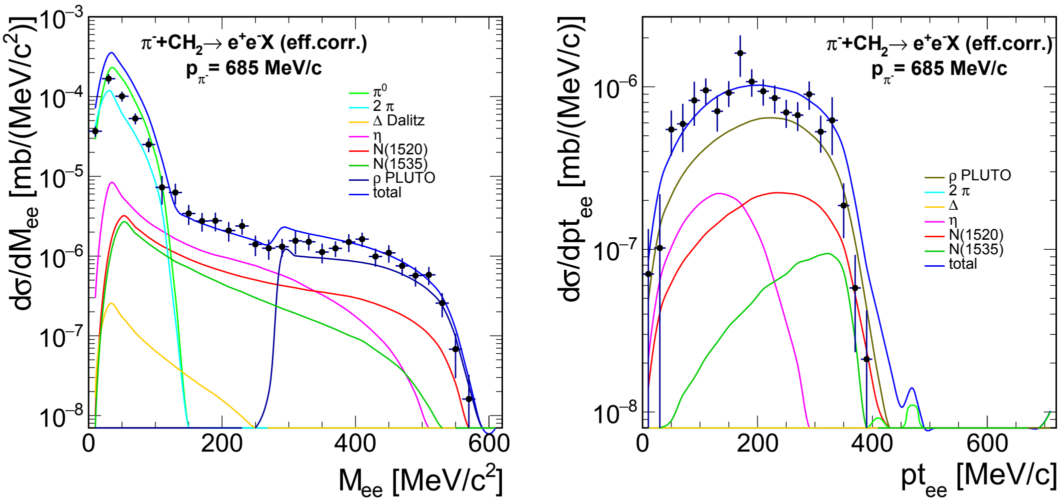

Figure 8.11: Comparison of the efficiency corrected inclusive e^+e^- experimental distributions with the Pluto cocktail in the 'mixed option'. The off-shell ρ contribution is included. Left: Invariant mass. Right: Transverse momentum distributions for invariant masses between 300 and 600 MeV/c^2.

is interesting to note that the η and baryonic contributions have very different transverse momenta distributions. The baryonic contribution produces a strong peak close to the maximum p_T values allowed by the kinematics. Such a peak is also visible in the data, albeit with a reduced yield. The η contributes at smaller transverse momenta and seems to be fairly well described. A rather strong contribution of unknown origin is also present at the smallest pt_{ee} values.

Off-shell ρ contribution

As mentioned previously, one way to take into account the time-like electromagnetic form factors is to use the Vector Dominance Model picture and calculate the effect as being due to the production of e^+e^- pairs by off-shell ρ. The off-shell ρ contribution has therefore been added in the simulation (see Sec.8.2.3). As can be observed in Fig. 8.11 (left), where the 'mixed option' is used for the point-like baryon contribution, this provides a good description of the yield for M$_{ee}$ larger than 300 MeV/c^2. As the cross section for the ρ production is deduced from the PWA analysis of HADES data measured in the two pion production channels, it also gives a good consistency between the $\pi\pi$ and e^+e^- channel. It can also be noted that the strict VDM model (Eq. 7.35) used to calculate the e^+e^- yield from the ρ decay gives a fair description of the shape of the invariant mass distribution.

The comparison of the transverse momentum distribution is displayed in Fig. 8.11 (right). A good agreement is obtained, which confirms the consistency of the interpretation in terms of an off-shell ρ contribution.

In this procedure, we take into account the isovector production of e^+e^- pairs, which can be assimilated to an off-shell ρ contribution, but neglect the isoscalar contribution corresponding to off-shell ω contribution, which seems therefore to have a small contribution. In Sec. 8.2.8, we will investigate the effect of the time-like transition form factor of Ramalho and Pena for the N(1520) resonance.

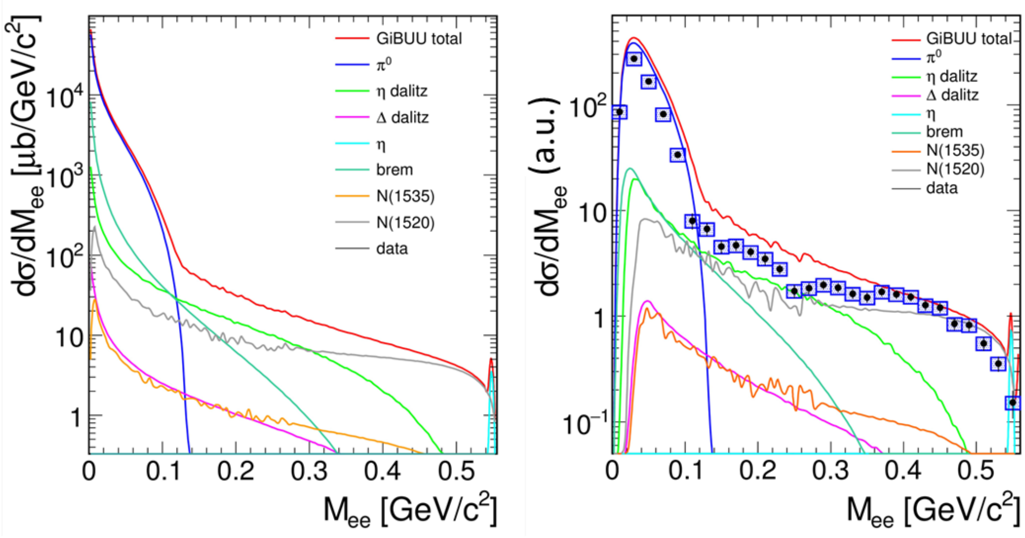

Figure 8.12: Predictions of the GiBUU transport model for the CH2 target for the inclusive e^+e^- production. Left: Model predictions in 4π. Right: The model predictions are smeared to take into account the reconstructed values of the momentum and angles and are compared to experimental data.

8.2.7 Comparison of Giessen BUU transport model predictions to inclusive e^+e^- data

The Giessen BUU transport model [145] provides calculation of the inclusive e^+e^- production off proton or carbon target. Predictions for the invariant mass spectra in the $\pi^- p$ reaction at $\sqrt{s}$=1.5 GeV are shown in the left panel of Fig. 8.12 without any acceptance or analysis cuts.

In the same way as our Pluto cocktail, the GiBUU transport code takes into account different sources of e^+e^- pairs, which are added incoherently (see Table 8.3). In addition to the π^0 and η Dalitz decay, the baryon Dalitz decay is also taken into account. However, it is modeled in a different way as in our Pluto cocktail. Indeed, the production of e^+e^- from the baryons is treated assuming an intermediate ρ, *i.e.* in two steps, $\pi^- p \to N(1520)/N(1535)$ and $N(1520)/N(1535) \to N\rho$. The yield of e^+e^- is therefore determined by the resonance production cross sections and their coupling to the ρN channel. This is very different from our Pluto cocktail where we used inputs from the γn reaction to simulate a point-like baryonic contribution and add an off-shell ρ contribution deduced from the PWA. Another difference is the shape of the e^+e^- invariant mass spectrum which is similar for the N(1520) and N(1535) resonances, while in the Pluto approach, the shapes are very different (Fig. 8.8 and Fig. 8.9), as expected from the respective theoretical approaches [143] and [146] they are based on.

The treatment of the carbon target is much more precise than in our Pluto cocktail, since it takes into account the propagation and re-interaction of the particles inside the nucleus. The comparison to the polyethylene data is done by calculating the cross section as

$$\sigma = \sigma_p + 0.5\sigma_C \qquad (8.25)$$

The comparison of the inclusive experimental e^+e^- invariant mas spectrum with the reconstructed events from the GiBUU model is displayed in Fig. 8.12 for the polyethylene target. While a slightly larger π^0 production cross section is used for interactions with proton, this is compensated by a smaller carbon contribution, which results in a similar yield for the CH_2 target. No smearing of the pion momentum is implemented, so the calculation was done at a fixed momentum p=0.687 GeV/c ($\sqrt{s}$=1.487 GeV), which is slightly above the η threshold. The η production cross section in the GiBUU model at this energy is 0.78 mb, which is slightly larger than in the GiBUU coupled-channel estimates, from which we extract a value close to 0.3 mb at the same energy. The difference with the cross section input in our Pluto model (0.563 mb) is reduced due to the pion beam momentum smearing. For the η production cross section on the carbon target, the GiBUU model uses a value of 3.6 mb, which is also only slightly larger than the input in our model. In this case, the ratio of carbon to proton cross sections is 4.6, which is compatible with our experimental measurement (see Sec. 5.6.1). The ratios of proton and carbon cross sections reflect the different re-interactions and absorption probabilities in the different channels. It is interesting to note that they are in good agreement with the ones we used as inputs for our Pluto simulation, based on the observed yields on the carbon and polyethylene targets.

The GiBUU model overestimates the e^+e^- yield in the region of invariant masses between 100 and 350 MeV/c^2. The main reason is probably the too large baryonic (coupled to ρ) contribution, which is enhanced at small invariant masses due to the 1/M^3 factor and extends even below the two pion threshold. In contrast with the Pluto model, this yield is not constrained by the $\gamma p \rightarrow \pi^- n$ results. Due to this VDM prescription, the point-like baryonic Dalitz decay is not added in this model, to avoid double counting. One can also notice that the baryon/ρ contribution in the GiBUU model has a cross section only a factor 2 larger than for the proton target. Also worth to be noted is the larger contribution of the $\Delta(1232)$ s channel production and decay. This is due to the Manley parametrization [67] of the $\Delta(1232)$ total width used in the GiBUU code. In Pluto, the parametrization from [147] is used which suppresses the high mass part of the distribution.

	Pluto				GiBUU			
	^{1}H (mb)	^{12}C (mb)	ratio	CH_2 (mb) (x 0.5)	^{1}H (mb)	^{12}C (mb)	ratio	CH_2 (mb) (x 0.5)
π^0X	14.9	70	4.7	54.9	18.6	71	3.8	54.1
η n	0.63	3.2	5.1	2.23	0.78	3.6	4.6	2.6
N*	30.1	153	5.1	-	-	-	-	-
ρ	1.3	6.6	5.1	4.6	0.86	2.1	2.4	1.91

Table 8.3: Cross sections (mb) for the different dilepton channels used for the generation of e^+e^- pairs for π^-+ p and π^-+ C interactions and the total cross sections $\sigma_{tot} = \sigma_H + 0.5 \times \sigma_C$ used for the comparison to the experimental data. For the Pluto simulation, the cross sections for the baryon contribution are taken in the 'PWA' option. In the case of the GiBUU model, the baryonic contribution and ρ contribution are coupled via the decay chain (N* $\rightarrow N\rho \rightarrow N\ e^+e^-$).

8.2.8 Comparison of Pluto cocktail to exclusive $\pi^-p \rightarrow ne^+e^-$spectra

As explained in Sec. 5.5, a selection on the missing mass for the reaction $\pi^-p \rightarrow ne^+e^-$ allows to study the exclusive free (for interactions of π^- with target protons) or quasi-free (for interactions with target carbon nuclei) $\pi^-p \rightarrow ne^+e^-$ channel for e^+e^- invariant masses larger than 140 MeV/c^2. The corresponding experimental distribution is shown in Fig. 8.13 in comparison with the predictions of the Pluto cocktail. Here, the 'mixed' option is shown for the baryonic contribution and the 'off-shell' ρ contribution is taken

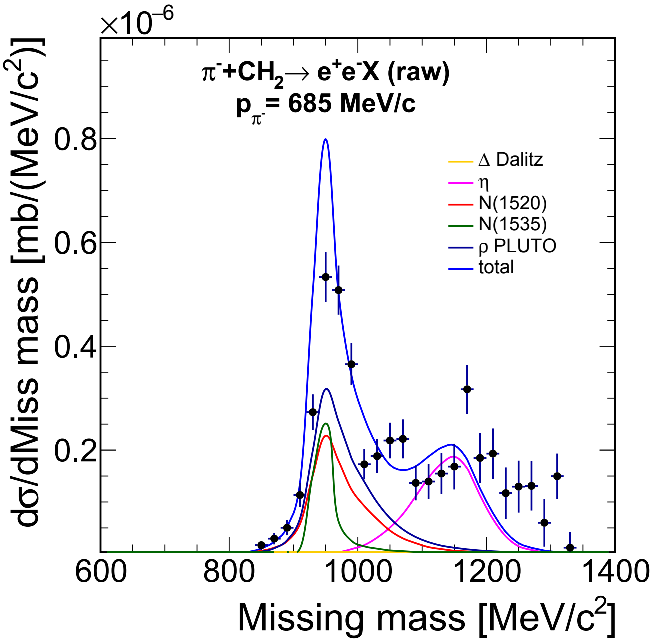

Figure 8.13: Comparison of the distribution of the missing mass MM_{ee} for the $\pi^- p \to n$ X reaction with the Pluto cocktail. The 'mixed' option is used for the baryonic contribution and the ρ contribution is taken with a Breit-Wigner distribution, as provided by the Pluto event generator.

with the Pluto standard prescription, *i.e.* with a Breit-Wigner distribution. The width of the neutron peak is well reproduced by the simulation. It has to be noted that this width is not sensitive to the details of the simulation, but rather to the description of the experimental effects and, for interactions with carbon, to the Fermi momentum distribution and participant-spectator assumption. The simulation reproduces the global trend of the missing mass distribution. However, it overestimates by 50 % the yield in the region of the neutron peak, which corresponds to the free or quasi-free $\pi^- p \to n\ e^+e^-$reaction, and is described in the simulation via the three contributions: N(1520), N(1535) and ρ. The yield for missing masses above 1 GeV/c^2, which is due in the simulation to η production, is underestimated by approximately the same amount. However, this excess is probably not due to an underestimated η contribution. It is indeed correlated to the excess observed at small pt_{ee} for invariant masses in the range 140-300 MeV/c^2 (see Fig. 8.10). In this region, the combinatorial background is large and maybe the systematic error of the subtraction for these small p_T should be reevaluated.

The invariant mass spectrum can be investigated after selection of events in the neutron peak (0.9 GeV $<$ M$_{ee}$ $<$ 1.03 GeV). The advantage with respect to the inclusive analysis presented above is that the η contribution is almost totally suppressed and we can test more directly the description of the baryonic and off-shell ρ contribution. A first comparison, using the simulation with the baryonic 'mixed' option and the 'Breit-Wigner ρ' is shown in Fig. 8.14. The point-like baryon contribution, which is now dominant below 200 MeV/c^2, is too large by about a factor 2. This discrepancy can maybe be attributed to the fact that we calculated the e^+e^- invariant mass distribution for resonances produced in the s-channel. Non-resonant t channel or resonant u-channel, where the mass of the emitting object is different would probably lead to steeper invariant mass distributions.

We can also observe that the ρ contribution with the Breit-Wigner mass distribution gives a good description of the e^+e^- yield above 400 MeV/c^2, which is fully consistent

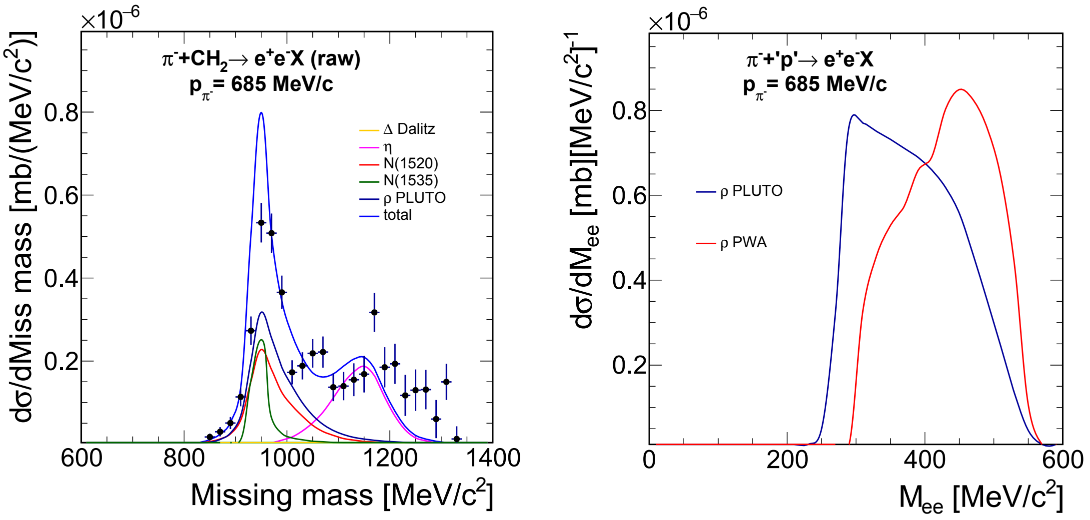

Figure 8.14: Left: Comparison of experimental exclusive invariant mass spectrum with the Pluto cocktail. The baryonic contribution is taken in the 'mixed option' and the ρ contribution with a Breit-Wigner mass distribution, as provided from the Pluto event generator. Right: Comparison of the e^+e^- invariant mass distributions in the simulation via an off-shell ρ decay with a Breit-Wigner mass distribution (black curve) and with a mass distribution deduced from the PWA of 2 pion production channels (red curve).

with the observation in the inclusive case. The point-like baryon Dalitz decay simulation underestimates the data by more than a factor 5 and the off-shell ρ contribution improves significantly the description. However, the yield between 250 and 400 MeV/c^2 is strongly overestimated. Due to the coupling of the ρ to baryon resonances, taking the mass distribution of the off-shell ρ as a tail of the free Breit-Wigner distribution of the ρ meson is probably too crude. Since the off-shell ρ mass distribution was extracted from the PWA of the two pion production analysis, it seems more realistic to use this ingredient to generate e^+e^- (see Sec. 8.2.3). In Fig. 8.14 (Right), we show the comparison between the simulated e^+e^- invariant mass distributions for the two ρ meson mass options and a significant difference is indeed observed. Since the ρ production cross section is the same in both cases, the different yield is due to the different ρ mass distributions and to the dependence of the branching ratio as a function of the invariant mass.

In the following, we use the ρ mass distributions from the PWA analysis and show in Fig. 8.15 and Fig. 8.16 the comparison with simulations with the different options for the treatment of the point-like baryon Dalitz decay. As mentioned above, after the missing mass selection, the yield for invariant masses in the region between 120 and 300 MeV/c^2 is dominated by the baryonic contribution and is therefore sensitive to the choice of the option. We can observe that for the three first cases (N(1520), N(1535) and 'mixed') the yield in the region between 140 and 300 MeV/c^2 is overestimated by almost a factor 2. This excess is correlated to the too high peak observed at large pt_{ee} in the same invariant mass range (see Fig. 8.10). As mentioned above, this points to a too large baryon contribution in our simple model. The 'PWA' baryonic option, where only the s-channel resonant contribution is taken into account, gives the best agreement with the data.

For invariant masses larger than 300 MeV/c^2, the off-shell ρ is strongly dominating and the yield in the simulation is therefore very similar in the different options. The off-shell ρ contribution with a mass distribution taken from the PWA gives a much better description of the experimental spectrum than the Breit-Wigner ρ (Fig. 8.14 Left and Fig. 8.16 Left). This nicely confirms the consistency of our simple approach, consisting in converting the

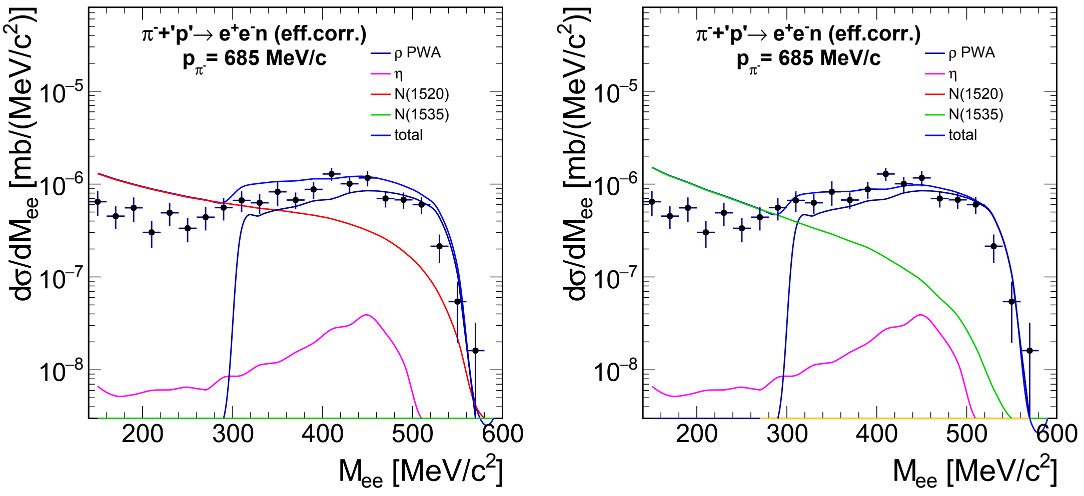

Figure 8.15: Comparison of experimental exclusive invariant mass spectrum with the Pluto cocktail in the "N(1520) effective" (left) and "N(1535) effective" (right) options. The off-shell ρ mass distribution is taken from the PWA of the two pion production channels.

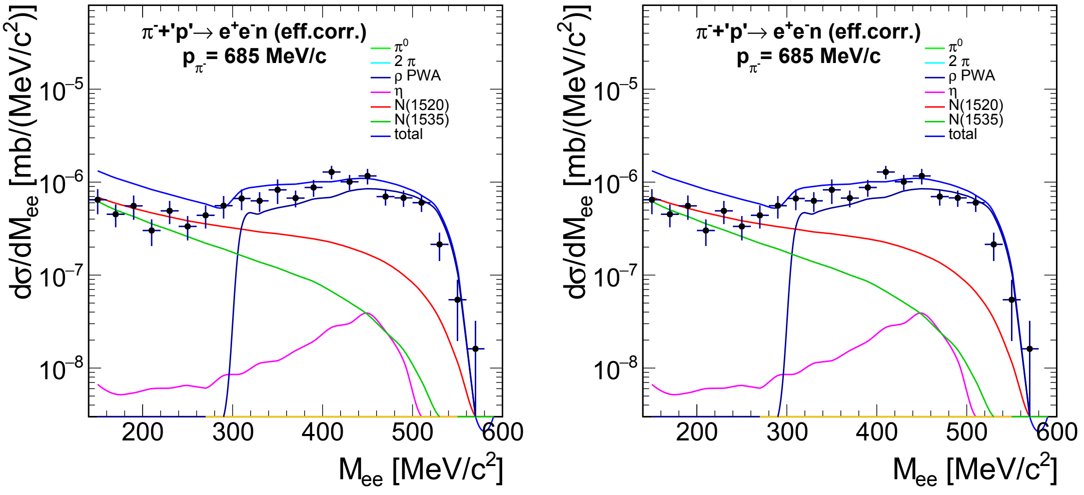

Figure 8.16: Comparison of experimental exclusive invariant mass spectrum with the Pluto cocktail in the "mixed" (left) and "PWA" options (right). The off-shell ρ mass distribution is taken from the PWA of the two pion production channels.

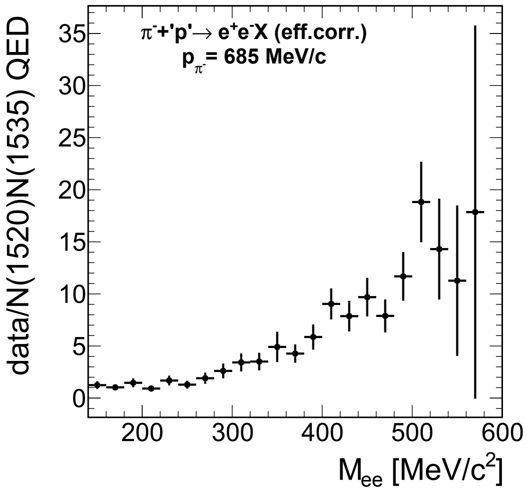

Figure 8.17: Ratio of exclusive invariant mass distributions to the point-like baryonic contribution (mixed option) in the simulation.

ρ contribution known from the pion channels into an e^+e^- production. The latter can be seen as a way to take into account the effect of time like electromagnetic form factors of the Vector Dominance type in a global way. This procedure gives the good order of magnitude for the e^+e^- yield and a good description of the invariant mass distribution.

The right part of Fig. 8.17 displays the ratio between the experimental invariant mass distribution and the point-like component of the cocktail (*i.e.* not taking into account the off-shell ρ contribution) in the 'PWA' option. This ratio quantifies the excess above the dielectron yield expected for point-like baryons and can be interpreted as an effective form factor.

Effect of the N(1520) time-like electromagnetic form factor

We further compared our experimental data with models for time-like electromagnetic baryon transitions. This work was done in collaboration with G. Ramalho who adapted the existing model for the N(1520)$^+$ decay into pe^+e^- for the case of the neutral state (N(1520)^0 $\rightarrow$ n e^+e^-) which is relevant for our experiment. The shape of G$_T$ for the N(1520)^0 -n transition is very similar to the N(1520)$^+$-p case which was shown in Fig. 7.12. This is due to the fact that the dominant component is the meson cloud which does not depend on the charge state. The quark core contribution does depend on the quark configuration and hence on the isospin, but it has a negligible contribution. To test the effect of this time-like electromagnetic form factor for the N(1520) resonance, we used the simulation in the 'PWA' option and weighted the yield of e^+e^- pairs produced in the N(1520) Dalitz decay by $|G_T|^2$. The comparison of the experimental e^+e^- invariant mass distribution with the simulation cocktail including the form factor is shown in Fig. 8.18. It can be observed that the simulation overestimates the data, so the effect of the form factor in the model seems to be too large, which needs further investigation.

In the following, we compare the data with several theoretical models described in Chapter 7.

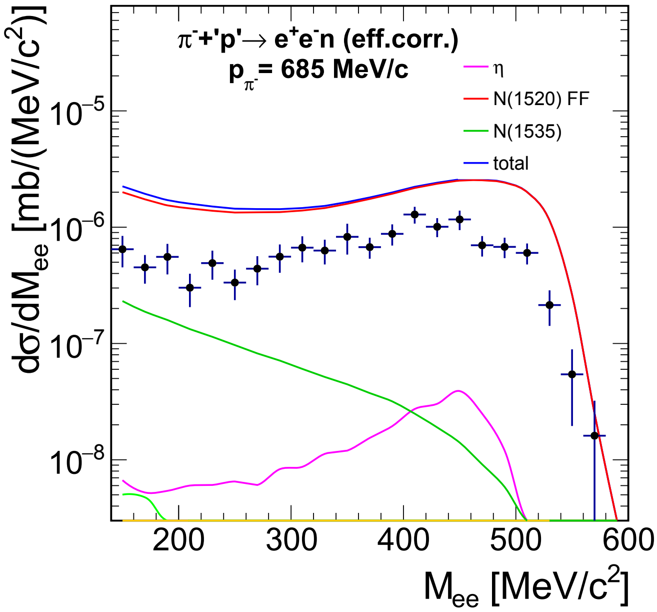

Figure 8.18: Comparison of the exclusive e^+e^- invariant mass spectrum with the cocktail using the "N(1520) effective" option together with the time-like electromagnetic form factor of Ramalho and Pena [133].

8.3 Comparison to models based on off-shell vector meson production

As discussed in Sec. 7.2, the model of [130] predicts a very low cross section for the $\pi^-p \to ne^+e^-$ reaction in our energy range. From Fig. 7.3, we can deduce a differential cross section

$$\frac{d\sigma}{dM_{ee}} = 2M_{ee} \times \frac{d\sigma}{dM_{ee}^2} \sim 0.06\ \mu b/GeV \tag{8.26}$$

at $M_{ee} = 0.5$ GeV/c. In comparison, our Pluto cocktail which reproduces fairly well the measured yield in acceptance, gives a value in 4π which is one order of magnitude higher at the same invariant mass. Since acceptance effects can not compensate for such a large difference, we can conclude that the model [130] strongly underestimates our dielectron yield. As discussed in Sec. 7.2, the very low cross section for the $\pi^-p \to ne^+e^-$ in [130] is due to the almost total cancellation between the ρ and ω contributions. However, the ρ contribution itself is of the order of $\frac{d\sigma}{dM_{ee}} = 0.5\mu$b/GeV at $M_{ee} = 0.5$ GeV/c^2, while the value extracted from the PWA of the 2π channel and converted in an e^+e^- yield using VDM is of the order of 46 μb/GeV. This suggests a possible underestimate of the couplings to the ρ meson derived in [148] and used in the calculation [130]. As mentioned in [149], the extraction of ρ production cross sections is ambiguous for center of mass energies below 1.7 GeV, due to the off-shellnes of the ρ meson. In our simple approach, including an off-shell ρ (isovector) contribution, but no off-shell ω (isoscalar) contribution, we have a reasonable agreement with the data, again in contrast with the calculations of [130] where the ω off-shell production is of the same order than the ρ contribution.

The calculations of [129] have been performed for a minimum center of mass energy of $\sqrt{s}$=1.6 GeV/c, and cannot therefore be directly compared to our data. However, one can notice that at $\sqrt{s}$=1.6 GeV/c, the ω contribution is of the same order of magnitude than in model [130], while the ρ contribution is by at least a factor of 6 larger.

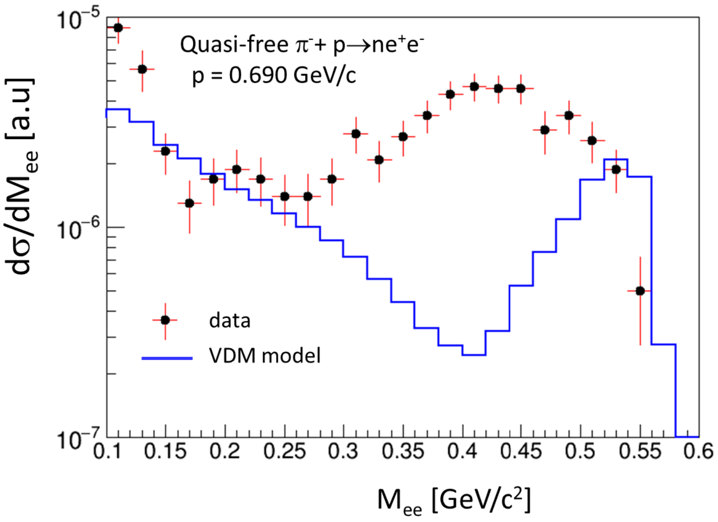

Figure 8.19: Comparison of the e^+e^- invariant mass spectrum obtained in a preliminary stage of the analysis for the exclusive reaction with the model predictions from [131].

8.4 Comparison to Lagrangian model

In a complete calculation, form factors should be applied at each electromagnetic vertex and all contributions should be added coherently. As described in Sec. 7.2, this was done in the model of [131] where many resonant and non-resonant graphs were included and VDM form factors were used for each baryonic transition. The comparison is shown in Fig. 8.19, at a preliminary stage of the analysis, but the main result remains the same. A striking feature of the theoretical distribution is the narrow peak at large invariant masses due to the specific VDM Lagrangian used in the model. Our data, which present a very broad structure, do not seem to be in agreement with this input.

8.5 Spin density coefficients

As discussed in Sec. 7.6, the analysis of the lepton angular distributions for e^+e^- pairs measured in the $\pi^-p \to ne^+e^-$ recation can help to disentangle the different contributions and extract more information on their electromagnetic structure.

First, we focus on the distribution of the virtual photon angle in the center-of-mass. As already discussed, this distribution is highly distorted by acceptance cuts. In particular, the acceptance for forward emission of the virtual photon is very poor. This angular distribution is shown in Fig. 8.20, where it is compared to a simulation where the e^+e^- pair is emitted isotropically in the center-of-mass. We can see that, despite the low statistics and drastic acceptance cuts, the angular distribution presents some sensitivity and it significantly deviates from isotropy. This gives already some information on the contributing partial waves. Indeed, in the presence of spin 1/2 waves, the angular distribution is expected to be isotropic. This deviation therefore signals the presence of contributions with spin 3/2 or larger, which is in agreement with the results from the PWA of two pion channels.

To illustrate the problem of acceptance, we show in Fig. 8.21 the (θ, ϕ) distributions for simulated events in the π^-p $\to$ nρ [$\rho = \gamma^* \to e^+e^-$] reaction in three bins of cos(θ_{γ^*}. The ρ meson is produced isotropically in the centre-of-mass and the lepton emission is also isotropic in the ρ (=γ^*) rest frame. At backward γ angles, only two bands in ϕ_{el}

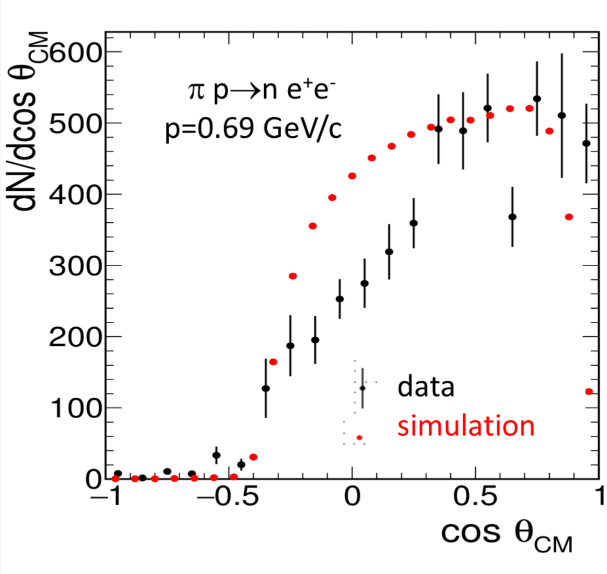

Figure 8.20: Distribution of the virtual photon angle in the center-of-mass for data (arbitrary units, black dots) and for a phase space simulation of the reaction $\pi^- p \to n e^+ e^-$.

are significantly covered by the detection. The acceptance is larger for forward emitted γ^*, but still there are large holes in the $(\cos\theta, \phi)$ coverage. This points to the absolute necessity of including the acceptance effects in the fitting procedure to extract the spin density coefficients. This is realized, thanks to the fitting procedure developed by [138]. We describe below its main features.

Following the spin density formalism, the squared of the transition amplitude for the reaction $\pi^- p \to n e^+ e^-$ at a given M$_{ee}$ and θ_{γ^*} is parametrized using the spin density matrix coefficients (see Eq. 7.71). Considering a given data sample, the probability w_i of each event is proportional to the squared amplitude and therefore also follows Eq. 7.71.

The first step of the procedure consists in producing simulated events (so-called Monte-Carlo events) using the simulation software (Sec. 7.6) with events generated with isotropic angular distributions (*i.e.* ρ_{11}=1/3, ρ_{10}=0, ρ_{1-1}=0) and fully reconstructed. All the Monte-Carlo events are generated with equal probability. After weighting each event k in the simulation by the factors

$$\begin{aligned} w_k = \quad & 1 - \rho_{11} + \cos^2\theta_e(k)(3\rho_{11} - 1) + \sqrt{2}\sin(2\theta_e(k))\cos\phi_e(k) Re\rho_{10} \\ & + \sin^2\theta_e(k) Re\rho_{1-1}\cos(2\phi_e(k))]. \end{aligned} \tag{8.27}$$

, these events should give a good approximation of the data. The optimization procedure therefore consists in calculating the density matrix coefficients ρ_{ij} which maximize in a bin of M$_{ee}$ and θ_{γ^*} the likelihood function:

$$L = \prod_{l=1}^{N^{data}} \frac{w_l}{\sum_{k=1}^{N_{rec}} w_k} \tag{8.28}$$

, where the products runs over all data in the corresponding bin and the sum over all the reconstructed events in the simulation sample.

In fact, the logarithm of the above function is maximized instead of the function itself,

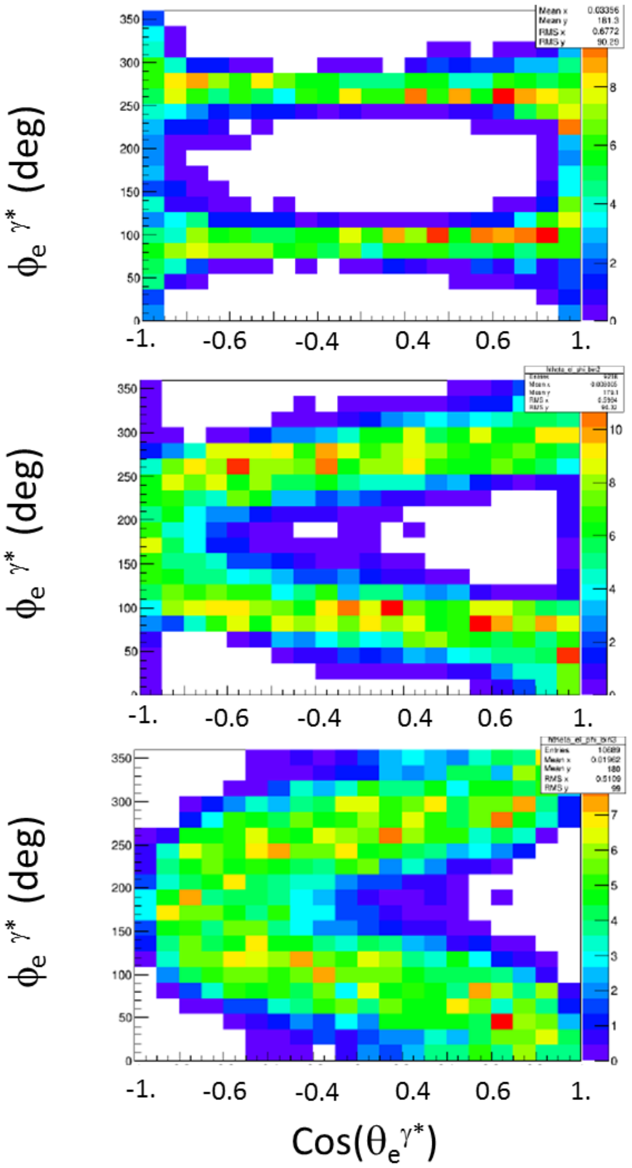

Figure 8.21: Results of simulations of the reaction $\pi^- p \to n\gamma^*(\gamma^* \to e^+e^-)$. The two steps are generated according to phase space. The distributions of reconstructed events as a function of the $\cos\theta$ and ϕ of the electron in the γ^* rest frame are displayed for three regions of γ^* angles: $-0.4 < \cos\theta_{\gamma^*} < 0.$ (Top) , $0. < \cos\theta_{\gamma^*} < 0.5$ (Middle) and $0.5 < \cos\theta_{\gamma^*} < 1$ (Bottom)

hence

$$\ln L = \frac{\sum\limits_{l=1}^{N^{data}} \ln w_l}{\sum\limits_{k=1}^{N_{rec}} w_k}. \tag{8.29}$$

The procedure was first tested on events simulated with known values of the density coefficients. Various tests were performed in order to check the capability of the fitting procedure to retrieve these coefficients. These tests were performed using different values of the density matrix coefficients. In overall, it could be checked that the fit gives a consistent result (see Fig. 8.22) and realistic errors. However, a strong sensitivity of the

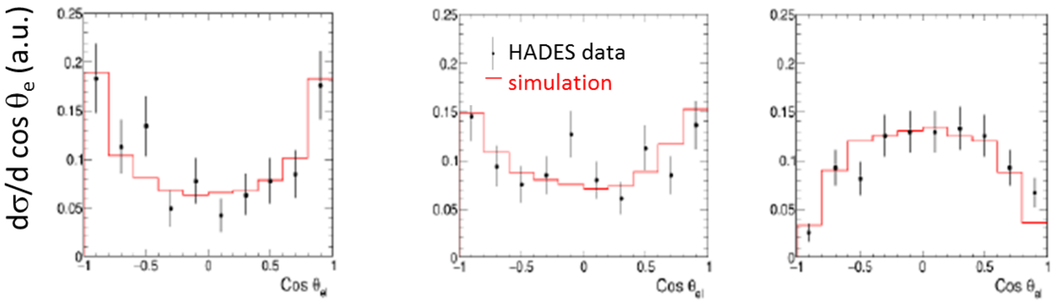

Figure 8.22: Distributions of the electron polar angle in the helicity frame compared to the fit function in the different bins of $\cos\theta_{\gamma^*}$.

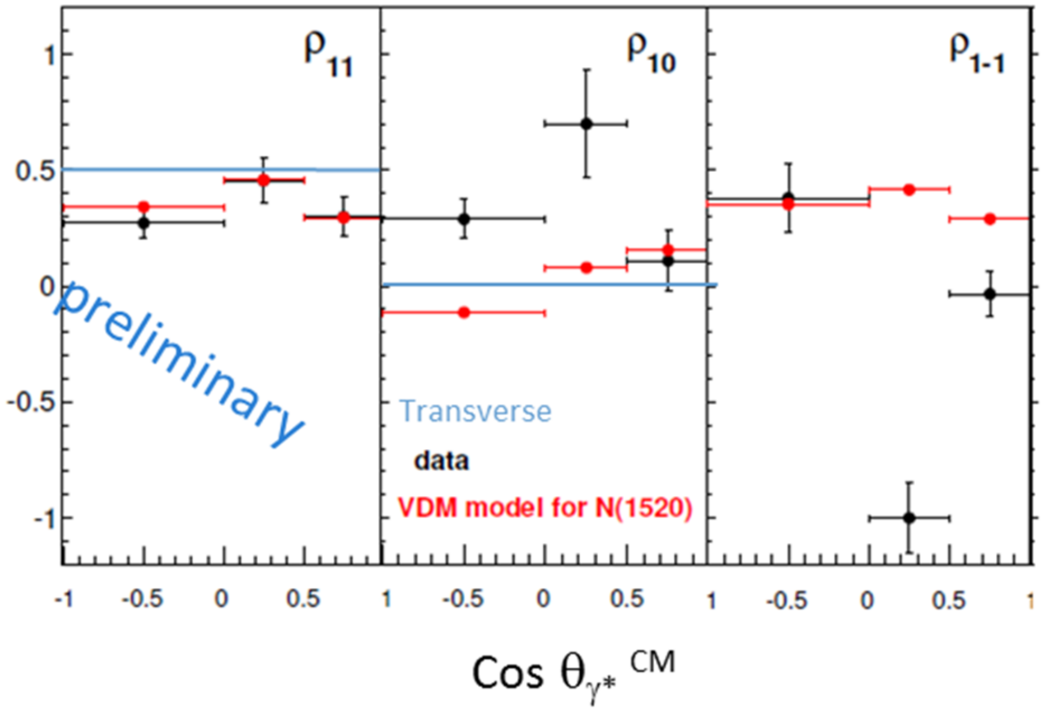

Figure 8.23: Density matrix coefficients ρ_{11}, ρ_{10}, ρ_{1-1} extracted from the data (black dots) and obtained in the model [142] for the N(1520) component only.

fitting procedure to the invariant mass distribution of the Monte Carlo events was observed. The fit is indeed performed using events integrated over a broad invariant mass window, due to the small statistics and the acceptance is changing quite rapidly as a function of the invariant mass. It is therefore important to use Monte-Carlo events generated with an invariant mass distribution close to the experimental one.

The procedure has been applied to the experimental raw data for $M_{ee} > 400$ MeV/c^2. The variations of the density matrix coefficients when changing by 20 MeV the invariant mass distribution for the Monte-Carlo events have been checked to stay within the error bars. In addition, fits were performed by shifting the bins in cosθ by ± 0.05 and the lower limit in invariant mass by 20 MeV. The results of all these fits are compatible within the error.

The final results are shown in Fig. 8.23 in three bins corresponding respectively to $\cos(\theta_{\gamma^*}) < 0.$, $0. < \cos(\theta_{\gamma^*}) < 0.5$ and $0.5 < \cos(\theta_{\gamma^*}) < 1.$. The first observation that can be made is that for some bins ρ_{11} is different from 0.5 and ρ_{10} is different from 0, which signals a longitudinal contribution, in contrast to real photons (see Sec. 7.6). This is already an interesting model-independent result.

The results are also compared to the expectations from the model [142] using only the N(1520) contribution and neglecting the N(1440) contribution, since the N(1440) amplitude extracted in the PWA of the two-pion production channels is very small. The ρ_{11} coefficient which reflects the polar angle anisotropy of the electron in the helicity frame is compatible with the model, while the ρ_{10} and ρ_{1-1}, which are linked to the azimuthal distribution deviate for some bins. These results show that information about the spin structure of the electromagnetic transition can be extracted from the analysis of the angular distribution.

Chapter 9

Conclusion and Outlook

9.1 Conclusion

The main objective of the experiments with the HADES experimental set-up is the study of hadronic matter in the region of high net baryon densities and moderate temperatures produced in heavy ion collisions at incident energies between 1 and 4A GeV. The results obtained by the HADES collaboration for the di-electron production in nucleus-nucleus, nucleon-nucleus and nucleon-nucleon interactions have demonstrated the importance of the coupling of baryonic resonances to ρ mesons. In the hadronic matter, a strong modification of ρ meson spectral function is observed, due to the excitation of baryonic resonances. The study of elementary proton-proton and neutron-proton reactions with HADES is useful to validate medium effects interpretation and to study the Dalitz decay of baryonic resonances, which are processes of the type ($R \rightarrow Ne^+e^-$). Such decays provide information on electromagnetic transitions in an unexplored kinematical region, where vector mesons (ρ, ω, ϕ) are expected to play a major role. The effect of coupling of baryons to ρ mesons is indeed clearly observed in the dielectron invariant mass spectra. However, for resonances higher than $\Delta(1232)$, the contribution of the different transitions is difficult to disentangle. The pion induced reaction, which is studied in this PhD work, allows for a much more selective excitation of the different baryons, depending on the incident pion energy. Data bases for pion induced reactions are old and very scarce. In particular, very few studies of the second resonance region (N(1440), N(1520), N(1535), ...) exist and the production of e^+e^- had never been measured in this energy range.

The data analysis presented in this manuscript is based on a commissioning experiment realized with the large acceptance HADES detector, the secondary GSI pion beam and polyethylene and carbon targets, at center-of-mass energy of 1.49 GeV, *i.e.* close to the pole of the N(1520) resonance. A detailed study of the RICH response has been necessary, in order to calculate precisely the efficiency of the electron and positron reconstruction. For this, the parameters of the RICH digitizer have been carefully adjusted in the simulation, to reproduce measured observables. A new method, based on the selection of a sample of positrons using only momentum and time of flight correlation was developed to check the efficiency of the RICH detector. In pion induced reactions in this energy range, the main contribution to the combinatorial background is due to the conversion of photons. Thanks to dedicated cuts implemented to specifically reject tracks originating from photon conversion, the combinatorial background is reduced to a contribution of 100% at maximum for invariant masses close to 110 MeV/c^2 and of less than 10% for most of the other invariant mass bins. The normalization is provided by the measurement of the elastic πp scattering in the same experiment. The precise subtraction of the interactions with carbon nuclei was shown to be possible only for the invariant mass region of the π^0 Dalitz decay, due to the lack of statistics for larger invariant masses. A selection on the missing mass allows to isolate the contribution from the free (for interactions with protons) or quasi-free (for interactions with carbon nuclei) $\pi^- p \to n e^+ e^-$ reaction. An important part of the work consisted in calculating the efficiency corrections. This is done in a model independent way, using GEANT3 simulations for electrons and positrons. The standard method where the efficiency was calculated as a function of generated values of the kinematical variables could not be applied to our experiment, mainly due to the large bremsstrahlung effect for the thick target used in this experiment and a new procedure was developed, taking into account the distortion of the kinematical variables due to experimental effects. The systematic errors are dominated by the normalization and efficiency correction uncertainties.

Another contribution of this PhD consisted in the construction of an event generator for the description of the data. The latter comprises several sources of e^+e^- production, with ingredients based on existing data. For the production of π^0 and η , existing data from pion induced reactions on proton can be directly used. The point-like baryon contribution to the e^+e^- production is estimated from Partial Wave Analysis of data measured in the reaction $\pi^- p \to n\gamma$, using different scenarios to calculate the shape of the invariant mass spectrum. Interactions with carbon nuclei are treated using the participant-spectator model. This simulation strongly underestimates the e^+e^- yield for invariant masses larger than 300 MeV/c^2, which is clearly due to the effect of time-like transition form factors which are not taken into account.

For the exclusive production, the η contribution is suppressed and the sensitivity to the baryonic contribution is enhanced. To take into account transition form factors, the first approach consisted in using the Vector Dominance Model, *i.e.* deduce the e^+e^- contribution from the off-shell ρ production, as extracted from the PWA of the $\pi^+\pi^-$ production measured by HADES in the same experiment. The description of both inclusive and exclusive spectra is highly improved by the adjonction of this off-shell ρ contribution. In the second approach, a model for the N(1520)-neutron electromagnetic time-like transition form factor was introduced instead of the off-shell ρ contribution, providing also good results. At present, these empirical approaches better reproduce the data than more complete models aiming at a coherent description of the $\pi^- p \to n e^+ e^-$ reaction. We hope that our results will stimulate new calculations for this reaction.

Angular distributions for the exclusive $\pi^- p \to n e^+ e^-$ are parametrized using the spin density matrix formalism and results are compared to a theoretical model based on resonant contributions, with form factors of the vector dominance type. The precision is limited due to the lack of statistics, but it is clear that these angular distributions bring supplementary information on the structure of electromagnetic baryon transitions and can discriminate among models. In particular, the spin structure of this time-like electromagnetic transition is different from expectations for real photons, and a significant longitudinal contribution is observed in some bins.

9.2 Outlook

9.2.1 Further pion beam experiments

While our commissioning experiment demonstrated the interest of the $\pi^- p \to n e^+ e^-$ reaction to extract information on the time-like electromagnetic structure of baryons, it is clear that a better precision is needed. Furthermore, to get unambiguous results, the reaction on the carbon has also to be measured with a good statistics. The use of the liquid hydrogen target will indeed still be avoided in future in combination with the pion beam due to the possible impact of the beam halo on the target material.

As for the present experiment, the information on electromagnetic channels will be coupled to the Partial Wave Analysis of hadronic channels. The interest of the study of the two-pion production channel in the reaction $\pi^- p$ for baryon spectroscopy, in particular to improve the ρN couplings of baryon resonances has been demonstrated in the energy region of $\sqrt{s}$=1.5 GeV. This will be of course valid for the even less known $\sqrt{s}$=1.7 GeV region. Precise differential distributions can be measured not only for the 2π production channels, but also for $K\Lambda, K\Sigma, \eta n, \omega n$. The new HADES measurements will complement the precise data obtained from photon and electron-scattering experiments and will allow for a better understanding of the resonance mass spectrum and their decays. An experimental proposal has been submitted to the GSI General Program Advisory committee in September 2017. The focus will be put this time on the region around $\sqrt{s} = 1.7$ GeV. We will start in March 2019 with a Ag+Ag experiment. The pion beam experiment can be realized in 2020. The requested beam time was based on the present measurements and on expected improvements due to the new RICH photon detector. Our analysis was performed with 1500 events measured on the polyethylene target. It was estimated that a total statistics of 10^4 events in the $\pi^- p \to n e^+ e^-$ reaction (hence after carbon subtraction) is needed to extract the density matrix elements with precision of few percent for four bins in the θ_{γ^*} angles in the forward direction, the backward region being affected by the HADES acceptance.

Similar studies can be performed in the fourth resonance region ($\sqrt{s} \sim 1.9$ GeV/c) in combination with measurements of the $\Lambda(1405)$ and kaonic states.

It is also important to measure at the same energy $\pi^+ p$ and $\pi^+ n$ reactions. The study of $\pi^+ p$ reactions would allow to test exclusively Δ resonances. The comparison of π^+ n and π^+ p reactions would allow to determine the isoscalar and isovector components of the e^+e^- production (see Sec. 7.2). It is also very important for baryon spectroscopy issues to include in PWA data for different isospin configurations. Such measurements with a positively charged (π^+) pion beam would therefore have a great impact. Secondary beams of π^+ can be produced at GSI, although the rejection of proton contamination using a time-of-flight has to be investigated.

It is also worth mentioning that the measurements on carbon have an intrinsic interest. They indeed allow for a study of meson and dielectron production in cold matter.

9.2.2 Studies of Hyperon Dalitz decays with HADES

The HADES collaboration also plans to start a program of hyperon Dalitz decay measurements (Y'→Ye^+e^-). This will complement the study of excited nucleon states that was started with proton and pion beams. The interest of hyperon electromagnetic structure has been pointed out long time ago [150]. The situation has been improved only recently thanks to measurements for $\Sigma(1385)$ and $\Lambda(1520)$ at JLab. HADES will also be able to measure radiative decays of hyperons in future, thanks to the new Electromagnetic Calorimeter. It is unique for the measurement of Dalitz decays, probing the time-like electromagnetic structure at finite q^2. It has also to be noted that, unlike the excited nucleon states, no easy measurement can be performed in the space like region, as hyperon targets are not available.

Since hyperons are narrow, they can be identified by pe^+e^- invariant mass peaks and therefore proton-proton reactions can be used. Simulations have been performed to check the feasibility of the measurements, which are planned by the HADES collaboration. These measurements will be complementary to annihilation experiments probing the time like electromagnetic structure at large q^2. Data have been published by the CLEO collaboration for q^2>14 GeV/c^2 which show the important role played by quark correlations. Data from BESIII for q^2 in the few GeV range are also currently being analyzed. HADES Dalitz decay measurements will have a strong impact for the electromagnetic structure of hyperons in the small q^2 range. An interesting open question is the validity of VDM in the hyperon sector. It will be for example instructive to compare $\Delta(1232)$ (Δ→Ne^+e^-)

and the $\Sigma(1385)$ Dalitz decays ($\Sigma(1385) \rightarrow \Lambda\ e^{+}e^{-}$) which have same quantum numbers and differ just by the quark content. It will be a valuable test of SU(3) symmetry. These measurements will take advantage of the new Forward Detector which is in construction and will complement the acceptance in the forward region ($0.6 < \theta_{lab} < 6.5^{0}$).

Résumé en français

L'objectif principal des expériences avec le dispositif HADES (High Acceptance Di-Electron Spetrometer) est l'étude de la matière hadronique, dans la région de forte densité (jusqu'à trois fois la densité nucléaire normale) et de températures modérées, produite en utilisant des collisions d'ions lourds à des énergies incidentes de l'ordre de 1 à 4A GeV. Les résultats obtenus par la collaboration HADES pour la production de di-électrons dans les réactions noyau-noyau, nucléon-noyau et nucléon-nucléon montrent l'importance du couplage des résonances baryoniques au méson ρ. Dans la matière nucléaire, une forte modification de la fonction spectrale du méson ρ est observée, due à l'excitation de résonances baryoniques. L'étude des réactions élementaires proton-proton et neutron-proton permet de valider les interprétations des effets de milieu et d'étudier la décroissance Dalitz des résonances baryoniques, de type ($B \rightarrow N\ e^+e^-$). Ces décroissances donnent des informations sur les transitions électromagnétiques dans une région inexplorée cinématiquement, où l'on s'attend à ce que les mésons vecteurs (ρ, ω, ϕ) jouent un rôle important. L'effet du couplage au méson ρ est observé très clairement mais, pour les résonances d'énergie plus haute que le Δ(1232), la contribution des différentes transitions baryoniques est difficile à séparer. La réaction π-nucléon étudiée dans cette thèse permet une excitation beaucoup plus sélective de chaque résonance en fonction de l'énergie dans le centre de masse. Les bases de données obtenues avec des faisceaux de pions sont très anciennes et très succintes et la seconde région de résonances (N(1440), N(1520), N(1535),..) a en particulier été très peu étudiée.

L'analyse présentée dans cette thèse est basée sur une expérience-test réalisée avec le détecteur de grande acceptance HADES, le faisceau secondaire de pions de GSI et des cibles de polyethylene et de carbone. Le détecteur est composé de six secteurs comprenant un RICH (Ring Imaging Cerenkov) pour l'identification des électrons et positrons, des chambres à dérive situées avant et après un aimant toroidal pour la reconstruction de trajectoires et des détecteurs pour la mesure de temps de vol. Des détecteurs placés dans le faisceau permettent de reconstruire la trajectoire et l'impulsion des pions et de déclencher l'acquisition. L'étude de la diffusion élastique π^-p permet de calibrer l'énergie du faisceau et de normaliser les données.

L'analyse de données est optimisée pour sélectionner efficacement les électrons et les positrons et éliminer la contribution de la conversion des photons dans les matériaux de la cible et du détecteur. Une étude détaillée de la réponse du détecteur RICH, qui est le plus important pour l'identification des électrons, a été nécessaire pour réaliser des simulations réalistes. Le bruit de fond combinatoire est faible et peut être soustrait précisément. Le problème de la soustraction de la contribution de noyaux de carbone dans les mesures sur la cible de polyethylene pour étudier la réaction π^-p a aussi été étudié. Compte-tenu de la statistique limitée mesurée sur la cible de carbone, une soustraction précise n'est pas possible, et la description des données doit prendre en compte les interactions avec les noyaux de carbone.

En vue de la comparaison aux modèles, les données sont corrigées pour l'efficacité du détecteur et des algorithmes de reconstruction, en utilisant les simulations. La procédure utilisée pour la correction d'efficacité tient compte de la distortion des observables mesurées, due en particulier au processus de bremsstrahlung. Toutes les contributions à l'efficacité de la mesure sont prises en compte avec soin dans le calcul des erreurs sytématiques. Les résultats sont présentés à la fois pour la production inclusive de paires e^+e^-, et pour la production exclusive correspondant à la réaction $\pi^-p \rightarrow ne^+e^-$ libre ou quasi-libre et obtenue après une sélection sur la masse manquante.

Un des travaux importants de cette thèse a consisté en l'élaboration d'un générateur d'événements pour la description des données. Celui-ci comprend plusieurs sources de production de paires e^+e^-dont les ingrédients sont basés sur des données existantes. Pour la production de π^0 et de η , les données existantes dans la réaction π^-p sont utilisées. La contribution baryonique est déduite des analyses en ondes partielles de la réaction $\gamma n \to \pi^- p$. Les interactions avec les noyaux de carbone sont prises en compte en utilisant le modèle participant-spectateur et un facteur de renormalisation déduit des données mesurées sur la cible de carbone. Cette simulation ne permet pas de reproduire la production très abondante de paires e^+e^- aux masses invariantes supérieures à 300 MeV/c^2. Celle-ci est clairement due à l'effet des facteurs de forme de transition qui ne sont pas pris en compte dans la simulation. Pour la production exclusive, la contribution du η est supprimée et la sensibilité à la contribution baryonique est donc accrue. Pour prendre en compte les facteurs de forme de transition, la première approche consiste à utiliser le modèle de dominance vectorielle. Ainsi, la contribution de paires e^+e^- est estimée via la décroissance de ρ virtuels dont la production est connue grâce à l'analyse en ondes partielles de la production de deux pions, mesurée avec HADES dans la même expérience. Une description satisfaisante des données est alors obtenue. Une autre approche, consistant à utiliser un modèle de facteur de forme électromagnétique dans la région temps pour la transition N(1520)^0-neutron, donne aussi de bons résultats. Dans ce modèle, les baryons sont décrits avec un coeur de quarks et un nuage de mésons. Ce dernier joue le rôle principal dans notre domaine cinématique. Ces approches semi-empiriques décrivent bien mieux les données que des calculs complets, basés sur des lagrangiens effectifs ou des modèles en voies couplées.

Les distributions angulaires sont paramétrisées en utilisant le formalisme de la matrice densité et les résultats sont comparés à un modèle théorique, basé sur les contributions cohérentes de plusieurs résonances, avec des facteurs de forme de type dominance vectorielle. Cette comparaison montre que les distributions angulaires apportent des informations supplémentaires sur la structure des transitions baryoniques électromagnétiques. Cette analyse, basée sur une expérience-test, sert de motivation pour les expériences futures. L'étude présentée dans cette thèse pourra ainsi être prolongée à plus haute énergie dans la troisième région de résonances (masses de l'ordre de 1.7 GeV/c^2). Il est aussi envisagé de mesurer les décroissances Dalitz de baryons étranges (hypérons) qui fourniront des informations inédites sur l'effet des quarks étranges dans les transitions électromagnétiques.

Bibliography

[1] B.-J. Schaefer, J. M. Pawlowski, and J. Wambach, Phys. Rev. **D76**, 074023 (2007), *The Phase Structure of the Polyakov–Quark-Meson Model.*

[2] B. Abbott *et al.*, Phys. Rev. Lett. **119**, 161101 (2017), *GW170817: Observation of Gravitational Waves from a Binary Neutron Star Inspiral.*

[3] U. Mosel, *Fields, Symetries and Quarks* (Springer, Berlin, 1999).

[4] S. Klimt, M. Lutz, and W. Weise, Phys. Lett. **B249**, 386 (1990), *Chiral phase transition in the SU(3) Nambu and Jona- Lasinio model.*

[5] Y. Aoki, G. Endrodi, Z. Fodor, S. D. Katz, and K. K. Szabo, Nature **443**, 675 (2006), *The order of the quantum chromodynamics transition predicted by the standard model of particle physics.*

[6] Y. Aoki, Z. Fodor, S. D. Katz, and K. K. Szabo, Phys. Lett. **B643**, 46 (2006), *The QCD transition temperature: Results with physical masses in the continuum limit.*

[7] Z. Fodor and S. D. Katz, Physics Letters B **534**, 87 (2002), *A new method to study lattice QCD at finite temperature and chemical potential.*

[8] G. E. Brown and M. Rho, Phys. Rev. Lett. **66**, 2720 (1991), *Scaling effective Lagrangians in a dense medium.*

[9] T. Hatsuda and S. H. Lee, Phys. Rev. **C46**, 34 (1992), *QCD sum rules for vector mesons in nuclear medium.*

[10] R. Rapp and J. Wambach, Eur. Phys. J. **A6**, 415 (1999), *Low mass dileptons at the CERN-SPS: Evidence for chiral restoration?*

[11] R. Rapp, G. Chanfray, and J. Wambach, Nucl. Phys. **A617**, 472 (1997), *Rho meson propagation and dilepton enhancement in hot hadronic matter.*

[12] R. Rapp and H. van Hees, Eur. Phys. J. **A52**, 257 (2016), *Thermal Electromagnetic Radiation in Heavy-Ion Collisions.*

[13] T. Galatyuk, P. M. Hohler, R. Rapp, F. Seck, and J. Stroth, Eur. Phys. J. **A52**, 131 (2016), *Thermal Dileptons from Coarse-Grained Transport as Fireball Probes at SIS Energies.*

[14] S. Teis *et al.*, Z. Phys. **A356**, 421 (1997).

[15] I. G. Aznauryan and V. D. Burkert, Few Body Syst. **59**, 98 (2018), *Electroexcitation of nucleon resonances in a light-front relativistic quark model.*

[16] V. D. Burkert, Few Body Syst. **59**, 57 (2018), *N^* Experiments and Their Impact on Strong QCD Physics.*

[17] B. Aubert *et al.*, Phys. Rev. **D76**, 092006 (2007), *Study of* $e^+e^- \to \Lambda\bar{\Lambda}$, $\Lambda\bar{\Sigma}^0$, $\Sigma^0\bar{\Sigma}^0$ *using initial state radiation with BABAR.*

[18] S. Dobbs, K. K. Seth, A. Tomaradze, T. Xiao, and G. Bonvicini, Phys. Rev. D **96**, 092004 (2017), *Hyperon form factors and diquark correlations.*

[19] K. Schönning and C. Li, EPJ Web Conf. **137**, 12002 (2017), *Future Perspectives on Baryon Form Factor Measurements with BES III.*

[20] J. J. Sakurai, Phys. Rev. Lett. **22**, 981 (1969), *Vector-Meson Dominance and High-Energy Electron-Proton Inelastic Scattering.*

[21] F. Iachello, A. D. Jackson, and A. Lande, Phys. Lett. **B43**, 191 (1973), *Semiphenomenological fits to nucleon electromagnetic form- factors.*

[22] R. Bijker and F. Iachello, Phys. Rev. **C69**, 068201 (2004), *Re-analysis of the nucleon space- and time-like electromagnetic form-factors in a two-component model.*

[23] Q. Wan and F. Iachello, Int. J. Mod. Phys. **A20**, 1846 (2005), *A unified description of baryon electromagnetic form factors.*

[24] I. Fröhlich *et al.*, Eur. Phys. J. **A45**, 401 (2010), *A versatile method for simulating* $pp \to pp$ *e+ e- and* $dp \to pn$ *e+ e-* p_{spec} *reactions.*

[25] G. Ramalho and M. Pena, Phys.Rev. **D85**, 113014 (2012), *Timelike gamma* N* $\to \Delta e^+e^-$ *Delta form factors and Delta Dalitz decay.*

[26] G. Ramalho *et al.*, Phys. Rev. **D93**, 033004 (2016), *Role of the pion electromagnetic form factor in the* $\Delta(1232) \to \gamma^* N$ *timelike transition.*

[27] G. Eichmann, H. Sanchis-Alepuz, R. Williams, R. Alkofer, and C. S. Fischer, Prog. Part. Nucl. Phys. **91**, 1 (2016), *Baryons as relativistic three-quark bound states.*

[28] W. Ehehalt and W. Cassing, Nucl. Phys. **A602**, 449 (1996), *Relativistic transport approach for nucleus nucleus collisions from SIS to SPS energies.*

[29] J. Weil *et al.*, Phys. Rev. **C94**, 054905 (2016), *Particle production and equilibrium properties within a new hadron transport approach for heavy-ion collisions.*

[30] J. Adamczewski-Musch *et al.*, to be published, 2018.

[31] G. Agakishiev *et al.*, Phys. Lett. **B715**, 304 (2012), *First measurement of low momentum dielectrons radiated off cold nuclear matter.*

[32] G. Agakichiev *et al.*, Phys. Lett. **B663**, 43 (2008), *Study of dielectron production in C+C collisions at 1 AGeV.*

[33] G. Agakichiev *et al.*, Phys. Rev. Lett. **98**, 052302 (2007), *Dielectron production in C-12 + C-12 collisions at 2-AGeV with HADES.*

[34] G. Agakishiev *et al.*, Phys. Rev. **C84**, 014902 (2011), *Dielectron production in Ar+KCl collisions at 1.76A GeV.*

[35] I. Fröhlich *et al.*, PoS **ACAT2007**, 076 (2007), *Pluto: A Monte Carlo Simulation Tool for Hadronic Physics.*

[36] R. Shyam and U. Mosel, Phys. Rev. **C82**, 062201 (2010), *Dilepton production in proton-proton and quasifree proton- neutron reactions at 1.25 GeV.*

[37] J. Adamczewski-Musch *et al.*, Phys. Rev. **C95**, 065205 (2017), Δ*(1232) Dalitz decay in proton-proton collisions at T=1.25 GeV measured with HADES at GSI.*

[38] M. Tanabashi *et al.*, Phys. Rev. D **98**, 030001 (2018), *Review of Particle Physics.*

[39] G. Agakishiev et al., Phys. Lett. **B690**, 118 (2010), *Origin of the low-mass electron pair excess in light nucleus-nucleus collisions.*

[40] J. Adamczewski-Musch *et al.*, Eur. Phys. J. **A53**, 149 (2017), *Analysis of the exclusive final state* npe^+e^- *in quasi-free np reaction.*

[41] B. Martemyanov, M. Krivoruchenko, and A. Faessler, Phys. Rev. **C84**, 047601 (2011), *Dilepton production in pp and np collisions at 1.25 GeV.*

[42] H. Kuc, Ph.D. thesis, Paris-Sud university, France, 2014.

[43] M. Bashkanov and H. Clement, Eur.Phys.J. **A50**, 107 (2014), *On a Possible Explanation of the DLS Puzzle.*

[44] G. Agakishiev *et al.*, Eur. Phys. J. **A50**, 82 (2014), *Baryon resonance production and dielectron decays in proton-proton collisions at 3.5 GeV.*

[45] G. Agakishiev *et al.*, Eur. Phys. J. **A48**, 64 (2012), *Inclusive dielectron spectra in p+p collisions at 3.5 GeV.*

[46] J. Weil, H. van Hees, and U. Mosel, Eur. Phys. J. **A48**, 111 (2012), *Dilepton production in proton-induced reactions at SIS energies with the GiBUU transport model.*

[47] G. Agakishiev *et al.*, Phys. Rev. **C85**, 054005 (2012), *Inclusive dielectron production in proton-proton collisions at 2.2 GeV beam energy.*

[48] B. Ramstein, Few Body Syst. **59**, 143 (2018), *Studying Time-Like Electromagnetic Baryon Transitions with HADES in* πN *Reactions.*

[49] N. P. Samios, Phys. Rev. **121**, 275 (1961), *Dynamics of Internally Converted Electron-Positron Pairs.*

[50] H. Kobrak, Nuovo Cim. **20**, 1115 (1961), *Internal Pairs from* π^- *proton Interactions at rest.*

[51] S. Devons, P. Nemethy, C. Nissim-Sabat, E. Di Capua, and A. Lanzara, Phys. Rev. **184**, 1356 (1969), *Measurement of neutral- and charged-pion form-factor slopes.*

[52] Yu. K. Akimov *et al.*, Yad. Fiz. **13**, 748 (1971), *Observation of reaction* $\pi^-p \to e^+e^-n$ *at 275 MeV.*

[53] S. F. Berezhnev, L. S. Vertogradov, A. V. Demyanov, A. V. Kulikov, A. V. Kuptsov, G. G. Mkrtchyan, L. L. Nemenov, G. I. Smirnov, D. M. Khazins, and Yu. M. Chirkin, Yad. Fiz. **16**, 185 (1972), *Estimation of pion and nucleon form-factors from analysis of* $\pi^-p \to e^+e^-n$ *process at E(π kin)=275 MeV.*

[54] S. F. Berezhnev *et al.*, Yad. Fiz. **17**, 85 (1973), *On measuring differential cross-sections of inverse pion electroproduction* $(\pi^-p \to e^+e^-n)$ *close to delta(1236) resonance.*

[55] S. F. Berezhnev *et al.*, Yad. Fiz. **18**, 102 (1973), *Measurement of the pion and nucleon formfactors at the time - like four-momentum transfers k-squared=1.7, 2.2 and 2.9 f-squared.*

[56] S. F. Berezhnev, T. D. Blokhintseva, A. V. Demyanov, A. V. Kuptsov, V. P. Kurochkin, L. L. Nemenov, G. I. Smirnov, and D. M. Khazins, Sov. J. Nucl. Phys. **24**, 591 (1976), *The Measurement of the Pion and Nucleon Form-Factors in the Region of the Timelike 4-Momentum Transfers from 1.5 Inverse fm**2 to 3.0 Inverse fm**2*, [Yad. Fiz.24,1127(1976)].

[57] V. V. Alizade, S. F. Berezhnev, T. D. Blokhintseva, A. V. Demyanov, A. V. Kuptsov, V. P. Kurochkin, L. L. Nemenov, Z. P. Pustylnik, G. I. Smirnov, and D. M. Khazins, Sov. J. Nucl. Phys. **33**, 189 (1981), *Determination of Nucleon and Pion Form-factors by Analyzing the* $\pi^- p \to e^+e^-\pi$ *Reaction at* $E\ (\pi) = 164$ *MeV*, [Yad. Fiz.33,357(1981)].

[58] C. M. Hoffman, J. S. Frank, R. E. Mischke, D. C. Moir, J. S. Sarracino, P. A. Thompson, and M. A. Schardt, Phys. Rev. **D28**, 660 (1983), *A mesurement of* $\pi^- p \to ne^+e^-$ *AT 300 MeV/c AND A SEARCH FOR SCALAR AND VECTOR BOSONS HEAVIER THAN THE* π^0.

[59] H. Fonvieille *et al.*, Phys. Lett. **B233**, 60 (1989), *Inverse pion electroproduction at threshold:* $\pi^- p \to ne^+e^-$.

[60] H. Fonvieille *et al.*, Phys. Lett. **B233**, 65 (1989), *Dalitz Decay:* $\pi^0 \to \gamma e^+e^-$ *and the* π^0 *Electromagnetic Transition Form-factor.*

[61] M. N. Khachaturyan *et al.*, Phys. Lett. **24B**, 349 (1967), *Observation of the* e^+e *decay modes of neutral vector mesons.*

[62] V. Shklyar, H. Lenske, and U. Mosel, Phys. Rev. **C93**, 045206 (2016), 2π *production in the Giessen coupled-channel model.*

[63] D. M. Manley, R. A. Arndt, Y. Goradia, and V. L. Teplitz, Phys.Rev. **D30**, 904 (1984), *An Isobar Model Partial Wave Analysis of* $\pi N \to \pi\pi N$ *in the Center-of-mass Energy Range 1320-MeV to 1930-MeV.*

[64] S. Prakhov *et al.*, Phys.Rev. **C69**, 045202 (2004), *Measurement of* $\pi^- p \to \pi^0\pi^0\ n$ *from threshold to 750-MeV/c.*

[65] M. Kermani *et al.*, Phys. Rev. **C58**, 3431 (1998), $\pi\ \pi \to \pi\ \pi$ *cross-sections near threshold.*

[66] I. G. Alekseev *et al.*, Phys. Atom. Nucl. **61**, 174 (1998), *Study of the reaction* $\pi^-\ p$ *(polarized)* $\to \pi^-\ \pi^+\ n$ *on the polarized proton target at 1.78-GeV/c: Experiment and amplitude analysis*, [Nucl. Phys.B541,3(1999)].

[67] D. Manley and E. Saleski, Phys.Rev. **D45**, 4002 (1992), *Multichannel resonance parametrization of pi N scattering amplitudes.*

[68] M. Shrestha and D. Manley, Phys.Rev. **C86**, 055203 (2012), *Multichannel parametrization of* πN *scattering amplitudes and extraction of resonance parameters.*

[69] A. Anisovich *et al.*, Eur.Phys.J. **A48**, 15 (2012), *Properties of baryon resonances from a multichannel partial wave analysis.*

[70] H. Kamano, S. Nakamura, T. S. H. Lee, and T. Sato, Phys.Rev. **C88**, 035209 (2013), *Nucleon resonances within a dynamical coupled-channels model of* πN *and* γN *reactions.*

[71] http://gwdac.phys.gwu.edu/.

[72] F. Bulos *et al.*, Phys. Rev. Lett. **13**, 558 (1964), *Total Cross Sections and Angular Distributions for pi-p Charge Exchange in the Second and Third Resonance Regions.*

[73] F. Bulos *et al.*, Phys. Rev. **187**, 1827 (1969), *Charge exchange and production of eta mesons and multiple neutral pions in* π^- *p reactions between 654 and 1247 MeV/c.*

[74] A. Starostin *et al.*, Phys. Rev. **C72**, 015205 (2005), *Measurement of* $\pi^- p \to \pi^0 n$ *in the vicinity of the* η *threshold.*

[75] R. A. Burnstein, G. R. Charlton, T. B. Day, G. Quareni, A. Quareni-Vignudelli, G. B. Yodh, and I. Nadelhaft, Phys. Rev. **137**, B1044 (1965), $\pi^- p$ *Interactions at 683 MeV/c.*

[76] A. D. Brody *et al.*, Phys. Rev. **D4**, 2693 (1971), *Experimental results on the reactions* $\pi^- p \to \pi\pi N$ *in the center-of-mass energy range 1400-MeV to 2000-Mev*, [Erratum: Phys. Rev.D5,2899(1972)].

[77] T. W. Morrison, Ph.D. dissertation, The George Washington University, 2000.

[78] R. A. Arndt, W. J. Briscoe, T. W. Morrison, I. I. Strakovsky, R. L. Workman, and A. B. Gridnev, Phys. Rev. **C72**, 045202 (2005), *Low-energy* η *N interactions: Scattering lengths and resonance parameters.*

[79] Penner, G., Vector meson production and nucleaon resonance analysis in a coupled-channel approach, PhD, Justus Liebig University, Giessen, 2002.

[80] S. Prakhov *et al.*, Phys. Rev. **C72**, 015203 (2005), *Measurement of* $\pi^- p \to \eta n$ *from threshold to* $p_{\pi^-} = 747$ *MeV/c.*

[81] D. R. Marlow *et al.*, Phys. Rev. **C30**, 1662 (1984), *Pion Scattering From C and Ca at 800-MeV/c.*

[82] T. E. O. Ericson and W. Weise, *Pions and Nuclei* (Clarendon Press, Oxford, UK, 1988), Vol. 74.

[83] R. P. Redwine, in *17th INS International Symposium on Nuclear Physics at Intermediate Energy Tokyo, Japan, November 15-17, 1988* (World Scientific, Singapore, 1989), pp. 131–143.

[84] M. Thies, Nucl. Phys. **A382**, 434 (1982), *Quasielastic Pion Scattering on* ^{16}O*: A Comparison Between the* Δ *Hole Approach and a Standard First Order Calculation.*

[85] E. Oset, H. Toki, and W. Weise, Phys. Rept. **83**, 281 (1982), *Pionic modes of excitation in nuclei.*

[86] K. Aoki *et al.*, Phys. Rev. **C76**, 024610 (2007), *Elastic and inelastic scattering of pi+ and pi- on C12 at 995 MeV/c.*

[87] A. S. Clough *et al.*, Nucl. Phys. **B76**, 15 (1974), *Pion-Nucleus Total Cross-Sections from 88-MeV to 860-MeV.*

[88] B. W. Allardyce *et al.*, Nucl. Phys. **A209**, 1 (1973), *Pion reaction cross-sections and nuclear sizes.*

[89] T. Takahashi *et al.*, Phys. Rev. **C51**, 2542 (1995), π^- *12C elastic scattering above the Delta resonance.*

[90] M. Crozon, P. Chavanon, A. Courau, T. Leray, J. Narjoux, and J. Tocqueville, Nuclear Physics **64**, 567 (1965), *Etude de la diffusion π-noyau entre 500 et 1300 MeV.*

[91] J. W. Cronin, R. Cool, and A. Abashian, Phys. Rev. **107**, 1121 (1957), *Cross Sections of Nuclei for High-Energy Pions.*

[92] C. J. Gelderloos, J. T. Brack, M. D. Holcomb, M. V. Keilman, D. J. Mercer, R. J. Peterson, R. A. Ristinen, and A. Saunders, Phys. Rev. **C62**, 024612 (2000), *Reaction and total cross-sections for 400 MeV-500 MeV π^- on nuclei.*

[93] E. Oset, D. Strottman, H. Toki, and J. Navarro, Phys. Rev. **C48**, 2395 (1993), *Core polarization phenomena in pion nucleus charge exchange reactions above the Delta resonance.*

[94] A. P. Krutenkova *et al.*, Phys. Rev. **C72**, 037602 (2005), *Inclusive pion double charge exchange on O-16 above the delta resonance.*

[95] M. K. Jones *et al.*, Phys. Rev. **C48**, 2800 (1993), *Pion absorption above the Delta (1232) resonance.*

[96] R. J. Peterson *et al.*, Phys. Lett. **B297**, 238 (1992), *Quasifree pion single charge exchange at 500-MeV.*

[97] B. L. Clausen, R. A. Loveman, R. J. Peterson, R. A. Ristinen, J. L. Ullmann, and F. Irom, Phys. Rev. **C35**, 1028 (1987), *Δ production by pion charge exchange on complex nuclei.*

[98] S. G. Mashnik, R. J. Peterson, A. J. Sierk, and M. R. Braunstein, Phys. Rev. **C61**, 034601 (2000), *Pion induced transport of π mesons in nuclei.*

[99] J. D. Zumbro *et al.*, Phys. Rev. Lett. **71**, 1796 (1993), *Inclusive scattering of 500-MeV pions from carbon.*

[100] J. Ouyang, S. Hoeibraten, and R. J. Peterson, Phys. Rev. **C47**, 2809 (1993), *Effective number of protons for quasifree (π^-, π^0) at 500-MeV and 400-MeV.*

[101] J. Ouyang, S. Hoibraten, and R. J. Peterson, Phys. Rev. **C48**, 1074 (1993), *Isovector nuclear response in carbon.*

[102] B.-A. Li, W. Bauer, and C. M. Ko, Phys. Lett. **B382**, 337 (1996), *Pion transparency in 500-MeV C (π, π') reactions?*

[103] A. Rahav *et al.*, Phys. Rev. Lett. **66**, 1279 (1991), *Measurement of the C-12(π, 2π) reactions and possible evidence of a double Delta excitation.*

[104] N. Grion *et al.*, Nucl. Phys. **A492**, 509 (1989), *Pion Production by Pions in the ^{16}O (π^+, $\pi^+\pi^-$) Reaction at $T(\pi^+)$ = 280-MeV.*

[105] F. Bonutti *et al.*, Nucl. Phys. **A677**, 213 (2000), *The $\pi\pi$ interaction in nuclear matter from a study of the $\pi^+ A \to \pi^+\pi^+ A'$ reactions.*

[106] P. Camerini *et al.*, Nucl. Phys. **A735**, 89 (2004), *General properties of the pion production reaction in nuclear matter.*

[107] A. Starostin *et al.*, Phys. Rev. Lett. **85**, 5539 (2000), *Measurement of $\pi^0\pi^0$ production in the nuclear medium by π^- interactions at 0.408 GeV/c.*

[108] J. C. Peng, in *Eta meson production in pion induced reactions* (World Scientific, Tokyo, 1988), pp. 233–247.

[109] B. V. Krippa and J. T. Londergan, Phys. Lett. **B286**, 216 (1992), *Inclusive* $(\pi,\eta\ )$ *reactions on nuclei.*

[110] M. Kohno and H. Tanabe, Nucl. Phys. **A519**, 755 (1990), *Pion induced eta production on nuclei.*

[111] B. V. Krippa and J. T. Londergan, Phys. Rev. **C48**, 2967 (1993), *Inclusive and exclusive production of* η *mesons by pions.*

[112] G. Agakichiev *et al.*, Eur. Phys. J. **A41**, 243 (2009), *The High-Acceptance Dielectron Spectrometer HADES.*

[113] G. Kornakov, New advances and developments on the RPC ToF wall pf the HADES experiment at GSI, PhD thesis, Universidad de Santiago de Compostela, 2012.

[114] J. Adamczewski-Musch *et al.*, Eur. Phys. J. **A53**, 188 (2017), *A facility for pion-induced nuclear reaction studies with HADES.*

[115] P. Sellheim, PhD, university of Frankfurt, 2017.

[116] J. Michel, Development and Implementation of a New Trigger and Data Acquisition System for the HADES Detector, PhD thesis, Johann Wolfgang Goethe Universität, 2012.

[117] M. L. Benabderrahmane *et al.*, Phys. Rev. Lett. **102**, 182501 (2009), *Measurement of the in-medium K0 inclusive cross section in pi- -induced reactions at 1.15-GeV/c.*

[118] J. Diaz *et al.*, Nucl. Instrum. Meth. **A478**, 511 (2002), *Design and commissioning of the GSI pion beam.*

[119] U. Rohrer, PSI Graphic Transport Framework by U. Rohrer based on a CERNSLAC- FERMILAB version by K.L. Brown et al, 2007.

[120] E. Atomssa, private communication.

[121] J. Markert, Untersuchung zum Ansprechverhalten der Vieldraht-Driftkammern niedriger Massenbelegung des HADES-Experiments, PhD Thesis Johann Wolgang Goethe-Universität Frankfurt, 2005.

[122] L. Fabbietti , Study of the $e^{+}e^{-}$ pair acceptance in the dilepton spectrometer HADES, Technischen Universität München, PHD, 2009.

[123] S. Constantinescu, S. Dita, and D. Jouan, Study of the estimation of the combinatorial muon pair background, Report PNO–DER–96–01, 1996.

[124] M. Gazdzicki and M. I. Gorenstein, Background subtraction from the dilepton spectra in nuclear collisions, arXiv:hep-ph/0003319 [hep-ph], 2000.

[125] D. A. Geffen, Phys. Rev. **125**, 1745 (1962), *Reaction,* $\pi^{-}+p \rightarrow e{+}{+}e{-}{+}n$*, as a Means of Measuring the Electromagnetic Form Factor of the Charged Pion.*

[126] M. P. Rekalo, Soviet. Jour. of Nucl. Phys. **1**, 760 (1965), *On a possibility of determining nucleon from factors for time-like measurements.*

[127] Yu. S. Surovtsev, T. D. Blokhintseva, P. Bydzovsky, and M. Nagy, Phys. Rev. **C71**, 055205 (2005), *Electro, photo and inverse electroproduction of pions in the first resonance region.*

[128] Lykasov, G., private communication, Orsay, 2009.

[129] A. I. Titov and B. Kämpfer, Eur. Phys. J. **A12**, 217 (2001), *Isoscalar-Isovector Interferences in* $\pi N \to Ne^{+}e^{-}$ *Reactions as a Probe of Baryon Resonance Dynamics.*

[130] M. Lutz, B. Friman, and M. Soyeur, Nuclear Physics A **713**, 97 (2003.).

[131] M. Zetenyi and G. Wolf, Phys. Rev. **C86**, 065209 (2012), *Dilepton production in pion–nucleon collisions in an effective field theory approach.*

[132] M. I. Krivoruchenko and A. Faessler, Phys. Rev. **D65**, 017502 (2002), *Comment on Delta radiative and Dalitz decays.*

[133] G. Ramalho and M. T. Pena, Phys. Rev. **D95**, 014003 (2017), γ**N→N*(1520) form factors in the timelike regime.*

[134] GIBUU transport model http://gibuu.physik.unigiessen. de.

[135] V. V. Sarantsev, JPS Conf. Proc. **10**, 010005 (2016), *Properties of Baryons from Bonn-Gatchina Partial Wave Analysis.*

[136] U. Thoma *et al.*, Phys. Lett. **B659**, 87 (2008), *N* and Delta* decays into N* $\pi^0\pi^0$.

[137] V. Sokhoyan *et al.*, Eur. Phys. J. **A51**, 95 (2015), *High-statistics study of the reaction* $\gamma p \to p\ 2\pi^0$, [Erratum: Eur. Phys. J.A51,no.12,187(2015)].

[138] V. V. Sarantsev, private communication.

[139] W. Przygoda, EPJ Web Conf. **130**, 01021 (2016), *Production and decay of baryonic resonances in pion induced reactions.*

[140] A. Shafi *et al.*, Phys. Rev. **C70**, 035204 (2004), *Measurement of inverse pion photoproduction at energies spanning the N(1440) resonance.*

[141] P. T. Mattione *et al.*, Phys. Rev. **C96**, 035204 (2017), *Differential cross section measurements for* $\gamma n \to \pi^- p$ *above the first nucleon resonance region.*

[142] E. Speranza, M. Zetenyi, and B. Friman, Phys. Lett. **B764**, 282 (2017), *Polarization and dilepton anisotropy in pion-nucleon collisions.*

[143] M. Zetenyi and G. Wolf, Phys. Rev. **C67**, 044002 (2003), *Baryonic contributions to the dilepton spectrum of nucleon nucleon collisions.*

[144] L. Landsberg, Phys. Rept. **128**, 301 (1985), *Electromagnetic Decays of Light Mesons.*

[145] O. Buss, T. Gaitanos, K. Gallmeister, H. van Hees, M. Kaskulov, O. Lalakulich, A. B. Larionov, T. Leitner, J. Weil, and U. Mosel, Phys. Rept. **512**, 1 (2012), *Transport-theoretical Description of Nuclear Reactions.*

[146] M. I. Krivoruchenko, B. V. Martemyanov, A. Faessler, and C. Fuchs, Annals Phys. **296**, 299 (2002), *Electromagnetic transition form factors and dilepton decay rates of nucleon resonances.*

[147] J. H. Koch, N. Ohtsuka, and E. J. Moniz, Annals Phys. **154**, 99 (1984), *Nuclear photoabsorption and compton scattering at intermediate-energy.*

[148] M. F. M. Lutz, G. Wolf, and B. Friman, Nucl. Phys. **A706**, 431 (2002), *Scattering of vector mesons off nucleons.*

[149] M. Post, W. Peters, and U. Mosel, Coherent photoproduction of dileptons on light nuclei: A New means to learn about vector mesons, Proceedings, 37th International Winter Meeting on Nuclear Physics (Bormio 1999), nucl-th/990300, 1999.

[150] R. A. Williams, C. R. Ji, and S. R. Cotanch, Phys. Rev. **C48**, 1318 (1993), *Kinematically accessible vector meson resonance enhancements in p (K^-, e^+ e^-),* Λ*,* Σ^0*,* Λ *(1405).*